Studies of earthquakes and microearthquakes using near-field seismic and geodetic observations

A thesis submitted for the degree of Doctor of Philosophy

Thomas B. O'Toole
University College

Supervised by:
Prof. J.H. Woodhouse, FRS
Department of Earth Sciences
University of Oxford

Trinity Term 2013

Studies of earthquakes and microearthquakes using near-field seismic and geodetic observations

A thesis submitted for the degree of Doctor of Philosophy

Thomas B. O'Toole
University College

Trinity Term 2013

Abstract

The Centroid–Moment Tensor (CMT) method allows an optimal point-source description of an earthquake to be recovered from a set of seismic observations, and, for over 30 years, has been routinely applied to determine the location and source mechanism of teleseismically recorded earthquakes. The CMT approach is, however, entirely general: any measurements of seismic displacement fields could, in theory, be used within the CMT inversion formulation, so long as the treatment of the earthquake as a point source is valid for that data. We modify the CMT algorithm to enable a variety of near-field seismic observables to be inverted for the source parameters of an earthquake.

The first two data types that we implement are provided by Global Positioning System receivers operating at sampling frequencies of 1 Hz and above. When deployed in the seismic near field, these instruments may be used as long-period–strong-motion seismometers, recording displacement time series that include the static offset. We show that both the displacement waveforms, and static displacements alone, can be used to obtain CMT solutions for moderate-magnitude earthquakes, and that performing analyses using these data may be useful for earthquake early warning.

We also investigate using waveform recordings — made by conventional seismometers deployed at the surface, or by geophone arrays placed in boreholes — to determine CMT solutions, and their uncertainties, for microearthquakes induced by hydraulic fracturing. A similar waveform inversion approach could be applied in many other settings where induced seismicity and microseismicity occurs.

Studies of earthquakes and microearthquakes using near-field seismic and geodetic observations

A thesis submitted for the degree of Doctor of Philosophy

Thomas B. O'Toole
University College

Trinity Term 2013

Extended Abstract

The Centroid–Moment Tensor (CMT) method allows an optimal point-source description of an earthquake to be recovered from a set of seismic observations, and, for over 30 years, has been routinely applied to determine the location and source mechanism of teleseismically recorded earthquakes. The CMT approach is, however, entirely general: any measurements of seismic displacement fields could, in theory, be used within the CMT inversion formulation, so long as the treatment of the earthquake as a point source is valid for that data, and we have some method for forward modelling the observations. We use the CMT algorithm to invert a variety of near-field seismic observables for the source parameters of an earthquake.

Over recent years, the development of space based geodetic techniques has enabled motions of the Earth's surface to be quantified with unprecedented accuracy. For seismologists, Synthetic Aperture Radar Interferometry (InSAR) and the Global Positioning System (GPS) represent new tools with which to study earthquakes and potentially also earth structure. Either technique can be used to measure the static displacement field caused by an earthquake with millimetric precision.

Recently, it has been shown that continuously operating GPS receivers with sampling rates of 1 Hz and higher can be used as long-period–strong-motion seismometers when they are deployed in the seismic near-field. The displacement time series recorded by these instruments represent a new type of seismic waveform data which contain the signal

both of the propagating seismic waves, and of the permanent ground displacement caused by the earthquake. The problem of calculating static and dynamic displacements is thus of interest, and is a prerequisite if we wish to use near-field geodetic and seismic data, in particular continuous GPS time series, to study the seismic source.

We present a new method for calculating dynamic and static displacements arising from a buried point source in a plane layered, isotropic, elastic half-space. We avoid the well-known problem of the loss of precision in solutions for P-SV wave motion by integrating a system of minor vector equations with solutions constructed from pairs of solutions to the equations of motion in the frequency–wavenumber domain. The resulting algorithm is efficient, and numerically stable at zero frequency and at high frequencies, and thus can be used to compute complete synthetic seismograms — and their partial derivatives with respect to source parameters — which include the static offset. An advantage of this approach is that a single algorithm can be used to model both seismological and geodetic measurements of ground motion. If the calculation is only carried out at 0 Hz, we obtain an image of the static surface deformation, and thus our method also has potential applications in the modelling of coseismic surface displacements measured with, for example, InSAR.

We show that both GPS-measured displacement waveforms, and static displacements alone, can be used to recover the mechanism and centroid coordinates of an earthquake. Our inversion approach is identical to that of the "classical" CMT algorithm, except that we forward model the observables using the minor vector method, which is amenable to the efficient computation of synthetic GPS data — seismograms and static offsets — and their partial derivatives. We demonstrate the validity of our approach by calculating CMT solutions using 1 Hz GPS data for two recent earthquakes in Japan. These results are in good agreement with independently determined source models of these events. With wider availability of data, we envisage the CMT algorithm providing a tool for the systematic inversion of GPS waveforms, as is already the case for teleseismic data. Furthermore, this general inversion method could equally be applied to other near-field earthquake observations such as those made using accelerometers.

The application of our inversion algorithm to static displacement data is demonstrated using static offsets observed after the 4 April 2010, M_{W} 7.2 El Mayor-Cucapah, Mexico, earthquake. The efficiency of our algorithm for forward modelling static displacements in a layered elastic medium allows the inversion to be performed in real-time on a single processor without the need for precomputed libraries of excitation kernels; we present simulated real-time results for the El Mayor-Cucapah earthquake. The only *a priori* information that our inversion scheme needs is a crustal model and approximate source location, both of which can be obtained in real time. The method proposed here may therefore represent an improvement on existing early warning approaches which rely on foreknowledge of fault locations and geometries. It may also be useful for rapidly providing a first order description of the seismic event, which can then be used as input for more sophisticated finite source modelling.

Another area where a real-time knowledge of earthquake source parameters is desirable is the monitoring of induced seismicity. We investigate two applications of our modified CMT algorithm to the problem of monitoring shale gas hydraulic fracturing operations, which cause microearthquake and potentially also small, felt, events. A knowledge of the source mechanisms of microseismic events provides a wealth of information about the subsurface. What is the state of stress in the reservoir? How are the fractures orientated, and what size are they? Is seismic energy being generated by shear on a plane, tensile failure, or some other mechanism? Since such information can be used to inform and optimise well treatment operations, there is a pressing need to develop new methods for determining earthquake source parameters from microseismic data. In particular, the small size of typical microseismic datasets leads us to investigate the possibility of using the whole waveform — rather than just body wave amplitude and polarity measurements, which have hitherto been mostly commonly used — for the purpose of modelling the microseismic source.

The first application relates to a hydraulic stimulation carried out at Cotton Valley, Texas, USA, which was monitored by two arrays of three component geophones deployed in observation wells adjacent to the treatment well. The possibility of performing moment

tensor inversion using data from a single monitoring well is important for downhole microseismic monitoring projects, because if it were possible much more information about the fracturing process could be obtained at much less expense. Preliminary inversions suggest that monitoring using a single downhole array cannot be used to recover reliable moment tensor solutions, at least for the receiver geometries deployed at Cotton Valley. We investigate the conditions under which inversions of single well data might be possible.

In the UK, shale gas hydraulic fracturing is of public and political interest because of its association with two felt earthquakes that occurred in Blackpool shortly after the stimulation of a nearby well. The second application of our waveform inversion algorithm is an investigation of the induced seismicity at Blackpool. Again, the dataset is limited: only four channels of waveform data from only two local seismic stations are available. We determine CMT solutions using this small dataset for a number of events with $0.4 < M_w < 2.3$, finding that failure is dominated by pure strike-slip mechanisms. We also investigate the uncertainties on the recovered source parameters, and use inversions of synthetic datasets to investigate how these errors might, in future, be reduced.

While our focus in this thesis has been on using GPS data and microseismic data to study seismic sources, the methods developed are general and could equally be applied to determine CMT solutions from other surface and borehole waveform observations. We hope that they will be of some use to future researchers.

Contents

Acknowledgements

It is only now that I reflect back on the past three or so years that I realise quite how much I owe to so many people for their help in getting me to the end of this thesis. I am sure that in the following I have forgotten many people who are deserving of mention: my apologies to you all. Believe me when I say that all of your help was greatly appreciated!

Firstly, I would like to thank John Woodhouse for his constant support and willingness to indulge my wandering thoughts, which have taken this project a long way away from where it was originally supposed to be headed. I am also immensely grateful to Andrew Valentine, who — as a friend and collaborator — has always been willing to give up his time to talk seismology, answer questions about code, and read a draft of this thesis. Andrew has also proved an excellent host for my three trips to Utrecht; I hope that there will be many more in years to come!

Financial support for my research has been provided by the Natural Environment Research Council. This funding has afforded me the opportunity to attend a number of conferences at home and abroad, and to visit several other departments. I have enjoyed all of these experiences, and this thesis has undoubtedly been improved as a result of the many interactions with other researchers on these occassions.

A number of past and present members of the Oxford geodesy group have provided much help over the course of my DPhil. John Elliott was kind enough to give me the InSAR data briefly examined in Chapter 2. In my early forays into GPS seismology, Kirill Palamartchouk gave a great deal of assistance in helping me understand these data,

and processed the GPS waveforms from an earthquake in Greece which are also used in Chapter 2 of this thesis.

In fact, none of the GPS data used in this thesis were processed by me. Thanks go to Reiji Kobayashi and Yusuke Yokota for their generosity in supplying the GPS waveforms examined in Chapter 3 in a format that could be readily used by seismologists. Similarly, Richard Allen also unselfishly shared with me the results of his static displacement picking algorithm for the El Mayor Cucapah earthquake; these data form the basis of the analyses presented in Chapter 4.

A good deal of credit for the parts of this thesis relating to hydraulic fracturing lies with Michael Worthington, who originally got me thinking about industrial applications of my research. Michael also put me in touch with Mike Kendall and James Verdon at Bristol. They — along with everyone else in BUMPS — have welcomed me warmly into their group, and have given me a great deal of help accessing and getting to grips with microseismic data.

In Oxford, I have enjoyed sharing an office with Sam Weatherley, Owen Weller, Linhao Fang, Cedric Twardzik, Teresa Kyrke-Smith, David Al-Attar, Eoin McManus, Paul Savage, Ros Armitage and Chao Liu. In addition to proving a worthy adversary on the squash court, I am particularly grateful to David for the many interesting and informative conversations — about seismology and much more — that we have had. Numerous other people have made the department a pleasant place to work in, and I would like to thank Mark Bourne in particular for providing welcome distractions from work when they were needed. Sam was also a great housemate in Stockmore Street, along with Ben Mansfield, Paul Anastasiades, Rob Winter, and Thomas Menauer. Some day we will get round to building that pizza oven!

It has been refreshing to leave Oxford on fairly regular occassions to see friends around the country, and especially Emma down in London. Thank you for all of your love over the years, and I am sorry that you have been neglected in the past months while I have been writing this thesis.

The final note of thanks goes to my parents and family, who have supported me throughout my education. I am especially grateful to my grandfather, Thomas Simcock, for instilling in me an interest in science from my earliest years, and for his curiosity about my work. It has been great fun seeing my brothers Sam and Richard whenever that has been possible as — apart from anything else — I can seldom persuade others to join me in a game of Settlers of Catan. Even though my sister Josie has been in Australia for the duration of my DPhil, she has always reminded me that there is a whole lot of world beyond the seismolab door.

Chapter 1

Introduction

Seismologists are faced with two fundamental problems: understanding the nature of earthquake sources, and determining the structure of the Earth. The inaccessible nature of Earth's interior means that the elastic waves generated by an earthquake are one of the principal means for elucidating the earthquake source process that generated these waves and internal structure of the Earth. To study seismic sources and earth structure, we therefore require some measurements of earthquake displacement fields and some physical theory to explain these observations. Progress in quantitative seismology is consequently driven by the development of new and improved instruments for recording seismic deformations, combined with the refinement of theories for calculating the deformations expected for a particular source and structural model. If we have some seismic data and a technique for forward modelling these data, we can pose the inverse problem and try to solve it, *i.e.* determine the set of source and structural models that best explain the observations subject to the modelling and data uncertainties. In practice, the solution of many seismological inverse problems requires significant computational effort, and so the development of efficient computer programs for processing and modelling seismic data — along with seemingly inexorable improvements in the performance of computer hardware — must also take some credit for the current state of the art in seismology.

Since the radiated seismic displacement field depends on the location, size and orientation of the causative fault, as well as the properties of the medium through which the waves have propagated, the source and structure problems are intimately related, and should, strictly speaking, be investigated simultaneously. In some circumstances, however, we can decouple the two by assuming that either the source or structure parameters are known *a priori*. For example, in active source surveys of hydrocarbon reservoirs — where explosives, air guns or vibrator trucks are used to excite seismic waves — the location and timing of the sources are known, simplifying the inverse problem for earth structure.

For natural earthquakes, we obviously cannot exert any control over the nature of the seismic source. However, various seismological, geophysical and geological data have been used to construct models of the gross depth-varying structure of the earth (e.g. Dziewonski and Anderson, 1981; Kennett *et al.*, 1995), the 3D structure of the mantle at high resolution (e.g. Woodhouse and Dziewonski, 1984; Ritsema *et al.*, 2011), and variations in crustal structure globally (e.g Mooney *et al.*, 1998). As a consequence, if we are primarily interested in studying the seismic source, we may take the structural model as being known, although it should be noted that if there are errors in the assumed model then these will impact our results. In this thesis, we will assume that a reasonable structural model is always known, as we are exclusively concerned with developing new techniques for determining seismic source parameters.

1.1 Seismic observables

The first reported seismogram recordings at teleseismic distance were made by von Rebeur-Paschwitz (1889) in Potsdam and Wilhelmshaven, Germany, after an earthquake in Japan on April 18, 1889. Ground motions were recorded as a function of time using a horizontal pendulum with an attached mirror which reflected light onto a drum covered in photographic paper rotating at a known rate and marked at hourly intervals (Dewey and Byerly, 1969). In the time since these first observations, great progress has been made in the design and manufacture of precision instruments for recording ground motions, and

in the systematic deployment of instrument networks globally. Modern broadband digital seismometers are capable of recording ground motion (velocity or acceleration) faithfully over more than 3 orders of magnitude in frequency and over large dynamic ranges without saturating (Dziewonski and Romanowicz, 2007). Global networks of such instruments, operated by various agencies, combined with regional and local networks equipped with instruments capable of handling strong ground motions, underpin the whole endeavour of seismology.

In addition to these established and well known waveform recording techniques, a number of new tools for observing seismic displacement fields have emerged over recent years. For example, Interferometric Synthetic Aperture Radar (InSAR) measurements of line of sight displacements — obtained by differencing the phase of two radar images of the ground acquired on successive orbits of a satellite — have enabled coseismic and post-seismic ground motions to be quantified with millimetric accuracy at unprecedented spatial resolution (Bürgmann *et al.*, 2000). These measurements are complemented by 3D measurements of the same surface displacement fields made by Global Positioning System (GPS) receivers. Both of these techniques relate to the long term deformation of the Earth, and so are often considered as part of geodesy, although the line between geodesy and seismology is becoming increasingly blurred (Lay and Kanamori, 2011).

This thesis aims to use a new type of seismic observation — displacement time-series measured by continuously recording Global Positioning System (GPS) receivers — and apply some that are not so new — static displacements (again measured by GPS networks), and high frequency waveforms observed by surface or buried seismic arrays — to study earthquake sources. Displacement waveforms measured by GPS are being observed increasingly often as more permanent GPS networks are deployed, and as receiver sampling rates are increased to 1 Hz and higher. Uniquely, these displacement seismograms contain the permanent offset of the GPS receiver that results from the earthquake, which poses a challenge for seismologists who are not used to dealing with signals containing a static displacement. However, these recordings of seismic waves made using high-rate GPS receivers have, to some extent, been treated as a curiosity rather than a new type of

seismic observable that could provide valuable information about earthquake sources and earth structure. In this thesis, we hope to redress the part of this problem relating to the seismic source by developing a framework that should enable GPS waveform data to be inverted routinely for the centroid and moment tensor of an event.

Our approach mimics the Centroid–Moment Tensor (CMT) algorithm (Dziewonski *et al.*, 1981), which has been applied to more conventional teleseismic waveform datasets with great success, most notably through the Global CMT project[1], which — as of 31 January 2013 — had calculated source parameters for 38,574 events, with the catalog growing at a rate of about 5 events per day. Using high-rate GPS data to generate CMT solutions may be useful, beyond pure academic interest, in the context of earthquake early warning, as GPS instruments sense the permanent displacement caused by an earthquake, and so can be used to compute accurate moment magnitudes and slip distributions relatively quickly after an earthquake has occurred (e.g. Blewitt *et al.*, 2009). We therefore proceed to investigate whether just the static displacement field measured by GPS receivers can be treated within the same inversion framework as that developed for GPS waveform data, and whether these data could be inverted to provide information about the earthquake in near real time.

Ultimately, we would like to improve our sampling of the seismic displacement field in both space and frequency through simultaneous inversion of seismic and geodetic earthquake observations (e.g. Lay, 2011). The CMT inversion formulation is well suited to a straightforward implementation of joint inversions, and so a first step towards this aim is to carry out inversions of GPS waveforms and static displacements alone. The use of these new data — measurements of ground displacements that are independent of the broadband seismometer recordings conventionally used for CMT inversions — may be of great value in quantifying and reducing uncertainties in earthquake source parameters determined using long-period teleseismic data. Global CMT inversions are, for example, known to have location errors of at least 10 km both laterally and in depth (Hjörleifsdóttir

[1] http://www.globalcmt.org/

and Ekström, 2010); near-field data will likely enable stronger constraints to be placed on the centroid position.

Furthermore, since the CMT approach is general, any seismic observable which we can forward model can also be inverted. As a consequence, our adapted inversion algorithm may also be applied to other near-field seismic observations, provided that instruments remain on scale (*i.e.* do not clip) during an earthquake. This thesis therefore concludes with some attempts at inverting high frequency seismograms — recorded during man-made microearthquakes caused by hydraulic fracturing — to recover the location and mechanism of these events. Such information may be useful from an induced seismicity hazard perspective, but is also valuable for understanding the fracturing process itself and optimizing the injection operations.

The different data types used in this thesis are described in more detail in the introductory sections of the relevant chapters. Although our motivations for using these data types to study the seismic source are as diverse as the data themselves are, the common theme running through this thesis is the parameterization of earthquakes and microearthquakes as point moment tensor sources, and the rest of this chapter forms an introduction to the moment tensor description of the seismic source.

1.2 The moment tensor

The radiation of seismic energy during an earthquake is almost always due to in-plane shear failure occurring on a planar fault surface (Beroza and Kanamori, 2007). A common undertaking in the field of earthquake seismology is to use recordings of the radiated wavefield to reconstruct the spatial and temporal evolution of slip on a fault of finite dimension and assumed orientation through kinematic (e.g. Robinson and Cheung, 2010; Twardzik *et al.*, 2012) or dynamic modelling (e.g. Barbot *et al.*, 2012). Such an undertaking is, in general, challenging, due to the large number of unknowns and limited data, often leading to highly non-unique solutions (e.g. Das and Kostrov, 1994).

Alternatively, we may consider only the part of the seismic signal that is long period and has large wavelength with respect to the rupture duration and dimensions, since this allows us to treat the earthquake as a point source, with energy being released at a single point in time and space. The definition of long period and large wavelength depends on the size of the earthquake being examined. For example, CMT analyses of teleseismic earthquakes bigger than M_w 5.0 typically use seismograms filtered in a pass band below $\frac{1}{45}$ Hz. This suggests that *large wavelengths* are those greater than ~ 100 km and *long periods* are those beyond ~ 45 s for moderate to large magnitude events. Longer wavelength data are less sensitive to velocity anomalies of a fixed size than are shorter wavelengths, and so using low frequency data also reduces the impact of velocity model errors on the recovered solution. A particularly convenient point-source parameterization for an earthquake or general seismic source is given by the so-called moment tensor.

The concept of the seismic moment tensor arises out of normal mode theory (see, for example Gilbert and Dziewonski, 1975). The equations of motion for the displacement field of a continuum, varying in space $\mathbf{x}$ and time t, $\mathbf{u}(\mathbf{x}, t)$ can be written (Dziewonski and Woodhouse, 1983a)

$$\rho_0 \ddot{\mathbf{u}} = \mathscr{H}\mathbf{u} + \mathbf{f} \tag{1.1}$$

where $\rho_0 = \rho_0(\mathbf{x})$ is the density at some initial time, $\dot{\mathbf{u}} = \partial_t \mathbf{u}$, and $\mathscr{H}$ is a linear integro-differential operator whose exact form depends on the physics of the problem under consideration and is not important here, although an explicit expression can be found in, for example, Dziewonski and Woodhouse (1983a, equation 2.1.18). For seismic displacement fields, we require an appropriate choice for $\mathbf{f}(\mathbf{x}, t)$ such that it is the force distribution which gives rise to the same displacement field as the true physical source — $\mathbf{f}$ is the body force equivalent of the earthquake. A seismic event occurring as pure shear on a planar discontinuity can be replaced by a force double couple (Burridge and Knopoff, 1964). The body force equivalent of the most general point earthquake source is obtained from the moment tensor (Gilbert and Dziewonski, 1975), as we show below.

Following Backus and Mulcahy (1976), we can write the general constitutive law for a

linearly elastic medium with pre-stress as

$$t_{ij} = d_{ijkl}\partial_l u_k \,, \tag{1.2}$$

where $t_{ij}(\mathbf{x}, t)$ is the stress tensor, $d_{ijkl} = d_{ijkl}(\mathbf{x})$ is the elastic tensor, ∂_l is the differential operator and summation over repeated indices is assumed. Since the earthquake itself represents a failure of this linear elastic law, to completely specify the state of stress in the medium we write

$$t_{ij} = d_{ijkl}\partial_l u_k - \Gamma_{ij} \,. \tag{1.3}$$

This expression defines the stress glut tensor Γ_{ij}, which, from the symmetries of the stress and elastic tensors, we see is also a symmetric tensor field. The stress glut is non-zero only in a small volume around the source — the so-called source region — where stress is not linearly related to strain by (1.2). From (1.1) and the definition of $\mathscr{H}$, it can be shown that the equivalent body force $\mathbf{f}$ is given by the divergence of the stress glut

$$f_i = -\partial_j \Gamma_{ij} \,, \tag{1.4}$$

that is the stress glut can be used to completely specify the action of the source.

The elastic displacement field due to a general source may be written as an expansion over the set of normal-mode eigenfunctions $\mathbf{s}_k(\mathbf{x})$ (Dziewonski and Woodhouse, 1983a)

$$\mathbf{u}(\mathbf{x}, t) = \sum_k a_k(t)\mathbf{s}_k(\mathbf{x}) \,, \tag{1.5}$$

where the index k references a normal mode of particular angular order, radial order, azimuthal order and mode type (spheroidal or toroidal). Since the normal-mode eigenfunctions are independent of the forcing, and can be computed for a known earth model, the dependence of displacement on the force term enters only via the expansion coefficient $a_k(t)$

$$a_k(t) = \int_{t_1}^{t_2} \int_{V_s} \dot{\Gamma}_{ij}(\mathbf{x}', t) h_k(t - t') \bar{e}_{ij}^{(k)} \, \mathrm{d}^3 x' \, \mathrm{d}t' \tag{1.6}$$

where $h_k(t)$ depends on the normal-mode eigenfrequency and attenuation, and $\mathbf{e}^{(k)}$ is the

strain tensor in the k-th mode with the overbar denoting complex conjugation. From (1.6), it is clear that, although the unknown spatio–temporal variations of the stress glut may be arbitrarily complex, the expansion coefficient — and hence seismic radiation — depends only on the integral of the stress glut over the source region V_s and time interval $[t_1, t_2]$ during which the source acts, that is it depends only on the average properties of the stress glut in the region where it is non zero. Approximating the integrand in (1.6) via its Taylor series expansion about some point $(\mathbf{x}_s, t_s)$ lying in the source region close to the origin time of the earthquake, we obtain to first order (Dziewonski and Woodhouse, 1983a)

$$a_k(t) = h_k(t - t_s) \left[M_{ij}^{(0,0)} \bar{e}_{ij}^{(k)} + M_{ijl}^{(1,0)} \bar{e}_{ij,l}^{(k)} \right] - \dot{h}_k(t - t_s) \left[M_{ij}^{(0,1)} \bar{e}_{ij}^{(k)} \right] \tag{1.7}$$

with the first three spatio-temporal glut moments defined (Backus, 1977)

$$M_{ij}^{(0,0)} = \int_{t_1}^{t_2} \int_{V_s} \dot{\Gamma}_{ij}(\mathbf{x}', t) \, \mathrm{d}^3x' \, \mathrm{d}t' \tag{1.8}$$

$$M_{ij,p}^{(1,0)} = \Lambda_{ijl}(\mathbf{x}) = \int_{t_1}^{t_2} \int_{V_s} \dot{\Gamma}_{ij}(\mathbf{x}', t)(x_l - x_l^{(s)}) \, \mathrm{d}^3x' \, \mathrm{d}t' \tag{1.9}$$

$$M_{ij}^{(0,1)} = H_{ij}(t) = \int_{t_1}^{t_2} \int_{V_s} \dot{\Gamma}_{ij}(\mathbf{x}', t)(t' - t_s) \, \mathrm{d}^3x' \, \mathrm{d}t' \,, \tag{1.10}$$

where for clarity we have used $x_l^{(s)}$ to denote the components of $\mathbf{x}_s$. The first of these expressions, corresponding to the zeroth order glut moment, is what is commonly referred to as *the* seismic moment tensor, $\mathbf{M}$. We may write the displacement field, with the source given in terms of the six independent elements of the moment tensor alone, via (Gilbert, 1970, 1973)

$$u(\mathbf{x}, t) = \sum_k h_k(t - t_s) \mathbf{M} : \bar{\mathbf{e}}^{(k)}(\mathbf{x}_s) s_k(\mathbf{x}) \,, \tag{1.11}$$

which corresponds to the assumption that $h(t - t_s)\mathbf{e}(\mathbf{x})$ is actually constant over the source region and duration, allowing the higher order terms in (1.6) to be discarded (Dziewonski and Woodhouse, 1983a). This assumption is approximately true if we examine displacements that have long periods and large wavelengths compared to the temporal and spatial

dimensions of the source, and for true point-sources we can write

$$\dot{\mathbf{\Gamma}}(\mathbf{x}, t) = \mathbf{M}\delta^3(\mathbf{x} - \mathbf{x}_s)\delta(t - t_s)\,, \tag{1.12}$$

where δ is the Dirac delta function, which can be used in (1.4) to give the equivalent body force for a point earthquake source. The Global CMT algorithm typically uses low frequency body and surface wave data filtered to contain periods longer than 45 s and 135 s respectively (Ekström *et al.*, 2012), making the point source assumption valid for all but the greatest earthquakes. For example, the Boxing Day 2004 great Sumatra earthquake broke a ~ 1200 km fault (Banerjee *et al.*, 2005) with a total rupture duration of 300–600 s (Ammon *et al.*, 2005), and so, even using long period data, source finiteness had to be taken into account in CMT analyses of this event. For this purpose, Tsai (2005) parameterized the Sumatra earthquake as a line of moment tensor sources whose action was delayed according to the estimated time for the unilateral rupture to reach the centroid position of each moment tensor. Alternatively, finite source effects can be examined through the second and higher order moments (e.g McGuire *et al.*, 2002). We also note also that the moment tensor is symmetric, which follows from the symmetry of the stress glut tensor.

The symmetry of the moment tensor arises for indigenous sources — those that do not involve the operation of any forces that are external to the earth (Woodhouse and Deuss, 2007) — from the requirement that no net force and no net torque is exerted by the source. These conditions lead to a physical interpretation of each element of the moment tensor as a force couple. The diagonal elements are then force dipoles acting along each coordinate axis, with the off-diagonal elements defining force couples acting along, and offset in, each combination of coordinate directions (see Figure 1.1).

The fact that the moment tensor is symmetric and real means that it possesses a set of three real eigenvalues λ_i and orthogonal eigenvectors. The eigendecomposition of $\mathbf{M}$ therefore defines a set of force dipoles acting along the principal axes with moment equal to the corresponding eigenvalues, and so is useful for giving a physical interpretation of the moment tensor. For example, a pure double couple source will have eigenvalues $[\lambda_1, 0, -\lambda_1]$

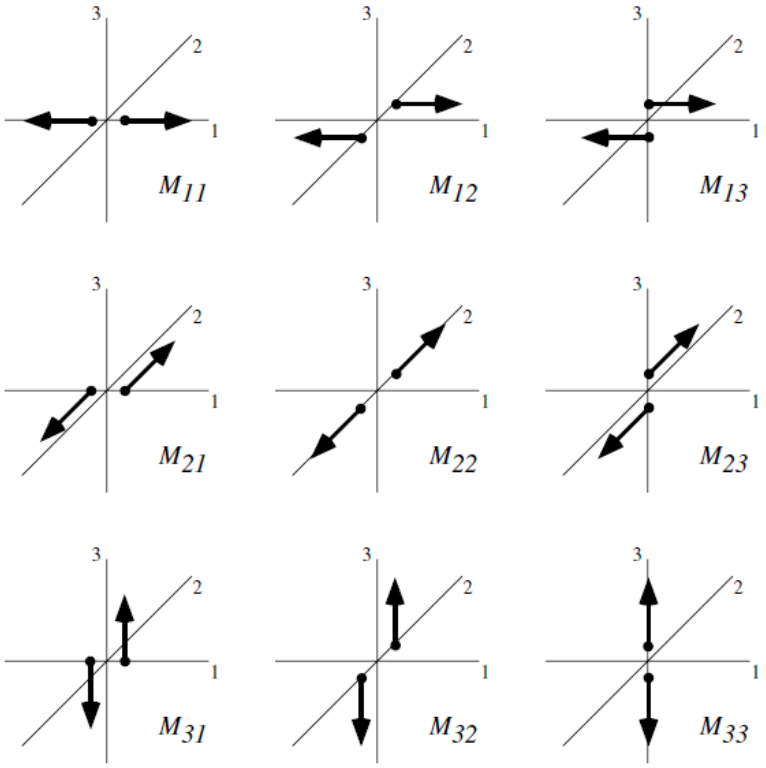

Figure 1.1: The nine force couples corresponding to the elements of the moment tensor, which can be used to describe a body force equivalent of a general point source (reproduced from Shearer, 2009, with kind permission of Cambridge University Press).

with the corresponding eigenvectors defining the direction of the compression, null and tension axes respectively.

Although there are, in theory, an infinite variety of moment tensor decompositions, we will later make use of a particularly common decomposition (see, for example Shearer, 2009), given by

$$\mathbf{M} = \mathbf{M}^{\mathrm{ISO}} + \mathbf{M}' \tag{1.13}$$

where we have an isotropic moment tensor $\mathbf{M}^{\mathrm{ISO}}$

$$\mathbf{M}^{\mathrm{ISO}} = \frac{1}{3}\mathrm{Tr}(\mathbf{M})\mathbf{I}\,, \tag{1.14}$$

with $\mathbf{I}$ being the 3×3 identity matrix, and a deviatoric moment tensor $\mathbf{M}'$. We may further

decompose $\mathbf{M}'$ into a compensated linear vector dipole $\mathbf{M}^{\mathrm{CLVD}}$ (Knopoff and Randall, 1970) and the largest double couple $\mathbf{M}^{\mathrm{DC}}$

$$\mathbf{M}' = \mathbf{M}^{\mathrm{CLVD}} + \mathbf{M}^{\mathrm{DC}} \tag{1.15}$$

$$= \begin{pmatrix} \frac{\lambda'_2}{2} & 0 & 0 \\ 0 & \lambda'_2 & 0 \\ 0 & 0 & \frac{\lambda'_2}{2} \end{pmatrix} + \begin{pmatrix} \frac{1}{2}(\lambda'_1 - \lambda'_3) & 0 & 0 \\ 0 & 0 & 0 \\ 0 & 0 & -\frac{1}{2}(\lambda'_1 - \lambda'_3) \end{pmatrix} \tag{1.16}$$

where λ'_i are the eigenvalues of $\mathbf{M}'$ with $\lambda'_1 > \lambda'_2 > \lambda'_3$. Indigenous sources such as earthquakes are not expected to have any associated volume change, and so it is common to constrain the trace of the moment tensor to be zero when performing CMT inversions, such that $M_{rr} + M_{\theta\theta} + M_{\phi\phi} = 0$. This constraint is applied throughout this thesis, except in Chapters 5 and 6, where we allow for the possibility that earthquakes related to fluid injection have a volumetric component.

1.3 The centroid

In addition to the moment tensor $\mathbf{M}$, we seek the spatio–temporal position of the earthquake. Backus (1977) defined the centroid as the point $(\mathbf{x}_c, t_c)$ about which the sum of the squares of the first glut moments $\mathbf{\Lambda}$ and $\mathbf{H}$ are minimised *i.e.* (Dziewonski and Woodhouse, 1983a)

$$\frac{\partial}{\partial x_k}[\Lambda_{ijl}(\mathbf{x})\Lambda_{ijl}(\mathbf{x})]_{\mathbf{x}=\mathbf{x}_c} = 0\,, \tag{1.17}$$

$$\frac{\partial}{\partial t}[H_{ij}(t)H_{ij}(t)]_{t=t_c} = 0\,. \tag{1.18}$$

In turn, these relationships with (1.9)–(1.10) imply that the first glut moments vanish at the centroid

$$\Lambda_{ijl}(\mathbf{x}_c)M_{ij} = 0\,, \tag{1.19}$$

$$H_{ij}(t_c)M_{ij} = 0\,. \tag{1.20}$$

The centroid therefore represents the average position of moment release in time and space, and so is clearly distinct from the hypocentre — the point of rupture initiation — for earthquakes of finite spatial and temporal extent. These definitions of the centroid and moment tensor lead to an expression which forms the basis of the solution to the inverse problem for recovering the centroid and moment tensor simultaneously, described in Section 2.3.2.

1.4 The near-field

When compared to conventional seismometers, GPS receivers are relatively insensitive. For example, the M_w 6.3 L'Aquila earthquake is the smallest event to date for which seismic waves have been recorded (Avallone *et al.*, 2011). As a consequence, GPS receivers typically have to be located within a few tens to hundreds of kilometres of the hypocentre of a moderate magnitude earthquake in order to record seismic displacements. Similarly, microearthquakes are, by definition, small earthquakes, and so the wavefield radiated by them can only be detected by seismic instruments deployed very close to the sources, typically within a few hundred metres of the events. The data that we examine in this thesis therefore relate to 'near-field' deformations, where we use the term near-field merely to refer to the region for which a flat earth model is approximately true. For example, Pollitz (1996) developed a method for calculating the static deformation of a spherical Earth due to seismic sources and found that within 100 km of the epicentre, peak displacements in a homogeneous spherical model differ by less than 2 % from those in an equivalent planar model. We can therefore take the term "near-field" to refer to observations within a few hundred kilometres of the epicentre, which coincides with the usual domain of geodetic measurements such as GPS. Clearly, this definition also means that when handling microseismic data we are always in the near-field.

The term near-field can also be more formally defined in terms of the non-dimensional parameter $\frac{\omega R}{\alpha}$ which arises in the solution of the problem of seismic radiation from a point source in an infinite homogeneous elastic wholespace (Madariaga, 2007). Here, R is the

source–receiver distance; ω and α are respectively the angular frequency and velocity of a P-wave. If this ratio is very much larger than 1, then the part of the solution that decays faster than R^{-1} can be neglected, and we may say that we are in the far field. In fact, using this definition all of the inversions performed later in this thesis are in the far field because — to eliminate finite source effects — we deliberately exclude data from stations at epicentral distances that are less than one rupture length away from the epicentre.

1.5 Thesis outline

Chapter 2 of this thesis presents theory for calculating the static and dynamic response of a plane-layered, elastic, isotropic medium to a buried point source. Our approach follows the minor vector theory of Woodhouse (1980), adapted so that the displacement at 0 Hz — the static displacement — can be stably computed. This theory is appropriate for modelling all of the seismic data types that we use later on in this thesis: coseismic displacements measured by GPS, high-rate GPS displacement waveforms and high-frequency microseismic waveforms. Since our intention is to use these data for centroid–moment tensor inversions, we also describe this inverse problem and one method of its solution.

The application of this theory is then demonstrated in Chapter 3 using GPS time-series recorded at a sampling frequency of 1 Hz for two recent, moderate magnitude, earthquakes. We determine CMT solutions for these events using GPS waveforms filtered in a pass band below 0.05 Hz, *i.e.* using wavelengths and periods similar to those employed in inversions of teleseismic waveforms. The data used in our inversions were acquired at epicentral distances of less than 100 km, and our solutions compare well with those that use global data. Consequently, in settings such as Japan and California, where high-rate GPS time-series are available in real-time, such data may be used to quickly characterize the first order characteristics of the earthquake such as location, magnitude and mechanism.

In situations where it is important to attain a knowledge of these parameters rapidly, instead of modelling the whole GPS waveform, a commonly-used approach is to invert

only the static displacement part of the signal. In Chapter 4, we investigate performing real-time inversions of static offsets measured by GPS, using the same formulation of the inverse problem as that developed for GPS waveform data. To ensure stability of the inversion in the relatively common situation whereby the azimuthal distribution of stations is poor, we find that it is necessary to limit the change in centroid coordinates permitted at any inversion iteration. A modified inversion scheme that includes damping of the location-update step length is presented in Chapter 4.

An advantage of the CMT method is its flexibility; once the inversion machinery is set up, it is straightforward to use different data types in the inversion. The generality of the CMT inversion algorithm leads us in Chapters 5 and 6 to investigate the quite different situation of monitoring small, induced, earthquakes — typically with $M_w < 0$ — caused by hydraulic fracturing of shale gas reservoirs.

Chapter 2

Theory

A set of seismograms, or some other recordings of a seismic displacement field, are, by themselves, of limited value for understanding the phenomenon that caused them and that we are interested in: the earthquake. To make progress, we also must have a theory describing how seismic waves propagate through the Earth in response to the action of a particular source model. By comparing a synthetic version of the observations — calculated by the application of this physical theory in an assumed earth model — to the real data, it is possible to find a correction to the input source parameters which brings the synthetics into better agreement with the measurements. In this chapter, we describe a method for forward modelling the different types of seismic data used in this thesis, and present the theory required to solve the inverse problem to obtain the centroid and moment tensor of an earthquake from these data.

2.1 Forward modelling: theory

If we are to use displacement waveforms measured using GPS receivers to study seismic sources, we require a method for calculating near-field static and dynamic displacements in plane layered media. A forward modelling technique which is stable at high frequencies

would also be beneficial given the bandwidth of ground motions that are recorded by geodetic grade GPS receivers with sampling rates of up to 10 Hz (e.g. Avallone *et al.*, 2011). For microseismic waveform data, high-frequency stability is essential, although the ability to calculate the static response is less important as the recording instruments are not sensitive to these. In any case, we require a forward modelling method that is stable both at high frequencies and at zero-frequency.

Methods for performing seismic calculations in layered media are well established, with corresponding computer codes widely available; for a review see Cormier (2007). Generally speaking, we seek solutions of the equations of motion in some transform domain, which depends on the particular solution method, and evaluate numerical inverse transforms to obtain displacement as a function of time and space. In this section, we describe a new method by which the integrands for displacement may be constructed in the frequency-wavenumber domain[1]; for a discussion of the inverse transformations we direct readers to the detailed works of Chapman (1978) and Chapman (2004, chapter 8).

The earliest solution to the layered-medium problem was the transfer matrix method, introduced by Thomson (1950) and refined by Haskell (1953), whereby solutions at any interface in the medium are constructed from solutions known elsewhere via successive layer matrix multiplications. However, for the problem of P-SV wave motion, the Thomson-Haskell propagator matrix method is known to be numerically unstable at high frequencies when evanescent waves are present in the structure. The propagator matrix contains exponential terms which grow at different rates; when frequency becomes large the evanescent P-wave term dominates that of the SV-wave; operations carried out on these terms using finite precision arithmetic cause the SV-solution to lose precision and become dependent on the P-wave solution.

This numerical problem has been tackled from several directions. A number of matrix methods based on the Thomson-Haskell method have been developed that are stable at high frequencies (e.g. Knopoff, 1964; Dunkin, 1965; Thrower, 1965; Abo-Zena, 1979;

[1]Much of the material in this chapter has been published in O'Toole and Woodhouse (2011)

Woodhouse, 1980; Chapman, 2003). Gilbert and Backus (1966) formalised the minor matrix method, whereby the numerical instability is entirely avoided by solving a related set of equations for the minors of the original system. Another approach has been given by Wang (1999), who re-orthogonalized solutions after each layer matrix multiplication, thus ensuring that solutions remain independent throughout propagation. Alternatively, reflectivity methods (Fuchs and Müller, 1971; Kennett, 1974; Kennett and Kerry, 1979; Kennett, 1983; Müller, 1985), where the wavefield is constructed in terms of reflection and transmission coefficients for all the rays in the medium, eliminate the problematic exponentially growing terms, ensuring stability at high frequencies.

An additional challenge of the problem posed here is the requirement for numerical stability at zero-frequency, so that the static offset is calculated as part of the synthetic GPS time series. At zero-frequency, conventional methods fail as the eigensystem of the governing equations becomes defective. Much work has been devoted to the stable computation of the static displacement field arising from a dislocation in a layered elastic medium (e.g. Pan, 1997, and references therein); both reflectivity (e.g. He *et al.*, 2003) and propagator methods (e.g. Fukahata and Matsu'ura, 2005) have been developed for this purpose.

Zhu and Rivera (2002) used the Jordan canonical form of the system matrix to show that the static response can be obtained by taking the zero frequency limit of the dynamic response. Their method has been applied to the calculation of acceleration seismograms (e.g. Wang *et al.*, 2008), coseismic displacements in layered media (e.g. Mellors *et al.*, 2004), and synthetic 1 Hz GPS time series (Miyazaki *et al.*, 2004; Kobayashi *et al.*, 2006; Yokota *et al.*, 2009). However, their alteration does not deal with the high-frequency instability inherent in the Thomson-Haskell propagator method. Furthermore, the approximation to the static displacement will become unstable at some frequency, and while it is possible to substitute the static propagator in at the appropriate point in the calculation, ideally we require an algorithm that is stable at both frequency extremes. Wang (1999) provide one such method, and Vigny *et al.* (2011) implemented the discrete-wavenumber reflectivity code `AXITRA` for this purpose.

We demonstrate here that the minor matrix method introduced by Gilbert and Backus (1966) may be adapted to allow stable and accurate static and dynamic displacement calculations to be carried out. The application of this theory results in a new, efficient algorithm for the calculation of the response of a plane layered elastic medium to a buried point source that is stable both at high frequencies and at zero frequency. The theory is exact, and allows the seismic deformation field to be stably constructed at frequencies including 0 Hz without the need for additional numerical procedures or approximations of the sort used by Wang (1999) and Zhu and Rivera (2002). The theory is based on that given by Woodhouse (1980), adapted so that the zero-frequency component of ground motion can be calculated; for completeness, in the following we restate some of his earlier results.

We obtain solutions to the equations of motion in the frequency-wavenumber domain, avoiding the explicit evaluation of determinants of pairs of solutions that causes the numerical instability in the Thomson-Haskell propagator method. This is achieved by integrating a related set of six first-order ordinary differential equations for the minor vectors of the original system of four first-order ordinary differential equations. A similar approach for a spherical Earth has been given by Friederich and Dalkolmo (1995) and Al-Attar and Woodhouse (2008).

The method developed here provides a versatile tool for both the seismological and geodetic communities as it leads to a single computer code that can be used to compute complete synthetic seismograms and static displacement fields. To demonstrate this flexibility, we present one seismological and one geodetic application of our method by modelling 1 Hz GPS displacement seismograms and InSAR data acquired for two recent earthquakes.

We begin by giving a brief, self-contained account of the problem of calculating the deformation of a layered half-space in response to a buried point source, which can be found in a number of monographs (e.g. Takeuchi and Saito, 1972; Kennett, 1983; Aki and Richards, 2002).

2.1.1 Statement of the problem

We consider a plane stratified medium consisting of horizontal homogeneous, isotropic layers. Let (x, y, z) be a set of right-handed Cartesian coordinates related to cylindrical polar coordinates (r, ϕ, z) by

$$\begin{aligned} x &= x_1 = r\,\cos\phi\,, \\ y &= x_2 = r\,\sin\phi\,, \\ z &= x_3\,, \end{aligned} \tag{2.1}$$

where we let the positive z-axis be directed upwards. Referencing these axes to a geographical coordinate system, we define the x and y directions as south and east respectively, in which case $\phi = 180 - \alpha$, where α is the azimuth measured clockwise from north. We call the top boundary of the medium z_1, the bottom boundary z_2, with the source at z_s and receiver at z_r with $z_1 \geq z_r > z_s \geq z_2$. We will make use of the Fourier transform pair in time, t, and horizontal space, x_1, x_2, defined

$$\mathbf{u}(k_1, k_2, z, \omega) = \int_{-\infty}^{\infty}\int_{-\infty}^{\infty}\int_{-\infty}^{\infty} \mathbf{u}(x_1, x_2, z, t)\, \mathrm{e}^{-\mathrm{i}(\omega t - k_1 x_1 - k_2 x_2)}\, \mathrm{d}x_1\, \mathrm{d}x_2\, \mathrm{d}t \tag{2.2}$$

$$\mathbf{u}(x_1, x_2, z, t) = \frac{1}{(2\pi)^3}\int_{-\infty}^{\infty}\int_{-\infty}^{\infty}\int_{-\infty}^{\infty} \mathbf{u}(k_1, k_2, z, \omega)\, \mathrm{e}^{\mathrm{i}(\omega t - k_1 x_1 - k_2 x_2)}\, \mathrm{d}k_1\, \mathrm{d}k_2\, \mathrm{d}\omega\,, \tag{2.3}$$

where ω denotes angular frequency and (k_1, k_2) are Cartesian coordinates in wavenumber space related to polar coordinates (k, θ) by

$$k_1 = k\,\sin\theta\,, \tag{2.4}$$

$$k_2 = -k\,\cos\theta\,. \tag{2.5}$$

We make no symbolic distinction between any function $g(x_1, x_2, z, t)$ and its so called Hankel transform $g(k_1, k_2, z, \omega)$ as this should be clear from the context. We will make use of suffix notation throughout, with summation over repeated indices assumed, and subscript commas denoting partial differentiation with respect to the spatial coordinates, *i.e.* $u_{i,j} = \partial u_i / \partial x_j$.

The equations of motion

The equations of motion for displacement $\mathbf{u}(\mathbf{x}, t)$ are given by

$$t_{ij,j} + f_i = \rho\, \partial_t^2 u_i \tag{2.6}$$

where $\mathbf{t}$ is the stress tensor, $\mathbf{f}$ is the representation of the earthquake source and ρ is the density of the medium. We assume that the medium is linearly elastic, piecewise homogeneous and isotropic, which allows us to write

$$t_{ij} = \mu(u_{i,j} + u_{j,i}) + \lambda u_{k,k}\delta_{ij} \tag{2.7}$$

where μ and λ are the Lamé parameters, and δ_{ij} is the Kronecker delta.

In the frequency–wavenumber domain, the equations of motion become

$$-\mathrm{i}k_1 t_{i1} - \mathrm{i}k_2 t_{i2} + \partial_z t_{i3} + f_i = -\rho\omega^2 u_i \tag{2.8}$$

under the assumption that the elastic properties of the medium vary only in depth, *i.e.* $\lambda = \lambda(z)$ and $\mu = \mu(z)$, with

$$t_{13} = \mu(\partial_z u_1 - \mathrm{i}k_1 u_3) \tag{2.9}$$

$$t_{23} = \mu(\partial_z u_2 - \mathrm{i}k_2 u_3) \tag{2.10}$$

$$t_{33} = 2\mu\partial_z u_3 + \lambda(-\mathrm{i}k_1 u_1 - \mathrm{i}k_2 u_2 + \partial_z u_3) \tag{2.11}$$

$$t_{11} = -2\mathrm{i}k_1 u_1 + \lambda(-\mathrm{i}k_1 u_1 - \mathrm{i}k_2 u_2 + \partial_z u_3) \tag{2.12}$$

$$t_{22} = -2\mathrm{i}k_2 u_2 + \lambda(-\mathrm{i}k_1 u_1 - \mathrm{i}k_2 u_2 + \partial_z u_3) \tag{2.13}$$

$$t_{12} = \mu(-\mathrm{i}k_1 u_2 - \mathrm{i}k_2 u_1)\,. \tag{2.14}$$

Solving (2.9)–(2.11) for $\partial_z u_i$, we obtain

$$\partial_z u_1 = \mu^{-1} t_{13} + \mathrm{i}k_1 u_3 \tag{2.15}$$

$$\partial_z u_2 = \mu^{-1} t_{23} + \mathrm{i}k_2 u_3 \tag{2.16}$$

$$\partial_z u_3 = \sigma^{-1}\left[t_{33} - \lambda(-\mathrm{i}k_1 u_1 - \mathrm{i}k_2 u_2)\right], \tag{2.17}$$

where $\sigma = \lambda + 2\mu$. Using these results in (2.12)–(2.14), the transformed equations of motion (2.8) can be rewritten as

$$\partial_z t_{13} = (\mu k^2 - \rho\omega^2)u_1 + \gamma k_1^2 u_1 + \gamma k_1 k_2 u_2 + \lambda\sigma^{-1}\mathrm{i}k_1 t_{33} - f_1 \tag{2.18}$$

$$\partial_z t_{23} = \gamma k_1 k_2 u_1 + (\mu k^2 - \rho\omega^2)u_2 + \gamma k_2^2 u_2 + \lambda\sigma^{-1}\mathrm{i}k_2 t_{33} - f_2 \tag{2.19}$$

$$\partial_z t_{33} = -\rho\omega^2 u_3 + \mathrm{i}k_1 t_{13} + \mathrm{i}k_2 t_{23} - f_3 \tag{2.20}$$

where $k^2 = k_1^2 + k_2^2$ and $\gamma = \mu(3\lambda + 2\mu)/(\lambda + 2\mu)$. We now have six coupled ordinary differential equations in z, which when expressed in polar coordinates in wavenumber space simplify to

$$\partial_z \begin{bmatrix} U \\ V \\ P \\ S \end{bmatrix} = \begin{bmatrix} 0 & k\lambda\sigma^{-1} & \sigma^{-1} & 0 \\ -k & 0 & 0 & \mu^{-1} \\ -\rho\omega^2 & 0 & 0 & k \\ 0 & k^2(\gamma+\mu) - \rho\omega^2 & -k\lambda\sigma^{-1} & 0 \end{bmatrix} \begin{bmatrix} U \\ V \\ P \\ S \end{bmatrix} + \begin{bmatrix} 0 \\ 0 \\ -\mathrm{i}\omega f_3 \\ \omega(f_1 \sin\theta - f_2 \cos\theta) \end{bmatrix} \tag{2.21}$$

$$\partial_z \begin{bmatrix} W \\ T \end{bmatrix} = \begin{bmatrix} 0 & \mu^{-1} \\ \mu k^2 - \rho\omega^2 & 0 \end{bmatrix} \begin{bmatrix} W \\ T \end{bmatrix} + \begin{bmatrix} 0 \\ -\omega(f_1 \cos\theta + f_2 \sin\theta) \end{bmatrix} \tag{2.22}$$

where we have used the definitions

$$\begin{aligned} U &= \mathrm{i}\omega u_3, & P &= \mathrm{i}\omega t_{33}, \\ V &= -\omega(u_1 \sin\theta - u_2 \cos\theta), & S &= -\omega(t_{13} \sin\theta - t_{23} \cos\theta), \\ W &= \omega(u_1 \cos\theta + u_2 \sin\theta), & T &= \omega(t_{13} \cos\theta + t_{23} \sin\theta). \end{aligned} \tag{2.23}$$

The second term on the right-hand side of equations (2.21) and (2.22) represents the action of the source. We consider the earthquake to be a point source at $\mathbf{x}_s = (0, 0, z_s)$. Such a source can be generally described (see, for example Woodhouse and Deuss, 2007)

$$f_i = (F_i - M_{ij}\partial_j)\,\delta(\mathbf{x} - \mathbf{x}_s)H(t), \tag{2.24}$$

where $\mathbf{F}$ is a point force, $\mathbf{M}$ is the moment tensor, $\delta(\mathbf{x}-\mathbf{x}_s)$ is the Dirac delta function and $H(t)$ is the Heaviside step function. For indigenous sources such as earthquakes, we require that no net force or moment is exerted, i.e. $F_i = 0$ and the moment tensor is symmetric ($M_{ij} = M_{ji}$), although we maintain the most general form in the following. Given our coordinate system definition (2.1), we note that the moment tensor in Cartesian coordinates is related to its equivalent in the usual spherical polar coordinate system via

$$\mathbf{M} = \begin{bmatrix} M_{11} & M_{12} & M_{13} \\ M_{21} & M_{22} & M_{23} \\ M_{31} & M_{32} & M_{33} \end{bmatrix} = \begin{bmatrix} M_{\theta\theta} & M_{\theta\phi} & M_{\theta r} \\ M_{\phi\theta} & M_{\phi\phi} & M_{\phi r} \\ M_{r\theta} & M_{r\phi} & M_{rr} \end{bmatrix}. \tag{2.25}$$

The moment tensors determined in subsequent chapters will be expressed in the spherical coordinate system for consistency with CMT solutions determined from teleseismic data. Applying the forward transform (2.2) to the force term (2.24) we obtain

$$f_i = \frac{1}{\mathrm{i}\omega}\left(F_i + M_{i1}\mathrm{i}k_1 + M_{i2}\mathrm{i}k_2 - M_{i3}\partial_z\right)\delta(z-z_s) \tag{2.26}$$

and hence expressions for the source terms in (2.21) and (2.22) are given by

$$-\mathrm{i}\omega f_3 = \left[-F_3 - \mathrm{i}kM_{31}\sin\theta + \mathrm{i}kM_{32}\cos\theta + M_{33}\partial_z\right]\delta(z-z_s) \tag{2.27}$$

$$\begin{aligned}\omega(f_1\sin\theta - f_2\cos\theta) = \big[&\tfrac{1}{2}k[M_{11}+M_{22}] + \mathrm{i}\sin\theta[-F_1 + M_{13}\partial_z] + \mathrm{i}\cos\theta[F_2 - M_{23}\partial_z] \\ &+\tfrac{1}{2}k\left([-M_{12}-M_{21}]\sin 2\theta + [M_{22}-M_{11}]\cos 2\theta\right)\big]\,\delta(z-z_s)\end{aligned} \tag{2.28}$$

$$\begin{aligned}-\omega(f_1\cos\theta + f_2\sin\theta) = \big[&\tfrac{1}{2}k[M_{12}-M_{21}] + \mathrm{i}\sin\theta[F_2 - M_{23}\partial_z] + \mathrm{i}\cos\theta[F_i - M_{13}\partial_z] \\ &+\tfrac{1}{2}k\left([M_{22}-M_{11}]\sin 2\theta + [M_{12}+M_{21}]\cos 2\theta\right)\big]\,\delta(z-z_s)\,,\end{aligned} \tag{2.29}$$

with the azimuthal dependence of the radiation shown by the terms in θ and 2θ. Clearly, we can write these source terms in the form $\mathbf{a}^{\text{P-SV}}\delta(z-z_s) + \mathbf{c}^{\text{P-SV}}\delta'(z-z_s)$, where

$\delta'(z-z_s) = \partial_z \delta(z-z_s)$. At this point, it is convenient to rewrite (2.21) and (2.22) as

$$\partial_z \mathbf{b}^{\text{P-SV}} = \mathbf{A}^{\text{P-SV}}\mathbf{b}^{\text{P-SV}} + \mathbf{a}^{\text{P-SV}}\delta(z-z_s) + \mathbf{c}^{\text{P-SV}}\delta'(z-z_s) \tag{2.30}$$

$$\partial_z \mathbf{b}^{\text{SH}} = \mathbf{A}^{\text{SH}}\mathbf{b}^{\text{SH}} + \mathbf{a}^{\text{SH}}\delta(z-z_s) + \mathbf{c}^{\text{SH}}\delta'(z-z_s)\,, \tag{2.31}$$

where we have introduced the superscripts $^{\text{P-SV}}$ and $^{\text{SH}}$ as the problem separates into one system of equations for *P-SV* motions — equivalently Rayleigh wave or spheroidal motions — and another system for *SH* motions — equivalently Love wave or toroidal motions. The corresponding solution vectors $\mathbf{b}^{\text{P-SV}}$ and $\mathbf{b}^{\text{SH}}$ are commonly referred to as "stress-displacement vectors" as their elements are functions of the displacements and stresses that we seek to evaluate.

The dependence of the source terms on θ is explicit in (2.27)–(2.29), which allows us to write

$$\begin{aligned} \mathbf{a}^{\text{P-SV}} &= \sum_{m=-2}^{2} \mathbf{a}_m^{\text{P-SV}}\, \mathrm{e}^{\mathrm{i}m\theta}, \quad \mathbf{c}^{\text{P-SV}} = \sum_{m=-2}^{2} \mathbf{c}_m^{\text{P-SV}}\, \mathrm{e}^{\mathrm{i}m\theta}, \\ \mathbf{a}^{\text{SH}} &= \sum_{m=-2}^{2} \mathbf{a}_m^{\text{SH}}\, \mathrm{e}^{\mathrm{i}m\theta}, \qquad \mathbf{c}^{\text{SH}} = \sum_{m=-2}^{2} \mathbf{c}_m^{\text{SH}}\, \mathrm{e}^{\mathrm{i}m\theta}\,, \end{aligned} \tag{2.32}$$

and specifically we obtain

$$\mathbf{a}_m^{\text{SH}}, \mathbf{c}_m^{\text{SH}} = \begin{cases} \begin{bmatrix} 0 \\ \frac{1}{2}k(M_{12}-M_{21}) \end{bmatrix}, \quad \begin{bmatrix} 0 \\ 0 \end{bmatrix} & m = 0 \\ \begin{bmatrix} 0 \\ \frac{1}{2}(\pm F_2 + \mathrm{i}F_1) \end{bmatrix}, \quad \begin{bmatrix} 0 \\ \frac{1}{2}(\mp M_{23} - \mathrm{i}M_{13}) \end{bmatrix} & m = \pm 1 \\ \begin{bmatrix} 0 \\ \frac{1}{4}k(M_{12}+M_{21}) \mp \frac{1}{4}\mathrm{i}k(M_{22}-M_{11}) \end{bmatrix}, \quad \begin{bmatrix} 0 \\ 0 \end{bmatrix} & m = \pm 2 \end{cases} \tag{2.33}$$

$$\mathbf{a}_m^{\text{P-SV}}, \mathbf{c}_m^{\text{P-SV}} = \begin{cases} \begin{bmatrix} 0 \\ 0 \\ -F_3 \\ \frac{1}{2}k(M_{11}+M_{22}) \end{bmatrix}, \begin{bmatrix} 0 \\ 0 \\ M_{33} \\ 0 \end{bmatrix} & m = 0 \\ \begin{bmatrix} 0 \\ 0 \\ \frac{1}{2}k(\mp M_{31} + \mathrm{i}M_{32}) \\ \frac{1}{2}(\mp F_1 + \mathrm{i}F_2) \end{bmatrix}, \begin{bmatrix} 0 \\ 0 \\ 0 \\ \frac{1}{2}(\pm M_{13} - \mathrm{i}M_{23}) \end{bmatrix} & m = \pm 1 \\ \begin{bmatrix} 0 \\ 0 \\ 0 \\ \frac{1}{4}k(M_{22}-M_{11}) \pm \frac{1}{4}\mathrm{i}k(M_{12}+M_{21}) \end{bmatrix}, \begin{bmatrix} 0 \\ 0 \\ 0 \\ 0 \end{bmatrix} & m = \pm 2 \end{cases} \tag{2.34}$$

The problem now consists of solving (2.30) and (2.31) with the source vectors $\mathbf{a}$ and $\mathbf{c}$ replaced by $\mathbf{a}_m$ and $\mathbf{c}_m$ for each value of $m \in \{-2,-1,0,1,2\}$ given by (2.34) and (2.33), which will produce solutions U_m, V_m, W_m that are independent of θ; the full solution can then be written $U = \sum_m U_m \mathrm{e}^{\mathrm{i}m\theta}$, $V = \sum_m V_m \mathrm{e}^{\mathrm{i}m\theta}$, $W = \sum_m W_m \mathrm{e}^{\mathrm{i}m\theta}$. The dependence of the solutions of (2.30) and (2.31) on θ allows us to simplify the inverse transform by carrying out the integration over the wavenumber domain using polar coordinates: $\int_{-\infty}^{\infty} \mathrm{d}k_1 \int_{-\infty}^{\infty} \mathrm{d}k_2 \rightarrow \int_0^{\infty} k \, \mathrm{d}k \int_{-\pi}^{\pi} \mathrm{d}\theta$, $k_1 x_1 \rightarrow kr\cos\phi\sin\theta$, $k_2 x_2 \rightarrow -kr\sin\phi\cos\theta$. For example, the vertical component of the displacement field in the time domain can be written

$$u_3 = (2\pi)^{-3} \int_{-\infty}^{\infty}\int_{-\infty}^{\infty}\int_{-\infty}^{\infty} \frac{1}{\mathrm{i}\omega} U \, e^{\mathrm{i}(\omega t - k_1 x_1 - k_2 x_2)} \, \mathrm{d}k_1 \, \mathrm{d}k_2 \, \mathrm{d}\omega \, . \tag{2.35}$$

Switching to polar coordinates and including the dependence on θ, we have

$$u_3 = (2\pi)^{-3} \sum_m \int_{-\infty}^{\infty} \frac{e^{\mathrm{i}\omega t}}{\mathrm{i}\omega} \int_0^{\infty} k \, U_m(k,z,\omega) \int_{-\pi}^{\pi} e^{\mathrm{i}m\theta} e^{-\mathrm{i}kr\sin(\theta-\phi)} \, \mathrm{d}\theta \, \mathrm{d}k \, \mathrm{d}\omega \, , \tag{2.36}$$

and changing the dummy variable so that $\theta \to \theta + \phi$, we obtain

$$u_3 = (2\pi)^{-3} \sum_m e^{\mathrm{i}m\phi} \int_{-\infty}^{\infty} \frac{e^{\mathrm{i}\omega t}}{\mathrm{i}\omega} \int_0^{\infty} k\, U_m \int_{-\pi}^{\pi} e^{\mathrm{i}m\theta - \mathrm{i}kr\sin\theta}\, \mathrm{d}\theta\, \mathrm{d}k\, \mathrm{d}\omega\,. \tag{2.37}$$

The integral in θ is clearly a function only of kr and m, and is of the form of a Bessel function $J_m(kr)$, defined

$$J_m(kr) = \frac{1}{2\pi} \int_{-\pi}^{\pi} \mathrm{e}^{\mathrm{i}m\theta - \mathrm{i}kr\sin\theta}\, \mathrm{d}\theta\,, \tag{2.38}$$

hence (2.37) becomes

$$u_3 = (2\pi)^{-2} \sum_m e^{\mathrm{i}m\phi} \int_{-\infty}^{\infty} e^{\mathrm{i}\omega t} \int_0^{\infty} k\, U_m J_m(kr)\, \mathrm{d}k\, \mathrm{d}\omega\,. \tag{2.39}$$

The results for the horizontal displacements take their simplest form for the radial and transverse components $u_r = u_1 \cos\phi + u_2 \sin\phi$, $u_\phi = -u_1 \sin\phi + u_2 \cos\phi$. Recalling the definitions of V and W from (2.23), we find

$$u_1 = -\omega^{-1}[V \sin\theta - W \cos\theta] \tag{2.40}$$

$$u_2 = \omega^{-1}[V \cos\theta + W \sin\theta] \tag{2.41}$$

$$u_r = -\omega^{-1}[V \sin(\theta - \phi) - W \cos(\theta - \phi)] \tag{2.42}$$

$$u_\phi = \omega^{-1}[V \cos(\theta - \phi) + W \sin(\theta - \phi)]\,. \tag{2.43}$$

Substituting (2.42) and (2.43) into the inverse transform (2.3), and reintroducing the dependence of V and W on m, we obtain

$$\begin{aligned} u_r &= (2\pi)^{-3} \sum_m \int_{-\infty}^{\infty} \frac{e^{\mathrm{i}\omega t}}{\mathrm{i}\omega} \int_0^{\infty} \int_{-\pi}^{\pi} [-\mathrm{i}kV_m \sin(\theta - \phi) + \mathrm{i}kW_m \cos(\theta - \phi)]\, e^{\mathrm{i}m\theta} e^{-\mathrm{i}kr\sin(\theta-\phi)}\, \mathrm{d}\theta\, \mathrm{d}k\, \mathrm{d}\omega \\ &= (2\pi)^{-2} \sum_m e^{\mathrm{i}m\phi} \int_{-\infty}^{\infty} \frac{e^{\mathrm{i}\omega t}}{\mathrm{i}\omega} \int_0^{\infty} [k\, V_m J_m'(kr) + \mathrm{i}mr^{-1} W_m J_m(kr)]\, \mathrm{d}k\, \mathrm{d}\omega \end{aligned} \tag{2.44}$$

$$\begin{aligned} u_\phi &= (2\pi)^{-3} \sum_m \int_{-\infty}^{\infty} \frac{e^{\mathrm{i}\omega t}}{\mathrm{i}\omega} \int_0^{\infty} \int_{-\pi}^{\pi} [\mathrm{i}kV_m \cos(\theta - \phi) + \mathrm{i}kW_m \sin(\theta - \phi)]\, e^{\mathrm{i}m\theta} e^{-\mathrm{i}kr\sin(\theta-\phi)}\, \mathrm{d}\theta\, \mathrm{d}k\, \mathrm{d}\omega \\ &= (2\pi)^{-2} \sum_m e^{\mathrm{i}m\phi} \int_{-\infty}^{\infty} \frac{e^{\mathrm{i}\omega t}}{\mathrm{i}\omega} \int_0^{\infty} [\mathrm{i}mr^{-1}\, V_m J_m(kr) - kW_m J_m'(kr)]\, \mathrm{d}k\, \mathrm{d}\omega \end{aligned} \tag{2.45}$$

where we have also used the identities

$$\int_{-\pi}^{\pi} e^{\mathrm{i}m\theta - \mathrm{i}x\sin\theta} \sin\theta \; \mathrm{d}\theta = 2\pi\mathrm{i}\, J'_m(x) \tag{2.46}$$

$$\int_{-\pi}^{\pi} e^{\mathrm{i}m\theta - ix\sin\theta} \cos\theta \; \mathrm{d}\theta = 2\pi m\, x^{-1} J_m(x)\,. \tag{2.47}$$

The results so far can be concisely written

$$u_z = (2\pi)^{-2} \sum_m \int \mathrm{d}\omega \, \frac{e^{\mathrm{i}\omega t}}{\mathrm{i}\omega} \int \mathrm{d}k \quad (kU_m) \quad J_m(kr)\, e^{\mathrm{i}m\phi} \tag{2.48}$$

$$u_r = (2\pi)^{-2} \sum_m \int \mathrm{d}\omega \, \frac{e^{\mathrm{i}\omega t}}{\mathrm{i}\omega} \int \mathrm{d}k \quad (V_m\partial_r + r^{-1}W_m\partial_\phi) \quad J_m(kr)\, e^{\mathrm{i}m\phi} \tag{2.49}$$

$$u_\phi = (2\pi)^{-2} \sum_m \int \mathrm{d}\omega \, \frac{e^{\mathrm{i}\omega t}}{\mathrm{i}\omega} \int \mathrm{d}k \quad (r^{-1}V_m\partial_\phi - W_m\partial_r) \quad J_m(kr)\, e^{\mathrm{i}m\phi}\,. \tag{2.50}$$

Introducing the scalar and vector surface harmonics

$$Y_k^m(r,\phi) = J_m(kr)\mathrm{e}^{\mathrm{i}m\phi}\,, \tag{2.51}$$

$$\mathbf{R}_k^m = \hat{\mathbf{z}} Y_k^m\,, \quad \mathbf{S}_k^m = \frac{1}{k}\left[\hat{\mathbf{r}}\partial_r + \frac{1}{r}\hat{\boldsymbol{\phi}}\partial_\phi\right] Y_k^m\,, \quad \mathbf{T}_\mathbf{k}^\mathbf{m} = \frac{1}{k}\left[\frac{1}{r}\hat{\mathbf{r}}\partial_\phi - \hat{\boldsymbol{\phi}}\partial_r\right] Y_k^m \tag{2.52}$$

where $\hat{\mathbf{r}}$, $\hat{\boldsymbol{\phi}}$, $\hat{\mathbf{z}}$ are unit vectors in co-ordinate directions, and substituting them into (2.48)–(2.50), we note that we obtain an expression for the displacement field equivalent to that given in (2.5) of Woodhouse (1980)

$$\mathbf{u}(r,\phi,z,t) = \int_{-\infty-\mathrm{i}\alpha}^{\infty-\mathrm{i}\alpha} \mathrm{d}\omega\, \mathrm{e}^{\mathrm{i}\omega t} \sum_{m=-\infty}^{\infty} \frac{1}{2\pi} \int_0^\infty k\,\mathrm{d}k \left(b_1^S \mathbf{R}_k^m + b_2^S \mathbf{S}_k^m + b_1^T \mathbf{T}_k^m\right) \tag{2.53}$$

where the b_i^S and b_i^T are the displacement elements of the stress-displacement vectors for spheroidal and toroidal motion respectively

$$b_1^S = (2\pi\mathrm{i}\omega)^{-1} U_m\,, \quad b_2^S = (2\pi\mathrm{i}\omega)^{-1} V_m\,, \quad b_1^T = (2\pi\mathrm{i}\omega)^{-1} W_m\,. \tag{2.54}$$

The summation over m in (2.53) is for the general case of a source whose radiation is not limited to terms in ϕ and 2ϕ. We also see that the integration over frequency is shifted into the lower half-plane by Woodhouse (1980), which will be discussed further in Section 2.2.1.

The displacement field can be expressed most simply by

$$u_r(r,\phi,t) = \int \mathrm{d}\omega \, \frac{\mathrm{e}^{\mathrm{i}\omega t}}{2\pi \mathrm{i}\omega} \sum_{m=-2}^{2} \mathrm{e}^{\mathrm{i}m\phi} \;\; K_r^m(r,\omega) \tag{2.55}$$

$$u_\phi(r,\phi,t) = \int \mathrm{d}\omega \, \frac{\mathrm{e}^{\mathrm{i}\omega t}}{2\pi \mathrm{i}\omega} \sum_{m=-2}^{2} \mathrm{e}^{\mathrm{i}m\phi} \;\; K_\phi^m(r,\omega) \tag{2.56}$$

$$u_z(r,\phi,t) = \int \mathrm{d}\omega \, \frac{\mathrm{e}^{\mathrm{i}\omega t}}{2\pi \mathrm{i}\omega} \sum_{m=-2}^{2} \mathrm{e}^{\mathrm{i}m\phi} \;\; K_z^m(r,\omega) \;\; . \tag{2.57}$$

where we have used the following shorthand for the wavenumber integrals

$$K_r^m = K_r^m(r,\omega) = (2\pi)^{-1} \int_0^\infty [k\, V_m J_m'(kr) + \mathrm{i}m r^{-1} W_m J_m(kr)] \, \mathrm{d}k \tag{2.58}$$

$$K_\phi^m = K_\phi^m(r,\omega) = (2\pi)^{-1} \int_0^\infty [\mathrm{i}m r^{-1}\, V_m J_m(kr) - k W_m J_m'(kr)] \, \mathrm{d}k \tag{2.59}$$

$$K_z^m = K_z^m(r,\omega) = (2\pi)^{-1} \int_0^\infty k\, U_m J_m(kr) \, \mathrm{d}k \, . \tag{2.60}$$

For the static case, division by ω in (2.55)–(2.57) is problematic. However, from the definition of the Fourier transform of a time derivative we see that the static displacements are given by $u_r(r,\phi,\infty) = \lim_{\omega \to 0} \mathrm{i}\omega \, \bar{u}_r(r,\phi,\omega)$ etc. and thus

$$u_r(r,\phi,\infty) = \sum_{m=-2}^{2} \mathrm{e}^{\mathrm{i}m\phi} \;\; K_r^m(r,0) \tag{2.61}$$

$$u_\phi(r,\phi,\infty) = \sum_{m=-2}^{2} \mathrm{e}^{\mathrm{i}m\phi} \;\; K_\phi^m(r,0) \tag{2.62}$$

$$u_z(r,\phi,\infty) = \sum_{m=-2}^{2} \mathrm{e}^{\mathrm{i}m\phi} \;\; K_z^m(r,0) \;\; . \tag{2.63}$$

The solutions to the boundary value problems given by (2.30) and (2.31) satisfy homogeneous equations of the form

$$\partial_z \mathbf{b} = \mathbf{A}\mathbf{b} \tag{2.64}$$

at all depths other than the source depth, z_s, where there is a discontinuity, $\mathbf{s}$, in the

solution vector, given by (Hudson, 1969)

$$\mathbf{s} = [\mathbf{b}]_{z_s^-}^{z_s^+} = \mathbf{a} + \mathbf{A}\mathbf{c}\,. \tag{2.65}$$

This result will be demonstrated in Section 2.4; at present all that we require are expressions for the discontinuity vectors. Using (2.34) and (2.33), we find

$$\mathbf{s}_m^{\text{P-SV}} = \begin{cases} \begin{bmatrix} \sigma^{-1}M_{33} \\ 0 \\ -F_3 \\ \frac{1}{2}k(M_{11}+M_{22}) - k\lambda\sigma^{-1}M_{33} \end{bmatrix}, & m = 0 \\ \begin{bmatrix} 0 \\ \frac{1}{2}\mu^{-1}(\pm M_{13} - \mathrm{i}M_{23}) \\ \pm\frac{1}{2}k(M_{13}-M_{31}) + \frac{1}{2}\mathrm{i}k(M_{32}-M_{23}) \\ \frac{1}{2}(\mp F_1 + \mathrm{i}F_2) \end{bmatrix} & m = \pm 1 \\ \begin{bmatrix} 0 \\ 0 \\ 0 \\ \frac{1}{4}k(M_{22}-M_{11}) \pm \frac{1}{4}\mathrm{i}k(M_{12}+M_{21}) \end{bmatrix} & m = \pm 2 \end{cases} \tag{2.66}$$

$$\mathbf{s}_m^{\text{SH}} = \begin{cases} \begin{bmatrix} 0 \\ \frac{1}{2}k(M_{12}-M_{21}) \end{bmatrix} & m = 0 \\ \begin{bmatrix} \frac{1}{2}\mu^{-1}(\mp M_{23} - \mathrm{i}M_{13}) \\ \frac{1}{2}(\pm F_2 + \mathrm{i}F_1) \end{bmatrix} & m = \pm 1 \\ \begin{bmatrix} 0 \\ \frac{1}{4}k(M_{12}+M_{21}) \mp \frac{1}{4}\mathrm{i}k(M_{22}-M_{11}) \end{bmatrix} & m = \pm 2 \end{cases} \tag{2.67}$$

We require also that the solution vectors at the top ($z = z_1$) and bottom ($z = z_2$) boundaries of the medium can be written as linear combinations of particular vectors

relevant to each respective boundary. That is we may write

$$\mathbf{b}^{\text{P-SV}}(z_1) = a_{11}\bar{\mathbf{v}}^{(1,1)} + a_{12}\bar{\mathbf{v}}^{(1,2)} \tag{2.68}$$

$$\mathbf{b}^{\text{P-SV}}(z_2) = a_{21}\bar{\mathbf{v}}^{(2,1)} + a_{22}\bar{\mathbf{v}}^{(2,2)} \tag{2.69}$$

$$\mathbf{b}^{\text{SH}}(z_1) = a_1\bar{\mathbf{v}}^{(1)} \tag{2.70}$$

$$\mathbf{b}^{\text{SH}}(z_2) = a_2\bar{\mathbf{v}}^{(2)} \tag{2.71}$$

where $a_{\alpha\beta}$ and a_α are scalars, and the vectors $\bar{\mathbf{v}}^{(\alpha,\beta)}$ and $\bar{\mathbf{v}}^{(\alpha)}$ ($\alpha = 1, 2$; $\beta = 1, 2$) are derived from the boundary conditions appropriate to the problem under consideration. Particular boundary conditions relevant to the calculation of seismograms in horizontally stratified media are given in Section 2.1.5.

Summary

The results given in the previous section for the case of *P-SV* displacements in a horizontally stratified medium can be summarised as follows. Given a 4×4 matrix $\mathbf{A}^{\text{P-SV}}(z)$ defined in the interval $z_1 \geq z \geq z_2$, a 4-vector $\mathbf{s}^{\text{P-SV}}$ and four 4-vectors $\bar{\mathbf{v}}^{(\alpha,\beta)}$ ($\alpha = 1, 2$; $\beta = 1, 2$), find the solution vector $\mathbf{b}^{\text{P-SV}}$ satisfying:

1. The homogeneous equation

$$\partial_z \mathbf{b}^{\text{P-SV}}(z) = \mathbf{A}^{\text{P-SV}}(z)\mathbf{b}^{\text{P-SV}}(z) \quad (z_2 < z < z_s, z_s < z < z_1)\,. \tag{2.72}$$

2. The solution vector $\mathbf{b}^{\text{P-SV}}$ is continuous except at the source depth z_s where it has a given discontinuity, that is

$$\mathbf{b}^{\text{P-SV}}(z_s + 0) - \mathbf{b}^{\text{P-SV}}(z_s - 0) = \mathbf{s}^{\text{P-SV}}\,. \tag{2.73}$$

3. There exist constants $a_{\alpha\beta}$ ($\alpha = 1, 2$; $\beta = 1, 2$) such that the solution at each boundary can be written as a linear combination of the boundary condition vectors $\bar{\mathbf{v}}^{(\alpha,\beta)}$ at

that boundary

$$\begin{aligned} \mathbf{b}^{\text{P-SV}}(z_1) &= a_{11}\bar{\mathbf{v}}^{(1,1)} + a_{12}\bar{\mathbf{v}}^{(1,2)} \\ \mathbf{b}^{\text{P-SV}}(z_2) &= a_{21}\bar{\mathbf{v}}^{(2,1)} + a_{22}\bar{\mathbf{v}}^{(2,2)}\,, \end{aligned} \tag{2.74}$$

which also implies that

$$\begin{aligned} \mathbf{b}^{\text{P-SV}}(z) &= a_{11}\mathbf{v}^{(1,1)} + a_{12}\mathbf{v}^{(1,2)} \quad (z_s < z < z_1) \\ \mathbf{b}^{\text{P-SV}}(z) &= a_{21}\mathbf{v}^{(2,1)} + a_{22}\mathbf{v}^{(2,2)} \quad (z_2 < z < z_s)\,. \end{aligned} \tag{2.75}$$

where $\mathbf{v}^{(\alpha,\beta)}$ are continuous functions of depth also satisfying (2.72).

The problem for SH motion is analogous, except the solution space is two dimensional, and only one boundary condition vector is required at each boundary. We now describe our solution method to these problems.

2.1.2 Solution of the boundary value problem

Solutions to the homogeneous equation (2.64) can be found using the Thomson-Haskell propagator matrix method. While this theory is exact, its numerical implementation is problematic for the case of P-SV wave motion, where the exponential growth of the pairs of solutions during propagation causes them to lose their linear independence. In the following section we summarise the propagator matrix method as it leads on to our adaptation that makes the problem stable.

Solution of the SH wave problem

We wish to evaluate the seismogram at a particular depth, z_r. We assume that $z_r > z_s$, that is the receiver is above the source. The stress-displacement vector for SH wave motion at the receiver must be proportional to the boundary condition vector at the top, $\bar{\mathbf{v}}^{\text{SH}(1)}$, propagated to the receiver depth z_r, that is

$$\mathbf{b}^{\text{SH}}(z_r) = a_r\mathbf{v}^{\text{SH}(1)}(z_r) = a_r\mathbf{P}(z_r, z_1)\bar{\mathbf{v}}^{\text{SH}(1)} \tag{2.76}$$

where a_r is some constant, and $\mathbf{P}(z_r, z_1)$ is the propagator matrix, propagating the solution at z_1 to z_r. Below the source, the stress-displacement vector is found from the lower boundary condition vector, $\bar{\mathbf{v}}^{\mathrm{SH}(2)}$, at z_2. Propagating this solution to the level immediately below the source (i.e. $z = z_s-$), we write

$$\mathbf{b}^{\mathrm{SH}}(z_s-) = a_s \mathbf{v}^{\mathrm{SH}(2)}(z_s) = a_s \mathbf{P}(z_s, z_2)\bar{\mathbf{v}}^{\mathrm{SH}(2)} \tag{2.77}$$

for some constant a_s. Combining this with the solution obtained from propagating the top boundary condition vector to just above the source (i.e. $z = z_s+$), we can write the source discontinuity vector as

$$\mathbf{s}_m^{\mathrm{SH}} = \mathbf{b}_m^{\mathrm{SH}}(z_s+) - \mathbf{b}_m^{\mathrm{SH}}(z_s-) \tag{2.78}$$

where we have introduced the index m as we seek the solutions corresponding to the five force distributions given by (2.33). We can propagate the solution just above the source, $\mathbf{b}_m^{\mathrm{SH}}(z_s+) = a_s \mathbf{v}^{\mathrm{SH}(2)}(z_s) + \mathbf{s}_m^{\mathrm{SH}}$, to the receiver using

$$\mathbf{b}_m^{\mathrm{SH}}(z_r) = \mathbf{P}(z_r, z_s)\left(a_s \mathbf{v}^{\mathrm{SH}(2)}(z_s) + \mathbf{s}_m^{\mathrm{SH}}\right) \tag{2.79}$$

$$= a_s \mathbf{v}^{\mathrm{SH}(2)}(z_r) + \mathbf{P}(z_r, z_s)\mathbf{s}_m^{\mathrm{SH}}. \tag{2.80}$$

Since (2.80) must equal (2.76), we have two equations for the two unknowns a_r and a_s

$$a_r \mathbf{v}^{\mathrm{SH}(1)}(z_r) - a_s \mathbf{v}^{\mathrm{SH}(2)}(z_r) = \mathbf{P}(z_r, z_s)\mathbf{s}_m^{\mathrm{SH}}\,. \tag{2.81}$$

By definition, $\mathbf{P}^{-1}(z_r, z_s) = \mathbf{P}(z_s, z_r)$, and so (2.81) becomes

$$a_r \mathbf{v}^{\mathrm{SH}(1)}(z_s) - a_s \mathbf{v}^{\mathrm{SH}(2)}(z_s) = \mathbf{s}_m^{\mathrm{SH}} \tag{2.82}$$

which we solve for a_r via Cramer's rule (e.g. Riley *et al.*, 2007)

$$a_r = \frac{D[\mathbf{s}_m^{\mathrm{SH}}, \mathbf{v}^{\mathrm{SH}(2)}(z_s)]}{D[\mathbf{v}^{\mathrm{SH}(1)}(z_r), \mathbf{v}^{\mathrm{SH}(2)}(z_r)]} \tag{2.83}$$

where $D[\ ]$ represents a 2×2 determinant as a function of its two columns. Hence from (2.76) the stress-displacement vector at the receiver is

$$\mathbf{b}_m^{\mathrm{SH}}(z_r) = \frac{D[\mathbf{s}_m^{\mathrm{SH}}, \mathbf{v}^{\mathrm{SH}(2)}(z_s)]}{D[\mathbf{v}^{\mathrm{SH}(1)}(z_r), \mathbf{v}^{\mathrm{SH}(2)}(z_r)]}\, \mathbf{v}^{\mathrm{SH}(1)}(z_r)\,. \tag{2.84}$$

Expanding the determinants in (2.84), we can factorize out $\mathbf{s}_m^{\mathrm{SH}}$, allowing the solution to be written

$$\mathbf{b}_m^{\mathrm{SH}}(z_r) = \mathbf{H}^{\mathrm{SH}}\mathbf{s}_m^{\mathrm{SH}} \tag{2.85}$$

where

$$\mathbf{H}^{\mathrm{SH}} = \frac{1}{\Delta(z_r)} \begin{pmatrix} v_{r1}^{(1)} v_{s2}^{(2)} & -v_{r1}^{(1)} v_{s1}^{(2)} \\ v_{r2}^{(1)} v_{s2}^{(2)} & -v_{r2}^{(1)} v_{s1}^{(2)} \end{pmatrix}, \tag{2.86}$$

$$\Delta(z_r) = v_{r1}^{(1)} v_{r2}^{(2)} - v_{r2}^{(1)} v_{r1}^{(2)}\,, \tag{2.87}$$

and we have abbreviated $v_i^{\mathrm{SH}(\alpha)}(z_r)$ to $v_{ri}^{(\alpha)}$ and similarly for z_s.

The above analysis leads to the following algorithm for evaluating $\mathbf{b}^{\mathrm{SH}}(z_r)$ at some angular frequency ω and wavenumber k

1. Specify the boundary condition vectors $\bar{\mathbf{v}}^{\mathrm{SH}(1)}$ and $\bar{\mathbf{v}}^{\mathrm{SH}(2)}$ at the top ($z = z_1$) and bottom ($z = z_2$) boundaries of the domain. Specific forms for $\bar{\mathbf{v}}^{\mathrm{SH}(1)}$ and $\bar{\mathbf{v}}^{\mathrm{SH}(2)}$ are given in Section 2.1.5.

2. Propagate $\bar{\mathbf{v}}^{\mathrm{SH}(2)}$ upwards from the bottom boundary to the receiver at z_r by layer matrix multiplications, to obtain $\mathbf{v}^{\mathrm{SH}(2)}(z_r)$, storing the value at the source, $\mathbf{v}^{\mathrm{SH}(2)}(z_s)$.

3. If the receiver is not at the top boundary (i.e. if $z_r < z_1$), propagate $\bar{\mathbf{v}}^{\mathrm{SH}(1)}$ downwards to z_r, to obtain $\mathbf{v}^{\mathrm{SH}(1)}(z_r)$.

4. Use these values of $\mathbf{v}^{\mathrm{SH}(2)}(z_r)$, $\mathbf{v}^{\mathrm{SH}(2)}(z_s)$ and $\mathbf{v}^{\mathrm{SH}(1)}(z_r)$ in (2.84) for each value of $m \in \{-2, -1, 0, 1, 2\}$.

Solution of the $P-SV$ problem

Using a similar analysis to that presented above for the SH problem, the solution of the problem given by (2.72)–(2.74) for P-SV motion at depths shallower than the source can be written (Woodhouse, 1980, equation 3.12)

$$\mathbf{b}^{\text{P-SV}}(z) = \frac{1}{\Delta(z_s)}\tilde{\mathbf{M}}^{(1)}(z)\mathbf{P}^{\text{T}}(z_s, z)\mathbf{M}^{(2)}(z_s)\mathbf{s} \tag{2.88}$$

with

$$M_{ij}^{(\alpha)}(z) = \epsilon_{ijkl}\, v_k^{(\alpha,1)}(z)\, v_l^{(\alpha,2)}(z) \tag{2.89}$$

$$\tilde{M}_{ij}^{(\alpha)}(z) = v_i^{(\alpha,1)}(z)\, v_j^{(\alpha,2)}(z) - v_i^{(\alpha,2)}(z)\, v_j^{(\alpha,1)}(z) \tag{2.90}$$

where ϵ_{ijkl} is the alternating tensor, which is defined as being completely antisymmetric in its indices with i, j, k and l ranging from 1 to 4 and $\epsilon_{1234} = 1$. The evaluation of (2.88) using (2.89) and (2.90) requires that we compute determinants of pairs of the linearly independent solution vectors $\mathbf{v}^{(1,1)}$ and $\mathbf{v}^{(1,2)}$. It is well known that the explicit calculation of antisymmetric products such as $v_i^{(1,1)}\, v_j^{(1,2)} - v_i^{(1,2)}\, v_j^{(1,1)}$ is problematic. At high frequencies, the difference between the two terms can be orders of magnitude smaller that the quantities themselves. While the individual terms can be computed accurately using finite precision arithmetic, all numerical precision may be lost when taking their difference if they differ only in the less significant digits (Abo-Zena, 1979; Woodhouse, 1980; Oliveira and Stewart, 2006). Physically, this numerical problem represents the neglect of exponentially decaying components of the solution, which — although having small values in an absolute sense — are as important as the exponentially growing terms in the computation of the antisymmetric products (Al-Attar and Woodhouse, 2008).

To avoid this difficulty, we repose the problem in terms of the minors of pairs of solutions of (2.30). Solving the system of minor equations essentially allows us to obtain these determinants directly without having to explicitly evaluate them using (2.89) and (2.90). We obtain a system of six first-order linear differential equations, and can obtain

solutions to our original system by integrating this new system. The solution method using minor vectors was first detailed by Gilbert and Backus (1966) and expanded upon by Woodhouse (1980); for completeness we restate here some of the results of these earlier works.

Solution of the P-SV problem using minor vectors

For any two 4-vectors $\mathbf{x}^{(1)}$, $\mathbf{x}^{(2)}$, say, the minor vector is defined as the vector of all six subdeterminants of the 4×2 matrix having the two vectors as columns. These are arranged in a standard order, taking the pair of rows that define the subdeterminant as $[(1,2),(1,3),(1,4),(2,3),(2,4),(3,4)]$. Explicitly

$$[\mathbf{x}^{(1)}, \mathbf{x}^{(2)}] = \begin{bmatrix} x_1^{(1)} x_2^{(2)} - x_2^{(1)} x_1^{(2)} \\ x_1^{(1)} x_3^{(2)} - x_3^{(1)} x_1^{(2)} \\ x_1^{(1)} x_4^{(2)} - x_4^{(1)} x_1^{(2)} \\ x_2^{(1)} x_3^{(2)} - x_3^{(1)} x_2^{(2)} \\ x_2^{(1)} x_4^{(2)} - x_4^{(1)} x_2^{(2)} \\ x_3^{(1)} x_4^{(2)} - x_4^{(1)} x_3^{(2)} \end{bmatrix} . \tag{2.91}$$

We define the minor vector $\mathbf{m}^{(\alpha)}(z)$ in terms of the pair of continuous solution vectors of (2.64)

$$\mathbf{m}^{(\alpha)}(z) = [\mathbf{v}^{(\alpha,1)}(z), \mathbf{v}^{(\alpha,2)}(z)]. \tag{2.92}$$

The minor vectors are continuous solutions to a system of six first-order linear homogeneous equations of the form

$$\partial_z \mathbf{m}^{(\alpha)}(z) = \mathscr{A}(z)\mathbf{m}^{(\alpha)} \tag{2.93}$$

subject to the initial conditions

$$\mathbf{m}^{(\alpha)}(z_\alpha) = [\bar{\mathbf{v}}^{(\alpha,1)}, \bar{\mathbf{v}}^{(\alpha,2)}], \tag{2.94}$$

at the top ($\alpha = 1$) and bottom ($\alpha = 2$) boundaries of the medium. Using this notation we may rewrite (2.89) and (2.90) as

$$\mathbf{M}^{(\alpha)} = \begin{bmatrix} 0 & m_6^{(\alpha)} & -m_5^{(\alpha)} & m_4^{(\alpha)} \\ -m_6^{(\alpha)} & 0 & m_3^{(\alpha)} & -m_2^{(\alpha)} \\ m_5^{(\alpha)} & -m_3^{(\alpha)} & 0 & m_1^{(\alpha)} \\ -m_4^{(\alpha)} & m_2^{(\alpha)} & -m_1^{(\alpha)} & 0 \end{bmatrix}, \tag{2.95}$$

$$\tilde{\mathbf{M}}^{(\alpha)} = \begin{bmatrix} 0 & m_1^{(\alpha)} & m_2^{(\alpha)} & m_3^{(\alpha)} \\ -m_1^{(\alpha)} & 0 & m_4^{(\alpha)} & m_5^{(\alpha)} \\ -m_2^{(\alpha)} & -m_4^{(\alpha)} & 0 & m_6^{(\alpha)} \\ -m_3^{(\alpha)} & -m_5^{(\alpha)} & -m_6^{(\alpha)} & 0 \end{bmatrix}. \tag{2.96}$$

The 6×6 coordinate matrix of the minor equations (2.93) can be written in terms of the elements of $\mathbf{A}$ via (Gilbert and Backus, 1966; Woodhouse, 1980)

$$\mathscr{A} = \begin{bmatrix} A_{11}+A_{22} & A_{23} & A_{24} & -A_{13} & -A_{14} & 0 \\ A_{32} & A_{11}+A_{33} & A_{34} & A_{12} & 0 & -A_{14} \\ A_{42} & A_{43} & A_{11}+A_{44} & 0 & A_{12} & A_{13} \\ -A_{31} & A_{21} & 0 & A_{22}+A_{33} & A_{34} & -A_{24} \\ -A_{41} & 0 & A_{21} & A_{43} & A_{22}+A_{44} & A_{23} \\ 0 & -A_{41} & A_{31} & -A_{42} & A_{32} & A_{33}+A_{44} \end{bmatrix}, \tag{2.97}$$

which upon substitution of the specific A_{ij} from (2.21) suggests that we actually need only solve a system of five equations since the second and fifth rows of the system matrix are the negative of each other. In other words, the second and fifth elements of the minor vector formed by any two continuous solutions of (2.93) sum to a constant value, C, for example

$$[\mathbf{b}(z), \bar{\mathbf{b}}(z)]_2 + [\mathbf{b}(z), \bar{\mathbf{b}}(z)]_5 = C \tag{2.98}$$

or, using (2.92), more generally

$$m_2^{(\alpha)}(z) + m_5^{(\alpha)}(z) = C \tag{2.99}$$

where C depends on the boundary conditions and for the physical problems under consideration here is always zero, *i.e.* $m_2^{(\alpha)}(z) = -m_5^{(\alpha)}(z)$. Expanding (2.98), we obtain a quadratic form given by

$$\mathbf{b}^{\mathrm{T}}(z)\mathbf{\Sigma}\bar{\mathbf{b}}(z) = C \tag{2.100}$$

with

$$\Sigma = \begin{bmatrix} \mathbf{0} & \mathbf{I} \\ -\mathbf{I} & \mathbf{0} \end{bmatrix} \tag{2.101}$$

where $\mathbf{I}$ and $\mathbf{0}$ are the 2×2 identity and null matrices respectively. The propagator matrix $\mathbf{P}(z, z_0)$ obeys a similar relation

$$\mathbf{P}^{\mathrm{T}}(z, z_0)\mathbf{\Sigma}\mathbf{P}(z, z_0) = \mathbf{\Sigma}\,. \tag{2.102}$$

Since $\mathbf{\Sigma}^{-1} = -\mathbf{\Sigma}$, we therefore have

$$\mathbf{P}^{\mathrm{T}}(z, z_0) = -\mathbf{\Sigma}\mathbf{P}(z_0, z)\mathbf{\Sigma} \tag{2.103}$$

which we can use in (2.88) to write the *P-SV* stress-displacement vector above the source as

$$\mathbf{b}^{\text{P-SV}}(z) = \frac{1}{\Delta(z_s)}\tilde{\mathbf{N}}^{(\alpha)}(z)\mathbf{P}(z, z_s)\mathbf{N}^{(\alpha)}(z_s)\mathbf{s}\,, \tag{2.104}$$

with

$$\mathbf{N}^{(\alpha)}(z) = \mathbf{\Sigma}\mathbf{M}^{(\alpha)}(z)\,, \tag{2.105}$$

$$\tilde{\mathbf{N}}^{(\alpha)}(z) = \tilde{\mathbf{N}}^{(\alpha)}(z)\mathbf{\Sigma}\,. \tag{2.106}$$

Recalling that $m_2^{(\alpha)}(z) = -m_5^{(\alpha)}(z)$, from (2.95) and (2.96) we find $\mathbf{N}^{(\alpha)}(z) = \tilde{\mathbf{N}}^{(\alpha)}(z)$, and explicitly

$$\mathbf{N}^{(\alpha)}(z) = \tilde{\mathbf{N}}^{(\alpha)}(z) = \begin{bmatrix} -m_2^{(\alpha)} & -m_3^{(\alpha)} & 0 & m_1^{(\alpha)} \\ -m_4^{(\alpha)} & -m_5^{(\alpha)} & -m_1^{(\alpha)} & 0 \\ 0 & -m_6^{(\alpha)} & -m_2^{(\alpha)} & -m_4^{(\alpha)} \\ m_6^{(\alpha)} & 0 & -m_3^{(\alpha)} & -m_5^{(\alpha)} \end{bmatrix}, \tag{2.107}$$

and so the solution becomes

$$\mathbf{b}_m^{\text{P-SV}}(z_r) = \frac{1}{\Delta(z_s)}\mathbf{N}^{(1)}(z_r)\mathbf{P}(z_r, z_s)\mathbf{N}^{(2)}(z_s)\mathbf{s}_m^{\text{P-SV}} \tag{2.108}$$

where the determinant $\Delta(z)$ is also given in terms of elements of the minor vectors as

$$\Delta(z) = m_{r1}^{(1)}m_{r6}^{(2)} - m_{r2}^{(1)}m_{r5}^{(2)} + m_{r3}^{(1)}m_{r4}^{(2)} + m_{r4}^{(1)}m_{r3}^{(2)} - m_{r5}^{(1)}m_{r2}^{(2)} + m_{r6}^{(1)}m_{r1}^{(2)}\,, \tag{2.109}$$

where we have abbreviated $m_i^{(\alpha)}(z_r)$ to $m_{ri}^{(\alpha)}$. In fact Δ is independent of z and, as described below we actually evaluate it at $z = z_r$. We apply the following method to calculate $\mathbf{b}^{\text{P-SV}}$:

1. Form the minor vector at the base of the medium, $\mathbf{m}^{(2)}$ from the bottom boundary condition vectors $\bar{\mathbf{v}}^{\text{P-SV}(2,1)}$ and $\bar{\mathbf{v}}^{\text{P-SV}(2,2)}$.

2. Propagate this solution upwards from z_2 to z_r using the 6×6 minor matrix, storing the value of the minor vector at the source $\mathbf{m}^{(2)}(z_s)$. We can now evaluate $\mathbf{N}^{(2)}(z_s)$.

3. Form the 4×4 propagator matrix $\mathbf{P}(z_r, z_s)$ by multiplying the propagator matrices for all layers between the source and receiver.

4. Form the minor vector $\mathbf{m}^{(1)}$ from the top boundary condition vectors $\bar{\mathbf{v}}^{\text{P-SV}(1,1)}$, $\bar{\mathbf{v}}^{\text{P-SV}(1,2)}$. If the receiver depth does not correspond to the free surface, propagate the minor vector downwards to the receiver depth by minor matrix multiplication to obtain $\mathbf{m}^{(1)}(z_r)$, so we can now form $\mathbf{N}^{(1)}(z_r)$ and $\Delta(z_r)$.

We shall write (2.108) in the form

$$\mathbf{b}_m^{\text{P-SV}}(z_r) = \mathbf{H}^{\text{P-SV}}\mathbf{s}_m^{\text{P-SV}}\,, \tag{2.110}$$

noting that the 2×2 matrix $\mathbf{H}^{\text{SH}} = \mathbf{H}^{\text{SH}}(\omega, k)$ and the 4×4 matrix $\mathbf{H}^{\text{P-SV}} = \mathbf{H}^{\text{P-SV}}(\omega, k)$ incorporate all the layer matrix calculations and are independent of m and of the source parameters, thus they each need only be calculated once for each value of ω and k.

2.1.3 Propagator matrices

In order to calculate displacement spectra using (2.108) we must compute the propagator matrix $\mathbf{P}(z, z_s)$. Numerical solutions to homogeneous equations of the form

$$\partial_z \mathbf{b}(z) = \mathbf{A}(z)\mathbf{b}(z) \tag{2.111}$$

can be found if we know some initial condition $\mathbf{b}(z_1)$ say, which we may also write

$$\mathbf{b}(z_1) = b_1 \begin{bmatrix} 1 \\ 0 \\ 0 \\ 0 \end{bmatrix} + b_2 \begin{bmatrix} 0 \\ 1 \\ 0 \\ 0 \end{bmatrix} + b_3 \begin{bmatrix} 0 \\ 0 \\ 1 \\ 0 \end{bmatrix} + b_4 \begin{bmatrix} 0 \\ 0 \\ 0 \\ 1 \end{bmatrix} . \tag{2.112}$$

Since a linear combination of any two solutions of (2.111) is also a solution, the solution at any other depth can be written

$$\mathbf{b}(z) = b_1(z_1) \begin{bmatrix} p_{11} \\ p_{12} \\ p_{13} \\ p_{14} \end{bmatrix} + b_2(z_1) \begin{bmatrix} p_{21} \\ p_{22} \\ p_{23} \\ p_{24} \end{bmatrix} + b_3(z_1) \begin{bmatrix} p_{31} \\ p_{32} \\ p_{33} \\ p_{34} \end{bmatrix} + b_4(z_1) \begin{bmatrix} p_{41} \\ p_{42} \\ p_{34} \\ p_{44} \end{bmatrix} , \tag{2.113}$$

that is

$$\mathbf{b}(z) = \mathbf{P}(z, z_1)\mathbf{b}(z_1) , \tag{2.114}$$

where $\mathbf{P}(z, z_1)$ is the propagator matrix of the system (2.111). Since the columns of $\mathbf{P}(z_2, z_1)$ are solutions of (2.111), it is obvious that the propagator matrix satisfies

$$\partial_z \mathbf{P}(z, z_1) = \mathbf{A}(z)\mathbf{P}(z, z_1) \tag{2.115}$$

and that to satisfy the initial condition we have

$$\mathbf{P}(z_1, z_1) = \mathbf{I} . \tag{2.116}$$

The propagator for a sequence of layers with different material properties is simply the product of each layers' propagator, *i.e.*

$$\mathbf{P}(z_3, z_1) = \mathbf{P}(z_3, z_2)\mathbf{P}(z_2, z_1) \tag{2.117}$$

Considering a homogeneous layer with boundaries at z and z_1, the coefficient matrix $\mathbf{A}$ is independent of depth, which allows us to solve (2.115) using a power series expansion about $z = z_1$ (Takeuchi and Saito, 1972)

$$\mathbf{P}(z, z_1) = \mathbf{I} + (z - z_1)\mathbf{A} + \tfrac{1}{2}(z - z_1)^2\mathbf{A}^2 + \ldots \tag{2.118}$$

$$= \exp\left((z - z_1)\mathbf{A}\right) , \tag{2.119}$$

using the specific forms for $\mathbf{A}^{\text{P-SV}}$ and $\mathbf{A}^{\text{SH}}$ from (2.21) and (2.22).

In order to include the static displacements in the solution, it is necessary to carry out these calculations for $\omega = 0$. The propagator matrix is a well-behaved function of ω at $\omega = 0$; however the eigensystem of $\mathbf{A}^{\text{P-SV}}$, which is usually used to calculate the propagator matrix, is ill-behaved, as $\mathbf{A}^{\text{P-SV}}$ is defective (*i.e.* does not possess a complete set of eigenvectors) when $\omega = 0$. It is our aim here to derive forms for the propagator matrices and algorithms for multiplication by propagator matrices that remain valid when $\omega = 0$.

We begin by introducing a similarity transformation that simplifies the calculation of the matrix exponential (2.119) by transforming $\mathbf{A}^{\text{P-SV}}$ into a block off-diagonal matrix. Defining

$$\mathbf{Z} = \begin{bmatrix} \rho^{-1/2} & 0 & 0 & 0 \\ 0 & 0 & 0 & -\rho^{-1/2} \\ 0 & 0 & \rho^{1/2} & -2\rho^{-1/2}\mu k \\ 2\rho^{-1/2}\mu k & \rho^{1/2} & 0 & 0 \end{bmatrix} , \tag{2.120}$$

$$\mathbf{Z}^{-1} = \begin{bmatrix} \rho^{1/2} & 0 & 0 & 0 \\ -2\rho^{-1/2}\mu k & 0 & 0 & \rho^{-1/2} \\ 0 & -2\rho^{-1/2}\mu k & \rho^{-1/2} & 0 \\ 0 & -\rho^{1/2} & 0 & 0 \end{bmatrix} \tag{2.121}$$

we find

$$\mathbf{A}^{\text{P-SV}} = \mathbf{Z}\,\mathbf{A}'\,\mathbf{Z}^{-1} \tag{2.122}$$

with $\mathbf{A}'$ given by

$$\mathbf{A}' = \begin{bmatrix} 0 & 0 & \rho/\sigma & -k \\ 0 & 0 & -k & \omega^2 \\ -\omega^2 & -k & 0 & 0 \\ -k & -\rho/\mu & 0 & 0 \end{bmatrix}. \tag{2.123}$$

Thus we now only need to exponentiate $h\mathbf{A}'$ where $h = (z_a - z_b)$ for a homogeneous layer lying between $z = z_a$ and $z = z_b$. The eigenvalues of $\mathbf{A}'$ are found to be ζ_{P}, ζ_{S}, $-\zeta_{\text{P}}$ and $-\zeta_{\text{S}}$ where

$$\zeta_{\text{P}} = \sqrt{k^2 - \frac{\omega^2}{v_{\text{P}}^2}} \tag{2.124}$$

$$\zeta_{\text{S}} = \sqrt{k^2 - \frac{\omega^2}{v_{\text{S}}^2}} \tag{2.125}$$

and v_{P} and v_{S} are respectively the compressional and shear wave velocity of the layer. The corresponding eigenvectors are given by the columns of $\mathbf{U}$

$$\mathbf{U} = \begin{bmatrix} -\zeta_{\text{P}} & -k & \zeta_{\text{P}} & -k \\ 0 & \omega^2 & 0 & \omega^2 \\ \omega^2 & 0 & \omega^2 & 0 \\ k & \zeta_{\text{S}} & k & -\zeta_{\text{S}} \end{bmatrix}. \tag{2.126}$$

Here it is obvious that the eigenvectors are incomplete when $\omega = 0$. Nevertheless they can be used to evaluate the propagator matrix at $\omega = 0$ by taking the limit as $\omega \to 0$. It is

straightforward to calculate

$$\exp(h\mathbf{A}') = \mathbf{U}\exp(h\mathbf{\Lambda})\mathbf{U}^{-1} \tag{2.127}$$

$$= \begin{bmatrix} c_{\mathrm{P}} & k\xi_1 & \zeta_{\mathrm{S}}^{-1}\xi_2 & -k\zeta_{\mathrm{S}}^{-1}s_{\mathrm{S}} \\ 0 & c_{\mathrm{S}} & -k\zeta_{\mathrm{S}}^{-1}s_{\mathrm{S}} & \omega^2\zeta_{\mathrm{S}}^{-1}s_{\mathrm{S}} \\ -\omega^2\zeta_{\mathrm{P}}^{-1}s_{\mathrm{P}} & -k\zeta_{\mathrm{P}}^{-1}s_{\mathrm{P}} & c_{\mathrm{P}} & 0 \\ -k\zeta_{\mathrm{P}}^{-1}s_{\mathrm{P}} & -\zeta_{\mathrm{P}}^{-1}\xi_3 & k\xi_1 & c_{\mathrm{S}} \end{bmatrix} \tag{2.128}$$

where $\mathbf{\Lambda}$ is the diagonalised form of $\mathbf{A}'$, and $c_{\mathrm{P}} = \cosh h\zeta_{\mathrm{P}}$, $s_{\mathrm{P}} = \sinh h\zeta_{\mathrm{P}}$, $c_{\mathrm{S}} = \cosh h\zeta_{\mathrm{S}}$, $s_{\mathrm{S}} = \sinh h\zeta_{\mathrm{S}}$ and where ξ_1, ξ_2, ξ_3 are terms involving negative powers of ω, but which have finite limits as $\omega \to 0$, explicitly

$$\xi_1 = \omega^{-2}\left(c_{\mathrm{P}} - c_{\mathrm{S}}\right), \tag{2.129}$$

$$\xi_2 = \omega^{-2}\left(k^2 s_{\mathrm{S}} - \zeta_{\mathrm{P}}\zeta_{\mathrm{S}}s_{\mathrm{P}}\right), \tag{2.130}$$

$$\xi_3 = \omega^{-2}\left(k^2 s_{\mathrm{P}} - \zeta_{\mathrm{P}}\zeta_{\mathrm{S}}s_{\mathrm{S}}\right). \tag{2.131}$$

The propagator for the *P-SV* system is then $\mathbf{P}(z_b, z_a) = \mathbf{Z}\exp(h\mathbf{A}')\mathbf{Z}^{-1}$. We also require the propagator matrix for *SH* in (2.83) which is

$$\mathbf{P}(z_b, z_a) = \begin{bmatrix} c_{\mathrm{S}} & \mu^{-1}\zeta_{\mathrm{S}}^{-1}s_{\mathrm{S}} \\ \mu\zeta_{\mathrm{S}}s_{\mathrm{S}} & c_{\mathrm{S}} \end{bmatrix}. \tag{2.132}$$

In (2.108), we also require a propagator for determining the minor vectors at the source and receiver depths from the minor vectors formed at the boundaries. Following from (2.91), we define the minor matrix $[\mathbf{X}]$ as a matrix whose columns are the minor vectors of pairs of the columns of $\mathbf{X}$ taken in a specific order. A 4×4 matrix with columns $\mathbf{x}^{(i)}$ has a 6×6 minor matrix given by

$$[\mathbf{X}] = \left([\mathbf{x}^{(1)}, \mathbf{x}^{(2)}], [\mathbf{x}^{(1)}, \mathbf{x}^{(3)}], [\mathbf{x}^{(1)}, \mathbf{x}^{(4)}], [\mathbf{x}^{(2)}, \mathbf{x}^{(3)}], [\mathbf{x}^{(2)}, \mathbf{x}^{(4)}], [\mathbf{x}^{(3)}, \mathbf{x}^{(4)}]\right) \tag{2.133}$$

and has the properties (Woodhouse, 1980)

$$[\mathbf{X}][\mathbf{x},\mathbf{y}] = [\mathbf{X}\mathbf{x},\mathbf{X}\mathbf{y}] \tag{2.134}$$

$$[\mathbf{X}][\mathbf{Y}] = [\mathbf{X},\mathbf{Y}] \tag{2.135}$$

where $\mathbf{x}$ and $\mathbf{y}$ are any two 4-vectors. The first identity allows us to write the propagator of the minor equations (2.93), since for any two solutions $\mathbf{b}(z_b)$, $\bar{\mathbf{b}}(z_b)$ of the homogeneous equations (2.64) we have

$$\left[\mathbf{b}(z_b), \bar{\mathbf{b}_{\mathbf{b}}}(z)\right] = \left[\mathbf{P}(z_b,z_a)\mathbf{b}(z_a), \mathbf{P}(z_b,z_a)\bar{\mathbf{b}}(z_a)\right] \tag{2.136}$$

$$= [\mathbf{P}(z_b,z_a)]\left[\mathbf{b}(z_a),\bar{\mathbf{b}}(z_a)\right] , \tag{2.137}$$

and hence the minor propagator matrix is given by

$$\mathscr{P}(z_b,z_a) = [\mathbf{P}(z_b,z_a)] \tag{2.138}$$

$$= [\mathbf{Z}]\left[\exp(h\mathbf{A}')\right]\left[\mathbf{Z}^{-1}\right] \tag{2.139}$$

where we have made use of (2.135). The second order minors of $\exp(h\mathbf{A}')$ are given explicitly by

$$\mathbf{\Gamma}(1:6,1:3) = \begin{bmatrix} c_{\mathrm{P}}c_{\mathrm{S}} & -k\zeta_{\mathrm{S}}^{-1}s_{\mathrm{S}}c_{\mathrm{P}} & \omega^2\zeta_{\mathrm{S}}^{-1}s_{\mathrm{S}}c_{\mathrm{P}} \\ -k\zeta_{\mathrm{P}}^{-1}s_{\mathrm{P}}c_{\mathrm{S}} & 1+k^2\zeta_{\mathrm{P}}^{-1}s_{\mathrm{P}}\zeta_{\mathrm{S}}^{-1}s_{\mathrm{S}} & -\omega^2k\zeta_{\mathrm{P}}^{-1}s_{\mathrm{P}}\zeta_{\mathrm{S}}^{-1}s_{\mathrm{S}} \\ \xi_4 & k\xi_8 & c_{\mathrm{P}}c_{\mathrm{S}}-k^2\zeta_{\mathrm{P}}^{-1}s_{\mathrm{P}}\zeta_{\mathrm{S}}^{-1}s_{\mathrm{S}} \\ \omega^2\zeta_{\mathrm{P}}^{-1}s_{\mathrm{P}}c_{\mathrm{S}} & -k\omega^2\zeta_{\mathrm{P}}^{-1}s_{\mathrm{P}}\zeta_{\mathrm{S}}^{-1}s_{\mathrm{S}} & \omega^4\zeta_{\mathrm{P}}^{-1}s_{\mathrm{P}}\zeta_{\mathrm{S}}^{-1}s_{\mathrm{S}} \\ k\zeta_{\mathrm{P}}^{-1}s_{\mathrm{P}}c_{\mathrm{S}} & -k^2\zeta_{\mathrm{P}}^{-1}s_{\mathrm{P}}\zeta_{\mathrm{S}}^{-1}s_{\mathrm{S}} & \omega^2k\zeta_{\mathrm{P}}^{-1}s_{\mathrm{P}}\zeta_{\mathrm{S}}^{-1}s_{\mathrm{S}} \\ -\zeta_{\mathrm{P}}^{-1}s_{\mathrm{P}}\zeta_{\mathrm{S}}s_{\mathrm{S}} & k\zeta_{\mathrm{P}}^{-1}s_{\mathrm{P}}c_{\mathrm{S}} & -\omega^2\zeta_{\mathrm{P}}^{-1}s_{\mathrm{P}}c_{\mathrm{S}} \end{bmatrix} , \tag{2.140}$$

$$\mathbf{\Gamma}(1:6,4:6) = \begin{bmatrix} \xi_5 & k\zeta_{\mathrm{S}}^{-1}s_{\mathrm{S}}c_{\mathrm{P}} & -\zeta_{\mathrm{S}}^{-1}s_{\mathrm{S}}\zeta_{\mathrm{P}}s_{\mathrm{P}} \\ k\xi_8 & -k^2\zeta_{\mathrm{P}}^{-1}s_{\mathrm{P}}\zeta_{\mathrm{S}}^{-1}s_{\mathrm{S}} & k\zeta_{\mathrm{S}}^{-1}s_{\mathrm{S}}c_{\mathrm{P}} \\ \xi_9 & -k\xi_8 & -\xi_5 \\ c_{\mathrm{P}}c_{\mathrm{S}} - k^2\zeta_{\mathrm{P}}^{-1}s_{\mathrm{P}}\zeta_{\mathrm{S}}^{-1}s_{\mathrm{S}} & \omega^2 k\zeta_{\mathrm{P}}^{-1}s_{\mathrm{P}}\zeta_{\mathrm{S}}^{-1}s_{\mathrm{S}} & -\omega^2\zeta_{\mathrm{S}}^{-1}s_{\mathrm{S}}c_{\mathrm{P}} \\ -k\xi_8 & 1 + k^2\zeta_{\mathrm{P}}^{-1}s_{\mathrm{P}}\zeta_{\mathrm{S}}^{-1}s_{\mathrm{S}} & -k\zeta_{\mathrm{S}}^{-1}s_{\mathrm{S}}c_{\mathrm{P}} \\ -\xi_4 & -k\zeta_{\mathrm{P}}^{-1}s_{\mathrm{P}}c_{\mathrm{S}} & c_{\mathrm{P}}c_{\mathrm{S}} \end{bmatrix} \tag{2.141}$$

where we have defined auxiliary variables

$$\xi_4 = \omega^{-2}(\zeta_{\mathrm{S}}s_{\mathrm{S}}c_{\mathrm{P}} - k^2\zeta_{\mathrm{P}}^{-1}s_{\mathrm{P}}c_{\mathrm{S}}) \tag{2.142}$$

$$\xi_5 = \omega^{-2}(\zeta_{\mathrm{P}}s_{\mathrm{P}}c_{\mathrm{S}} - k^2\zeta_{\mathrm{S}}^{-1}s_{\mathrm{S}}c_{\mathrm{P}}) \tag{2.143}$$

$$\xi_6 = \omega^{-2}(k^2 - \zeta_{\mathrm{P}}\zeta_{\mathrm{S}}) \tag{2.144}$$

$$\xi_7 = \omega^{-4}(1 - c_{\mathrm{P}}c_{\mathrm{S}} + s_{\mathrm{P}}s_{\mathrm{S}}) \tag{2.145}$$

$$\xi_8 = \zeta_{\mathrm{P}}^{-1}s_{\mathrm{P}}\zeta_{\mathrm{S}}^{-1}s_{\mathrm{S}}\xi_6 + \omega^2\xi_7 \tag{2.146}$$

$$\xi_9 = \zeta_{\mathrm{P}}^{-1}s_{\mathrm{P}}\zeta_{\mathrm{S}}^{-1}s_{\mathrm{S}}\xi_6^2 + 2k^2\xi_7\,. \tag{2.147}$$

2.1.4 Algorithm for minor vector propagation

The foregoing analysis leads to the following algorithm for propagating a minor vector $\mathbf{m}_a$ at z_a to $\mathbf{m}_b$ at $z_b = z_a + h$, *i.e.* for computing

$$\mathbf{m}(z_b) = [\mathbf{Z}]\,\mathbf{\Gamma}\left[\mathbf{Z}^{-1}\right]\mathbf{m}(z_a)\,. \tag{2.148}$$

Rather than directly evaluating and multiplying the minor matrices in (2.148), we can improve computational efficiency by exploiting the structure of the minor matrices $[\mathbf{Z}]$ and $[\mathbf{Z}^{-1}]$ since they contain many zero elements. The procedure consists of first multiplying by the minor matrix of $\mathbf{Z}^{-1}$ to obtain x_i, then multiplying by the minor matrix of $\exp(h\mathbf{A}')$ (*i.e.* $\mathbf{\Gamma}$), using some auxiliary variables t_i, to obtain y_i and finally multiplying by the minor

matrix of $\mathbf{Z}$:

$$
\begin{aligned}
x_1 &= m_{a3} \\
x_2 &= -2\mu k m_{a1} + m_{a2} \\
x_3 &= -\rho m_{a1} \\
x_4 &= 2\rho^{-1}\mu k(m_{a5} - m_{a2} + 2\mu k m_{a1}) - \rho^{-1} m_{a6} \\
x_5 &= m_{a5} + 2\mu k m_{a1} \\
x_6 &= m_{a4} \\
t_1 &= k(x_2 - x_5) - \omega^2 x_3 \\
t_2 &= c_{\mathrm{S}} x_1 - \zeta_{\mathrm{S}}^{-1} s_{\mathrm{S}} t_1 \\
t_3 &= -c_{\mathrm{P}}\zeta_{\mathrm{S}}^{-1} s_{\mathrm{S}} x_6 + \zeta_{\mathrm{P}}^{-1} s_{\mathrm{P}} t_2 - \xi_8 x_4 \\
y_1 &= -\zeta_{\mathrm{P}} s_{\mathrm{P}} \zeta_{\mathrm{S}}^{-1} s_{\mathrm{S}} x_6 + c_{\mathrm{P}} t_2 + \xi_5 x_4 \\
y_2 &= x_2 - k t_3 \\
y_3 &= x_3 + \xi_4 x_1 - \xi_5 x_6 + \xi_8 t_1 + \xi_9 x_4 \\
y_4 &= x_4 + \omega^2 t_3 \\
y_5 &= k t_3 + x_5 \\
y_6 &= c_{\mathrm{P}} c_{\mathrm{S}} x_6 + c_{\mathrm{S}} \zeta_{\mathrm{P}}^{-1} s_{\mathrm{P}} t_1 - \zeta_{\mathrm{P}}^{-1} s_{\mathrm{P}} \zeta_{\mathrm{S}} s_{\mathrm{S}} x_1 - \xi_4 x_4 \\
m_{b1} &= -\rho^{-1} y_3 \\
m_{b2} &= y_2 - 2\rho^{-1} k\mu y_3 \\
m_{b3} &= y_1 \\
m_{b4} &= y_6 \\
m_{b5} &= y_5 + 2\rho^{-1} k\mu y_3 \\
m_{b6} &= 2k\mu(-y_2 + 2\rho^{-1} k\mu y_3 + y_5) - \rho y_4 \,.
\end{aligned}
$$

The quantities $\xi_1, \ldots, \xi_7$ can be calculated stably for arbitrarily small ω by manipulating their formulae in such a way that the factors ω^{-2} and ω^{-4} cancel. The only remaining term for which a limit needs to be taken is of the form $\sinh(\omega^2 a)/\omega^2$, for some $a = a(\omega)$ that is well-behaved at $\omega = 0$; $\sinh(\omega^2 a)/\omega^2$ can be calculated stably for arbitrarily small

$|\omega|$ and can be replaced by $a(0)$ in the case that $\omega = 0$. Introducing further auxiliary variables $\chi_1, \ldots, \chi_4$

$$\chi_1 = 2\omega^{-2} \sinh \tfrac{1}{2} h(\zeta_{\mathrm{P}} - \zeta_{\mathrm{S}}) = 2\omega^{-2} \sinh \left(\tfrac{1}{2} \omega^2 h \frac{\rho/\mu - \rho/\sigma}{\zeta_{\mathrm{P}} + \zeta_{\mathrm{S}}} \right) \tag{2.149}$$

$$\chi_2 = \omega^{-2} \sinh h(\zeta_{\mathrm{P}} - \zeta_{\mathrm{S}}) = \chi_1 \cosh \tfrac{1}{2} h(\zeta_{\mathrm{P}} - \zeta_{\mathrm{S}}) \tag{2.150}$$

$$\chi_3 = \omega^{-2}(s_{\mathrm{P}}^2 - s_{\mathrm{S}}^2) = \chi_2 \sinh h(\zeta_{\mathrm{P}} + \zeta_{\mathrm{S}}) \tag{2.151}$$

$$\chi_4 = k^2(\rho/\mu + \rho/\sigma) - \omega^2 \rho^2 / \mu\sigma, \tag{2.152}$$

we obtain the following results for $\xi_1, \ldots, \xi_7$

$$\xi_1 = \chi_1 \sinh \tfrac{1}{2} h(\zeta_{\mathrm{P}} + \zeta_{\mathrm{S}}) \tag{2.153}$$

$$\xi_2 = \frac{-k^4 \chi_3 + \chi_4 s_{\mathrm{P}}^2}{k^2 s_{\mathrm{S}} + \zeta_{\mathrm{S}} \zeta_{\mathrm{P}} s_{\mathrm{P}}} \tag{2.154}$$

$$\xi_3 = \frac{k^4 \chi_3 + \chi_4 s_{\mathrm{S}}^2}{k^2 s_{\mathrm{P}} + \zeta_{\mathrm{P}} \zeta_{\mathrm{S}} s_{\mathrm{S}}} \tag{2.155}$$

$$\xi_4 = -\frac{k^4 \chi_3 + \chi_4 c_{\mathrm{P}}^2 s_{\mathrm{S}}^2}{\zeta_{\mathrm{P}}(k^2 s_{\mathrm{P}} c_{\mathrm{S}} + \zeta_{\mathrm{P}} \zeta_{\mathrm{S}} c_{\mathrm{P}} s_{\mathrm{S}})} \tag{2.156}$$

$$\xi_5 = \frac{k^4 \chi_3 - \chi_4 c_{\mathrm{S}}^2 s_{\mathrm{P}}^2}{\zeta_{\mathrm{S}}(k^2 s_{\mathrm{S}} c_{\mathrm{P}} + \zeta_{\mathrm{S}} \zeta_{\mathrm{P}} c_{\mathrm{S}} s_{\mathrm{P}})} \tag{2.157}$$

$$\xi_6 = \frac{\chi_4}{k^2 + \zeta_{\mathrm{P}} \zeta_{\mathrm{S}}} \tag{2.158}$$

$$\xi_7 = -\tfrac{1}{2} \chi_1^2 \,. \tag{2.159}$$

To obtain solutions, all that remain to be specified are the boundary condition vectors for the particular problem being considered.

2.1.5 Boundary condition vectors

A number of model geometries are of interest in geophysical problems. Below we state boundary condition vectors appropriate to the problem of the calculation of seismograms in layered media which can include an overlying ocean layer.

Free surface

If the structure is terminated at z_1 (the top) by a free surface, we require that the stress components of the stress-displacement vectors $\mathbf{b}^{\text{P-SV}}$ and $\mathbf{b}^{\text{SH}}$ vanish, *i.e.*

$$\mathbf{b}^{\text{SH}}(z_1) = \alpha \begin{bmatrix} 1 \\ 0 \end{bmatrix}, \quad \mathbf{b}^{\text{P-SV}}(z_1) = \alpha_1 \begin{bmatrix} 1 \\ 0 \\ 0 \\ 0 \end{bmatrix} + \alpha_2 \begin{bmatrix} 0 \\ 1 \\ 0 \\ 0 \end{bmatrix} \tag{2.160}$$

for some α, α_1 and α_2. Therefore, to represent a free surface we choose the boundary condition vectors to be

$$\bar{\mathbf{v}}^{\text{SH}(1)} = \begin{bmatrix} 1 \\ 0 \end{bmatrix}, \quad \bar{\mathbf{v}}^{\text{P-SV}(1,1)} = \begin{bmatrix} 1 \\ 0 \\ 0 \\ 0 \end{bmatrix}, \quad \bar{\mathbf{v}}^{\text{P-SV}(1,2)} = \begin{bmatrix} 0 \\ 1 \\ 0 \\ 0 \end{bmatrix}. \tag{2.161}$$

The ocean floor

If the top boundary of the solid part of the structure is an interface with an overlying ocean, we still require the shear traction to vanish at the ocean floor, and therefore choose

$$\bar{\mathbf{v}}^{\text{SH}(1)} = \begin{bmatrix} 1 \\ 0 \end{bmatrix}. \tag{2.162}$$

In order to specify $\bar{\mathbf{v}}^{\text{P-SV}(1)}$, we need to consider wave propagation in the ocean, and to apply the condition of zero shear traction at the ocean floor and zero normal traction at

the ocean surface. For a uniform ocean of depth h_{w}, we choose (for positive ω)

$$\bar{\mathbf{v}}^{\text{P-SV(1,1)}} = \begin{bmatrix} \cosh(h_{\mathrm{w}}\zeta_{\mathrm{P}}) \\ 0 \\ \rho_{\mathrm{w}}\omega^2\zeta_{\mathrm{P}}^{-1}\sinh(h_{\mathrm{w}}\zeta_{\mathrm{P}}) \\ 0 \end{bmatrix}, \quad \bar{\mathbf{v}}^{\text{P-SV(1,2)}} = \begin{bmatrix} 0 \\ 1 \\ 0 \\ 0 \end{bmatrix}. \tag{2.163}$$

where ρ_{w} is the density of ocean water, and we use the P-wave velocity of water in evaluating ζ_{P} in (2.124). The normalisation of these vectors is arbitrary, so in the case that the arguments of cosh and sinh have large real parts, the first of these vectors can be multiplied by a small factor, to cancel the exponentially large terms. Since ζ_{P} is defined so that $\mathrm{Re}\,\zeta_{\mathrm{P}} \geq 0$, it is convenient to renormalise by a factor $2\mathrm{e}^{-h_{\mathrm{w}}\zeta_{\mathrm{P}}}$, in which case we have

$$\bar{\mathbf{v}}^{\text{P-SV(1,1)}} = \begin{bmatrix} 1+\mathrm{e}^{-2h_{\mathrm{w}}\zeta_{\mathrm{P}}} \\ 0 \\ \rho_{\mathrm{w}}\omega^2\zeta_{\mathrm{P}}^{-1}\left(1-\mathrm{e}^{-2h_{\mathrm{w}}\zeta_{\mathrm{P}}}\right) \\ 0 \end{bmatrix}, \quad \bar{\mathbf{v}}^{\text{P-SV(1,2)}} = \begin{bmatrix} 0 \\ 1 \\ 0 \\ 0 \end{bmatrix}. \tag{2.164}$$

Interface with an underlying homogeneous solid half-space

If the structure is terminated at z_2 (the bottom) by an interface with an underlying homogeneous half-space, we need to ensure that the continuation of the solution into the half-space represents only downward traveling or downward decaying waves. A solution to the system of homogeneous equations (2.64) for SH-wave motion with depth-dependence proportional to $e^{\zeta z}$ is given by $\mathbf{b}^{\mathrm{SH}} = \mathbf{b}e^{\zeta z}$ for some constant vector $\mathbf{b}$, *i.e.*

$$\partial_z \mathbf{b}\, e^{\zeta z} = \mathbf{A}^{\mathrm{SH}}\mathbf{b}\, e^{\zeta z}, \tag{2.165}$$

which implies $\mathbf{A}^{\mathrm{SH}}\mathbf{b} = \zeta\,\mathbf{b}$ and hence ζ is an eigenvalue of $\mathbf{A}^{\mathrm{SH}}$. The eigenvalues of $\mathbf{A}^{\mathrm{SH}}$ are found to be $\pm\zeta_{\mathrm{S}}$ with corresponding eigenvectors $[1, \pm\mu\zeta_{\mathrm{S}}]^{\mathrm{T}}$. If we include the time-dependence, our solutions are now proportional to $e^{\mathrm{i}\omega t \pm \zeta_{\mathrm{S}} z}$. For $\omega > 0$ the solution with $+\zeta_{\mathrm{S}}$ represents downward-traveling or downward-decaying waves, and that with $-\zeta_{\mathrm{S}}$

represents upward-traveling or upward-decaying waves, hence we choose

$$\bar{\mathbf{v}}^{\mathrm{SH}(2)} = \begin{bmatrix} 1 \\ \mu\zeta_{\mathrm{S}} \end{bmatrix}. \tag{2.166}$$

where the material parameters correspond to those of the underlying half-space.

Similarly, the *P-SV* system has eigenvalues $\pm\zeta_{\mathrm{P}}$, $\pm\zeta_{\mathrm{S}}$, with corresponding eigenvectors $\left[\pm\zeta_{\mathrm{P}}, k, 2\mu k^2 - \rho\omega^2, \pm 2\mu k\zeta_{\mathrm{P}}\right]^{\mathrm{T}}$ and $\left[k, \pm\zeta_{\mathrm{S}}, \pm 2\mu k\zeta_{\mathrm{S}}, 2\mu k^2 - \rho\omega^2\right]^{\mathrm{T}}$. Again, we chose the solutions with $+\zeta_{\mathrm{P}}$ and $+\zeta_{\mathrm{S}}$ as these correspond to downward traveling or downward decaying *P*- and *SV*-waves, leading to

$$\bar{\mathbf{v}}^{\text{P-SV}(2,1)} = \begin{bmatrix} \zeta_{\mathrm{P}} \\ k \\ 2\mu k^2 - \rho\omega^2 \\ 2\mu k\zeta_{\mathrm{P}} \end{bmatrix}, \quad \bar{\mathbf{v}}^{\text{P-SV}(2,2)} = \begin{bmatrix} k \\ \zeta_{\mathrm{S}} \\ 2\mu k\zeta_{\mathrm{S}} \\ 2\mu k^2 - \rho\omega^2 \end{bmatrix}, \tag{2.167}$$

Once more, we use the material parameters of the underlying half-space to evaluate the components of the boundary condition vectors. The minor vector formed from the *P-SV* boundary condition vectors can be written (omitting an overall factor of $\rho\omega^2$, which is of no account for $\omega \neq 0$, as the normalisation is arbitrary, but would invalidate the results for $\omega = 0$)

$$\mathbf{m}^{(2)} = \begin{bmatrix} \mu^{-1}\xi \\ 2k\left(\xi + \frac{1}{2}\right) \\ -\zeta_{\mathrm{P}} \\ \zeta_{\mathrm{S}} \\ -2k\left(\xi + \frac{1}{2}\right) \\ \rho\omega^2 - 4k^2\mu(\xi + 1) \end{bmatrix} \tag{2.168}$$

where

$$\xi = \frac{\mu(\zeta_{\mathrm{P}}\zeta_{\mathrm{S}} - k^2)}{\rho\omega^2} = \frac{\rho\omega^2\sigma^{-1} - k^2(1 + \mu\sigma^{-1})}{k^2 + \zeta_{\mathrm{P}}\zeta_{\mathrm{S}}}. \tag{2.169}$$

The second equality here exhibits ξ in a form that is well-behaved as $\omega \to 0$. Thus we can

now calculate the stress-displacement vectors $\mathbf{b}^{\mathrm{SH}}$ and $\mathbf{b}^{\mathrm{P\text{-}SV}}$, which we can integrate over wavenumber and frequency to obtain displacements.

2.2 Forward modelling: examples

The foregoing theory was implemented in a computer program which evaluates the integrals $K_r^m(r,\omega)$, $K_\phi^m(r,\omega)$, $K_z^m(r,\omega)$ from (2.55)–(2.57), as described in Appendix A. Here, we discuss some aspects pertinent to obtaining accurate numerical solutions, and present some example calculations and results of benchmark tests against existing computer codes.

2.2.1 Computational considerations

Integration along the real frequency axis in (2.3) is not possible due to the occurrence of poles corresponding to surface wave contributions. We move the integration contour into the lower half-plane to avoid these poles by calculating displacements at complex frequencies $\omega - \alpha\mathrm{i}$ for some positive constant α. As a consequence, the inverse Fourier transform computed with (2.3) contains the desired displacement time series multiplied by a decreasing factor $\mathrm{e}^{-\alpha t}$, which must be corrected for through multiplication by $\mathrm{e}^{\alpha t}$. Care must be taken in choosing α: too small a value and poles on the real frequency axis will not be avoided, too large a value and a loss of precision will occur towards the end of the time series as the decreasing exponential factor becomes small. We choose α such that the correcting factor does not exceed 10 by the end of the time series, i.e. $\alpha \sim \frac{\ln 10}{t_{\max}}$ where $t_{\max}$ is the required duration of the time series; Friederich and Dalkolmo (1995) gave a similar rule of thumb.

The value of α also impacts the choice of wavenumber spacing, Δk, since increasing α produces smoother k-integrands. However, it is not the only influence on Δk as the Bessel functions become increasingly oscillatory with radius r, so the distance to the most remote observation point, $r_{\max}$, is also important. Choosing suitable values for the wavenumber

Thickness (km)	$v_{\rm P}$ (km/s)	$v_{\rm S}$ (km/s)	ρ ($\times 10^3$ kg/m^3)
3.00	1.80	0.00	1.02
2.00	4.50	2.40	2.57
5.00	5.80	3.30	2.63
20.00	6.50	3.65	2.85
∞	8.00	4.56	3.34

Table 2.1: Crustal model adapted from the P-wave velocity model of Papoulia and Makris (2004), used in the calculation of the displacement seismograms shown in Figs. 2.1 and 2.5. We used $v_{\rm P}$:$v_{\rm S}$ and $v_{\rm P}$:ρ ratios for the corresponding layers of the local crustal model given by CRUST2.0 to obtain all of the crustal parameters.

and frequency spacing, we use Simpson's rule to carry out the numerical quadrature (e.g. Press *et al.*, 1993).

The wavenumber integration is truncated at $k_{\rm max}$, whose value is chosen in consideration of the spatial length scales of the problem using

$$k_{\rm max} = \max\left(2.5 \times \frac{2\pi}{z_d}, 2 \times \frac{2\pi}{h_l}\right) \tag{2.170}$$

where h_l is the smallest horizontal wavelength of deformation that we wish to resolve, and z_d is the difference between the source and receiver depths. The first of the expressions in (2.170) is taken from Pollitz (1996), and is only invoked for sources shallower than $1.25h_l$.

Figure 2.1 shows displacement seismograms output from a typical calculation using the layered crustal structure given in Table 3.1. Seismograms are calculated at 18 equally spaced stations between 30 and 200 km due north of the epicentre, using a symmetrical cosine tapered boxcar moment rate function of half-duration 4.5 s. For this $t_{\rm max}$ and $r_{\rm max}$ we choose $\alpha = 0.023$ and $\Delta k = 1.7 \times 10^{-3}$ km to obtain solutions at 1400 k-values and 257 frequencies between 0 and 1 Hz. The source corresponds to a left-lateral strike-slip earthquake, striking 340° at a depth of 34 km with seismic moment $M_0 = 2.4 \times 10^{27}$ dyne-cm.

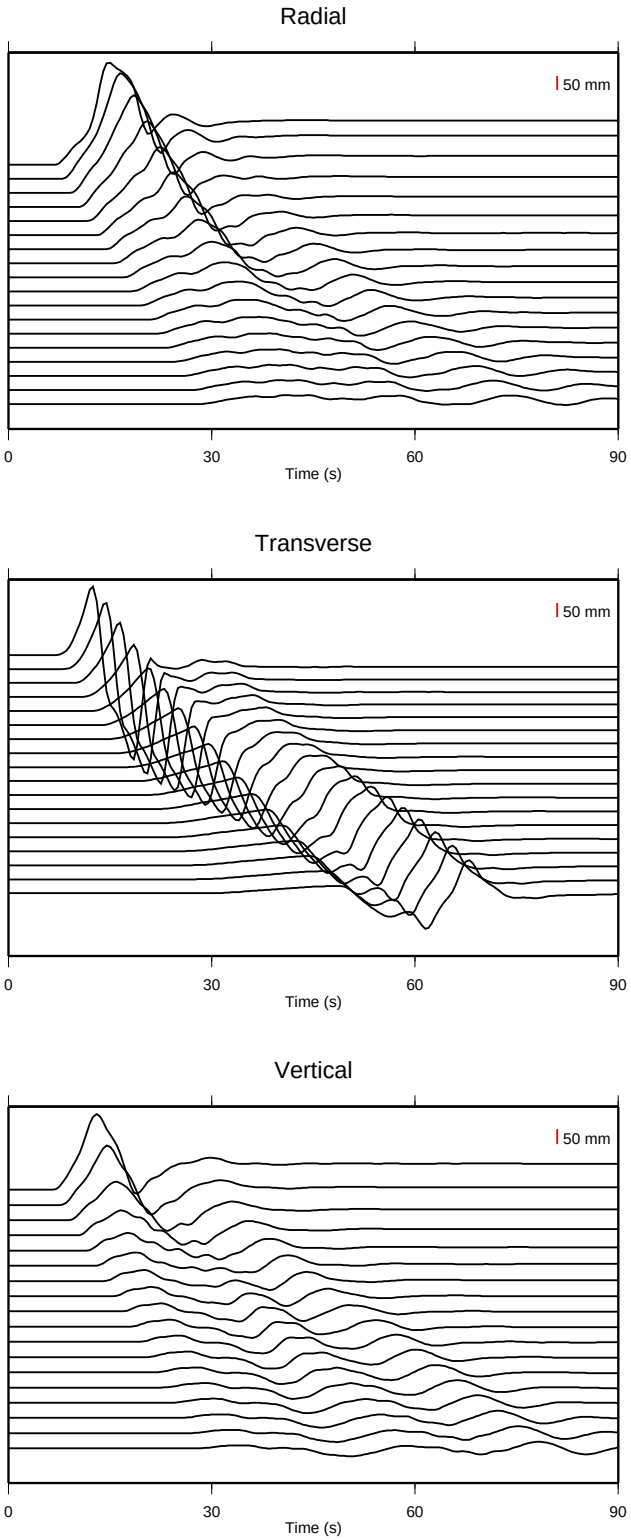

Figure 2.1: Radial (top), transverse (middle) and vertical (bottom) component displacement seismograms calculated in the layered crustal structure given in Table 3.1 for a left-lateral strike-slip earthquake, striking 340° at a depth of 34 km. Seismograms are plotted for stations at 10 km intervals along a profile from $r = 30$ km to $r = 200$ km, due north of the epicentre.

2.2.2 Verification of numerical solution

We carried out two tests to verify the accuracy of our method and its implementation. Firstly, the analytical expressions of Okada (1985) for the static displacement of a homogeneous half-space provide a convenient initial check on the accuracy of our numerical solution. Secondly, a comparison of our displacement time series with those calculated using a publicly available discrete wavenumber-reflectivity code, `AXITRA` (a program by O. Coutant available at http://www.orfeus-eu.org/), allows us to assess the accuracy of the full dynamic calculation in both homogeneous and plane layered media.

Static displacement of a homogeneous half-space

Figure 2.2 shows the northwards (top row), eastwards (middle row) and vertical (bottom row) components of the coseismic displacement of the Earth's surface arising from a moment tensor source buried in an elastic, isotropic and homogeneous half-space (with $v_{\mathrm{P}} = 6.00$ km/s, $v_{\mathrm{S}} = 3.46$ km/s, and $\rho = 2.7 \times 10^3$ kg/m^3). The source is identical to that used in Figure 2.1. The static displacement fields are calculated on a 100 km $\times$ 100 km grid using our method (left column) and the method of Okada (1985) (middle column). The absolute disagreement between these two methods (right column) is everywhere smaller than 10^{-5} m, verifying the accuracy of our numerical solution. In fact, for this special case of a homogeneous half-space it can be shown that our method leads to analytical expressions for the static displacement field that are equivalent to those of Okada (1985) (see the appendix to O'Toole and Woodhouse (2011)).

Dynamic displacement of homogeneous and layered media

Figure 2.3 shows north (left column), east (middle column) and vertical (right column) displacement seismograms, calculated for the same homogeneous crustal structure as used in Figure 2.2, using our method (solid black line) and `AXITRA` (dashed red line). Comparisons

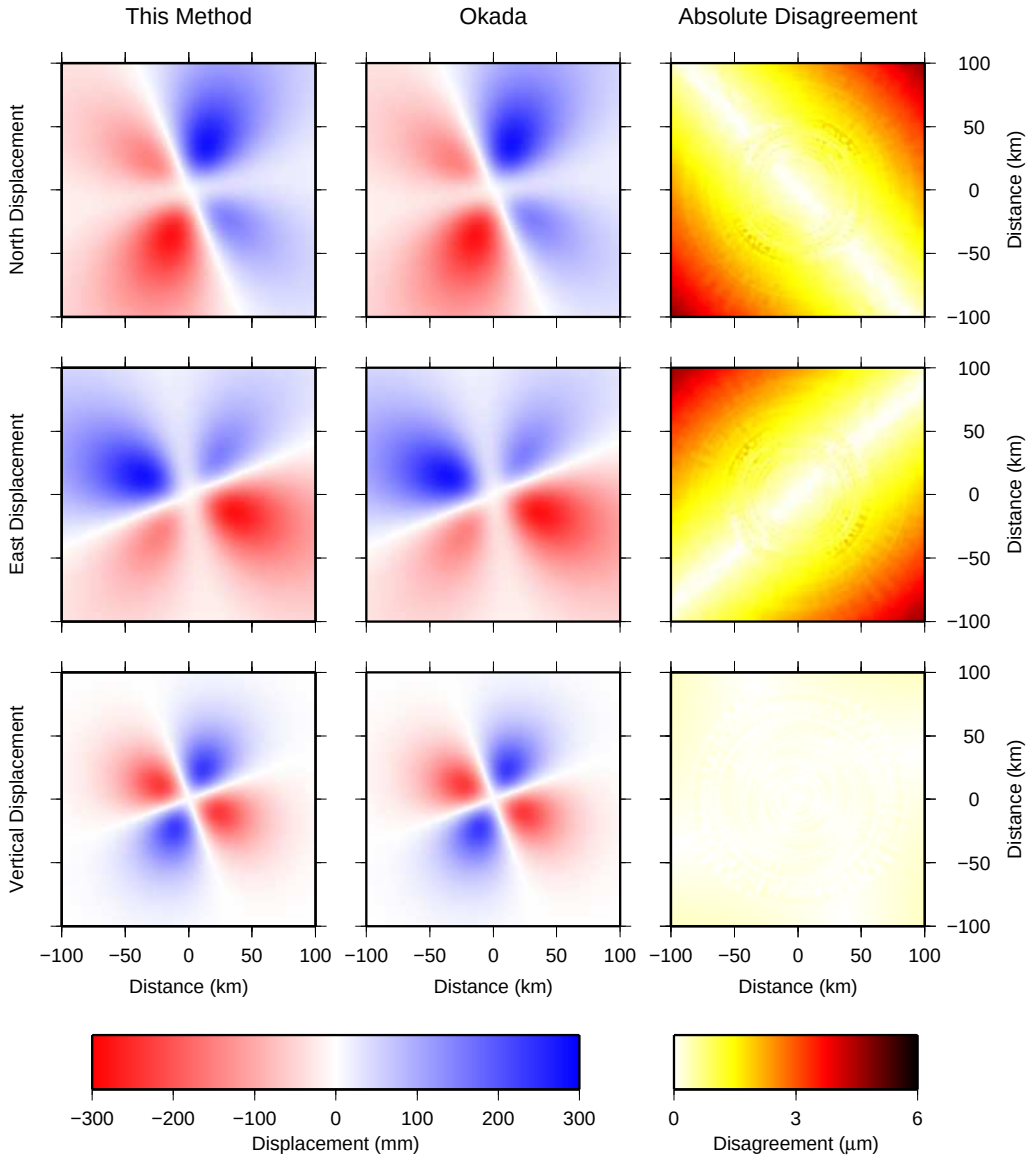

Figure 2.2: Northward (top row), eastward (middle row) and vertical (bottom row) static surface displacements in a homogeneous half-space with $v_{\mathrm{P}} = 6.00$ km/s, $v_{\mathrm{S}} = 3.46$ km/s and $\rho = 2.70 \times 10^3$ kg/m^3, due to a generic left-lateral strike-slip earthquake identical to that used in Fig, 2.1. Coseismic displacements are calculated using our method (left column) and the method of Okada (1985) (middle column). Displacements (in mm) are indicated by the shading. The absolute disagreement between the two methods (in μm) is plotted in the right column, and is clearly negligible everywhere, validating our method for the homogeneous case. Axis labels indicate distance from the epicentre (in km). North is up the page.

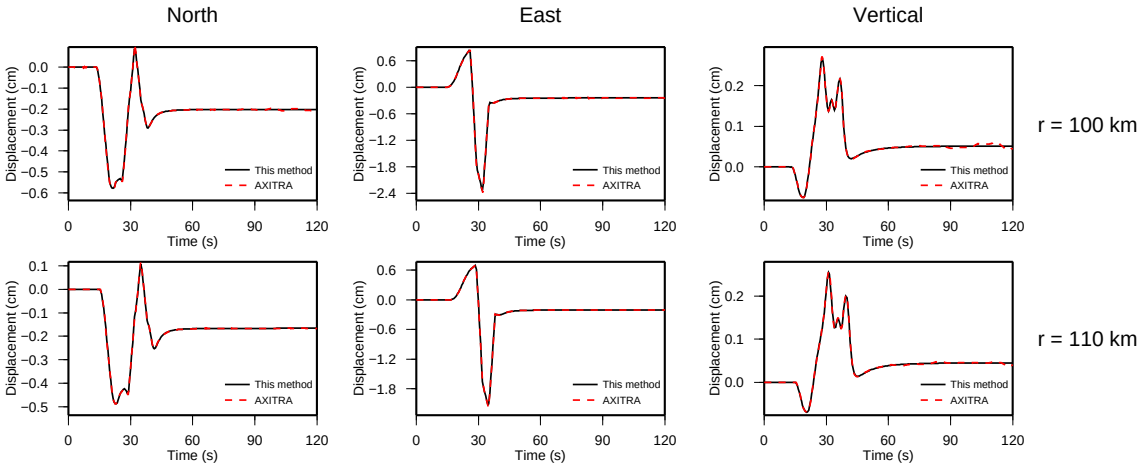

Figure 2.3: Comparison of synthetic displacement seismograms computed using our method (solid black line) and `AXITRA` (dashed red line) when a homogeneous crustal model with $v_P = 6.00$ km/s, $v_S = 3.46$ km/s, and $\rho = 2.7 \times 10^3$ kg/m^3 is used, for stations at a distance of 100 km (top row) and 110 km (bottom row). The source mechanism is a north-striking right-lateral strike slip fault at a depth of 10 km, with a symmetrical trapezoidal moment rate function of half-duration 4.5 s.

are made at stations located on a bearing 10° clockwise from north, at radii of 100 km (top row) and 110 km (bottom row). The source mechanism is a north-striking right-lateral strike slip earthquake at a depth of 10 km with seismic moment $M_0 = 1.1 \times 10^{26}$ dyne-cm. The moment rate function is a symmetrical trapezoid of half-duration 4.5 s. The two methods show a high degree of agreement, verifying the accuracy of our method.

Similarly, Figure 2.4 shows the same calculation when the layered crustal model shown in Table 2.2 is used. Again, the two methods are in excellent agreement, confirming the accuracy of our calculation when a more complicated crustal structure is used.

2.2.3 Comparisons to data

The implementation of the minor vector theory of Woodhouse (1980), and its adaptation for computing static displacements, described above was motivated by the availability of new seismic observations made by continuously recording GPS receivers. These time-series contain both static and dynamic displacement signals, which makes them challenging to

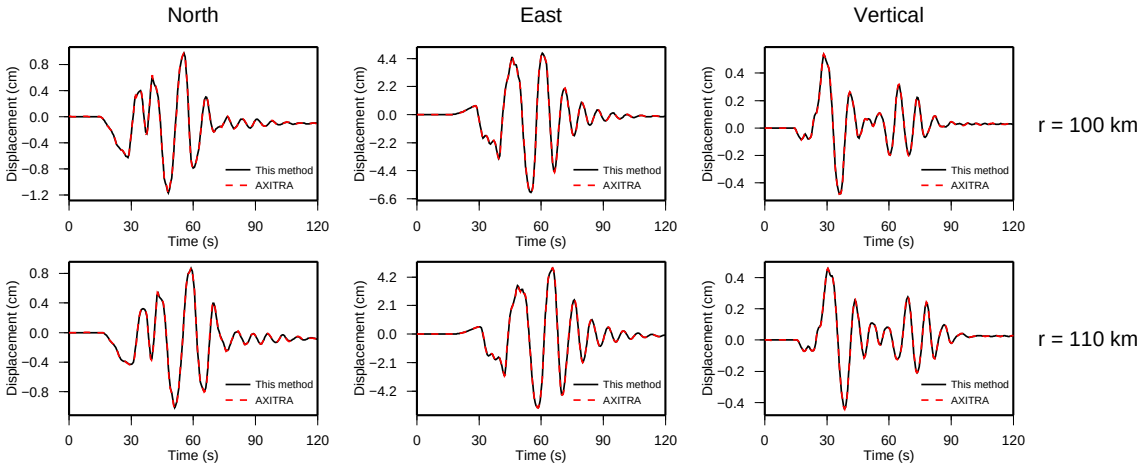

Figure 2.4: As for Figure 2.3 except here seismograms are calculated using the layered crustal model given in Table 2.2.

Thickness (km)	v_P (km/s)	v_S (km/s)	ρ ($\times 10^3$ kg/m^3)
1.50	2.20	1.00	2.20
6.50	4.30	2.30	2.60
7.00	6.00	3.40	2.70
6.00	6.60	3.70	2.90
6.00	7.20	4.00	3.05

Table 2.2: Crustal structure adapted from model S5 of CRUST2.0, used in the calculation of the seismograms shown in Figs. 2.4

model using some conventional techniques. Here we present example forward calculations compared to actual GPS observations, to demonstrate the potential utility of the method developed here. A second motivation was the desire to compute static displacement fields in layered media, since many inversions of geodetic data rely on the simplistic assumption that the earth can be modelled as a homogeneous elastic half space. We use line of sight displacements recorded by InSAR to demonstrate this application. The stability of the minor vector method at any frequency also means that high frequency waveforms can also be modelled using this approach. To this end, comparisons of observed and synthetic seismograms computed at frequencies up to 100 Hz will be presented in the context of

monitoring microearthquakes induced by hydraulic fracturing operations in Chapters 6 and 5.

GPS waveforms

We obtained three-component 1 Hz continuous GPS data for 5 sites operated by the Centre for Observation and Modelling of Earthquakes and Tectonics (COMET) for the 14$^{\text{th}}$ February 2008 M_{W} 6.9 South West Aegean Sea earthquake. Most of the time series were low quality, with high-frequency noise and longer period ($\sim$ 60 s) oscillations dominating the signal. There are several causes of the noise which are difficult to remedy, especially when the time series are short (Segall and Davis, 1997), and we make no attempt to correct the data.

We calculated synthetic displacement seismograms for this event using the method described in Section 2.1. The earthquake source parameters we used are given in Table 2.3, taken from the Global Centroid Moment Tensor catalogue. The hypocentral depth was adjusted to 30 km as, using the method of Fox (2007) and Fox *et al.* (2012), we found this to be the best fitting crustal depth from teleseismic data, in agreement with the work of Roumelioti *et al.* (2009). The earth model used in the calculations is given in Table 3.1. This model is adapted from the P-wave velocity model of Papoulia and Makris (2004); we used v_{P}:v_{S} and v_{P}:ρ ratios for the corresponding layers of the local crustal model given by CRUST2.0[2] to obtain all of the crustal parameters.

Since we are not investigating data processing techniques, we confine our attention here to the single time series that visually shows an unambiguous signal of the dynamic and static displacements caused by this event, the east component of motion at Kerya (36.493270697° N, 22.383514667° E, elevation 199.7927826 m). We filtered the data and synthetics by convolving them with a boxcar function of duration 5 s. We experimented with other filters but found that these did not enable a clear signal to be extracted from any additional channels, so we used this simple filter which removes enough high-frequency

[2]http://igppweb.ucsd.edu/~gabi/rem.html

Event	Lat. (° N)	Long. (° E)	Depth (km)	Strike (°)	Dip (°)	Rake (°)	Moment (dyne-cm)
C200802141009A	36.24	21.79	30	332	6	120	2.4×10^{26}

Table 2.3: Source parameters for the 14$^{\text{th}}$ February 2008 South West Aegean Sea earthquake, taken from the Global CMT catalogue, with the depth altered to the best fitting crustal depth found using the method of Fox (2007) and Fox *et al.* (2012) from teleseismic data.

noise without excessively smoothing out the important features of the time series. The symmetrical cosine tapered boxcar moment rate function of half-duration 4.5 s used in the calculation of synthetic seismograms is an implicit filtering operation which cannot be equivalently applied to the data.

Figure 2.5 shows the data (solid line) with the corresponding synthetic displacement seismogram (dashed line) calculated in our layered earth model. Qualitatively speaking, the synthetic seismogram emulates the data well. The first motions occur at the same time, and the amplitude and duration of ground motion also agree well. Finally, the magnitude of the static offset (14.3 mm) is reasonable in comparison with the data. This motion is $\sim$ 50% larger than that predicted for any other available channel, thus the clear signal observed in this time series likely results from the relatively large westward displacement that occurred at Kerya.

Line of sight displacements measured using InSAR

We obtained line of sight displacements measured using InSAR for the 6 October 2008, M_w 6.3 Damxung, Tibet, earthquake. An unwrapped interferogram for this event, generated by differencing SAR phase measurements from two ascending track satellite passes on dates either side of the earthquake, is shown in Figure 2.6; further details of the data processing are given in Elliott *et al.* (2010). The azimuth of the look direction from the satellite to the ground is $\sim$77°, with an incidence angle of 41°from the vertical, so this satellite is most sensitive to vertical and east-west motions.

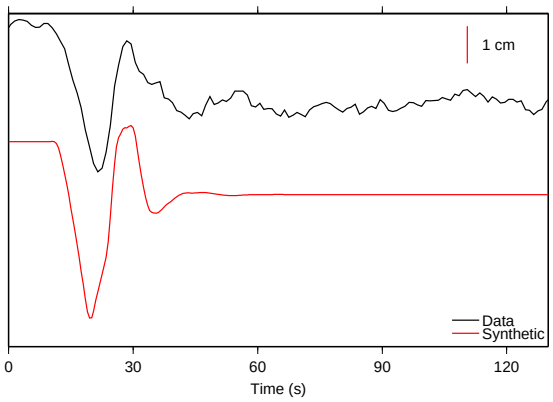

Figure 2.5: East component data (black line) and synthetic (red line) displacement seismograms at Kerya. The synthetic seismogram was calculated using the crustal and earthquake models given in Tables 3.1 and 2.3 respectively. The arrival time and amplitude of the first motion are in close agreement, and the synthetic static displacement (14.3 mm) is also reasonable, suggesting our method is useful for modelling existing continuous GPS datasets.

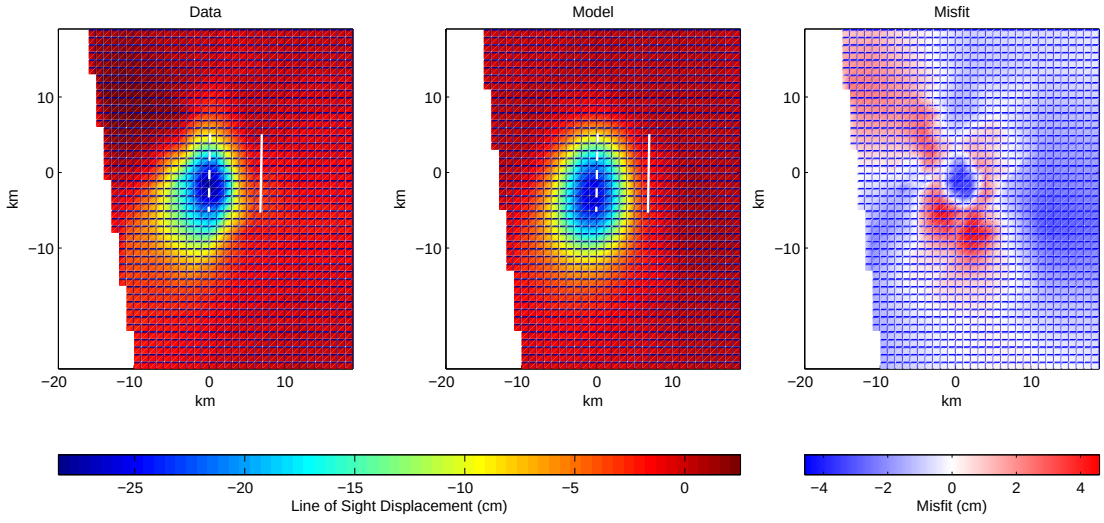

Figure 2.6: Observed and modelled line of sight displacements for the 6 October 2008 M_w 6.3 Damxung earthquake assuming a line source (dashed line). The local crustal model from CRUST2.0 was used in the modelling of the displacement field. The average residual is 1.08 cm.

This event ruptured a westward dipping normal fault, as suggested by the negative range changes, which imply motion away from the satellite on the down-thrown side of the fault. The up-dip projection of the fault plane to the earth's surface is indicated by the solid white line in Figure 2.6. Coseismic surface displacements were computed for a line source (dashed white line), approximated by summing the deformation field from ten point sources. The geometry of the individual sources is chosen to match the preferred faulting parameters determined by Elliott *et al.* (2010) from the same dataset assuming uniform slip on a planar fault in a homogeneous half space. Each of our point sources has the same seismic moment $M_0 = 3.1 \times 10^{17}$, *i.e.* one tenth of the overall value determined in the aforementioned study. Similarly, the extent of the line source matches the along-strike fault length at the centroid depth (7.4 km), both of which are taken from Elliott *et al.* (2010).

Static displacements and residuals, computed assuming the crustal model in the epicentral region taken from CRUST2.0, are shown in Figure 2.6. The average residual for our line source synthetics is 1.08 cm, which is similar to the value obtained by Elliott *et al.* (2010) for their best fitting planar source model with spatially varying slip vectors determined by inversion of the InSAR data. The fact that our comparatively simple forward model in a layered crust explains the data as well as a more complicated source model in a homogeneous model indicates that a trade off exists between the complexity of source and structural models. Further work is required to understand how to fairly partition the complexity between the two, and is left to future studies.

2.2.4 Discussion

We have shown that it is possible to calculate complete synthetic seismograms in plane layered elastic media that contain the zero-frequency (i.e. static) component of motion. While the methods of Wang (1999) and Zhu and Rivera (2002) have already been used for this purpose, the method presented here is stable at both high and low frequency

extremes, and allows the displacements to be obtained accurately, efficiently and stably using a single algorithm.

The comparison of synthetic seismograms to continuous GPS data acquired for a recent earthquake illustrates that data already exist that could be modelled in this way, and that even when there is noise in the data it is possible to achieve a reasonable fit to the dynamic and static displacements when an appropriate crust and source model are implemented. A number of studies have already exploited such data in inversions for the earthquake rupture process (Ji *et al.*, 2004; Miyazaki *et al.*, 2004; Kobayashi *et al.*, 2006; Yokota *et al.*, 2009; Shi *et al.*, 2010; Delouis *et al.*, 2010, e.g.); this number will increase as high quality data becomes more widely available.

Our method also enables solely the static component of deformation to be readily calculated for layered earth models, as demonstrated by the comparison to a line of sight displacement field measured by InSAR. At present, the formulae of Okada (1985) for the static deformation of a homogeneous half-space arising from a finite fault are often used in geodetic studies of Earth's surface displacement (e.g. Vigny *et al.*, 2005). Our knowledge of the Earth's crustal structure tells us that such a homogeneous model, while being potentially useful, is physically unrealistic. Geodetic inversions for earthquake source parameters can already include complications such as multiple faults and spatially varying slip distributions (e.g Guerrieri *et al.*, 2010), and we believe an important development is to include more realistic crustal structures in such inversions, as attempted by Simons *et al.* (2002), Fialko (2004) and others.

Of course, a plane layered structure is also unrealistic (Hsu *et al.*, 2011). However, accurate wavefield calculations for laterally heterogeneous media from, for example, spectral element method simulations (e.g. Komatitsch *et al.*, 2004) are not feasible for almost all of the world, which lacks detailed 3D crustal models. If we take a pragmatic approach, a plane layered earth model represents a compromise between homogeneous and 3D models, that should be applicable globally given the already existing datasets of crustal structure, such as CRUST2.0. Furthermore, where the effects of 3D structure are known and impor-

tant, they could be approximated by determining a 1D earth model for each station–event pair from the path-averaged 3D model. While we have presented calculations for point and line sources, a more general finite source model could be straightforwardly implemented by superposition of deformation fields calculated for spatially and temporally distributed point sources.

2.3 The inverse problem

Given a particular point earthquake source and crustal structure, the foregoing theory allows us to calculate the deformation field expected for that choice of model parameters; in other words, to solve the forward problem. Often, we actually have a set of observations of seismic deformations — be they coseismic offsets from GPS or InSAR, displacement waveforms measured by high-rate GPS receivers, or conventional seismograms — and our problem is to invert these data to inform us about the physics of the source and propagation medium. Here, we describe our method of solution to the inverse problem for the Centroid–Moment Tensor (CMT) solution of an earthquake, which follows closely that originally given by Dziewonski *et al.* (1981).

2.3.1 Least squares theory

The so-called equations of condition for a general discrete linear problem relating some n model parameters $\mathbf{x}$ to m synthetic data $\mathbf{s}$ can be written

$$\mathbf{A}\mathbf{x} = \mathbf{s}\,. \tag{2.171}$$

The $m \times n$ matrix $\mathbf{A}$ describes the physical relationship between the model and the data, and can be evaluated by solving the forward problem — the columns of $\mathbf{A}$ being the partial derivatives of the data with respect to each model parameter. Equivalently, each row of $\mathbf{A}$ can be thought of as describing the sensitivity of the corresponding datum to the model.

We assume that $m > n$ so that the system is overdetermined and we have more equations than model parameters.

Our problem is then to estimate the set of model parameters that best explains some actual data observations $\mathbf{d}$, which requires us to choose a measure of the degree of agreement between observed and synthetic data. For this purpose, we use the least squares misfit, m^2, defined

$$m^2 = \frac{(\mathbf{d}-\mathbf{s})^{\mathrm{T}}(\mathbf{d}-\mathbf{s})}{\mathbf{d}^{\mathrm{T}}\mathbf{d}}\,. \tag{2.172}$$

Errors in the data, and forward modelling — which arise due to our imperfect knowledge of the physics of the system under consideration — mean that we should never expect to exactly fit the data. In fact, we should be suspicious of very low misfit values as they may imply that we are using too fine a model parameterization and over-fitting the data (e.g. Trampert and Spetzler, 2006). For the time being, we neglect these sources of error, although they will be introduced in Chapter 6 when we consider the uncertainties in the model parameters recovered by an inversion.

Expanding (2.172) and writing it in component form, we have

$$m^2 d_i d_i = d_i d_i - 2 d_i A_{ij} x_j + x_i A_{ji} A_{jk} x_k\,, \tag{2.173}$$

which we minimise by differentiating with respect to each of the model parameters x_l and setting the result to zero

$$d_i d_i m^2_{,l} = 0 = -2 d_i A_{il} + 2 x_i A_{ji} A_{jl} \tag{2.174}$$

$$x_i A_{ji} A_{jl} = 2 d_i A_{il} \tag{2.175}$$

where we have made use of the Kronecker delta $\delta_{il} = x_{i,l}$ and its substitution property, and the symmetry of $\mathbf{A}^{\mathrm{T}}\mathbf{A}$. From (2.175), we obtain the least squares solution for the model parameters as

$$\mathbf{x} = \left(\mathbf{A}^{\mathrm{T}}\mathbf{A}\right)^{-1}\mathbf{A}^{\mathrm{T}}\mathbf{d}\,. \tag{2.176}$$

Thus for linear systems it is straightforward to obtain the optimal model in a single step, the only real challenge being the computation of matrix $\mathbf{A}$.

If the forward modelling equation (2.171) is weakly nonlinear, we must linearize the problem, so that for a small perturbation $\delta\mathbf{x}$ in the model we have

$$\mathbf{s}(\mathbf{x} + \delta\mathbf{x}) \approx \mathbf{A}\mathbf{x} + \mathbf{A}\delta\mathbf{x}\,, \tag{2.177}$$

where we have neglected terms of order $\delta\mathbf{f}^2$ and higher. Our problem is then to find the model update which brings data and synthetics into better agreement. We can therefore think of the synthetics calculated for the perturbed source (2.177) as being equivalent to the data vector that we seek to emulate, which allows us to write

$$\mathbf{d} - \mathbf{s}(\mathbf{x}) = \mathbf{A}\delta\mathbf{x}\,, \tag{2.178}$$

a linear equation of the same form as (2.171), with least squares solution for the update to the model parameters given by (*c.f.* (6.3))

$$\delta\mathbf{x} = \left(\mathbf{A}^{\mathrm{T}}\mathbf{A}\right)^{-1}\mathbf{A}^{\mathrm{T}}\left[\mathbf{d} - \mathbf{s}(\mathbf{x})\right]\,. \tag{2.179}$$

Recalling that (2.177) is only approximate, the change to the model suggested by (2.179) will only reduce, and not minimise, the data–synthetic misfit. Therefore we must apply the iterative scheme

$$\mathbf{x}_{\mathrm{i}+1} = \mathbf{x}_{\mathrm{i}} + \left(\mathbf{A}_{\mathrm{i}}^{\mathrm{T}}\mathbf{A}_{\mathrm{i}}\right)^{-1}\mathbf{A}_{\mathrm{i}}^{\mathrm{T}}\left[\mathbf{d} - \mathbf{s}(\mathbf{x}_{\mathrm{i}})\right] \tag{2.180}$$

in order to find the optimal model, where $\mathbf{A}_{\mathrm{i}} = \mathbf{A}(\mathbf{x}_{\mathrm{i}})$ and so must be recalculated at each iteration. Obviously, the application of (2.180) requires us to know a starting model $\mathbf{x}_0$ that is in some sense close to the actual best model, and we will assume that such an $\mathbf{x}_0$ is always available.

In many inverse problems, we require not only that our solution minimises the misfit, but also that it satisfies some constraints on the permitted model parameter values. For example, such constraints may arise in physical systems to satisfy conservation laws.

Linear constraints on model parameters — *i.e.* those that can be written in the form

$$\mathbf{Bx} = \mathbf{c} \tag{2.181}$$

can be enforced using the method of Lagrange multipliers. The constraint equations (2.181) are incorporated into the inverse problem, leading to the solution (e.g. Menke, 1989)

$$\begin{pmatrix} \mathbf{x} \\ \boldsymbol{\lambda} \end{pmatrix} = \begin{pmatrix} \mathbf{A}^{\mathrm{T}}\mathbf{A} & \mathbf{B}^{\mathrm{T}} \\ \mathbf{B} & \mathbf{0} \end{pmatrix}^{-1} \begin{pmatrix} \mathbf{A}^{\mathrm{T}}\mathbf{d} \\ \mathbf{c} \end{pmatrix} \tag{2.182}$$

where $\boldsymbol{\lambda}$ is the vector of Lagrange multipliers whose values are recovered in the inversion, but are not actually needed any further and so can be ignored.

2.3.2 CMT inversions

For completeness, here we briefly summarizing the CMT algorithm; for a detailed description of the method as originally conceived for long-period teleseismic waveform data, see Dziewonski *et al.* (1981), Dziewonski and Woodhouse (1983b) and Dziewonski *et al.* (1983). In the following, we use the word "seismogram" generally to describe any functional of the seismic source for which observations and forward modelling methods exist since any such data could, in principle, be used in inversions for earthquake source parameters.

Linear inversion: the moment tensor at an assumed centroid location

An indigenous source such as an earthquake is required to exert no net force or torque on the Earth. Supposing that the location of a seismic event is known in time t and space $\mathbf{x}$, we can completely specify the source, $\mathbf{m}$, in terms of the six independent elements of a symmetric moment tensor $\mathbf{M}$ (e.g Dziewonski *et al.*, 1981)

$$\mathbf{m} = (M_{rr}, M_{\theta\theta}, M_{\phi\phi}, M_{r\theta}, M_{r\phi}, M_{\theta\phi})^{\mathrm{T}}. \tag{2.183}$$

The forward problem for the predicted waveforms arising from such a source located at $\mathbf{x_s}$ can be written (Gilbert and Dziewonski, 1975)

$$u_k(\mathbf{x}, t) = \sum_{i=1}^{6} \psi_{ki}(\mathbf{x}, \mathbf{x_s}, t) m_i \,. \tag{2.184}$$

The k^{th} synthetic seismogram in the dataset, u_k, is given by a linear combination of the so-called excitation kernels, ψ_{ki}, weighted by the moment tensor vector. These kernel functions are the partial derivatives of the seismogram with respect to the components of $\mathbf{m}$

$$\psi_{ki} = \frac{\partial s_k}{\partial m_i} \,, \tag{2.185}$$

and represent the response excited by unit sources corresponding to each independent component of the moment tensor, and so also depend on the assumed earth model. From (2.184), it is clear that we have a linear inverse problem of the form $\mathbf{Ax} = \mathbf{s}$, with a least squares solution given by (e.g. Menke, 1989)

$$\mathbf{m} = (\mathbf{A}^{\mathrm{T}}\mathbf{A})^{-1}\mathbf{A}^{\mathrm{T}}\mathbf{d} \,. \tag{2.186}$$

where the 6 columns of matrix $\mathbf{A}$ are the excitation kernels corresponding to the discretized and filtered seismograms contained in the data vector $\mathbf{d}$. The fact that $\mathbf{A}$ and $\mathbf{d}$ are concatenations of all of the traces used in an inversion leads to efficient approaches for computing the quantities in (2.186), as described by Valentine (2010).

Given some estimate of the source location — for example, the hypocentre as determined from P-wave arrival times — we can use this linear inversion scheme to obtain the moment tensor. Within the limitations of this source representation, the solution is exact, and convergence is reached after a single iteration.

Nonlinear inversion: retrieval of all 10 source parameters

Since the assumed source location may not correspond to the position of the earthquake's centroid, we should actually determine the location of the earthquake in space and time in

addition to the moment tensor, which requires the solution of a nonlinear inverse problem. In this case, the source vector $\mathbf{f} = (\mathbf{m}, \mathbf{x}_c, t_c)^{\mathrm{T}}$ has ten components

$$\mathbf{f} = (M_{rr}, M_{\theta\theta}, M_{\phi\phi}, M_{r\theta}, M_{r\phi}, M_{\theta\phi}, \theta_c, \phi_c, z_c, t_c)^{\mathrm{T}} \ , \tag{2.187}$$

where the centroid latitude, longitude and depth are given by $\mathbf{x}_c = (\theta_c, \phi_c, z_c)$ and t_c is the centroid time. We assume that nonlinearity is weak, allowing us to linearize the problem and perform an iterative least-squares inversion for the best fitting point source via

$$\mathbf{f}_{\mathrm{i}+1} = \mathbf{f}_{\mathrm{i}} + \left(\mathbf{A}_{\mathrm{i}}^{\mathrm{T}}\mathbf{A}_{\mathrm{i}}\right)^{-1}\mathbf{A}_{\mathrm{i}}^{\mathrm{T}}\left[\mathbf{d} - \mathbf{s}(\mathbf{f}_{\mathrm{i}})\right] \tag{2.188}$$

where $\mathbf{A}$ now includes the location kernels $\partial_{\theta_c} s_k$, $\partial_{\phi_c} s_k$, $\partial_{z_c} s_k$ and $\partial_{t_c} s_k$. The starting source, $\mathbf{f}_0$, is typically the result of the linear inversion from the previous section.

2.3.3 Program architecture

Valentine (2010) developed a modular computational framework for performing tomographic inversions, whereby the problem was partitioned into separate "preparation" and "inversion" stages. Such an approach facilitates experimentation by allowing the user to change one aspect of the inversion work flow while leaving the other unchanged. In this thesis, we aim to exploit the flexibility offered by this system to investigate using a number of different data types to perform source inversions. This undertaking amounts to developing a new preparation object for near-field observations that is capable of handling high-rate GPS time-series, static displacements and microseismic waveforms.

The preparation stage can be thought of as a black box which takes in some seismic data, an earth model and an initial source model, and returns a set of partial derivatives with respect to the model parameters, and a vector of the residuals between data and synthetics computed for the input source. These outputs are the ingredients for solving the inverse problem, and so become inputs for another black box — the inversion object

— which generates a model update vector. The corrected source can then be fed back into the preparation object and the process repeated until convergence is achieved.

Within the preparation object, different data types are identified using so called "data slices" (see Valentine, 2010, , chapter 2). The slice name is defined by the user during data selection. It is possible to extract multiple slices from a single trace, for example by picking body and mantle wave windows from globally recorded seismograms. For each seismogram in the input data file, slice names are read from the trace's header, and instructions are looked up detailing how that data slice should be processed, and how synthetics should be computed. As a consequence, by using a data file containing more than one slice type it is straightforward to combine different data types within the framework of Valentine (2010), although only preliminary work on joint inversions has been performed to date (Gilligan, 2010).

The computation of synthetics using the method described in this chapter is an example of a so-called embarrassingly parallel problem and can be easily distributed over the nodes of a computational cluster. After broadcasting input parameters like the earth model, station locations and moment tensor to all nodes, each processor can generate solutions at a subset of the desired frequency range without the need for to communicate with the other nodes. The spectra are then recombined by the root process. A parallel implementation of our forward modelling code is achieved with the Message Passing Interface.

The inversion object takes the partial derivatives and residuals output from the preparation stage, assembles these into the quantities needed to solve the inverse problem, and proceeds to compute the solution. We will generally use (2.180) to perform source inversions but, as we will see in Chapter 4, "intelligent" damping of the location-update step-length is needed in some source inversions using static displacement data. We have therefore modified the inversion object such that (4.12) and (4.13) may, at the request of the user, be used to perform the source inversion.

2.4 Calculation of partial derivatives

The calculation of excitation and location kernels appropriate to a particular type of data is a prerequisite for applying the foregoing theory to the inversion of those data. The CMT algorithm uses normal mode summation to compute long-period teleseismic waveform synthetics and their partial derivatives. While we could also use normal mode summation to compute synthetic GPS waveforms, it is unlikely to be the best choice for the application of GPS data presented in this thesis. Apart from the well-known problem of computing mode catalogues at frequencies higher than about 100 mHz (e.g. Yang *et al.*, 2010) the construction of whole earth eigenfunctions is computationally expensive for near-field data. Furthermore, we would like to compute kernels using the local crustal model at the centroid location; to use mode summation for the same calculation would require the recalculation of mode catalogues every time we encountered a new crustal structure.

Instead, we apply the minor propagator matrix method presented in Section 2.1 to compute accurate high-rate GPS time-series, microseismic waveforms and coseismic displacement fields for a plane layered elastic medium. This approach ensures numerical stability at all frequencies, including 0 Hz, as is required if we wish to recover the static displacement as part of the synthetic time-series. Furthermore, this method is advantageous as it can be straightforwardly adapted to enable the efficient computation of excitation and location kernels, as shown in Section 2.4.2.

2.4.1 Excitation kernels

The excitation kernels, being the partial derivatives of a synthetic seismogram with respect to the elements of the moment tensor, are simply the displacements arising from six elementary sources corresponding to each component of the moment tensor (2.184). Figure 2.7 shows an example set of excitation kernels computed for a 1 Hz GPS receiver at a distance of 39.6 km and azimuth of 118.2°for a source with a depth of 35 km. The earth model used in the computation of these kernels is given in Table 3.1. The relatively

small amplitudes of the M_{rr}, $M_{\theta\theta}$ and $M_{\phi\phi}$ kernels indicate that this location is not very sensitive to explosive sources. Furthermore, it is clear that these moment tensor components do not generate significant static displacements, and so if any coseismic offset were observed at this station it would require the excitation of the off-diagonal elements of the moment tensor.

2.4.2 Location kernels

Here, we derive expressions for the location kernels which we use in our CMT inversions of near-field seismic data. These derivations follow from the theory presented in Section 2.1, and the notation and coordinate systems used here are consistent with those from earlier. We have verified our implementation of the theory presented here through comparisons to derivative kernels calculated using a simple forward difference finite difference scheme $f'(a) \approx (f(a+h) - f(a))/h$ for small h (e.g. Riley *et al.*, 2007). In addition to being more accurate, direct calculation of the derivatives is advantageous because it is computationally cheaper than taking finite differences, an important consideration if we wish to perform source inversions in real time.

Centroid time kernel

The centroid time kernel is the negative of the time derivative of the synthetic seismogram and is straightforward to calculate in the frequency domain via multiplication of the synthetic spectra by $-\mathrm{i}\omega$.

Epicentral location kernels

Consider a seismic source located at $\mathbf{x}_s = (x_s, y_s, z_s)$. We seek the derivative of the displacement field, $\mathbf{u}(r, \phi, t)$, with respect to the epicentral location. Using the chain rule,

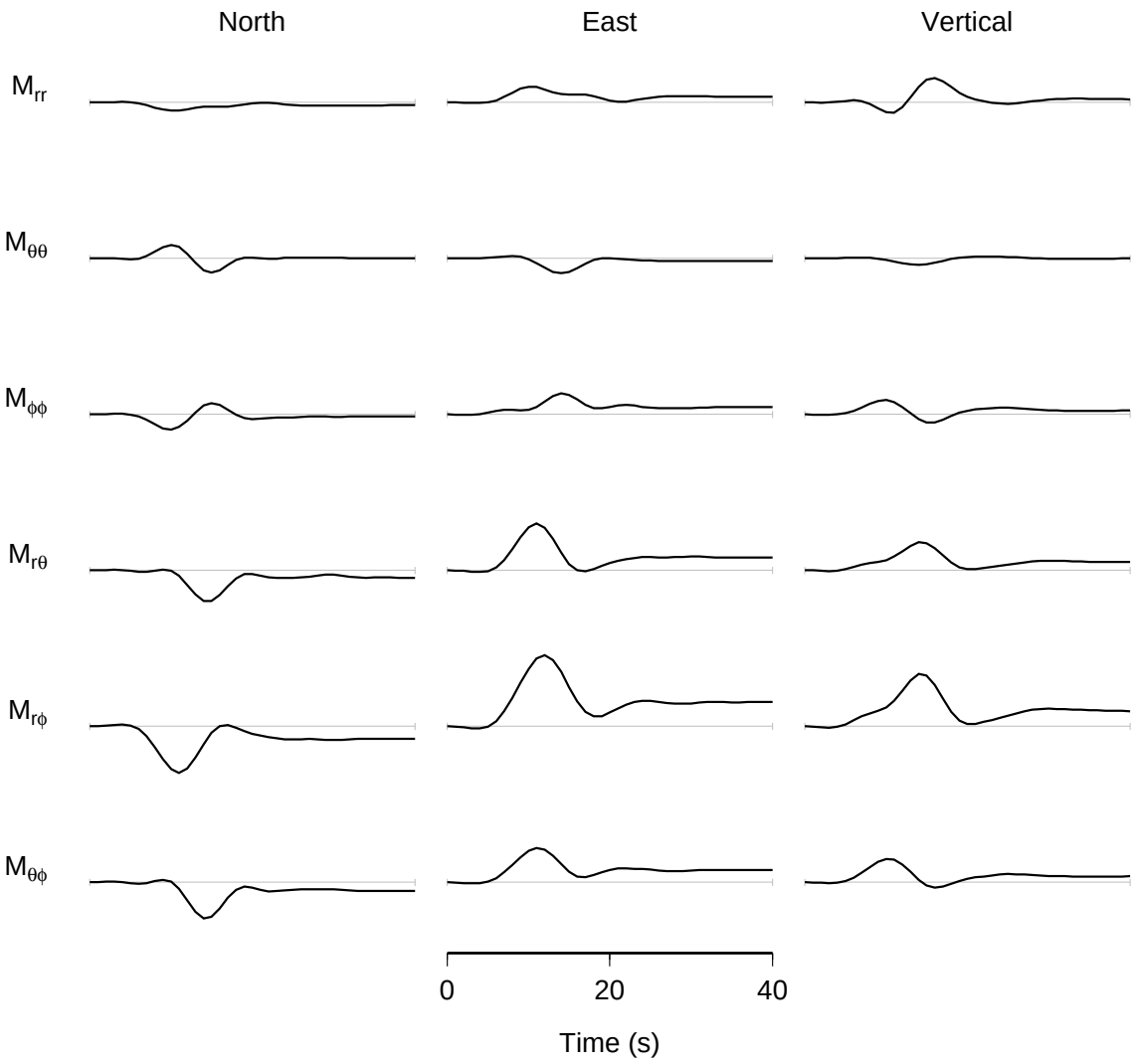

Figure 2.7: An example set of GPS excitation kernels computed for a station located at a distance of 39.6 km and azimuth 118.2° for an earthquake with a depth of 35 km. These six traces represent the ground motion excited by unit sources corresponding to each individual component of the moment tensor. The synthetic seismogram for a particular component of ground motion is then a linear combination of the six traces, weighted by the moment tensor. The CMT algorithm allows us to determine the optimum moment tensor by minimising the difference between HRGPS data and synthetics. The earth model used in this calculation is given in Table 3.1. The arbitrary vertical scale is common to all seismograms.

we can write

$$\frac{\partial \mathbf{u}}{\partial x_s} = \frac{\partial \mathbf{u}}{\partial r}\frac{\partial r}{\partial x_s} + \frac{\partial \mathbf{u}}{\partial \phi}\frac{\partial \phi}{\partial x_s} \tag{2.189}$$

$$\frac{\partial \mathbf{u}}{\partial y_s} = \frac{\partial \mathbf{u}}{\partial r}\frac{\partial r}{\partial y_s} + \frac{\partial \mathbf{u}}{\partial \phi}\frac{\partial \phi}{\partial y_s} \tag{2.190}$$

with

$$\frac{\partial r}{\partial x_s} = -\cos\phi\,, \quad \frac{\partial \phi}{\partial x_s} = \frac{\sin\phi}{r}\,, \tag{2.191}$$

$$\frac{\partial r}{\partial y_s} = -\sin\phi\,, \quad \frac{\partial \phi}{\partial y_s} = \frac{-\cos\phi}{r}\,. \tag{2.192}$$

Differentiating expressions (2.55)–(2.57) with respect to ϕ we obtain

$$\frac{\partial u_i}{\partial \phi} = \int \mathrm{d}\omega\, \frac{\mathrm{e}^{\mathrm{i}\omega t}}{2\pi \mathrm{i}\omega} \sum_m \mathrm{i}m \mathrm{e}^{\mathrm{i}m\phi} \quad K_i^m(r,\omega) \quad . \tag{2.193}$$

The derivatives of (2.55)–(2.57) with respect to the radial coordinate are of the form

$$\frac{\partial u_i}{\partial r} = \int \mathrm{d}\omega\, \frac{\mathrm{e}^{\mathrm{i}\omega t}}{2\pi \mathrm{i}\omega} \sum_{m=-2}^{2} \mathrm{e}^{\mathrm{i}m\phi} \quad \frac{\partial K_i^m}{\partial r} \quad . \tag{2.194}$$

From (2.58)–(2.60) we write

$$\frac{\partial K_r^m}{\partial r} = \frac{1}{2\pi}\int_0^\infty \left[kV_m \frac{\partial}{\partial r} J'_m(kr) - \frac{\mathrm{i}m}{r^2} W_m J_m(kr) + \frac{\mathrm{i}m}{r} W_m k J'_m(kr) \right] \mathrm{d}k \tag{2.195}$$

$$\frac{\partial K_\phi^m}{\partial r} = \frac{1}{2\pi}\int_0^\infty \left[-\frac{\mathrm{i}m}{r^2} V_m J_m(kr) + \frac{\mathrm{i}m}{r} V_m k J'_m(kr) - kW_m \frac{\partial}{\partial r} J'_m(kr) \right] \mathrm{d}k \tag{2.196}$$

$$\frac{\partial K_z^m}{\partial r} = \frac{1}{2\pi}\int_0^\infty k^2 U_m J'_m(kr)\,\mathrm{d}k\,. \tag{2.197}$$

To improve computational efficiency, we seek an expression for the second derivative of the Bessel function

$$\frac{\partial}{\partial r} J'_m(kr) = k J''_m(kr) \tag{2.198}$$

in terms of its lower derivatives, which we have already calculated. Rearranging Bessel's equation we obtain

$$\frac{\partial}{\partial r} J'_m(kr) = \frac{1}{kr^2} \left[-krJ'_m(kr) - (k^2r^2 - m^2)J_m(kr) \right] \tag{2.199}$$

which we use in (2.195)–(2.197) to calculate the radial derivatives of the displacement.

Source depth kernel

The algorithm derived in Section 2.1 allows us to solve systems of inhomogeneous ordinary differential equations of the form

$$\partial_z \mathbf{b} = \mathbf{A}\mathbf{b} + \mathbf{f}\,, \tag{2.200}$$

where the stress-displacement vector $\mathbf{b}$, the system matrix $\mathbf{A}$ and the source representation $\mathbf{f}$ are functions only of the vertical coordinate, z. Assuming that the source does not lie on a structural discontinuity, we can differentiate (2.200) with respect to the source depth z_s to obtain

$$\frac{\partial}{\partial z}\frac{\partial \mathbf{b}}{\partial z_s} = \mathbf{A}\frac{\partial \mathbf{b}}{\partial z_s} + \frac{\partial \mathbf{f}}{\partial z_s}\,. \tag{2.201}$$

Since this expression is of the same form as (2.200), we can use the same method of solution to obtain the source depth kernel by replacing the force term with its derivative with respect to source depth. The action of the source is implemented as a discontinuity in the solution at the source depth. After Al-Attar and Woodhouse (2008), who presented a similar result for the equivalent problem in a spherical geometry, we convert the force term into a slip condition at the source depth as follows.

A trial solution of (2.200) is

$$\mathbf{b}(z) = \mathbf{P}(z, z_2)\mathbf{v}(z)\,, \tag{2.202}$$

where $\mathbf{v}(z)$ is to be determined and $\mathbf{P}(z, z_2)$ is the propagator matrix. Differentiating (2.202) with respect to z, we obtain

$$\partial_z \mathbf{b}(z) = \mathbf{P}'(z, z_2)\mathbf{v}(z) + \mathbf{P}(z, z_2)\mathbf{v}'(z) = \mathbf{A}(z)\mathbf{b}(z) + \mathbf{f} \tag{2.203}$$

and recalling that $\partial_z \mathbf{P}(z, z_2) = \mathbf{A}(z)\mathbf{P}(z, z_2)$ this expression reduces to

$$\mathbf{v}'(z) = \mathbf{P}^{-1}(z, z_2)\mathbf{f}\,. \tag{2.204}$$

Integrating this expression upwards from some arbitrary depth z_2 below the source (i.e. $z_2 < z_s$) we find a particular integral of (2.200) is

$$\mathbf{v}(z) = \int_{z_2}^{z} \mathbf{P}^{-1}(z', z_2)\mathbf{f}(z')\ \mathrm{d}z' + \mathbf{v}(z_2) \tag{2.205}$$

and recalling the definition (2.202) we can express the stress-displacement vector as

$$\mathbf{b}(z) = \int_{z_2}^{z} \mathbf{P}(z, z')\mathbf{f}(z')dz' + \mathbf{P}(z, z_2)\mathbf{v}(z_2)\,. \tag{2.206}$$

Since the solution to the homogeneous equation is a continuous function of depth, the discontinuity at the source depth comes from the consideration of this particular integral alone. The force term is given by

$$\mathbf{f} = \mathbf{a}\delta(z - z_s) + \mathbf{c}\delta'(z - z_s) \tag{2.207}$$

where $\delta(z - z_s)$ is the Dirac delta function and the prime denotes its derivative. Using this expression in (2.206), the solution above the source is

$$\mathbf{b}(z) = \mathbf{P}(z, z_s)\mathbf{a}(z_s) - \int_{z_2}^{z} \frac{\partial}{\partial z'}\mathbf{P}(z, z')\mathbf{c}(z')\delta(z' - z_s)\,\mathrm{d}z' + \mathbf{P}(z, z_2)\mathbf{v}(z_2)\,, \tag{2.208}$$

where we have used the result (Riley *et al.*, 2007)

$$\int_I f(z)\delta^{(n)}(z)\,\mathrm{d}z = (-1)^n \int_I f^{(n)}(z)\delta(z)\,\mathrm{d}z \tag{2.209}$$

for the n^{th} derivative of the Dirac delta function in the interval I. We obtain the derivative of the propagator matrix with respect to its second argument by considering

$$\frac{\partial}{\partial z'}\left(\mathbf{P}(z,z')\mathbf{P}^{-1}(z,z')\right)=\mathbf{0} \tag{2.210}$$

which leads to

$$\frac{\partial}{\partial z'}\mathbf{P}(z,z')=-\mathbf{P}(z,z')\mathbf{A}(z')\,. \tag{2.211}$$

Using this result in (2.208), we can write the solution as

$$\mathbf{b}(z)=\begin{cases}\mathbf{P}(z,z_2)\mathbf{v}(z_2) & z\in[z_2,z_s)\\ \mathbf{P}(z,z_2)\mathbf{v}(z_2)+\mathbf{P}(z,z_s)\mathbf{a}(z_s)+\mathbf{P}(z,z_s)\mathbf{A}(z_s)\mathbf{c}(z_s) & z\in(z_s,z_1]\,.\end{cases} \tag{2.212}$$

It follows that the point source (2.207) produces a discontinuity, $\mathbf{s}$, in the solution vector at the source depth, given by

$$\mathbf{s}=\lim_{\epsilon\downarrow 0}[\mathbf{b}(z_s+\epsilon)-\mathbf{b}(z_s-\epsilon)]=\mathbf{a}(z_s)+\mathbf{A}(z_s)\mathbf{c}(z_s)\,. \tag{2.213}$$

Applying the same argument to (2.201), we find the derivative of the force term with respect to the source depth is

$$\frac{\partial\mathbf{f}}{\partial z_s}=-\mathbf{a}\delta'(z-z_s)-\mathbf{c}\delta''(z-z_s) \tag{2.214}$$

which we use in (2.206) along with $\partial_{z'}\mathbf{P}'(z,z')=\mathbf{P}(z,z')\mathbf{A}(z)\mathbf{A}(z)$ to obtain the discontinuity in the solution vector at the source depth given by

$$\mathbf{s}=\lim_{\epsilon\downarrow 0}\left[\frac{\partial\mathbf{b}(z_s+\epsilon)}{\partial\,\mathrm{d}z_s}-\frac{\partial\mathbf{b}(z_s-\epsilon)}{\partial\,\mathrm{d}z_s}\right]=-\mathbf{A}(z_s)\mathbf{a}(z_s)-\mathbf{A}(z_s)\mathbf{A}(z_s)\mathbf{c}(z_s)\,. \tag{2.215}$$

Thus we can easily calculate the derivative with respect to source depth by changing the discontinuity vector at the source depth to that given in (2.215). We write the discontinuity

vectors explicitly as

$$\mathbf{s}_m^{\text{P-SV}} = \begin{cases} \begin{bmatrix} \frac{F_3}{\sigma} \\ -\frac{k(\sigma(M_{11}+M_{22})-2(\lambda+\mu)M_{33})}{2\mu\sigma} \\ -\frac{1}{2}k^2\left(M_{11}+M_{22}\right)+\frac{\left(k^2\lambda+\rho\omega^2\right)M_{33}}{\sigma} \\ -\frac{k\lambda F_3}{\sigma} \end{bmatrix} & m=0 \\ \begin{bmatrix} \frac{k}{2\mu\sigma}\left((\lambda+\mu)(\mp M_{13}+\mathrm{i}M_{23})+\mu\left(\pm M_{31}-\mathrm{i}M_{32}\right)\right) \\ \frac{1}{2\mu}(\pm F_1-\mathrm{i}F_2) \\ \frac{1}{2}k(\pm F_1-\mathrm{i}F_2) \\ \frac{1}{2\sigma}\left[k^2\lambda(\mp M_{31}+\mathrm{i}M_{32})+\frac{1}{\mu}(\pm M_{13}-\mathrm{i}M_{23})(k^2(\lambda\mu-(\gamma+\mu)\sigma+\rho\sigma\omega^2))\right] \end{bmatrix} & m=\pm 1 \\ \begin{bmatrix} 0 \\ \frac{1}{4\mu}k(M_{11}-M_{22})\mp\frac{1}{4\mu}\mathrm{i}k(M_{12}+M_{21}) \\ \frac{1}{4}k^2(M_{11}-M_{22})\mp\frac{1}{4}\mathrm{i}k^2(M_{12}+M_{21}) \\ 0 \end{bmatrix} & m=\pm 2 \end{cases} \tag{2.216}$$

and

$$\mathbf{s}_m^{\text{SH}} = \begin{cases} \begin{bmatrix} \frac{k}{2\mu}(-M_{12}+M_{21}) \\ 0 \end{bmatrix} & m=0 \\ \begin{bmatrix} \frac{1}{2\mu}(\mp F_2-\mathrm{i}F_1) \\ \frac{1}{2\mu}(k^2\mu-\rho\omega^2)(\pm M_{23}+\mathrm{i}M_{13}) \end{bmatrix} & m=\pm 1 \\ \begin{bmatrix} \frac{-k}{4\mu}(M_{12}+M_{21})\pm\frac{\mathrm{i}k}{4\mu}(M_{22}-M_{11}) \\ 0 \end{bmatrix} & m=\pm 2\,. \end{cases} \tag{2.217}$$

Example location kernels

Example location kernels are shown in Figure 2.8; these were calculated using the same crustal model and source–receiver geometry as in Figure 2.7. These kernels are scaled so that the $\partial_{\theta_c} s_k$, $\partial_{\phi_c} s_k$, and $\partial_{z_c} s_k$ kernels represent the change in the seismogram with respect to a 10 km perturbation in each hypocentral co-ordinate; similarly the time kernel, $\partial_{t_c} s_k$, corresponds to a 2 s shift in origin time. Here, the variety of waveforms suggests that high-rate GPS data should allow us to resolve the location of the centroid in space and time, as we require. The shape of these kernels depends on the moment tensor, which is given in Table 3.3 ("Iteration 0" column); the synthetic HRGPS time-series corresponding to this source and station are also shown in Figure 2.8 for comparison to the location kernels.

Summary

In this chapter, we have developed the theory required to forward model and invert some seismic observables to obtain the centroid and moment tensor of an earthquake. The comparisons of synthetics to data made so far suggest that GPS and other types of near-field seismic observations contain a signal that can be used for studying earthquake sources. The chapters that follow discuss the implementation of specific data types within the source inversion framework outlined here, and present the results of inversions of these data.

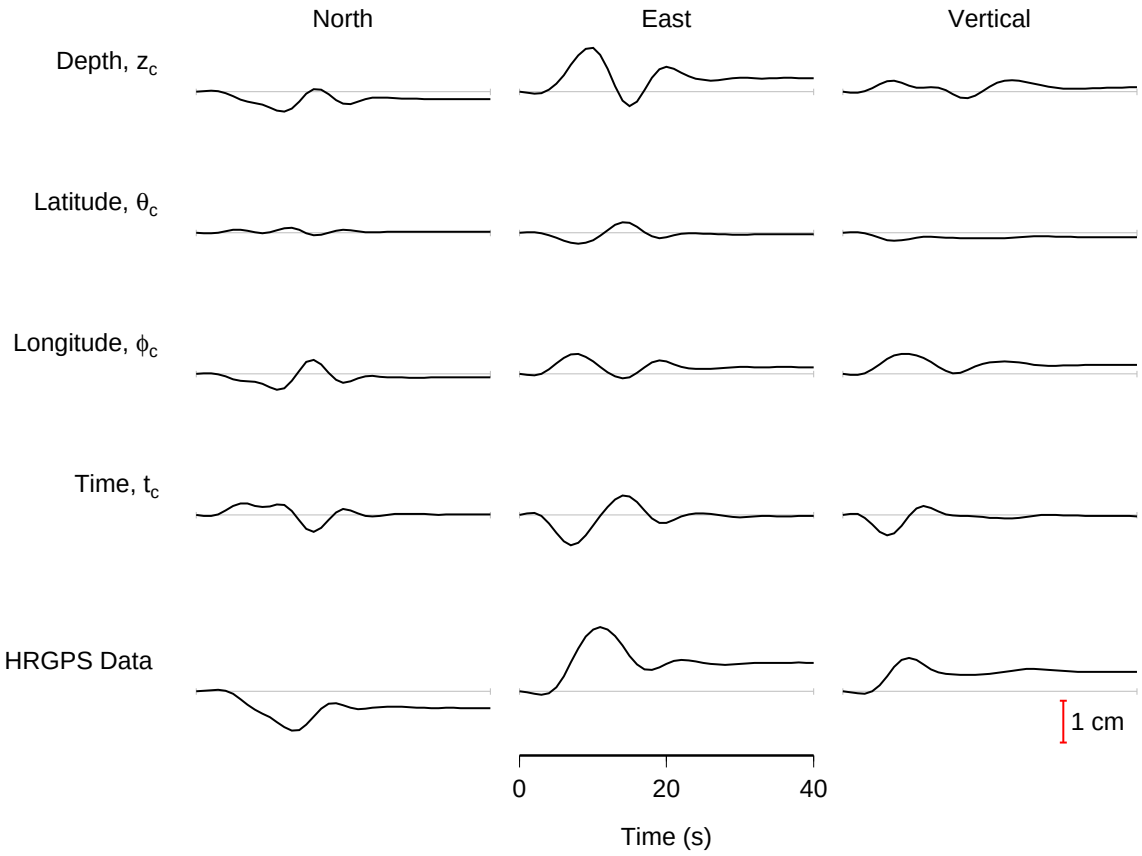

Figure 2.8: An example set of GPS location kernels computed for the same station and earth model as in Figure 2.7, scaled to represent the change in seismogram caused by a 10 km shift of the source in each spatial coordinate and a 2 s perturbation of the origin time. The diversity of waveforms suggest that this location is sensitive to changes in the centroid's position in space and time. These kernels also depend on the moment tensor, which is given in Table 3.3 ("Iteration 0" column); synthetic HRGPS data corresponding to this source are also shown for comparison purposes. All traces are plotted using the same vertical scale, indicated by the scale bar.

Chapter 3

CMT inversions using high-rate GPS waveforms

As its name implies, the Global Positioning System (GPS) is designed to enable users situated anywhere on Earth to quickly and accurately determine their location at any time (Hofmann-Wellenhof *et al.*, 2001). The distance from a GPS satellite to a receiver can be precisely calculated from the time taken for an electromagnetic signal — containing the time of broadcast — to propagate from the former to the latter, so long as the two have perfectly synchronised clocks. The distance is simply the difference between the time at which the signal was received and the time at which it was broadcast, multiplied by the speed of light. Using the distances to at least 3 satellites and a knowledge of their orbits, the receiver position can be determined by trilateration (Blewitt, 2007). The approximate satellite positions are known at the receiver in real time from the so called broadcast ephemerides: reference orbits that are improved by ground tracking, uploaded to the satellite, and then encoded into the signal transmitted to the GPS receiver (Hofmann-Wellenhof *et al.*, 2001).

GPS receivers must be portable and inexpensive if they are to be useful for navigation and so typically use a crystal clock for timing, which has some unknown error relative

to the precise atomic clocks on board the satellites. The satellite–receiver distances are therefore called pseudoranges as they are contaminated by this timing uncertainty. As a consequence, the pseudorange to a fourth satellite is required in practice so that the clock bias can also be solved for. The GPS satellite constellation is designed so that — neglecting local line of sight obstructions — at least four satellites are always visible from any point on Earth, with 7 or more satellites being visible 80 % of the time (Tsui, 2000). Any additional satellites that are available can be used to improve the positioning accuracy. The success of GPS technology is evident in the ubiquity of GPS receivers in items ranging from aircraft to mobile phones.

Beyond navigation, GPS has found great use in geophysics, as a tool for studying phenomena over arbitrarily long baselines, in consistent reference frames, and over time scales ranging from seconds to decades (for a comprehensive review, see Blewitt, 2007). For example, global GPS networks have been instrumental in quantifying long-term, long-wavelength geodynamical processes such as rigid plate motions (Sella *et al.*, 2002) and plate boundary strain rates (Kreemer *et al.*, 2003), while, at the opposite end of the spectrum, measurements of coseismic displacement fields made by local GPS networks are now routinely used to infer earthquake slip distributions (e.g. Blewitt *et al.*, 1993; Bock *et al.*, 1993) and their implications for seismic hazard (e.g. Murray-Moraleda and Simpson, 2009).

Recently, observations of dynamic displacements — seismic waves — made by GPS receivers operating at high sampling frequencies (e.g. Nikolaidis *et al.*, 2001; Larson *et al.*, 2003) have brought GPS data to the attention of seismologists. The versatility of GPS as a tool to measure Earth's deformation at time scales varying over 10 orders of magnitude has meant that dense permanent GPS networks are now routinely deployed in tectonically active regions. Such networks, typically operating at 1 Hz sampling rates, will capture local seismicity regardless of their original observational purpose. Furthermore — partly in response to the demands of seismologists (Hammond *et al.*, 2010) — data acquisition, storage and processing systems have become more sophisticated over time so that state of the art GPS networks are now able to stream 10 Hz data, yielding displacement waveforms

with millimetre-level accuracy in real-time (Bock *et al.*, 2011). This potentially rich data resource is yet to be fully exploited, and so there is a pressing need to develop methods for the routine analysis of high-rate GPS (HRGPS) waveforms.

In this chapter, we aim to develop and test methods for inverting high-rate GPS time-series for an earthquake's CMT solution[1]. We begin by giving a brief review of Global Positioning System hardware, positioning techniques and previous applications to earthquake studies. To validate our implementation of GPS data into the CMT inversion algorithm, we present a series of test inversions that use synthetic 1 Hz GPS datasets. As a proof of concept, we conclude by determining CMT solutions for two moderate sized earthquakes that were well observed by GPS instruments in Japan.

3.1 The Global Positioning System

A complete description of the Global Positioning System is beyond the scope of this thesis, and in any case has been given in a number of monographs (e.g Strang and Borre, 1997; Parkinson and Spiker, 1996; Teunissen and Kleusberg, 1998; Tsui, 2000; Hofmann-Wellenhof *et al.*, 2001). Here, we aim to introduce only the basic concepts necessary for us to proceed to use high-rate GPS for seismological purposes. GPS can be thought of in terms of space, control and user segments (e.g. Torge, 1998, chapter 5). The space segment consists of the satellite hardware, which are tracked and managed by the control segment, allowing anyone with a GPS receiver — the user segment — who can see four satellites to determine their position.

3.1.1 Space segment

A particular GPS satellite orbits the Earth in one of six equally spaced planes, each of which are inclined at an angle of 55°from the equator (see Figure 3.1). At least four

[1]Much of the material in this chapter has been published as O'Toole, Thomas B. and Valentine, Andrew P. and Woodhouse, John H. (2012).

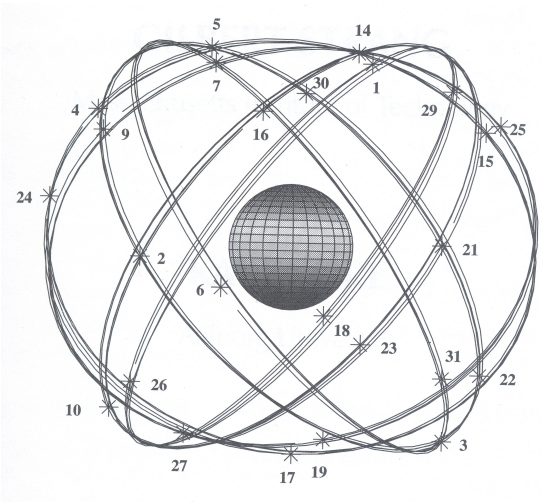

Figure 3.1: The GPS satellite constellation (reproduced from Strang and Borre, 1997, with kind permission of Wellesley–Cambridge Press).

satellites typically orbit within each of these orbital planes; a minimum of 21 GPS satellites must be operational at any time for precise global positioning to be possible, and so under normal conditions three of the available satellites are, strictly speaking, redundant (Teunissen and Kleusberg, 1998, chapter 2). Within each orbital plane the satellites are not uniformly separated to minimise the impact of the loss of any individual satellite. This satellite constellation represents the cheapest way to achieve global coverage with some resilience to satellite breakdown (Hofmann-Wellenhof *et al.*, 2001), and is constantly being updated and improved: the most recent GPS satellite launch was on 5 May 2013[2].

The first block of 11 GPS satellites (including one failed launch) were launched between 1978 and 1985 (Parkinson and Spiker, 1996, chapter 1), with initial operating capacity achieved in July 1993 when a total of 24 satellites came on line (Hofmann-Wellenhof *et al.*, 2001). Since GPS positioning is based upon precise timing, these GPS satellites are basically accurate chronometers. The earliest GPS satellites carried two atomic clocks, with the current generation carrying four (Hofmann-Wellenhof *et al.*, 2001). These clocks also supply the fundamental frequency $f_0 = 10.23\,\mathrm{MHz}$ used to generate the GPS signals.

[2]http://www.gps.gov/systems/gps/space/

The signals broadcast by a GPS satellite comprise two carrier waves, Link 1 (L1) and Link 2 (L2), of different frequencies, $f_{L1} = 1575.42\,\text{MHz}$ and$f_{L2} = 1227.60\,\text{MHz}$. The carrier waves are synthesised by integer multiplication of the fundamental clock frequency after it has been reduced by about 5 mHz to account for relativistic effects: $f_{L1} = 154 f_0$ and $f_{L2} = 120 f_0$. The carriers are then modulated by pseudorandom noise (PRN) codes, which take the value of ± 1 and so cause a 180°shift in the phase of the carrier whenever the value of the code changes. An example of this so-called biphase modulated signal is shown in Figure 3.2. Each satellite has unique PRN codes which modulate either or both of the carrier waves. The algorithms by which the PRN codes are generated permit 37 unique codes, placing a constraint on the total number of GPS satellites that can fly simultaneously. The PRN codes form an orthonormal basis so that the cross correlation of the signal with a copy generated in the receiver is zero unless the PRN code chosen at the receiver corresponds to that of the satellite from which the signal was received. The satellite clock reading at the time of broadcast and orbital parameters are also encoded in the signal, so that the propagation time and hence pseudorange can be measured at the receiver. The pseudorange can be measured either from the cross correlation of the code, or the phase of the carrier, as described in Section 3.1.4. A Doppler correction is also required in the receiver to account for the motion of the satellite. The description of the GPS signal given here is somewhat simplified; for a complete description see Parkinson and Spiker (1996, chapter 3).

The fact that the field of GPS seismology did not emerge sooner than the publication of Nikolaidis *et al.* (2001) is in part due to the fact that, before 2000, the civilian GPS signal was degraded in a process known as selective availability, by truncating the accuracy of the broadcast satellite positions and "dithering" the satellite clock. The effects of these signal manipulations on positioning accuracy are demonstrated dramatically by the GPS time-series in Figure 3.3, which spans the moment on 2 May, 2000 when selective availability was turned off.

The satellites follow almost circular orbits of radius ∼26,560 km, *i.e.* the orbits have an altitude of approximately $3r_e$ where r_e is the radius of the earth (Strang and Borre,

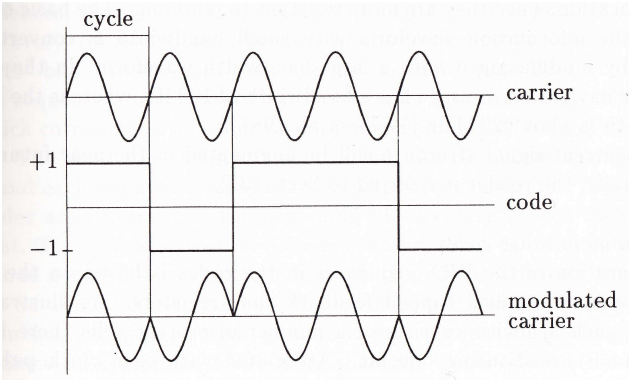

Figure 3.2: The basic structure of the GPS signal (reproduced from Hofmann-Wellenhof *et al.*, 2001, with kind permission of Springer Science+Business Media).

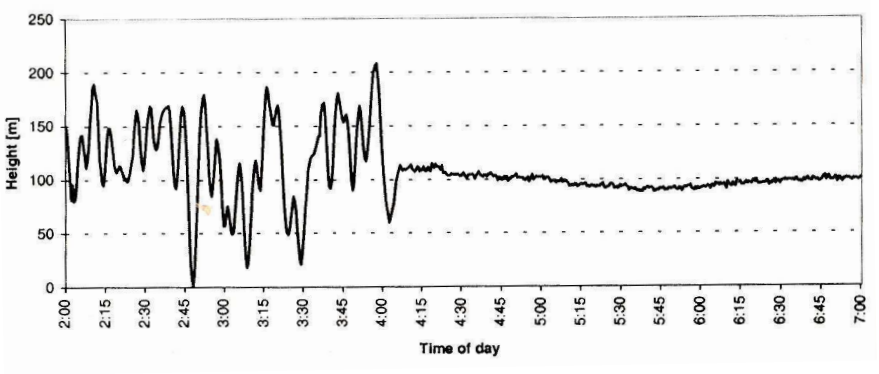

Figure 3.3: Vertical displacement of a GPS receiver at Kootwijk, the Netherlands for the time interval spanning the switch-off of selective availability (reproduced from Hofmann-Wellenhof *et al.*, 2001, with kind permission of Springer Science+Business Media).

1997). The orbital period of each satellite is 11 hours 58 minutes — approximately half a sidereal day (Teunissen and Kleusberg, 1998, chapter 2). A sidereal day is the time taken for the earth to make one complete revolution and so is slightly shorter than an apparent solar day (Tsui, 2000). The orbits are designed so that the satellites repeat their ground track every sidereal day, which allows errors caused by satellite geometry and repeating noise sources to be largely eliminated.

An important error source arises from the satellite geometry. Since the satellite constellation essentially returns to the same position every sidereal day, for GPS seismology

we can use the receiver position determined on the day preceding an earthquake to correct high rate displacement time-series recorded during shaking. We assume that the receiver did not move the day before the event, and so any observed motion is an artefact of the geometry of the satellite constellation at that moment, which can be subtracted from the displacements on the day of interest, a process known as sidereal filtering (Bock, 1991). In addition to reducing satellite geometry effects, sidereal filtering is useful for removing signal multipath noise caused by reflections from surfaces close to the transmitter and recorder. In fact, the ground repeat periods differ slightly from one sidereal day, with this deviation changing over time, and so precise orbital determination is a vital part of GPS positioning (Choi *et al.*, 2004) and is amongst the responsibilities of the control segment.

3.1.2 Control segment

Although GPS satellites are able to operate largely autonomously, some monitoring and control from the ground is necessary to ensure ongoing functionality. In particular, for accurate GPS positioning we require accurate satellite positioning and accurate timing, and so the major task of the control segment is to track the satellites, compute their orbits and maintain time synchronization of all the satellite clocks. This information is uploaded to each satellite about once per day to maintain the accuracy of the satellite clock and broadcast ephemerides (Hofmann-Wellenhof *et al.*, 2001).

Tracking is officially performed by five monitoring stations maintained by the US Department of Defence located at Hawaii, Colorado Springs, Ascension Island (South Atlantic), Diego Garcia (Indian Ocean) and Kwajalein (North Pacific Ocean) (Hofmann-Wellenhof *et al.*, 2001). An observatory at each of these locations monitors the pseudoranges to all visible satellites, which — after correction for ionospheric and meteorological effects — are communicated to the master control station at Colorado Springs, along with timing parameters determined by atomic clocks at the observatories. This information is used at the master control station to calculate satellite orbit and clock corrections, which are returned to the individual monitoring stations for upload to the satellite. Broadcast

ephemerides determined in this way yield orbital parameters accurate to ∼1.6 m in space, and satellite clocks errors of 7 ns (Blewitt, 2007).

Civilian tracking of GPS satellites was initiated by the International Association for Geodesy in 1994 (Segall and Davis, 1997). The resulting International GPS Service for Geodynamics (IGS) global tracking network currently consists of 360 stations[3], and, amongst other things, produces the most accurate estimates of GPS satellite orbit and clock errors, with values of <5 cm and 0.1 ns respectively. These products are free and available about 2 weeks after the observations are made, and so have been very widely used by the scientific community in *post hoc* analyses of GPS data for geodesy and seismology (e.g. Emore *et al.*, 2007; Vigny *et al.*, 2011). In fact, Larson (2009) argues that the IGS network and data products have been instrumental in creating the field of GPS seismology.

3.1.3 User segment

In addition to the space hardware and ground control systems, to determine our location using GPS we require a receiver: the user segment. A typical geodetic GPS station consists of an antenna mounted on a stable monument, the receiver electronics, a microprocessor with hard-disk, and a power supply — all of which are miniaturised in hand-held GPS devices. As GPS is a one-way ranging system, the receiver is passive, which is advantageous as it means that receivers can operate with minimal power demands. Furthermore, for applications where data is not required in real time, GPS receivers can be left to acquire data for as long as their power supply lasts, or until their memory is full. Data acquired in this way may be referred to as continuous GPS, in contrast to campaign GPS where the same geodetic mark is reoccupied on successive occasions, perhaps before and after an earthquake. High rate GPS then refers to continuous GPS receivers operating with high sampling rates; such data are usually telemetered in real-time for simultaneous

[3]http://igscb.jpl.nasa.gov/network/list.html

reprocessing at a data centre. The choice of receiver sampling rate depends on the intended application of the data: daily solutions are usually obtained by averaging positions determined every 30 s. Without a doubt, the trend is towards 1 Hz and higher sampling frequencies as memory and real-time telemetry become respectively cheaper and easier.

The receiver has multiple processing channels — each handling the signal from one visible satellite — which determine a set of pseudoranges and thence the three dimensional position of the receiver. For geodetic applications, dual frequency GPS receivers are the standard as they permit both the L1- and L2-frequency signals to be acquired, allowing errors arising from ionospheric refraction to be eliminated (Hofmann-Wellenhof *et al.*, 2001).

3.1.4 Principles of positioning using GPS

The observed pseudorange to the i^{th} satellite ρ_i, is related to the true range ρ_i^{true} by (e.g. Tsui, 2000)

$$\rho_i = \rho_i^{\text{true}} + \Delta d_i + \mathrm{c}(\Delta b_i - b) + \mathrm{c}(\Delta T_i + \Delta I_i + v_i + \Delta v_i) \tag{3.1}$$

where Δd_i is pseudorange error due to imprecise knowledge of the satellite position, Δb_i is the satellite clock error, b is the receiver clock error, ΔT_i is the delay caused by propagation through the troposphere, ΔI_i the ionospheric delay, v_i is the measurement error due to noise at the receiver such as multipath, Δv_i is the relativistic time correction, and c is the speed of light. As we have already seen, the satellite position and clock errors can be eliminated once accurate IGS orbits and time information has been disseminated, the ionospheric delay can be measured and removed if we use dual frequency receivers, and receiver noise errors can be minimised by careful siting of instruments and sidereal filtering. The tropospheric delay and relativistic term can also be mitigated by modelling, and hence only one error source from (3.1) remains significant: the receiver clock error, b.

Our problem is then to estimate the receiver position and clock error (x_r, y_r, z_r, b) from the known position of four or more satellites (x_i, y_i, z_i) and pseudoranges to these

satellites, ρ_i. From the forward modelling equation

$$\rho_i = \sqrt{(x_i - x_r)^2 + (y_i - y_r)^2 + (z_i - z_r)^2} + cb \tag{3.2}$$

we have a non-linear inverse problem, which we can solve using an iterative least squares scheme (2.180), with the initial receiver location chosen, perhaps, as the centre of the tetrahedron defined by the four closest GPS satellite projected down onto Earth's surface. All that we require now is to measure the pseudoranges.

Pseudorange measurement using the pseudorandom noise code

The satellite clock reading at the time that a GPS signal was broadcast is known some time later at the receiver because it is encoded into the pseudorandom noise signal. The travel time of the signal can be computed in the receiver as the difference between this broadcast time and the time at which the signal was received. This time shift Δt is determined by cross correlating the received signal with a copy reconstructed in the receiver. The code pseudorange ρ_i^c, biased by the unknown clock error, is then simply (e.g Hofmann-Wellenhof *et al.*, 2001)

$$\rho_i = c\Delta t \ = \rho_i^{\text{true}} + \text{c}b\,. \tag{3.3}$$

Pseudorange measurement using the carrier phase

Instead of measuring the time delay between the broadcast and received signals, the pseudorange could alternatively be determined by counting the number of oscillations of the carrier wave during propagation from satellite to receiver, and multiplying by its wavelength, λ. In the receiver, the PRN code is removed from the received signal to leave the original carrier wave, which can then be cross correlated with a reference carrier of the same frequency to obtain the phase delay. Such an approach can only ever constrain the fractional part of the total number of cycles, and so there is an integer ambiguity,

N, in this phase pseudorange ρ_i^p, which is again biased by the unknown clock error (e.g. Hofmann-Wellenhof *et al.*, 2001)

$$\rho_i^p x\lambda = \rho_i^{\text{true}} + \mathrm{c}b - N\lambda\,. \tag{3.4}$$

From the frequencies of the L1 and L2 carriers we can see that each integer ambiguity corresponds to a range ambiguity of ∼19 or ∼24 cm respectively. Despite the integer ambiguity, (3.4) is still useful if we can continually track a signal and difference the phase pseudorange between epochs since N is constant, although problems can occur due to cycle slipping or if signal lock is temporarily lost due to obstruction of the satellite-receiver line of sight. The integer ambiguity may also be resolved from the code pseudorange (e.g Blewitt, 1989).

Processing strategies

Code and phase pseudoranges are the basic GPS observables that are used for positioning, and we recall that these can be made at two frequencies corresponding to the L1 and L2 carrier waves. Hence, at any epoch we have four pseudorange measurements. Various data processing approaches have been developed that aim to combine all of this information to produce robust position estimates, both after the event and in real time. These can be broadly separated into two categories: absolute and relative positioning.

Precise point positioning (PPP) (Zumberge *et al.*, 1997) allows phase and pseudorange data from GPS receivers in a local or regional network to be processed on a receiver by receiver basis, yielding absolute station positions with accuracy akin to those obtained by simultaneous processing of the entire network but at much less computational cost. This approach uses accurate orbital and clock parameters determined using global networks such as the IGS tracking network, which is advantageous as it means that the positions of the stations in the local network are determined independently and in a global reference frame. In contrast to network based processing methods which must assume that some reference GPS receiver is stationary, PPP allows reliable positions to be computed even

when all stations in a network are moving, which is important for GPS seismology. However, PPP is also currently less precise than relative positioning because of the difficulty of resolving the integer ambiguity in the phase pseudorange when data from only a single station are used (Kouba, 2003). However, PPP processing algorithms that include ambiguity fixing are now available (e.g. Ge *et al.*, 2007; Li *et al.*, 2013), and the trend appears to be towards using PPP for GPS seismology, particularly when one considers that accurate satellite ephemerides are rapidly available from data centres (see, for example Ohta *et al.*, 2012).

Network positioning techniques provide the position of a GPS receiver relative to a base station whose location is known and is assumed to be fixed for the duration of the observational period. Such techniques have long been used for conventional kinematic geodetic surveying (Genrich and Bock, 1992), but have been adapted for use with high rate (e.g. Larson *et al.*, 2003; Kobayashi *et al.*, 2006; Yokota *et al.*, 2009) and real-time (e.g. Ohta *et al.*, 2012) data over recent years. By processing data from multiple stations simultaneously, satellite and receiver clock errors can be eliminated, and integer phase ambiguities can be estimated. For example, the method of instantaneous positioning (Bock *et al.*, 2000; Genrich and Bock, 2006) allows a single epoch of dual frequency phase and pseudorange data to resolve the integer phase ambiguity, yielding independent estimates of station coordinates at the receiver sampling rate that are precise to 6 mm horizontally and about 60 mm vertically (Langbein and Bock, 2004), which is sufficient for real-time GPS seismology.

3.1.5 Seismological applications of GPS data

GPS networks have been used to make many observations of dynamic displacements caused by earthquakes (e.g. Nikolaidis *et al.*, 2001; Kouba, 2003; Davis and Smalley, 2009; Shi *et al.*, 2010; Houlié *et al.*, 2011; Bock *et al.*, 2011), and the fidelity of high-rate GPS displacement records has been clearly demonstrated by shake-table tests (Elósegui *et al.*, 2006), and comparisons to colocated seismic instruments (Larson *et al.*, 2003; Irwan *et al.*,

2004; Emore *et al.*, 2007; Wang *et al.*, 2007; Bilich *et al.*, 2008; Li *et al.*, 2013; Hung and Rau, 2013; Yin *et al.*, 2013). However such data have only been used to construct source models for a handful of events: the 2003 Tokachi–Oki earthquake (Miyazaki *et al.*, 2004), the 2003 San Simeon earthquake (Ji *et al.*, 2004), the 2005 Fukuoka earthquake (Kobayashi *et al.*, 2006), the 2008 Iwate–Miyagi earthquake (Yokota *et al.*, 2009), the 2008 L'Aquila earthquake (Avallone *et al.*, 2011), the 2010 Maule earthquake (Delouis *et al.*, 2010; Vigny *et al.*, 2011), and the 2011 Tohoku earthquake (Ammon *et al.*, 2011; Yue and Lay, 2011). All of these studies inverted HRGPS data to obtain a kinematic rupture model of the earthquake on a finite fault of assumed location, size and orientation. The application of GPS data presented here differs from these earlier studies as — by an adaptation of the CMT algorithm — we solve for the optimal long-period point-source description of an earthquake without making any *a priori* assumption about the location or mechanism.

Several characteristics of HRGPS time-series make them suitable for inversion using the CMT algorithm. The fact that GPS receivers measure displacement directly means that they record waveforms that are inherently rich in long-period information. Indeed since GPS receivers capture the permanent "static" displacement caused by an earthquake, they are actually sensitive to frequencies down to 0 Hz. Furthermore, Bock *et al.* (2004) showed that GPS receivers can detect arbitrarily large ground displacements without clipping. As a consequence GPS receivers are, in effect, long-period–strong-motion displacement seismometers. Since the CMT method requires long-period, long-wavelength data to justify its parameterization of an earthquake as a point source, HRGPS data should be well suited to an inversion within the CMT framework. Of course, when compared to teleseismic observations, finite fault effects will be more significant in the near-field. However for the earthquakes examined in this report, we find that rupture complexity does not preclude the stable recovery of a CMT solution from low-pass filtered HRGPS waveforms.

Thickness (km)	v_P (km/s)	v_S (km/s)	ρ (kg/m^3)
0.10	3.20	2.00	2.10
1.90	5.15	2.85	2.50
3.00	5.50	3.20	2.60
13.00	6.00	3.46	2.70
14.00	6.70	3.87	2.80
∞	7.70	4.30	3.30

Table 3.1: Crustal model used for the computations shown in Figures 2.7 and 2.8, and in the inversion of GPS waveforms for the 2005 Fukuoka earthquake described in Section 3.3.1. This earth model was used by Kobayashi *et al.* (2006) in their finite fault inversions of HRGPS data for this event.

3.2 A test of the CMT method using synthetic GPS waveforms

GPS waveform data were implemented into the CMT inversion framework of Valentine (2010) by means of a `GPS` data slice. The only preprocessing that these data receive is filtering using a cosine low pass filter with corner frequencies of 0.05 and 0.2 Hz. No instrument response function needs to removed because the time-series produced by high-rate GPS receivers are, in theory, direct measurements of ground displacement.

To validate our implementation of GPS data into the inversion framework described in earlier, we performed a series of inversions of a synthetic 1 Hz GPS waveform dataset. We computed three component GPS seismograms for a M_w 6.6 earthquake occurring on a fault with strike 30°, dip 80°and rake 20°(see Table 3.2 "True" column). Synthetics were calculated using a realistic local crustal model given in Table 3.1. For these experiments, we used a realistic distribution of stations, shown in Figure 3.4, which corresponds to GPS receivers that observed the 2005 M_w 6.6 Fukuoka, Japan, earthquake; we invert the actual GPS data for this earthquake in Section 3.3.1.

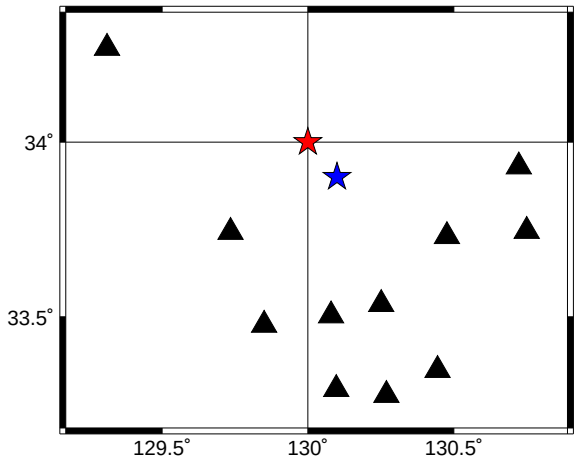

Figure 3.4: A realistic distribution of GPS receivers (black triangles) used in the inversions of synthetic GPS data shown in Tables 3.2, 3.3 and 3.4. This station distribution corresponds to that of the 2005 Fukuoka earthquake; we present an analysis of the actual HRGPS data for this earthquake in Section 3.3.1.

Linear inversion for the moment tensor at a known location

We begin by performing the simplest experiment of attempting to recover the moment tensor under the assumption that the centroid location is known exactly *a priori*. In this case, the inverse problem is linear, and we should recover the correct source in a single iteration. The results of such an experiment are shown in Table 3.2, and indicate that our inversion scheme for GPS data is self consistent.

Recovery of location and origin time

To verify that the iterative inversion scheme for the centroid location and origin time has been correctly implemented, we performed four further tests. In each, one coordinate of the initial source location was perturbed by a small amount: 5 km in depth, 0.1° in both latitude and longitude, and 2 s in origin time. We then ran our inversion for 5 iterations. Even though the starting source is perturbed in only one location parameter, we allow all of the hypocentral coordinates to vary, so this test also allows us to investigate trade-offs between the different location parameters. The results of these experiments are shown

	Initial	Recovered	True
Location:			
Origin time	01:53:41.80	01:53:41.80	01:53:41.80
Longitude	130.0000°E	130.0000°E	130.0000°E
Latitude	34.0000°N	34.0000°N	34.0000°N
Depth (km)	35.000	35.000	35.000
Moment tensor:			
M_{rr}	0.0000	0.1170	0.1170
$M_{\theta\theta}$	0.0000	-0.8310	-0.8310
$M_{\phi\phi}$	0.0000	0.7140	0.7140
$M_{r\theta}$	0.0000	0.0194	0.0194
$M_{r\phi}$	0.0000	0.3600	0.3600
$M_{\theta\phi}$	0.0000	-0.5130	-0.5130

Table 3.2: Results of a moment tensor inversion using a synthetic GPS waveform dataset computed for the source mechanism given in the "True" column. The initial location is the correct centroid location, and we solve only the linear inverse problem for the moment tensor, recovering the correct input parameters in a single iteration. The moment tensor unit is arbitrary.

in Fig 3.5, and indicate that our inversion algorithm retrieves the correct source model after about 5 iterations for all perturbations of the initial source location and time that we tested.

Recovery of all ten source parameters

The foregoing experiments showed that each aspect of our inversion scheme works in isolation. Of course, in reality, the initial centroid will be incorrect in both space and time, and so we now investigate simultaneously recovering both the centroid and moment tensor for a general perturbation in the initial location and origin time. For this purpose, we emulate the synthetic experiment set out in Dziewonski *et al.* (1981), which used a source representing the superposition of a strike-slip earthquake with an explosion in the computation of the synthetics (see Table 3.3,"Input" column). The starting coordinates for the inversion are 15 km away from those of the true source, and the initial origin time is 2 s earlier than the correct value. The event location and station distribution are identical to those used in the earlier experiments.

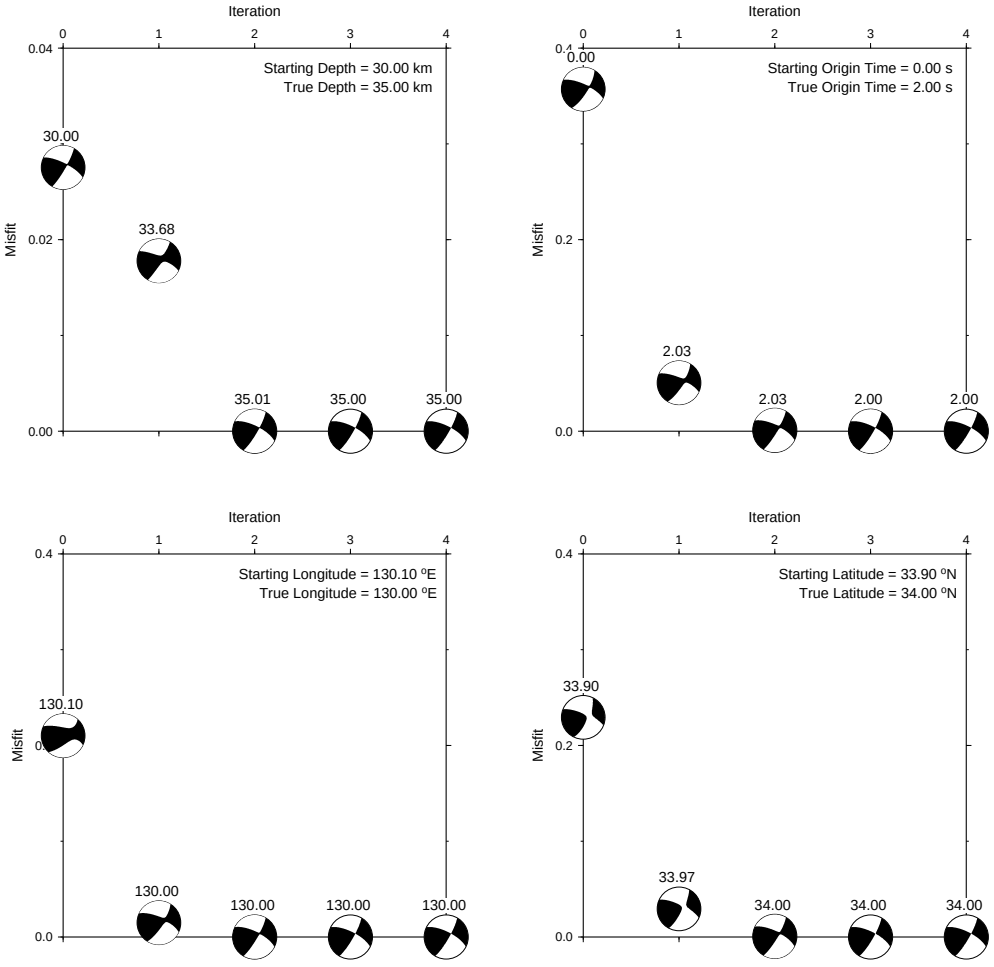

Figure 3.5: Iteration by iteration misfit for synthetic inversions where the initial source has been perturbed in depth (top left), origin time (top right), longitude (bottom left) and latitude (bottom right). Note that the vertical scale is an order of magnitude smaller for the depth plot.

Table 3.3 shows the results of this synthetic test at each inversion iteration. The initial mislocation of the source means that the zeroth iteration produces a moment tensor that is far removed from the actual solution. Subsequently, the centroid moves towards its true position, resulting in incremental improvements in the values of the moment tensor. There is some trade off between the origin time and depth, hence these parameters overshoot their true values during the second and third iterations respectively. We recover the correct source parameters after 5 iterations of the inversion algorithm; this number is broadly comparable to our experience with inversions of teleseismic data. The success of this experiment demonstrates that our implementation of GPS data into the CMT algorithm is sound as it gives self-consistent results.

Since GPS data errors are typically largest in the vertical coordinate, in reality we may wish to ignore these data and invert just the horizontal component waveforms. To simulate one such situation, we performed a second synthetic source inversion using horizontal displacements only. In CMT inversions of real earthquake data it is generally assumed that the event does not have an explosive component — equivalently, that there is no volume change caused by the seismic event — and so we also impose the additional constraint that the trace of the moment tensor is zero in this synthetic test. As a consequence, we revert to using HRGPS waveforms computed for a M_w 6.6 earthquake occurring on a fault with strike 30°, dip 80°and rake 20°for this test. The results of this experiment are shown in Table 3.4, and indicate that the inversion algorithm performs well even in the absence of any vertical displacement data being available. The evolution of the fit between the data and synthetics over the inversion is illustrated in Figure 3.6.

The "radius of convergence" of the algorithm depends on the local form of the misfit function; in other synthetic experiments carried out under ideal conditions we were able to recover the true source parameters even when the initial location was in error by as much as 70 km and 25 s. In fact, for both of the earthquakes we examine later in this study, the USGS Preliminary Determination of Epicenters (PDE) hypocentre, which we assume for the zeroth iteration, is close enough to the centroid for our inversions of GPS data to converge.

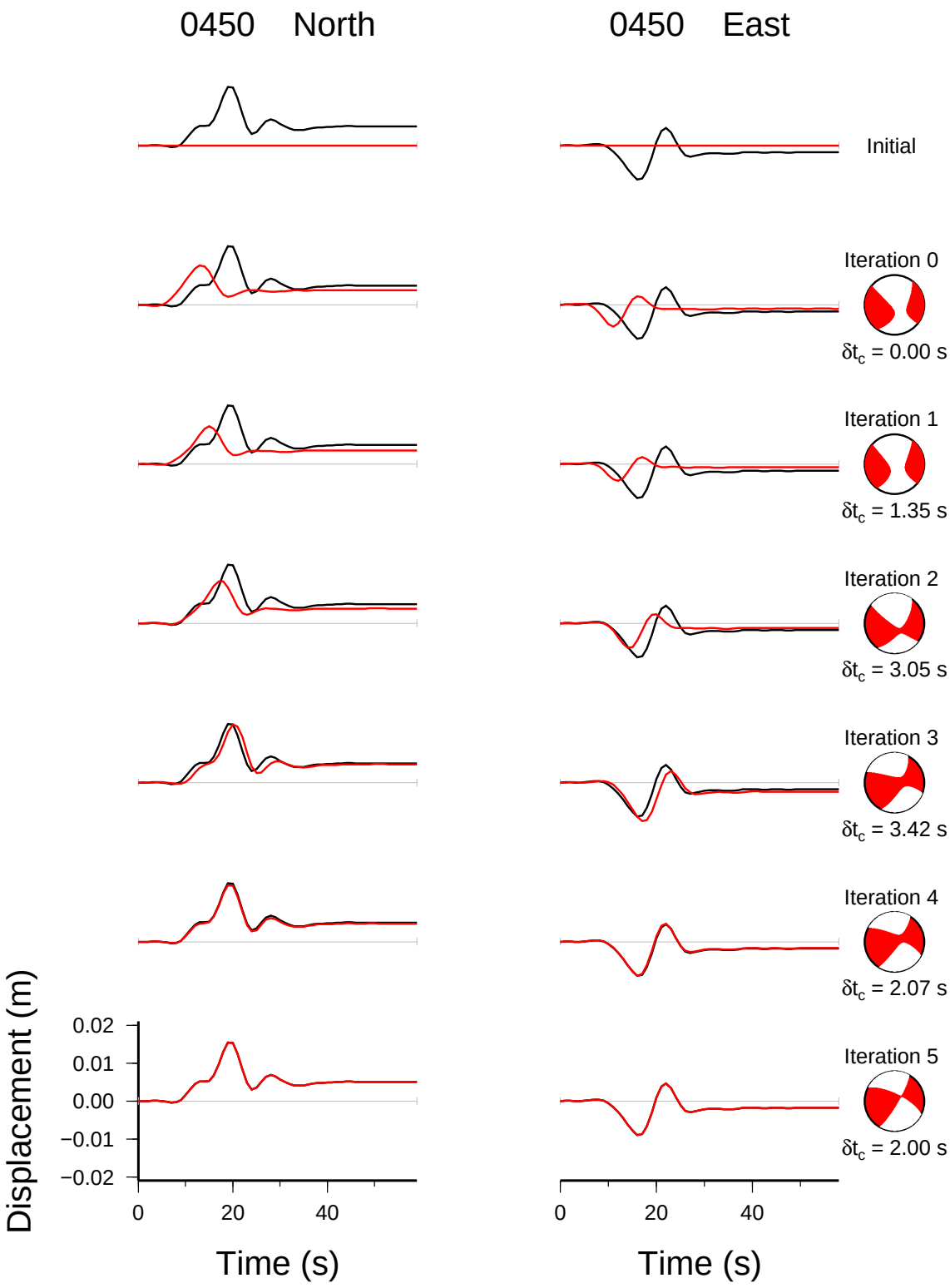

Figure 3.6: The fit between observed (black traces) and synthetic (red traces) HRGPS waveforms over the first five iterations of an inversion of a synthetic dataset (see Table 3.4). Refer to Figure 3.7 for the location of this station.

Nonlinearities encountered when a station lies in-between the inversion's starting location and the true centroid position may cause the inversion to become unstable. In practice this problem can be avoided by ignoring all stations within a certain distance of the initial epicenter. This approach obviously decreases the quantity of data available for inversion, however the loss of data is acceptable since it actually helps reduce the risk of the dataset being contaminated by finite source effects. For the earthquakes we examine in Section 3.3 — both of which have $M_w < 7.0$ — we find a threshold distance of 25 km is enough to prevent instabilities and finite source effects hampering the inversion. It would be straightforward to implement an interactive inversion scheme, which would allow the user to evaluate whether the discarded stations could be used in subsequent iterations.

3.3 Application to real data

As a proof of concept, we now attempt to perform CMT inversions using real 1 Hz GPS data obtained by Japan's GEONET for two recent events: the 2005 M_w 6.6 Fukuoka earthquake, and the 2008 M_w 6.9 Iwate–Miyagi earthquake. Rupture histories for these events have already been determined using these GPS waveforms by Kobayashi *et al.* (2006) and Yokota *et al.* (2009) respectively. Both sets of GPS time-series used here are post-processed kinematic solutions; further details of the GPS processing methodologies can be found in the original papers. Motion of the reference station is not a problem given the moderate magnitude of these events and the great spatial extent of GEONET. The performance of our inversion scheme can be assessed by comparing our CMT solutions to the first-order features of the finite fault slip models determined in these earlier studies, although one should bear in mind the differences in the inversion approaches which will be reflected in the results.

		Iteration					
	Input	0	1	2	3	4	5
Location:							
origin time (s)	2.00	0.00	1.80	2.45	1.88	2.01	1.99
latitude	34.00° N	33.90° N	33.90° N	34.02° N	33.99° N	34.00° N	34.00° N
longitude	130.00° E	130.10° E	130.07° E	129.98° E	130.01° E	130.00° E	130.00° E
depth (km)	35.00	30.00	31.76	32.05	35.86	34.99	35.00
Moment tensor:							
M_{rr}	1.0000	0.3406	0.4638	0.5376	1.0565	0.9938	1.0000
$M_{\theta\theta}$	1.0000	0.7798	0.8958	0.8990	1.0398	0.9991	0.9999
$M_{\phi\phi}$	1.0000	0.6349	0.7844	0.9232	1.0310	0.9994	1.0001
$M_{r\theta}$	0.0000	0.0005	-0.0281	0.0040	0.0143	0.0013	0.0000
$M_{r\phi}$	0.0000	0.1610	0.1638	0.1457	0.0102	0.0006	0.0000
$M_{\theta\phi}$	1.0000	0.1430	0.1736	0.5333	0.9308	0.9983	1.0000
Relative RMS		0.6023	0.4336	0.1463	0.0105	0.0000	0.0000

Table 3.3: The results of a numerical test of the CMT method using synthetic GPS waveforms. Synthetic data were computed for a strike-slip earthquake superimposed on an explosion ("Input" column); the initial location is 15 km away from the actual centroid. The CMT algorithm converges to the true source parameters after 5 iterations of the nonlinear inversion scheme described in Section 2.3.1. The origin time is expressed relative to some reference value such as the hypocentral time determined from body wave arrivals; here the centroid of moment release occurred two seconds after this time. The moment tensors are given in units of 10^{19} Nm

		Iteration						
	Input	0	1	2	3	4	5	6
Location:								
origin time (s)	2.00	0.00	1.35	3.04	3.41	2.06	2.00	2.00
latitude	34.00°N	33.90°N	33.84°N	33.87°N	33.95°N	33.99°N	34.00°N	34.00°N
longitude	130.00°E	130.10°E	130.14°E	130.09°E	129.95°E	130.00°E	130.00°E	130.00°E
depth (km)	35.00	30.00	38.64	37.41	35.35	35.09	35.03	35.01
Moment tensor:								
M_{rr}	0.1170	-0.0389	-0.0693	-0.0357	0.1369	0.1322	0.1174	0.1171
$M_{\theta\theta}$	-0.8310	-0.2069	-0.3207	-0.3242	-0.5655	-0.7777	-0.8310	-0.8311
$M_{\phi\phi}$	0.7140	0.2458	0.3900	0.3599	0.4286	0.6455	0.7136	0.7140
$M_{r\theta}$	0.0194	-0.0926	-0.0937	-0.1602	-0.1750	-0.0178	0.0197	0.0194
$M_{r\phi}$	0.3600	0.0578	0.0455	0.0621	0.1848	0.2719	0.3581	0.3600
$M_{\theta\phi}$	-0.5130	-0.0616	-0.0807	-0.1073	-0.4616	-0.4206	-0.5131	-0.5129
Relative RMS		0.7421	0.6625	0.3941	0.2168	0.0112	0.0000	0.0000
								

Table 3.4: As for Table 3.3 except that the synthetic HRGPS dataset was calculated for a M_w 6.6 earthquake occurring on a fault with strike 30°, dip 80°and rake 20°, and only horizontal component waveforms were used in the inversion. We also impose the constraint that the trace of the moment tensor is zero $M_{rr} + M_{\theta\theta} + M_{\phi\phi} = 0$. The beachballs output after each inversion iteration are also shown, and suggest that an error in the source location introduces a spurious non double component into the solution. The moment tensors are given in units of 10^{19} Nm

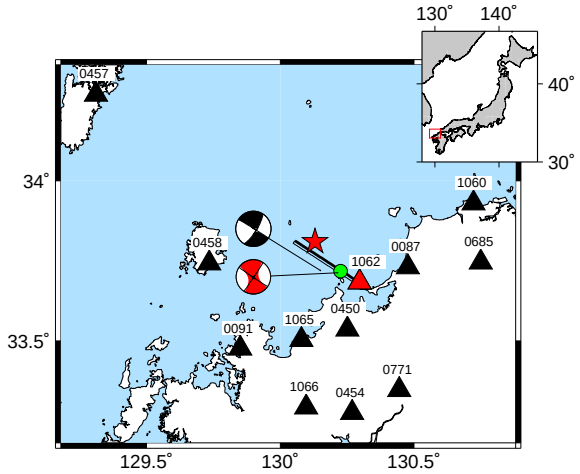

Figure 3.7: The distribution of GEONET GPS receivers (black triangles) used in our inversion of GPS waveforms from the 2005 M_w 6.6 Fukuoka earthquake. Our CMT solution is shown by the red beachball. The red star denotes the PDE catalogue hypocentre, which we use as the starting location for our inversion. For comparison, the Global CMT solution (black beachball) is also shown. The rectangle denotes the near-vertical fault plane assumed by Kobayashi *et al.* (2006); the top edge of their fault is indicated by the bold line. The centroid inferred from their inversion of three component data from the same 11 GPS stations is shown by the green circle. Our CMT solution is essentially colocated with the centroid of Kobayashi *et al.* (2006), and our best double couple mechanism also compares favourably with the orientation of their fault plane (see Table 3.6). Data from station 1062 (red triangle) were not used in either inversion.

3.3.1 The 2005 M_w 6.6 Fukuoka, Japan earthquake

Figure 3.7 shows the distribution of GEONET stations (triangles) that recorded 1 Hz GPS displacement waveforms for the March 20, 2005 M_w 6.6 Fukuoka earthquake. Kobayashi *et al.* (2006) inverted these data to infer the source process of this event, assuming that the earthquake occurred on a near-vertical fault (Figure 3.7, rectangle), with a left-lateral strike-slip mechanism. They recovered a simple rupture history characterized by a single slip patch. Consequently, this event provides a good test of the CMT method applied to GPS data since we should recover a centroid location and mechanism close to that obtained by Kobayashi *et al.* (2006).

Apart from the obvious difference between our source parameterization and that employed by Kobayashi *et al.* (2006), we aim to emulate their inversion as closely as possible;

we use their crustal model, shown in Table 3.1, and extract identical minute-long windows from each displacement seismogram. One important difference is that we invert horizontal displacements only, as the vertical channels appear to be dominated by noise; the vertical component data were heavily downweighted by Kobayashi *et al.* (2006). Also, to mitigate against finite source effects contaminating the dataset, we omit station 1062 (Figure 3.7, red triangle) from our inversion as it lies within 25 km of the PDE hypocentre. Kobayashi *et al.* (2006) present an inversion that also ignores this station; in the following, any comparisons that we make relate to this particular solution.

As with our synthetic test, we apply a cosine low-pass filter to the data and synthetics, with corner frequencies at 0.05 and 0.2 Hz. Following the Global CMT algorithm, we constrain the trace of the moment tensor to be zero (*i.e.* $M_{rr} + M_{\theta\theta} + M_{\phi\phi} = 0$), so that there is no explosive component to the source. We take the starting location for the inversion from the PDE catalogue (Figure 3.7, red star).

The result of our CMT inversion is given in Table 3.5, and shown as the red beachball in Figure 3.7. Our moment tensor resembles the Global CMT mechanism (Figure 3.7, black beachball), and is positioned about 7 km east of the catalogue solution, which is reasonable given the expected errors in Global CMT locations that arise from unmodelled 3D earth structure (e.g. Valentine and Trampert, 2012). Our centroid, located at 130.21° E, 33.71° N with depth 6.82 km, is consistent with the slip patch obtained by Kobayashi *et al.* (2006) from the same HRGPS data, which has approximate centroid coordinates of 130.23° E, 33.72° N and a depth of 6 km (Figure 3.7, green circle). Since Kobayashi *et al.* (2006) assumed that the earthquake occurred purely as slip on a plane, it is instructive to compare our best double couple solution to the orientation of their assumed fault. As Table 3.6 shows, our best double couple solution corresponds to a fault mechanism that is almost identical to the one adopted by Kobayashi *et al.* (2006), and also compares favourably to the Global CMT best double couple solution. Thus the mechanism and location that we recover appear to be consistent with those previously determined for this earthquake.

The non double couple component of a moment tensor can be expressed by the param-

	Initial	Final
Location:		
origin time (UT)	01:53:41.80	01:53:48.04
latitude	33.81° N	33.71° N
longitude	130.13° E	130.21° E
depth (km)	10.00	6.82
Moment tensor:		
M_{rr}		0.1365
$M_{\theta\theta}$		0.4420
$M_{\phi\phi}$		-0.5785
$M_{r\theta}$		0.0161
$M_{r\phi}$		0.0151
$M_{\theta\phi}$		0.2097
Relative RMS		0.0895

Table 3.5: The results of our CMT inversion of GPS waveforms recorded for the 2005 M_w 6.6 Fukuoka earthquake. The moment tensor is given in units of 10^{19} Nm.

eter $\epsilon = \lambda_{min}/\lambda_{max}$ where λ_{min} and λ_{max} are respectively the smallest and largest absolute values of the moment tensor's eigenvalues, with $\epsilon = 0$ corresponding to a pure double couple. Values of ϵ for each solution are also given in Table 3.6. These ϵ values indicate that the Global CMT solution is almost pure double couple whereas our CMT solution from HRGPS waveforms has a significant non double couple component, as is also apparent from a visual comparison of the beachballs plotted in Figure 3.7. This difference likely arises due to unmodelled complexities in source and structure, which will more strongly affect the near-field data. Regardless of the similarity of our result to earlier solutions, the excellent agreement between the observed GPS waveforms and those calculated for our final source, as shown in Figure 3.8, suggests that it is possible to recover a reliable CMT solution from GPS waveform data.

3.3.2 2008 M_w 6.9 Iwate–Miyagi, Japan earthquake

To further validate the CMT method as applied to HRGPS data, we inverted a second set of 1 Hz GPS waveforms that were obtained for the June 13, 2008 M_w 6.9 Iwate–Miyagi earthquake. Figure 3.9 shows the distribution of GEONET GPS receivers (triangles) that

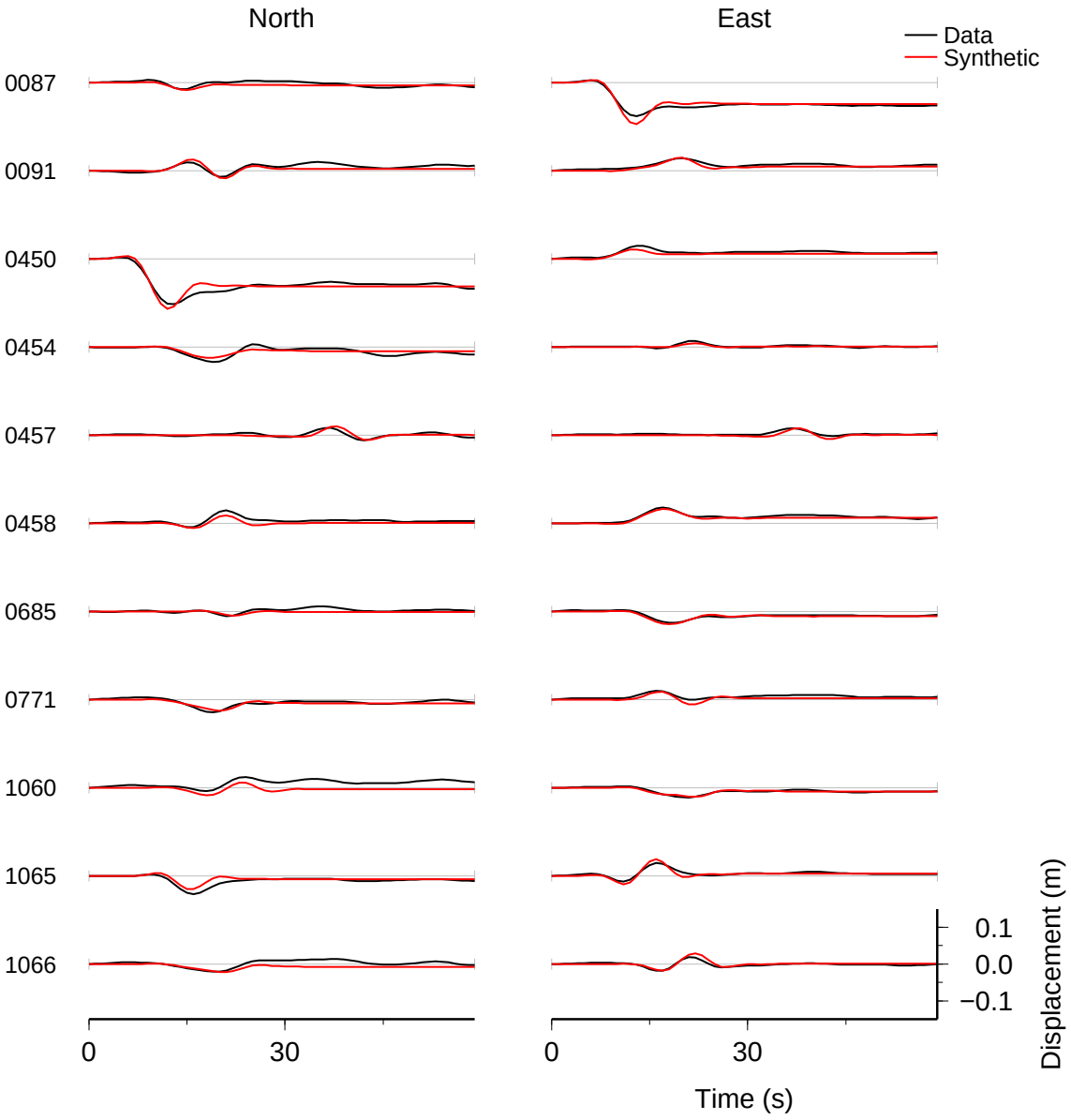

Figure 3.8: GPS waveforms (black traces) observed at the stations shown in Figure 3.7 after the 2005 M_w 6.6 Fukuoka earthquake, and used in our CMT inversion. Synthetic seismograms (red traces) computed using the CMT solution recovered after the final iteration of our inversion fit the data well in both phase and amplitude, with an overall variance reduction of 91%. Time is relative to the PDE hypocentral time.

	Strike (°)	Dip (°)	Rake (°)	Moment ($\times 10^{19}$ Nm)	ϵ	Best Double Couple
This study	124	87	+2	0.55	0.22	
Kobayashi *et al.* (2006)	123	88	−1	0.88	0.00	
Global CMT catalogue	302	88	−14	0.92	0.02	

Table 3.6: A comparison of double couple mechanisms for the 2005 M_w 6.6 Fukuoka earthquake. Our solution is very similar to the fault plane assumed in the finite fault inversion of Kobayashi *et al.* (2006) and the best double couple mechanism from the Global CMT catalogue. The parameter ϵ, defined in Section 3.3.1, describes the deviation of the solution from a pure double couple, which has $\epsilon = 0$.

recorded this event. Yokota *et al.* (2009) inverted these data to infer the source process of this event, assuming a westward dipping thrust fault (Figure 3.9, rectangle); they found that the rupture was best described by a single main slip patch with approximate centroid coordinates 140.88° E, 38.96° N and a depth of 3.6 km. The first-order features of this solution provide a useful check on the reasonableness of our CMT solution derived from the same GPS dataset. However it should be kept in mind that, apart from the obvious differences in our source parameterizations, Yokota *et al.* (2009) used station-specific crustal models which we have not implemented, and — since three stations lie within 25 km of the hypocentre — we invert only a subset of the data that they used. We use the same filter parameters as before, and again invert only the horizontal GPS waveforms as the vertical displacements appear to be dominated by noise. The kernel functions are computed in the local earth model taken from CRUST2.0[4].

The result of our CMT inversion is given in Table 3.7, and shown as the red beachball in Figure 3.9. Our centroid and moment tensor are similar to the Global CMT solution (Figure 3.9, black beachball). Furthermore, our centroid is located close to that inferred from the slip distribution of Yokota *et al.* (2009) (Figure 3.9 green circle); the level of agreement between these locations is reasonable given the differences in earth models used.

[4]http://igppweb.ucsd.edu/~gabi/rem.html

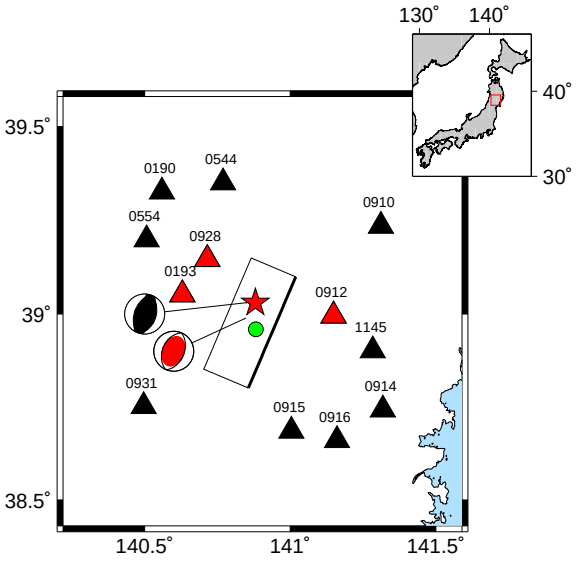

Figure 3.9: The distribution of GEONET GPS receivers (black triangles) used in our inversion of GPS waveforms from the 2008 M_w 6.9 Iwate–Miyagi earthquake. Our CMT solution is shown by the red beachball. We did not invert data from stations 0928, 0193 and 0912 (red triangles) because of their proximity to the PDE catalogue hypocentre (red star) which we use as the starting location for our inversion. For comparison, the Global CMT solution (black beachball) is also shown. The rectangle denotes the westward dipping thrust fault assumed by Yokota *et al.* (2009); the top edge of their fault is indicated by the bold line. The centroid inferred from their inversion of three component data from all of the above stations is shown by the green circle. Our best double couple mechanism compares favourably with the orientation of their fault plane (see Table 3.8).

As Table 3.8 shows, our best double couple mechanism is almost identical to the fault plane that Yokota *et al.* (2009) used, and also compares well to the best double couple solution from the Global CMT catalogue. The ϵ values corresponding to these different results, also shown in Table 3.8, indicate that both our CMT solution and the Global CMT solution have a non double component, although the deviation from a pure double couple is larger for our near-field solution. Thus, the CMT solution that we obtain from GPS data for this earthquake is consistent with independently determined mechanisms and locations. Furthermore the excellent agreement between the observed and synthetic GPS waveforms, as Figure 3.10 shows, demonstrates that our CMT solution explains the data very well and implies that — at low frequencies — a point moment tensor source is a sufficient model for this earthquake, although it should be noted that the fact that this

	Starting	Final
Location:		
origin time (UT)	23:43:45.40	23:43:52.37
latitude	39.03° N	38.99° N
longitude	140.88° E	140.84° E
depth (km)	7.80	3.24
Moment tensor:		
M_{rr}		2.5372
$M_{\theta\theta}$		-0.6496
$M_{\phi\phi}$		-1.8876
$M_{r\theta}$		0.0270
$M_{r\phi}$		0.1362
$M_{\theta\phi}$		-0.6299
Relative RMS		0.0815

Table 3.7: The results of our CMT inversion of GPS waveforms recorded for the 2008 M_w 6.9 Iwate–Miyagi earthquake. The moment tensor is given in units of 10^{19} Nm.

	Strike (°)	Dip (°)	Rake (°)	Moment ($\times 10^{19}$ Nm)	ϵ	Best Double Couple
This study	203	43	+91	2.3	0.15	
Yokota *et al.* (2009)	203	37	+90	2.7	0.00	
Global CMT catalogue	201	48	+92	2.6	0.07	

Table 3.8: A comparison of double couple mechanisms for the 2008 M_w 6.9 Iwate–Miyagi earthquake. Our solution is very similar to the fault plane assumed in the finite fault inversion of Yokota *et al.* (2009) and the best double couple mechanism from the Global CMT catalogue. The parameter ϵ, defined in Section 3.3.1, describes the deviation of the solution from a pure double couple, which has $\epsilon = 0$.

source model explains the main features of the data reasonably well does not necessarily mean that it is a good description of the true event.

3.4 Discussion

Our inversions of synthetic and real GPS waveforms clearly demonstrate the potential value of HRGPS data for determining the first-order source parameters of an earthquake. The good agreement between our CMT solutions and other independent source models

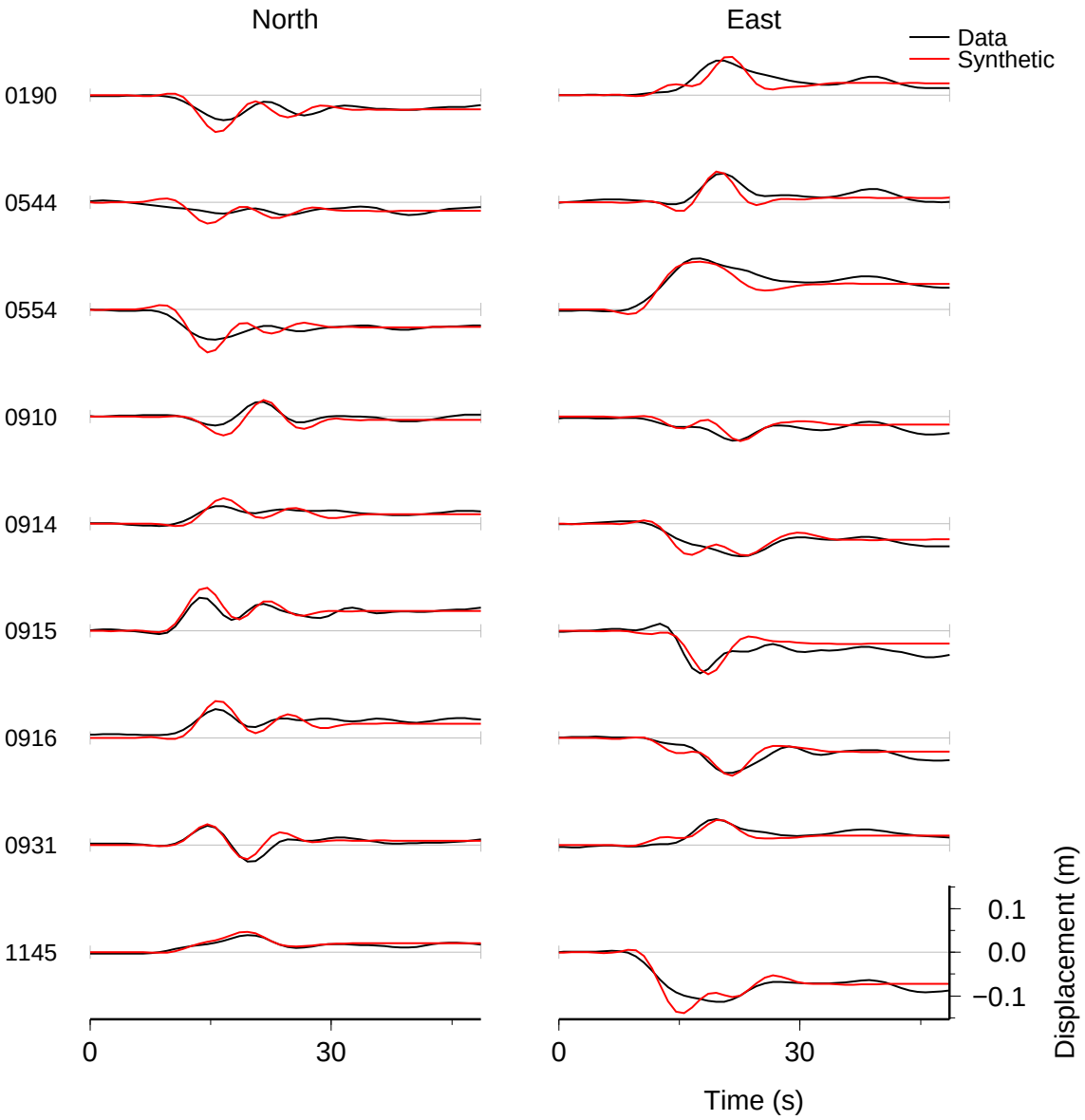

Figure 3.10: GPS waveforms (black traces) observed at the stations shown in Figure 3.9 after the M_w 6.9 Iwate–Miyagi earthquake, and used in our CMT inversion. Synthetic seismograms (red traces) computed for our recovered CMT solution fit the data well in both phase and amplitude, with an overall variance reduction of 91%. Time is relative to the PDE hypocentral time.

strongly suggests that the data selection, processing and inversion schemes described in this paper are robust. For both of the earthquakes that we have analysed our CMT solution explains the GPS data very well, with a variance reduction of over 90%. This level of agreement suggests that a point moment tensor source is a good model for these moderate magnitude earthquakes, even for near-field data.

Although we have only analysed two events, some features of these preliminary results are worthy of further discussion. For both earthquakes, we find that the origin time perturbation is positive, *i.e.* the centroid time is later than the hypocentral time, which is expected for a rupture of finite duration and follows from the definition of the centroid as opposed to the hypocentre. The larger earthquake required a greater shift in origin time, which is consistent with the observation that, for simple ruptures, the time perturbation is analogous to the earthquake's half-duration (Dziewonski and Woodhouse, 1983b).

Both of the HRGPS CMT solutions that we have determined have non double couple components that are larger than those in the corresponding Global CMT solutions. These could arise from source complexities such as curved or multiple faults, and unmodelled 3D structural effects that impact the near-field data more heavily than the longer-period teleseismic waveforms used to construct Global CMT solutions.

We also find that both of our data inversions yield lower moment estimates than the Global CMT solutions. Some of this disagreement can be explained by the shallow centroid depths that we recover relative to the catalogue solutions, which are fixed to a depth of 12 km during the inversion. Since our focal depths agree with those obtained from finite fault slip inversions we believe that the shallow depths we recover are real and can be trusted. It is interesting that we can obtain stable moment tensors for earthquakes as shallow as 3 km using GPS waveforms, given the well known problem of determining the $M_{r\theta}$ and $M_{r\phi}$ components of shallow events from long-period teleseismic data. High-rate GPS waveforms from more earthquakes obviously must be analysed to assess the general validity of this observation.

The scope of our analysis has so far been limited to only two events principally because seismologists' access to GPS waveforms is on a somewhat *ad hoc* basis. Melgar *et al.* (2011) estimate that since 2002 Japan's GEONET has recorded 1 Hz GPS data for 29 earthquakes larger than magnitude 7.0. As noted by Larson (2009) it is desirable for further HRGPS waveform datasets to be made publicly available in seismological repositories. With better access to data, it is possible that the method outlined in this paper could be applied systematically to determine earthquake source parameters from GPS waveforms. Such an undertaking may be useful for improving the completeness of seismic catalogues in the immediate aftermath of great earthquakes, when teleseismic data may be unusable due to the interference of waves generated by closely spaced aftershocks. Since we use only a short window of data, and a small number of near-field stations, it may be possible to avoid any such interference by using HRGPS data. Dynamic displacements have been observed using modern GPS networks for earthquakes that are as small as M_w 6.3; this magnitude represents a lower bound on the size of events which could be studied using the HRGPS waveform inversion algorithm we have developed.

To fully exploit the available GPS data resource, we need to validate our method for larger earthquakes. Thus far we have assumed that the source acts instantaneously, which is only reasonable if the data is long-period relative to the duration of the earthquake. For larger events, in addition to filtering the data at lower frequencies, we will need to implement a source time function of realistic duration. As the spatial dimensions of the source grow, our strategy to minimise finite fault effects — excluding data from stations that are less than 25 km away from the source — will also need to be refined. Neither of these implementation issues fundamentally prohibits CMT inversions of HRGPS waveforms from larger earthquakes, and existing scaling laws (e.g. Kanamori and Anderson, 1975) suggest that simple rules can be applied to accommodate the finite spatial and temporal extent of the earthquake source.

There is growing interest in using GPS data to rapidly characterize seismic sources for the purpose of earthquake early warning (e.g. Crowell *et al.*, 2009). The inversion method described in this paper could be used to determine the location, mechanism and moment of

earthquakes from HRGPS waveforms in real-time. So far, rapid source inversions of GPS data streams have exploited only the static displacement field (Melgar *et al.*, 2011; Allen and Ziv, 2011); additional information about the source could be gained by including frequencies other than 0 Hz in the inversion. Furthermore, the CMT algorithm is amenable to real-time implementation since the data can be windowed automatically and the only *a priori* information needed is a starting source location, such as the hypocentre determined from P-wave arrival times, and an earth model, which — in the absence of a more appropriate local alternative — can be found from CRUST2.0. The rate determining step in the inversion is the time taken to compute the derivative kernels. Using 18 processors, typical inversion times for datasets of the size presented in this report are of the order 5 minutes; this time can doubtless be significantly decreased using larger, state of the art cluster supercomputers.

Throughout this discussion, we have used teleseismic CMT solutions as a benchmark against which to assess our inversions of HRGPS waveforms. This comparison serves to demonstrate the reasonableness of source parameters retrieved from GPS data. In future, by providing a framework for the inversion of HRGPS waveforms that mirrors the one used for teleseismic CMT inversion, the present work will allow direct comparison and amalgamation of information from both datasets.

Summary

In this chapter, we have developed a method for retrieving the best point source parameters of an earthquake from displacement seismograms measured using GPS receivers. While we have focused on the application of GPS time-series to studies of the seismic source at low frequencies, the generality of this method should enable us to use additional long-period near-field data — perhaps provided by accelerometers — in future CMT inversions. Our approach is based on the waveform inversion algorithm described by Dziewonski *et al.* (1981), which has been widely applied to long-period teleseismic data.

Using this method, we have inverted 1 Hz GPS datasets pertaining to two recent earthquakes in Japan. The CMT solutions that we recover are consistent with finite source models determined independently from the same GPS datasets, and also with the Global CMT catalogue solutions obtained from long-period teleseismic waveform data. This agreement suggests that we can recover reliable source parameters from GPS data. Our CMT solutions explain the GPS data very well, implying that a point moment tensor source is a good model for these earthquakes even in the seismic near-field. There is much scope for further development of the method presented in this study, particularly in the context of earthquakes larger than magnitude 7.0. By providing a framework for the inversion of HRGPS waveforms that mirrors the one used for CMT inversions of teleseismic data, the present work should allow direct comparison and amalgamation of information from diverse datasets, yielding an improved understanding of earthquake source models and their uncertainties. Another obvious extension of the present work is to adapt it to the inversion of more widely available static displacement data, which we investigate in the following chapter.

Chapter 4

Real-time inversion of GPS–measured static displacements

The short term prediction of earthquake locations, times and magnitudes is something of a "holy grail" for earthquake seismologists (e.g. Allen, 2007). Despite recent advances in dynamical modelling of the seismic cycle (e.g Barbot *et al.*, 2012), even if a rupture nucleation signature can be identified, it is not clear that the total extent of the eventual failure can be known before the event: small and large earthquakes may have identical precursors (Beroza and Kanamori, 2007). As a consequence, current efforts to mitigate seismic hazard have concentrated on predicting peak ground motions (displacements, velocities and accelerations) at particular sites over some time interval, using instrumental and historical earthquake records (e.g. Giardini and Grünthal, 1999). Probabilistic seismic hazard maps can then be constructed and used to inform local planning and building codes which, if properly enforced, will reduce the long-term exposure of society to earthquake risks.

An alternative, and increasingly popular, short-term approach to civil defence from seismic hazards is that of earthquake early warning (EEW), using real-time seismic or

geodetic monitoring systems to raise alarms before potentially dangerous ground motions begin at vulnerable locations. Typically, these systems use some characteristic of the detected P-wave to determine whether the earthquake is hazardous or not, compute the event's magnitude, and forecast the shaking expected at later times. Although only a few seconds of warning may be realised, when combined with automated shut-down systems for critical infrastructure such as high speed and underground trains, nuclear facilities, and gas pipelines, considerable savings to life and property can be achieved (Allen *et al.*, 2009). Timely information about an earthquake is also of great value for directing first responders to the locations where they are most needed, and for longer term management of the emergency (Kanamori, 2005). Furthermore, rapid determination of earthquake source parameters — particularly the slip distribution — for offshore events is vital for determining the tsunamigenic potential of an event (e.g. Sobolev *et al.*, 2007).

Earthquake early warning using seismic instruments was initiated in Japan in the 1960s, when individual seismometers were used to protect sections of train line by cutting the power supply and halting trains in the event of an earthquake (Allen, 2007). Local warnings such as these can be triggered based on P-wave amplitudes combined with a scaling law for magnitude. It is desirable to use amplitude information in conjunction with the predominant or average period of the P-wave, as this combination allows relatively small events occurring very close to the receiver to be discriminated from larger, more distant events that are likely to generate strong shaking (Kanamori, 2005). As real time data telemetry has become easier, EEW has evolved to use monitoring networks rather than single stations, although the basic goals of location, magnitude determination and source characterisation remain the same. Currently, early warning systems are operational in Mexico, Romania, Turkey, Japan and Taiwan, and under development in California, Switzerland, Italy and China (Allen *et al.*, 2009).

As we have already noted in this thesis, over recent years there has been a marked growth in, and improvement of, GPS networks deployed in tectonically active regions, which has led to a considerable increase in the quantity and quality of GPS-derived observations of seismic deformations. The coseismic displacement fields measured by these

networks are valuable for earthquake early warning because they enable accurate and rapid determinations of moment magnitude from near-field data that, unlike seismic methods, do not saturate for events larger than $M_w \sim 8.0$ (Blewitt *et al.*, 2006, 2009). Near-field geodetic measurements also allow construction of slip models in the minutes following an earthquake (Crowell *et al.*, 2012; Wright *et al.*, 2012), which in turn enables ocean-floor displacements to be estimated — an important first step in tsunami modelling (Satake, 2007).

To make such inversions tractable in real-time the fault's location and orientation are commonly assumed *a priori* using catalogues of known active faults, thus rendering the inverse problem linear. Since such information may be ambiguous, erroneous or lacking, and earthquakes can occur on previously unidentified faults, an alternative approach is to construct a fault plane from the best point source recovered from the same geodetic dataset. Crowell *et al.* (2012) found that aspects such as the total moment, location of peak slip, and slip extent obtained in source inversions using fault geometries taken from fault catalogues and moment tensor inversions are — broadly speaking — comparable. Consequently there is great potential value in determining moment tensors from static displacement data for earthquake early warning, as it eliminates the need for *a priori* knowledge of the style of faulting in a particular area. If required, this moment tensor can also then be used to constrain the location, geometry and moment release for more sophisticated slip inversions on a finite fault.

Although geodetic source inversions assuming a finite fault are now routinely carried out, we are aware of only one previous study that performed inversions of static displacement data for an earthquake's CMT parameters (Melgar *et al.*, 2011). Using a precomputed library of excitation kernels, they performed a series of inversions on a grid of points distributed in space, choosing the location and moment tensor which yield the lowest data misfit as their CMT solution. The method proposed here is an alternative to that of Melgar *et al.* (2011), the main differences being that we solve directly for the centroid position without restriction to a grid, and our forward modelling method is efficient enough that all necessary computations are performed on-the-fly, allowing *a priori*

assumptions about possible earthquake locations to be minimised. All that we require to perform an inversion is a static displacement dataset, a crustal model, and an initial estimate of the source location from which we iterate to find the centroid position and moment tensor that best explain the data.

In this chapter, we adapt the GPS waveform inversion scheme described in Chapter 3 to suit more widely available static displacement data, and test this implementation by means of an inversion of a synthetic dataset [1]. Initial attempts at performing source inversions using static displacements observed for the 2010 M_{W} 7.2 El Mayor-Cucapah, Mexico, earthquake suggest that the iterative inversion produces unrealistically large location updates. We therefore introduce damping of the centroid location update into the inversion scheme to ensure that the inversion converges stably. We conclude by demonstrating the potential of this new method for rapid source characterization, by performing a CMT inversion of the El Mayor-Cucapah static displacement dataset in simulated real-time.

4.1 CMT inversions using synthetic static displacements

Static displacements can be readily incorporated into our source inversion algorithm because they are essentially a special case of a displacement time-series containing a single datum: $u_i(t \to \infty)$. The static displacement is already computed during inversions of GPS waveform data, as we saw in the previous chapter. Consequently, if our data consist solely of coseismic displacements, we can use the same computational scheme, except that we only need calculate the deformation field at $\omega = 0$. For this purpose, we have introduced a static displacement GPS data slice, `STGP`. No filtering or removal of instrument response is needed for static displacement data, and so the purpose of this slice is merely to identify the data type within the inversion.

To validate the implementation of static displacement data into our source inversion algorithm, we performed a synthetic test. Coseismic displacements were computed using

[1] Much of the material in this chapter has been published as O'Toole *et al.* (2013).

the Global CMT solution for the 2011 M_w 7.2 Van, Turkey, earthquake at 20 stations of the Turkish continuous GPS network (see Figure 4.1). This event was chosen because it has a good receiver coverage in both azimuth and epicentral distance. The station distribution and static displacement data were taken from the Group on Earth Observation's website for this event[2]. The local crustal model from CRUST2.0[3] was used in the forward modelling and inversion. Horizontal component displacements were used as input for a source inversion initiated at the PDE catalogue hypocentre, results from which are shown in Table 4.1. The successful recovery of the input source model demonstrates that the adaptations made to our inversion code to accommodate static displacement data were effective. The experiment also shows that these data, in the absence of noise, are sufficient to completely resolve the source, although the relatively large number of iterations taken for the event depth to converge to its true value does suggest that this parameter is not so well constrained by static displacement data. For consistency, vertical displacements were not used in this test because their relatively high noise levels mean that we ignore them in our inversions of real data that follow. Note that because static displacements are, by definition, independent of time, we only solve for the spatial coordinates of the centroid. Since we are examining earthquake sources — which should have no explosive component — we also constrain the trace of the moment tensor to equal zero in the following.

4.2 The 2010 M_w 7.2 El-Mayor Cucapah earthquake

This chapter was motivated by a desire to invert GPS measurements of coseismic displacement fields in near real time to provide constraints on event locations, magnitudes and mechanisms, which are useful as inputs for more sophisticated source modelling and for effective early response. The success of our inversion of synthetic static displacements prompts us now to investigate inverting a real dataset, before we attempt a simulated real time implementation. For this purpose, we use a GPS dataset recorded during the 4

[2]http://supersites.earthobservations.org/van.php
[3]http://igppweb.ucsd.edu/gabi/rem.html

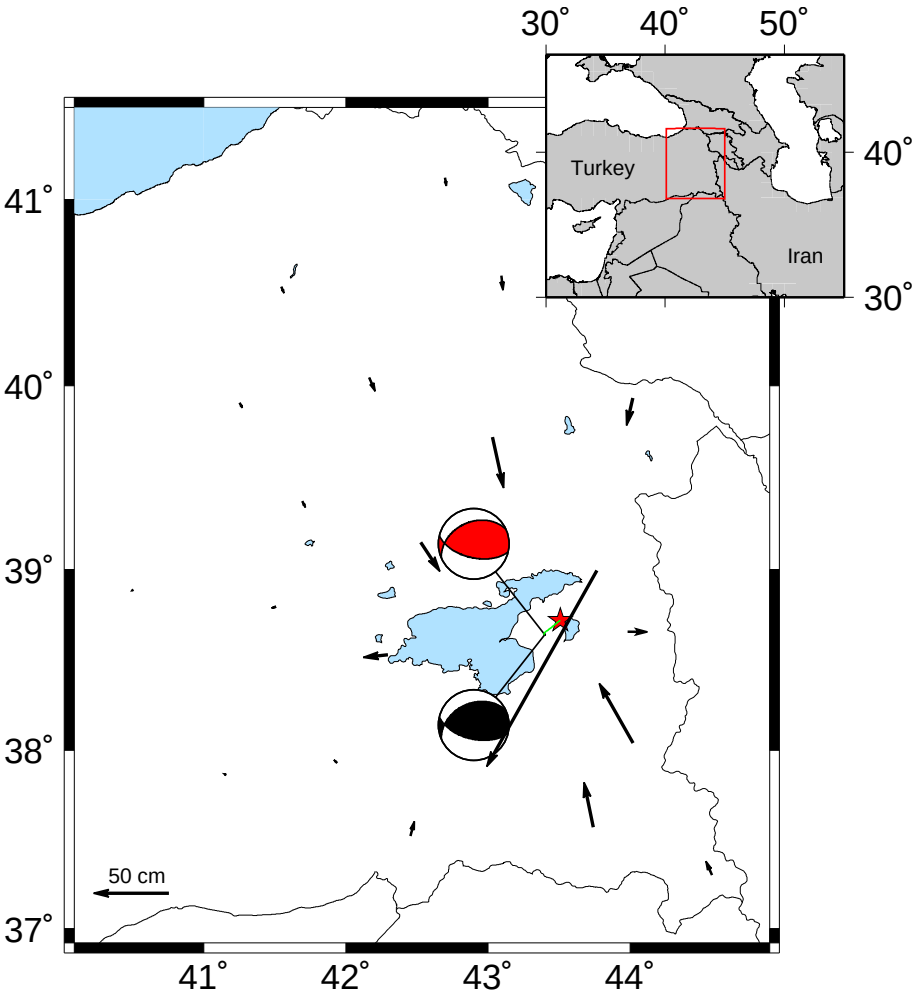

Figure 4.1: Station distribution used in the synthetic inversion of static displacements for the 2011 M_w 7.2 Van, Turkey, earthquake. Horizontal static displacements (black arrows) were computed using the Global CMT solution for this event (black beachball). The iterative inversion was initiated at the PDE catalogue hypocenter (red star); our solution after 10 iteration (red beachball) is essentially identical to the input source.

	Input	Iteration									
		0	1	2	3	4	5	6	7	8	9
Location:											
latitude	38.64°N	38.72°N	38.66°N	38.65°N	38.64°N	38.64°N	38.64°N	38.64°N	38.64°N	38.64°N	38.64°N
longitude	43.40°E	43.51°E	43.41°E	43.39°E	43.39°E	43.40°E	43.40°E	43.40°E	43.40°E	43.40°E	43.40°E
depth (km)	12.89	16.00	17.07	11.49	10.39	11.50	12.11	12.45	12.64	12.75	12.81
Moment tensor:											
M_{rr}	5.2700	4.9184	5.3597	5.0396	5.0822	5.1546	5.2041	5.2324	5.2483	5.2572	5.2623
$M_{\theta\theta}$	-5.8600	-4.9432	-5.7272	-5.7346	-5.7589	-5.7979	-5.8250	-5.8403	-5.8488	-5.8537	-5.8564
$M_{\phi\phi}$	0.5910	0.0247	0.3675	0.6951	0.6767	0.6433	0.6209	0.6079	0.6006	0.5964	0.5941
$M_{r\theta}$	2.1300	1.2789	2.0014	1.9843	2.3154	2.2229	2.1823	2.1589	2.1463	2.1393	2.1353
$M_{r\phi}$	-1.7800	-0.9056	-1.7839	-1.7764	-2.0223	-1.8904	-1.8425	-1.8146	-1.7995	-1.7912	-1.7865
$M_{\theta\phi}$	-0.6120	-0.9087	-0.8574	-0.5703	-0.5993	-0.6031	-0.6068	-0.6090	-0.6103	-0.6110	-0.6114
Relative RMS:		0.0136	0.0099	0.0046	0.0001	0.0000	0.0000	0.0000	0.0000	0.0000	0.0000
											

Table 4.1: Result of a source inversion of a synthetic static displacement dataset calculated for the 2011 M_w 7.2 Van, Turkey, earthquake. Moment tensors are given in units of 10^{19} Nm. The event origin time cannot be resolved from static displacement data, and so is not included.

April 2010, M_W 7.2 El Mayor-Cucapah, Mexico, earthquake, as a real time dataset is also available for this event.

The El Mayor-Cucapah earthquake ruptured a $\sim$ 120 km long series of faults within the Pacific–North American plate boundary of Mexico (Hauksson *et al.*, 2010). The Global CMT solution for this event displays a significant non double couple component, which has been interpreted in terms of rupture initiation along a normal fault with subsequent strike-slip motion (Hauksson *et al.*, 2010; Uchide *et al.*, 2013). This earthquake was recorded by 105 GPS receivers of the California Real Time Network (CRTN) and Plate Boundary Observatory (PBO) located throughout southern California, all operating at 1 Hz. The raw GPS data were processed in real-time using the method of instantaneous positioning (Bock *et al.*, 2000) and made available to the community, along with the resulting 1 Hz GPS time-series, as described by Bock *et al.* (2011). Although GPS waveform data are available for this event (Zheng *et al.*, 2012), our focus here is solely on using static displacements extracted from these waveforms for rapid source characterization.

4.2.1 Approaches to extracting static offsets in real-time

Rapid source inversions of geodetic data require some method for estimating the static displacement field while transient deformations due to the propagation of surface waves are still ongoing. For this purpose, a number of approaches of varying sophistication have been proposed for extracting static offsets from GPS time-series in real time.

Most simplistically, Wright *et al.* (2012) assumed that the value of the GPS–measured displacement field at any moment is the static displacement. This complete neglect of dynamic deformations is problematic because the large amplitude of surface waves means that the static displacement field will initially be vastly overestimated, with the potential for causing false alarms. Melgar *et al.* (2011) overcame this problem by applying a 120 s moving average filter to the GPS time-series, which successfully smooths out the contribution of the dynamic deformation. However, the length of the window used by Melgar

et al. (2011) limits the time at which representative displacements are obtained to such an extent that it is not clear that much has been gained over waiting for shaking to stop before inverting.

Allen and Ziv (2011) noted that a typical GPS waveform resembles a step function, corresponding to the static displacement, with oscillations, dynamic displacements, superimposed onto it. A good estimate of the static displacement can therefore be obtained quite soon after shaking begins at a particular station by averaging out the dynamic contribution. The coseismic displacement is then just the difference between this average and the pre-earthquake position of the receiver. Allen and Ziv (2011) implemented this approach by computing a running average of the GPS trace, starting from the time when a short term (2 s) average is more than 10 times larger than a long term (100 s) average. The initial estimate of the static displacement is returned after the GPS waveform has crossed the trigger amplitude twice — i.e. after one full oscillation — and is updated at every subsequent epoch. It is possible that the trigger amplitude will not be crossed twice, in this case the first static displacement estimate is returned 10 s after the initial trigger.

An example of the application of these three approaches to extracting static displacements is shown in Figure 4.2, using north component data from PBO station P494 for the El Mayor-Cucapah earthquake. For each processing technique, we plot the estimated displacement as a function of time, compared to the "true" static displacement (Figure 4.2, grey step function), which was determined using 24 hours of data spanning the day before and after the event. The final static displacements in the raw and smoothed time-series are consistent with each other, but smaller than the post-processed value. This offset may indicate that a post-seismic signal is contaminating the daily solution. However, the magnitude of this discrepancy, at ~ 2 mm, is not significant and so each approach gives a good estimate of the static displacement field from about 140 s after the earthquake origin time onwards.

Figure 4.2 clearly shows that the static displacement picking algorithm of Allen and Ziv (2011) is superior to the others for use in combination with real-time inversion, because it

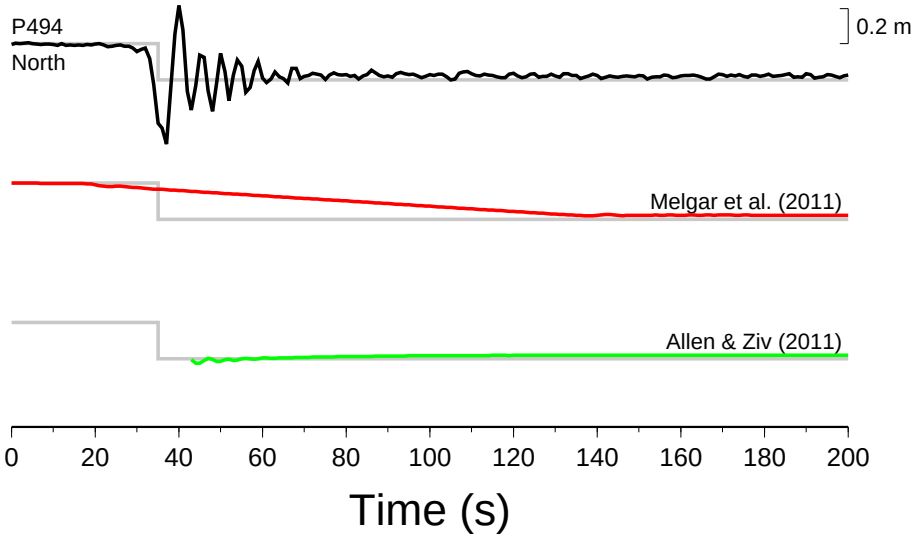

Figure 4.2: A comparison of methods for extracting static displacements from GPS waveforms in real-time. Wright *et al.* (2012) assume that the value of the displacement waveform (black trace) at each epoch gives the static offset. Melgar *et al.* (2011) compute a 120 s moving average to remove the dynamic displacement. Allen and Ziv (2011) use a running average of the displacement waveform. Averaging starts after some short term average–long term average trigger, indicated by the step function, and static displacement estimates then start to be delivered after one full oscillation, or 10 s, later (whichever is sooner). The amplitude of the step function indicates the value of the "true" static displacement computed using 24 hours of GPS data from before and after the earthquake. Adapted from Allen and Ziv (2011).

delivers a good estimate of the static displacement rapidly: in this case 7 s after shaking is first detected at the station. In contrast, neglecting the dynamic displacement, as done by Wright *et al.* (2012), will lead to large errors until shaking stops at about 80 s after the earthquake origin time. The strategy adopted by Melgar *et al.* (2011) is conservative as its estimates of the static displacement tend smoothly to the true value over time. However the rate of convergence limits the real-time usefulness of such an approach.

Of course, the relative performance of the three methods outlined here will vary according to factors like the source–receiver distance, event magnitude and rupture directivity, as these will all affect the duration of shaking at a particular station. However, the scheme for extracting static offsets proposed by Allen and Ziv (2011) appears to be most effective at delivering representative displacement estimates in a timely manner, and so will be used

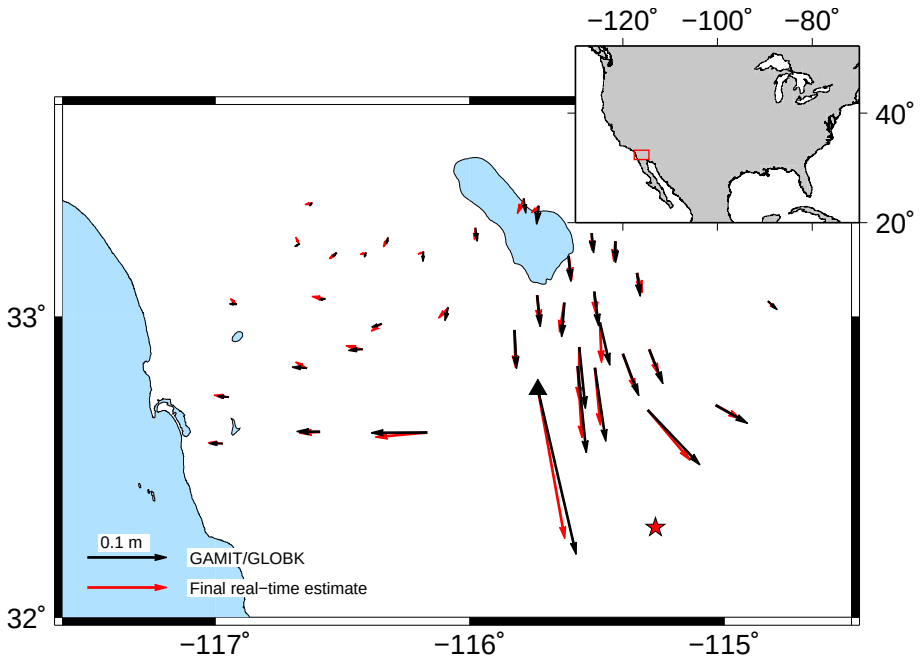

Figure 4.3: A comparison of horizontal static displacement fields determined for the El Mayor-Cucapah earthquake using different techniques. The final static displacements output by the algorithm of Allen and Ziv (2011) (red arrows) show good agreement with the daily GPS solutions (black arrows). The location of station P494, data from which are used in the comparison presented in Figure 4.2, is indicated by the triangle. The PDE hypocentre of this event is shown by the red star.

in the following. Furthermore, the robustness of this approach is demonstrated for the El Mayor Cucapah earthquake in the consistency between the final offsets estimated by Allen and Ziv (2011) with the post-processed displacements at all stations (see Figure 4.3).

4.2.2 *Post hoc* analysis

The 1 Hz GPS dataset acquired during the El Mayor-Cucapah earthquake, combined with the static displacement picking algorithm of Allen and Ziv (2011), allows us to investigate performing inversions for the centroid and moment tensor of this event in simulated real-time. However, we should first attempt a *post hoc* inversion of a single set of static displacements, to assess the performance of the inversion algorithm when real data are used. For this purpose, we use the final set of estimates determined by the method of

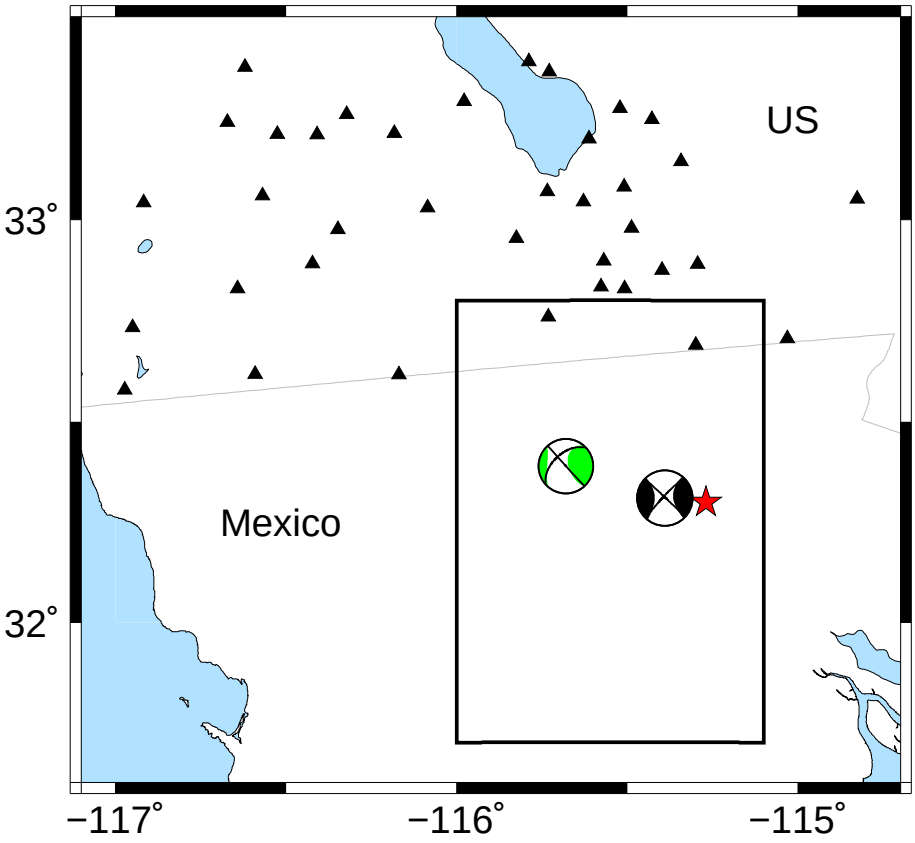

Figure 4.4: Distribution of CRTN and PBO GPS receivers (triangles) used in this study. The hypocenter of the 4 April 2010, M_W 7.2 El Mayor-Cucapah earthquake, taken from the USGS PDE catalogue is indicated by the red star. CMT solutions from the Global CMT catalogue and Melgar *et al.* (2011) are shown by the black and green beachballs respectively. The rectangle denotes the area enlarged in Figure 4.5a.

Allen and Ziv (2011) from 37 stations (Figure 4.4, triangles). We invert only the horizontal component static displacements as the amplitudes of vertical offsets excited in this earthquake are comparable to their measurement uncertainties.

Previously, Melgar *et al.* (2011) used a similar static displacement dataset to determine a CMT solution for this event. Their solution (Figure 4.4, green beachball), provides a useful benchmark to compare with our results. The starting location for our source inversion is taken from the USGS Preliminary Determination of Epicenters (PDE) catalogue (Figure 4.4, red star). We compute derivative kernels using the same layered crustal model

as Melgar *et al.* (2011), and apply the iterative inversion scheme given in (4.1) to recover a CMT solution for this event.

It is well known that the $M_{r\theta}$ and $M_{r\phi}$ excitation kernels vanish as the source approaches the free surface, and hence these components of the moment tensor cannot be reliably determined for shallow earthquakes (e.g Kanamori and Given, 1981). Consequently we must impose a limit on the shallowest depth that is allowed to be recovered during the inversion. If the inversion tries to move the centroid depth shallower than 4 km, we fix the event depth to this value in subsequent iterations and no longer solve for this parameter. A similar approach is taken in Global CMT inversions, although depths are typically fixed slightly deeper at ∼12 km; the threshold depth used here is chosen in an effort to maintain comparability of our solution with that of Melgar *et al.* (2011), which has a depth of 4 km.

The evolution of the source location over 10 iterations of the inversion algorithm is shown by the blue line in Figure 4.5a; large changes in centroid location are apparent from one iteration to the next. Since the inversion immediately moves the source to the shallowest permitted depth (4 km), the misfit function at this depth — calculated by performing a series of moment tensor inversions on a grid of points — is also shown by the shaded contour map. The inversion algorithm should move the centroid downhill on this misfit surface towards the global minimum. Clearly, the inversion fails to behave in this way; the actual evolution of the misfit over the iterative inversion is shown by the blue line in Figure 4.5b. The large oscillations in misfit between iterations confirm that the attempted inversion of static displacement data is unstable, and goes beyond the limit of our linear approximation's validity.

The failure of the linearization is apparent in the great disparity between the misfit of each source output by the inversion (Figure 4.5b, blue line), and the true minimum misfit value at each location visited during the inversion, which is given by the misfit surface in Figure 4.5a. The large changes in source location mean that the moment tensor output by the inversion is a very poor approximation of the actual best moment tensor at the new

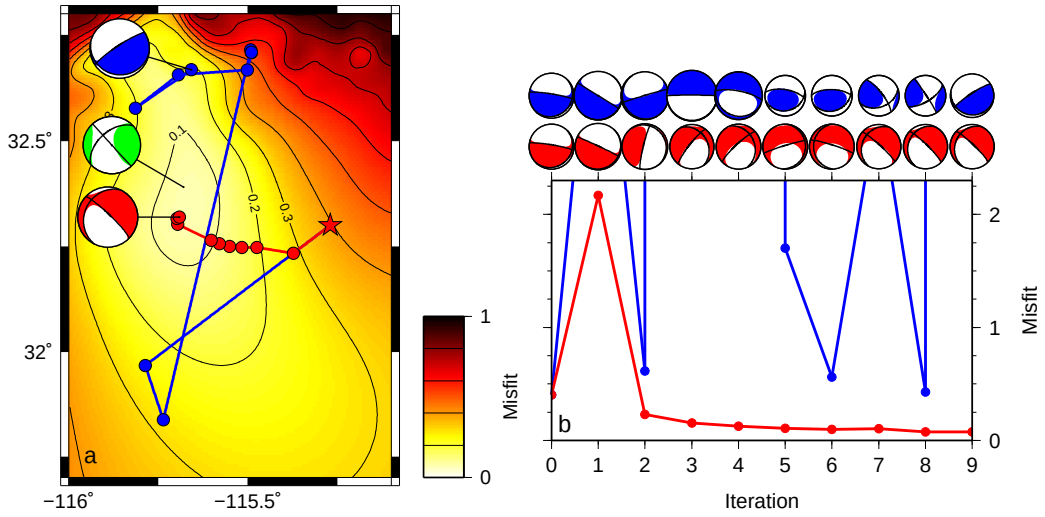

Figure 4.5: The evolution of centroid location (a) and misfit (b) over 10 iterations of our source inversion algorithm before and after the introduction of location step-length damping (blue and red respectively). The solution of Melgar *et al.* (2011) is indicated by the green beachball. Our inversions start at the PDE hypocenter (red star). The contours and shading denote the value of the misfit function at a depth of 4 km.

location, and hence the misfit function over the 10 iterations is poorly behaved. In order to stabilize the inversion, it is therefore necessary to adapt the iterative scheme so that the change in source location allowed in any one iteration is restricted.

4.2.3 Location step-length damping

In the naive inversions of static displacement data just attempted, nonlinearity in the relationship between data and source parameters — particularly the centroid location — caused instabilities leading to unrealistically large location updates. While we could damp the location update simply by taking the change in centroid coordinates output by the inversion and, for example, multiplying by a damping factor, the output moment tensor is computed assuming that the source location changed by the full amount. As a consequence the moment tensor is sub-optimal for the damped location, and the iterative inversion may still be unstable. To counteract this problem, we wish to limit the size of the location change permissible on any given iteration in an "intelligent" way.

We begin by recalling that the least-squares solution of a linearised inverse problem is of the form

$$\mathbf{f}_{\mathrm{i}+1} = \mathbf{f}_{\mathrm{i}} + \left(\mathbf{A}_{\mathrm{i}}^{\mathrm{T}}\mathbf{A}_{\mathrm{i}}\right)^{-1}\mathbf{A}_{\mathrm{i}}^{\mathrm{T}}\mathbf{e}\,. \tag{4.1}$$

Alternatively, we can separate our vector of unknown source parameters into moment tensor and centroid coordinate parts, *i.e.* $\mathbf{f} = (\mathbf{m}, \mathbf{x})^{\mathrm{T}}$, allowing us to write a synthetic seismic dataset, $\mathbf{s}$, as

$$\mathbf{s}(\mathbf{f}) = \mathbf{A}\mathbf{m} + \mathbf{B}\mathbf{x}\,, \tag{4.2}$$

$$\mathbf{s}(\mathbf{f} + \delta\mathbf{f}) = \mathbf{A}\mathbf{m} + \mathbf{A}\delta\mathbf{m} + \mathbf{B}\mathbf{x} + \mathbf{B}\delta\mathbf{x} \tag{4.3}$$

to first order, where $A_{ij} = \frac{\partial s_i}{\partial m_j}$ and $B_{ij} = \frac{\partial s_i}{\partial x_j}$ are the excitation and location kernels respectively. We seek the model perturbation bringing static displacement data, $\mathbf{d}$, and synthetics into better agreement, which corresponds to the assumption that the update $\delta\mathbf{f}$ gives synthetics that exactly agree with $\mathbf{d}$, hence we have

$$\mathbf{d} - \mathbf{s}(\mathbf{f}) = \mathbf{A}\delta\mathbf{m} + \mathbf{B}\delta\mathbf{x}\,. \tag{4.4}$$

Defining a vector of residuals, $\mathbf{e} = \mathbf{d} - \mathbf{s}$, (4.4) becomes

$$\mathbf{e} = \begin{pmatrix}\mathbf{A} & \mathbf{B}\end{pmatrix}\begin{pmatrix}\delta\mathbf{m} \\ \delta\mathbf{x}\end{pmatrix}\,, \tag{4.5}$$

which has a least squares solution

$$\begin{pmatrix}\delta\mathbf{m} \\ \delta\mathbf{x}\end{pmatrix} = \begin{pmatrix}\mathbf{A}^{\mathrm{T}}\mathbf{A} & \mathbf{A}^{\mathrm{T}}\mathbf{B} \\ \mathbf{B}^{\mathrm{T}}\mathbf{A} & \mathbf{B}^{\mathrm{T}}\mathbf{B}\end{pmatrix}^{-1}\begin{pmatrix}\mathbf{A}^{\mathrm{T}}\mathbf{e} \\ \mathbf{B}^{\mathrm{T}}\mathbf{e}\end{pmatrix}\,, \tag{4.6}$$

hence we can rewrite (4.1) as

$$\begin{pmatrix}\mathbf{m}_{\mathrm{i}+1} \\ \mathbf{x}_{\mathrm{i}+1}\end{pmatrix} = \begin{pmatrix}\mathbf{m}_{\mathrm{i}} \\ \mathbf{x}_{\mathrm{i}}\end{pmatrix} + \begin{pmatrix}\mathbf{A}^{\mathrm{T}}\mathbf{A} & \mathbf{A}^{\mathrm{T}}\mathbf{B} \\ \mathbf{B}^{\mathrm{T}}\mathbf{A} & \mathbf{B}^{\mathrm{T}}\mathbf{B}\end{pmatrix}^{-1}\begin{pmatrix}\mathbf{A}^{\mathrm{T}}\mathbf{e} \\ \mathbf{B}^{\mathrm{T}}\mathbf{e}\end{pmatrix}\,. \tag{4.7}$$

From (4.6), we see that

$$\mathbf{A}^{\mathrm{T}}\mathbf{A}\delta\mathbf{m} + \mathbf{A}^{\mathrm{T}}\mathbf{B}\delta\mathbf{x} = \mathbf{A}^{\mathrm{T}}\mathbf{e} \tag{4.8}$$

$$\mathbf{B}^{\mathrm{T}}\mathbf{A}\delta\mathbf{m} + \mathbf{B}^{\mathrm{T}}\mathbf{B}\delta\mathbf{x} = \mathbf{B}^{\mathrm{T}}\mathbf{e}\,. \tag{4.9}$$

Solving the first of these equations for $\delta\mathbf{m}$, we find

$$\delta\mathbf{m} = \left(\mathbf{A}^{\mathrm{T}}\mathbf{A}\right)^{-1}\mathbf{A}^{\mathrm{T}}\left(\mathbf{e} - \mathbf{B}\delta\mathbf{x}\right) \tag{4.10}$$

and substituting this result into (4.9), we obtain

$$\delta\mathbf{x} = \left(\mathbf{B}^{\mathrm{T}}\mathbf{B} - \mathbf{B}^{\mathrm{T}}\mathbf{A}\left(\mathbf{A}^{\mathrm{T}}\mathbf{A}\right)^{-1}\mathbf{A}^{\mathrm{T}}\mathbf{B}\right)^{-1}\left(\mathbf{B}^{\mathrm{T}}\mathbf{e} - \mathbf{B}^{\mathrm{T}}\mathbf{A}\left(\mathbf{A}^{\mathrm{T}}\mathbf{A}\right)^{-1}\mathbf{A}^{\mathrm{T}}\mathbf{e}\right). \tag{4.11}$$

We can now rewrite (4.7) as two coupled equations

$$\mathbf{x}_{\mathrm{i}+1} = \mathbf{x}_{\mathrm{i}} + \left[\mathbf{B}^{\mathbf{T}}\mathbf{B} - \mathbf{B}^{\mathbf{T}}\mathbf{A}\left(\mathbf{A}^{\mathbf{T}}\mathbf{A}\right)^{-\mathbf{1}}\mathbf{A}^{\mathbf{T}}\mathbf{B}\right]^{-\mathbf{1}}\left[\mathbf{B}^{\mathbf{T}}\mathbf{e} - \mathbf{B}^{\mathbf{T}}\mathbf{A}\left(\mathbf{A}^{\mathbf{T}}\mathbf{A}\right)^{-\mathbf{1}}\mathbf{A}^{\mathbf{T}}\mathbf{e}\right] \tag{4.12}$$

$$\mathbf{m}_{\mathrm{i}+1} = \mathbf{m}_{\mathrm{i}} + \left(\mathbf{A}^{\mathbf{T}}\mathbf{A}\right)^{-\mathbf{1}}\left[\mathbf{A}^{\mathbf{T}}\mathbf{e} - \mathbf{A}^{\mathbf{T}}\mathbf{B}\left(\mathbf{x}_{\mathrm{i}+1} - \mathbf{x}_{\mathrm{i}}\right)\right] \tag{4.13}$$

We may introduce a damping parameter η to multiply the second term on the right hand side of (4.12). When $\eta = 1$ this form is exactly equivalent to (4.1). Setting $\eta < 1$, however, allows us to damp the location update from one iteration to the next, and we can use the true, restricted $\mathbf{x}_{\mathrm{i}+1}$ in (4.13) to obtain a self-consistent set of source parameters. A similar approach has been adopted by a number of authors in the context of joint determination of earthquake source parameters and earth structure (Pavlis and Booker, 1980; Morelli and Dziewonski, 1991; Valentine and Woodhouse, 2010).

The effect of damping the location update step-length is illustrated in Figure 4.6 via the evolution of misfit during the inversion of synthetic static displacements for the Van earthquake (see Section 4.1), using various values of the damping parameter, η. We use this data for this test as we know that the undamped inversion converges, and so we can see what effect the location update damping has when the inversion is well behaved. As expected the undamped inversion using (4.1) gives results identical those obtained when

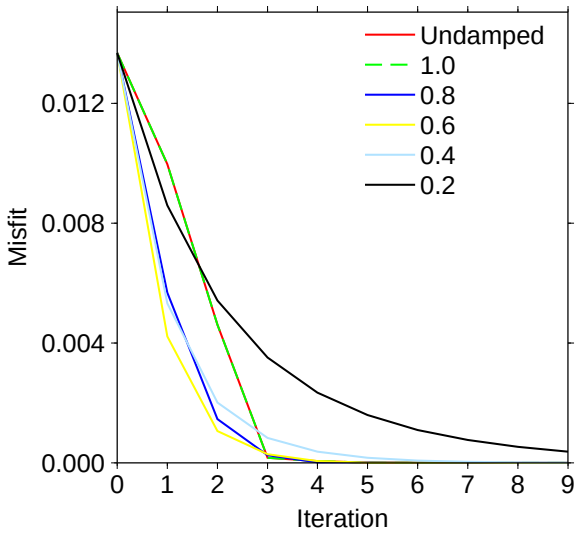

Figure 4.6: The effect of particular choices of the damping parameter η on the convergence of inversions of a synthetic static displacements computed for the Van earthquake (see Section 4.1.

$\eta = 1$. Moderate amounts of damping initially cause the inversion to converge more rapidly, because reducing the change in location helps to ensure that the linearization is reasonable. However, excessive damping results in unacceptably slow convergence rates.

We repeated the previous inversion of static displacements from the El Mayor Cucapah earthquake, except that we now damp the location step-length heavily, choosing $\eta = 0.2$. In contrast to the earlier attempt, the centroid now moves smoothly downhill in misfit space to converge at the global minimum (Figure 4.5a, red line), demonstrating that the damping we have introduced successfully stabilizes the inversion. The improved behaviour of the damped inversion is also apparent in the evolution of the misfit during the inversion (Figure 4.5b, red line), which is a much better approximation of the true minimum misfit. Although the misfit increases after the first iteration, where the restricted location update is still large enough for the linearization to fail, the damping is sufficient that the solution is still close enough to the actual best solution at that location for the misfit to decrease on subsequent iterations and the inversion to converge.

A consequence of applying damping is that convergence is slowed as the solution ap-

proaches the global minimum. To avoid this issue, we apply damping only when the suggested location update is larger than some value over which we assume the linearisation holds, here this length is chosen as 10 km. For real-time inversions, where the amount of damping required is not known *a priori*, one could adopt this approach and set η to be conservatively small ($\eta = 0.1$, say). This would ensure stability of the inversion, but also allows rapid convergence when the solution is close to the global minimum. For comparison, the CMT solution of Melgar *et al.* (2011) is also shown in Figure 4.5a (green beachball).

The misfit function plotted in Figure 4.5a is sufficiently well-behaved that one could start a step-length damped inversion at any point, and it would converge to the global minimum. While there is a local minimum visible at the north-east corner of this plot, this arises from the fact that there is a GPS station directly above this point, data from which was used in the construction of the misfit function. In practice, one would ignore data from this station if the starting point for our iterative inversion was located nearby, and there would be no local minimum to potentially hamper the inversion.

While step-length damping clearly stabilizes the inversion, the final solution is physically unrealistic due to the large dip-slip components, which — despite our depth fixing — dominate the solution (see Table 4.2). To avoid this problem, we perform a further inversion where we impose the condition that $M_{r\theta} = M_{r\phi} = 0$. While other forms of regularization could be applied, we employ this constraint as it is also used in Global CMT analyses of some earthquakes with centroid depths shallower than ∼15 km. We find that introducing this constraint also helps to stabilize the inversion so that weaker step-length damping is required; source parameters output for a constrained inversion with $\eta = 0.5$ are shown in Table 4.2. When compared to the "full" moment tensor obtained previously, the solution with $M_{r\theta} = M_{r\phi} = 0$ explains the data almost as well whilst also having a much smaller norm, and so could be preferred on the principle of parsimony.

	Damped, $\eta = 0.2$	$M_{r\theta} = M_{r\phi} = 0$, $\eta = 0.5$
Location:		
latitude	32.32°N	32.34°N
longitude	115.69°W	115.74°W
depth (km)	4.00 F	4.00 F
Moment tensor:		
M_{rr}	-5.45	-1.17
$M_{\theta\theta}$	-4.73	-7.16
$M_{\phi\phi}$	10.18	8.33
$M_{r\theta}$	14.39	0.00 F
$M_{r\phi}$	-11.17	0.00 F
$M_{\theta\phi}$	-1.79	0.18
Best double couple:		
M_0	20.28	7.75
M_W	7.50	7.23
Nodal plane 1:		
strike/dip/rake (°)	206/24/-20	136/90/-180
Nodal plane 2:		
strike/dip/rake (°)	314/82/-112	226/90/0
Relative r.m.s.	0.08	0.10
		

Table 4.2: Source parameters, and corresponding beachballs, obtained after 10 iterations of our inversion. 'F' indicates values that are fixed during the inversion. Moment is given in units of 10^{19} Nm.

4.2.4 Real-time application

The success of our modified source inversion scheme leads us to investigate whether this method could be applied to invert static displacement data in real-time. The exact setup of the real-time inversion described below is somewhat arbitrary, and we make no claim that the current scheme is ideal; rather we merely hope to demonstrate that real-time inversion is possible without the need for precomputed libraries of excitation kernels, or *a priori* knowledge of fault locations and geometries. Here, we use the real-time static displacement dataset extracted from the 1 Hz GPS waveforms using the algorithm of Allen and Ziv (2011).

Our inversion approach is much the same as before; we apply step-length damping

with $\eta = 0.5$ along with the constraint that $M_{r\theta} = M_{r\phi} = 0$. The only difference is that we simulate a real-time application. The algorithm of Allen and Ziv (2011) generates an estimate of the static offset at all stations that is being continually updated, with each new measurement available at the receiver sampling period (1 s, here). At the end of each iteration of our inversion we take the most recent estimate of the static displacement field and use this updated data vector in the next iteration.

In this experiment, the inversion begins when more than 20 data points become available. This is a somewhat arbitrary choice, and could adapted to suit particular circumstances. We find that the inverse problem may be unstable if the inversion commences when substantially fewer data are available. The inversion continues until the final set of static displacements are reported and the misfit falls below a predefined threshold. Alternatively, the inversion could run until there is no significant decrease in the misfit between iterations, or the change in the model is very small from one iteration to the next; these stopping conditions may be more suitable for a real-time implementation than the simple misfit threshold currently used. Here, the inversion is triggered 61 s after the PDE catalogue origin time. The final solution — which is essentially identical to that given in Table 4.2 — is available 82 s later (all run times quoted are for a single 2.4 GHz processor).

The results of the real-time inversion are summarised in Figure 4.7. Unlike inversions that use precomputed libraries of excitation kernels or model the crust as a homogeneous half-space (e.g. Melgar *et al.*, 2011; Wright *et al.*, 2012), each iteration of our inversion takes longer than 1 s. As a consequence, we do not produce a solution for every set of static displacement estimates, although further optimisation of our forward modelling code is possible; in future inversions we expect to reduce the time taken to perform an iteration. However, the time at which our final solution is available is comparable to that of Melgar *et al.* (2011); this time is mainly controlled by when the data are representative of the final static offsets, and not how long it takes to do an iteration of the inversion. The duration of an iteration depends most strongly on the number of data points used, and so increases as more stations start reporting static displacements, peaking at $\sim$16 s when data from all 37 stations are available.

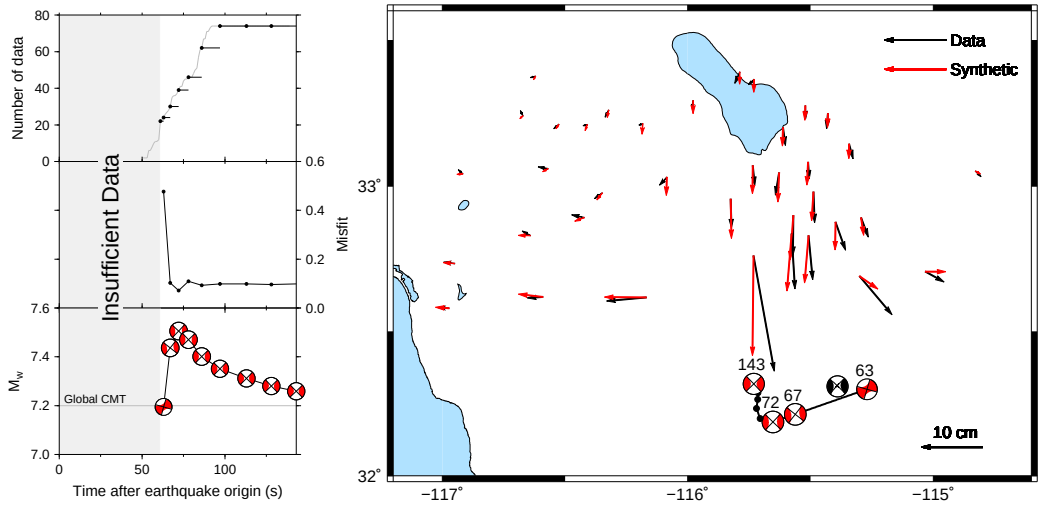

Figure 4.7: Results of a simulated real-time source inversion of static displacement data for the El Mayor-Cucapah, earthquake. Left, top: amount of data available as a function of time (grey line). The black "tadpoles" indicate the amount of data used in, and duration of, each iteration of our inversion. Left, middle: evolution of misfit as function of time. Left, bottom: source mechanism and moment magnitude output by the inversion over time. The Global CMT magnitude is indicated by the grey line. Right: map showing the fit between horizontal static displacement data (black arrows) and synthetics (red arrows) for our final solution. A selection of the CMT solutions produced during the real-time inversion are also plotted; the number above each beachball indicates the time (in seconds after the earthquake origin time) at which that solution is available using a single 2.4 GHz processor. The Global CMT solution is indicated by the black beachball.

The first iteration moves the centroid $\sim$ 30 km westward, and produces a marked decrease in misfit. The misfit does not change significantly on subsequent iterations, even though it is calculated with respect to the updated dataset rather than just the data used in that iteration. This behaviour indicates that each solution must explain the new data added after that iteration reasonably well. The moment magnitude of our solution decreases towards the Global CMT value of M_{W} 7.2 as the centroid moves northwards and closer to the network.

Solutions from a select number of iterations are shown on the map in Figure 4.7, and are annotated with the time that they are available, in units of seconds after the earthquake began. The advantage of performing an inversion in real-time — rather than waiting for the final static displacement dataset to be available — is that the early iterations allow

the centroid to move close to its true, final position, so that convergence is very rapid once all the data are available. Observed and synthetic static displacements computed for our final source are also shown; the level of agreement reflects the low misfit value of this inversion.

4.3 Discussion

Our source inversion of real-time static displacements for the El Mayor-Cucapah earthquake shows that the method developed in this chapter may be useful for determining the location, magnitude, and style of faulting in the context of earthquake early warning. Ideally, the GPS network would provide complete azimuthal coverage of the source, allowing the radiation pattern to be fully sampled. Here, all stations lie north of the event, so this study represents something of a worst-case scenario. The fact that our step-length damped inversion converges even in this situation indicates that our algorithm is robust with respect to network geometry. This result is important in the context of monitoring subduction zone events, where land based real-time GPS networks are necessarily one-sided.

Since our inversion approach aims to minimise the amount of *a priori* information required, it is amenable to automation. In addition to the data, all that we need to perform an inversion is a preliminary hypocenter, which can be obtained within a few seconds of the detection of wave arrivals using existing seismic or geodetic early warning systems (e.g. Allen *et al.*, 2009; Crowell *et al.*, 2009), and a crustal model, which — in the absence of better knowledge of the local earth structure — can be taken from an appropriate global model, such as Crust 2.0 (http://igppweb.ucsd.edu/~gabi/rem.html). No assumptions about possible fault locations and geometries need be made, nor do we require any knowledge of pre-existing faults in the area.

Furthermore, we demonstrate that it is possible to obtain a CMT solution rapidly without the need for large precomputed databases of excitation kernels which have been

required in previous implementations (Melgar *et al.*, 2011). The efficiency of our forward modelling method is such that all of the requisite derivative kernels can be calculated on-the-fly using a standard workstation with a single 2.4 GHz processor, even when a layered crustal model is used. As a consequence, our inversion method may be useful in improving the resilience of earthquake early warning systems, as it is flexible enough to cope with earthquakes occurring in unexpected locations, and can be performed on a laptop computer.

Given the average density of receivers in modern geodetic networks, along with typical GPS measurement uncertainties, we expect that earthquakes with $M_{\mathrm{W}} \geq 6.0$ will have sufficiently high signal-to-noise ratios to be analysed with the algorithm proposed here. Of course, this magnitude threshold will vary spatially within a network depending on the proximity of the centroid to subsets of receivers, and is also partly controlled by the source mechanism due to the relatively large uncertainties in vertical displacement measurements made using GPS (e.g. Langbein and Bock, 2004). It should also be noted that our assumption of a point source breaks down for near-field static displacements measured during the largest seismic events such as the 2011 M_{W} 9.1 Tohoku earthquake. These great ruptures may be treated more appropriately using finite fault inversions, although moment tensor inversions are still useful in these situations as they can be used as the starting point for an iterative procedure in which multiple point sources are used to approximate the finite extent of the rupture (see, for example Tsai, 2005).

Amoruso *et al.* (2004) and Hearn and Bürgmann (2005) showed that it is important to account for the effect of crustal layering in inversions of static displacement data, and the present work raises the possibility that Green's functions calculated in layered elastic media could also be computed in real-time for use in rapid slip inversions, in addition to the CMT-style analyses presented here. Since measurement uncertainties in GPS positions have been well studied (e.g. Langbein and Bock, 2004), in future the inversion scheme could be reformulated to incorporate this information; such an undertaking would allow the vertical displacement data to be included and enable quantification of uncertainties in recovered model parameters.

In addition to earthquake early warning, the method developed in this chapter can be used to determine candidate fault-planes for the purpose of finite fault slip inversions, both in real-time and after the event. Furthermore, since our inversion approach mirrors that of the CMT algorithm, the present work should enable near- and far-field data to be combined and reconciled in a single inverse problem, with the potential for quantifying and reducing errors in CMT solutions. While we have focused on using GPS-measured static displacement data to obtain the first order information about an earthquake, line of sight displacements measured by synthetic aperture radar interferometry could also be inverted using the techniques developed here.

Summary

In this chapter, we have shown that inversions for the centroid location and moment tensor of an earthquake may be performed using static displacements measured by geodetic GPS networks. These data may be useful for rapidly determining the basic parameters describing an earthquake — location, magnitude and mechanism — for early warning, which can then be used as inputs for more sophisticated finite source modelling. Beyond earthquake seismology, real time source inversions are also important for monitoring activities like shale gas hydraulic fracturing which induce microearthquakes, as we investigate in the following chapter.

Chapter 5

Microearthquake moment tensor determination using downhole arrays

Microearthquakes — small magnitude seismic events which cannot, generally, be felt — occur both naturally, and in response to a number of human activities which perturb the state of stress at depth, including mining, hydrocarbon extraction, and CO_2 sequestration. Passive seismic monitoring is often our only practical means of studying how these processes are affecting the subsurface in real time. Such knowledge may be useful and important, for example, to mitigate the hazard posed by rockbursts to miners (Young, 1993), or to monitor caprock integrity during pumping of CO_2 for storage in the subsurface (Verdon *et al.*, 2011). Recently, microseismic monitoring has found particular success as applied to hydraulic fracturing operations for shale gas and oil, where it is used to map the fracture network generated or reactivated by the fluid injection. It is estimated that this area alone accounts for 85% of all expenditure on microseismic monitoring, a growing market that is currently worth $250 million a year (Wilson, 2013).

Despite this financial investment, routine analyses of microseismic data tend to be restricted to determining event locations from travel time and particle motion measure-

ments; the rich resource of the seismic waveform is not fully exploited. Furthermore, information that is valuable for interpreting the microseismicity, such as a knowledge of the moment tensor of an event, can very rarely be obtained using conventional techniques because monitoring networks are often limited to a single array of geophones deployed in a nearby well. Monitoring geometries of this sort are insufficient for fully constraining the moment tensor from body wave amplitude measurements alone. In this chapter, our goal is to implement borehole-recorded seismic waveforms into the source inversion algorithm developed earlier in this thesis. For testing purposes, we invert data acquired during hydraulic fracturing experiments at Cotton Valley, Texas, USA. With a view to improving the design of future downhole microseismic monitoring arrays, we also use synthetic tests to investigate the extent to which receiver geometry affects performance of the inversion.

5.1 A brief introduction to microseismicity

There is no strict definition of what exactly constitutes a microearthquake or, equivalently, a microseismic event. Maxwell *et al.* (2010) define a microseism as any earthquake with moment magnitude less than 0, while others use a local magnitude threshold of 2 (NRC, 2012) or 2.5[1] in their definition. Regardless of the particular definition that one chooses, it is clear that the term "microearthquake" refers to the bottom end of the earthquake magnitude spectrum: events that can be recorded by local monitoring instruments, but that will not, generally, be felt.

The well-known magnitude–frequency scaling relationship that earthquakes are observed to obey (e.g. Gutenberg and Richter, 1944) means that, where they can be recorded, microearthquakes dominate seismic catalogues. Over recent years, the increase in the number and density of seismic networks, combined with the development of automated event detection and location techniques, has enable more routine observation and analysis of microearthquake datasets. For example, Valoroso *et al.* (2013) used the hypocentral locations of 64,000 events with $M_l > 0.7$ to image the fault system in the vicinity of the 2009

[1] http://www.norsar.no/seismology/Earthquakes/MicroseismicMonitoring/

M_w 6.1 L'Aquila, Italy, earthquake. At the same time, there has also been an increasing recognition that a number of human activities can induce microseismic, and larger, events. These activities include mining, carbon sequestration, conventional and unconventional hydrocarbon extraction, as well as the development of enhanced geothermal systems and construction of water reservoirs. Microseismic monitoring is one of the few available techniques that we can use to remotely-sense the response of the subsurface to these activities.

5.1.1 Shale gas hydraulic fracturing

Shale deposits are common hydrocarbon source rocks (e.g. Selley, 1985). However, their low permeability has, until recently, prevented shales from being considered as *reservoir* rocks from which hydrocarbons can be extracted on commercial scales. The development of horizontal drilling and hydraulic fracturing technologies has fundamentally changed this situation: shale gas accounts for 23% of current US natural gas production, a figure that is expected to rise to 46% by 2035 (US Energy Information Administration, 2011).

The development of a shale gas reservoir requires us to artificially increase its porosity. This process typically begins by drilling vertically towards a shale gas prospect, and deviating the well-bore to run horizontally along the target horizon. Horizontal drilling maximises the volume of the reservoir that can communicate with the well. After the well has been cased and cemented, an interval within the well-bore adjacent to the shale formation is perforated, perhaps using a number of small explosive charges. Large volumes of fluid are then pumped into the well at high pressure to fracture the shale, before a plug is inserted "above" — in the sense of measured, rather than true, vertical depth in the horizontal well — the perforated interval. This process is repeated so that the entire horizontal leg of the well is perforated and fractured; each episode of pumping is called a "stage". Finally, the plugs are removed, and the fracturing fluid is allowed to flow back to the surface. The fracturing fluid is usually water, with a few reagents added to

decrease the viscosity, reduce friction, and keep the well clean. These additives are volumetrically insignificant, typically comprising 0.2% of the fluid mixture (The Royal Society, 2012). "Proppant" — sand or a similar material — may also be added to the fluid, with the intention that it will penetrate into the newly-created fracture network to hold these fractures open after the fluid is allowed to flow back out of the well.

Ideally high-volume, multi-stage hydraulic fracturing will create a large, open, fracture network through which hydrocarbons can flow to the well. The breaking of the rock releases elastic strain energy and so radiates seismic waves, which can be detected and used to study the fracturing process, as described in section 5.1.2. The mechanical processes involved in the creation of the hydraulic fracture can be analysed using the Mohr circle (see Figure 5.1). When all of the principal stress components σ_i, with $\sigma_1 > \sigma_2 > \sigma_3$, are positive (*i.e.* compressive), shear failure may occur on a pre-existing plane of some orientation α if the shear stress τ resolved onto that plane exceeds some critical value $\tau_c = \tau_0 + \mu\sigma$ — the Navier-Coulomb criterion — where σ is the normal stress, τ_0 is the cohesion and μ the coefficient of internal friction (Scholz, 2002). A fluid injection which increases pore pressure by an amount p can therefore induce shear failure by lowering the effective stress $\sigma_i \rightarrow \sigma_i - p$ and thus shifting the Mohr circle to the left such that it intersects the failure envelope.

From the lower part of Figure 5.1 we can also see that the pore pressure perturbation caused by the fluid injection must reduce the minimum principal stress to equal the tensile strength of the rock if tensile failure is to occur — although a smaller deviatoric stresses, $\sigma_1 - \sigma_3$, is also required. In this case, $\alpha = 0$ and the fracture opens in the σ_3 direction, and so we would expect a tensile hydraulic fracture to propagate along the maximum principal stress direction. The general failure envelope shown in Figure 5.1, which includes tensile failure, is described by the modified Griffith criterion (Scholz, 2002).

Although the possible failure modes that can occur during hydraulic fracturing are well understood, the actual mechanisms by which the rock breaks during and after a fluid injection are relatively unknown. This information is of great interest to the operator

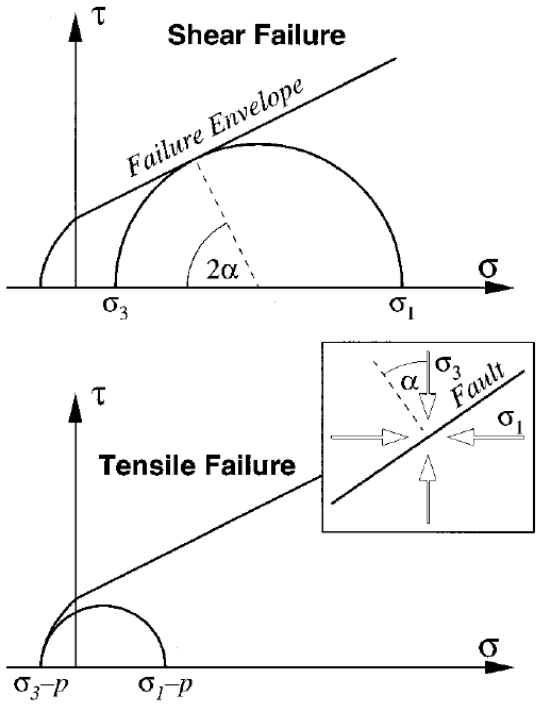

Figure 5.1: Mohr circle representation of the conditions under which a crack will fail in a shear or tensile mode. σ_1 and σ_3 are respectively the maximum and minimum stresses, τ is the shear stress acting across a fault plane whose normal is oriented at an angle α from the minimum stress direction. p is the pore pressure perturbation, perhaps resulting from fluid injection during hydraulic fracturing. (Reproduced from Julian *et al.*, 1998, with kind permission of John Wiley and Sons).

who, amongst other things, would like to use constraints from the observed microseismicity — typically event locations — to build a fracture model which can be combined with other geological information to forecast production from a particular well. It would therefore be useful if additional information, such as the failure mechanisms of microseismic events, could also be routinely determined; this chapter investigates whether microseismic waveform data can be used for this purpose.

5.1.2 Microseismic monitoring approaches

Microearthquakes are, by definition, small, and the seismic signals that they generate are often below the noise level of instruments deployed at the surface. Two approaches

have commonly been adopted to boost signal to noise ratios of microseisms: either we can place the receivers in a low noise environment closer to the events by deploying them in a borehole proximal to the region of interest, or we can stack signals recorded on a dense surface array. The pros and cons of either approach are hotly debated at industry conferences (e.g. Baig and Urbancic, 2012; Thornton and Duncan, 2012); we do not intend to enter into this debate here, but merely to give a general introduction to the two end-member monitoring strategies.

Passive seismic monitoring using surface arrays developed from the field of active source seismology, and so typically only uses information from the P-wave recorded on single component geophones. Events are located by computing the semblance for each hypothetical source position and origin time within some search volume, by stacking the surface records after they have been corrected for the P-wave travel time from that source position to each receiver. For isotropic sources, such as perforation shots, the hypocentral coordinates can then be inferred from maxima in the semblance function (Chambers *et al.*, 2010). For a general source, the semblance calculation will be contaminated by the seismic radiation pattern, complicating interpretation. This problem can be avoided by incorporating the moment tensor into the stack, efficient methods for which have recently been developed by Chambers *et al.* (2013). Computational efficiency is an important consideration for surface microseismic techniques because of the great number of image points that must be explored, and the large number of receivers — typically more than 1000 — in each dataset, although the high degree of automation that can be achieved is advantageous where real-time monitoring is required. Generally speaking, surface monitoring provides more accurate lateral event locations than can be obtained using downhole arrays, however depths are relatively uncertain and trade off with origin time because information from only one seismic phase is used (Eisner *et al.*, 2010; Chambers *et al.*, 2010). Magnitudes of events monitored from the surface can be inferred from the stack amplitude at the chosen source point. However, it is not clear how magnitudes determined in this way compare to those calculated with conventional waveform processing techniques because monitoring is seldom carried out using both surface and downhole arrays, and arrivals are rarely visible

in surface data except in exceptional circumstances (see Chapter 6). Our focus here is on using data recorded by downhole arrays, because to perform waveform inversion we require that the seismic signal is perceptible in unstacked records.

Borehole seismic monitoring uses retrievable or permanent arrays of three component geophones deployed in observation wells to record induced microearthquakes. By placing instruments close to the microseismic sources, both laterally and in depth, and away from surface noise, high fidelity seismograms can be recorded even for events as small as $M_w = -3$ (e.g. Baig and Urbancic, 2010a). Event locations can then be determined by a number of standard techniques (see, for example Maxwell *et al.*, 2010). Pumping of a typical hydraulic fracturing stage may last for a few hours, and so temporary downhole arrays are often used to monitor only the seismicity that occurs *during* the injection. Strings of instruments are lowered into an adjacent well, clamped to the casing mechanically or electromagnetically, and retrieved upon completion of the fracturing stages. For longer term reservoir monitoring, instrument pods are cemented into the well. Typical downhole arrays, whether temporary or permanent, might contain ~ 10 instruments and have a total length of at least 100 m, and are generally deployed at depths that are as close as possible to the stimulated interval.

Passive seismic monitoring in boreholes poses certain technical challenges not encountered in the operation of surface arrays. Firstly, receiver positions are not necessarily known accurately. "Vertical" wells may depart by as much as 5° from the upright, causing significant errors in the assumed geophone locations at depth if a borehole deviation survey is not carried out before array installation (Bulant *et al.*, 2007). Secondly, the orientations of receivers in the well are not known. For retrievable arrays, instrument orientation must be determined using particle motions observed from sources with "known" locations and origin time such as perforation shots. For permanent arrays cemented into the borehole, a radioactive bead can be placed in each instrument pod, allowing geophone alignment to be inferred from a gamma ray log (Nolen-Hoeksema and Ruff, 2001). Although these issues add some complexity to the processing of microseismic data, they can be addressed, and so in the following we will assume that receiver locations and orientations are known.

Other potential difficulties faced during downhole monitoring include time synchronisation of the receivers, coupling of instruments to the borehole and noise generated by resonances of the instrument string, although much progress has been made in improving tool design to reduce these problems (Wuestefeld *et al.*, 2013). High-quality data can therefore now be routinely obtained during downhole microseismic monitoring, allowing waveform modelling and inversion techniques to be applied to the problem of characterizing microseismic sources.

5.1.3 Moment tensor inversion of borehole-monitored microearthquakes

Downhole monitoring is often restricted to a single array because drilling is expensive, typically costing $4 million per well (Stevens, 2012). In the case of monitoring using a single well, particle motion information must be used in addition to body wave travel times to constrain hypocentral positions (e.g. Jones *et al.*, 2010). When the source and receivers are confined to one plane, as is the situation if monitoring using a single vertical array, it is not possible to resolve all elements of the moment tensor from P and S-wave amplitudes (Nolen-Hoeksema and Ruff, 2001; Vavrycuk, 2007). As a consequence, most downhole microseismic analyses are restricted to determining event locations and magnitudes

When the source and all receivers are coplanar, far-field P- and S-wave amplitudes are independent of the force dipole perpendicular to this plane, and so this part of the moment tensor cannot be resolved (Vavrycuk, 2007). One strategy for avoiding this problem, suggested by Eaton (2009) and Vera Rodriguez *et al.* (2011), is to place geophones in both the vertical and horizontal legs of a deviated well. However, such an approach does not yet appear to have been adopted widely, and so other solutions — particularly those that do not involve further drilling — are sought.

Recently, Song and Toksoz (2011) showed that all elements of the moment tensor could be reliably retrieved from waveform observations made using a single monitoring well, so long as the source–receiver distance is less than about 5 times the dominant shear wave

wavelength. As a consequence, waveform inversion as applied to borehole recordings of microseismic events has great potential for increasing the amount of information about the seismic source — and hence fracturing process — that can be extracted from these data. The waveform modelling and inversion techniques developed for GPS data earlier in this thesis can be adapted to accommodate borehole recordings of microseismic events.

The only real differences between these two problems are the frequency ranges of the observations, the epicentral distances, and the magnitude of events. The fact that we are now using data recorded at much smaller distances of less than 1 km does not invalidate the assumption of a point source because the events we are examining are also smaller, typically with $M_w < 0$. Of course, finite source effects are still present, but one can make progress with a point source representation. Because our forward modelling algorithm is stable at arbitrarily high frequency, our ability to perform waveform inversions for source parameters of microseismic events is only limited by whether it is appropriate to parameterize the medium as planar, isotropic, elastic layers, and whether such a crustal model is known. Typically, shale and tight gas fields are structurally simple over the microseismic source–receiver length scales, consisting of horizontal or shallowly dipping beds. Furthermore, we usually have a reasonable knowledge of seismic velocities and densities in the subsurface from vertical seismic profiles and well logs. Consequently, waveform inversion should be possible, as we investigate in the following.

Microseismic waveform data can be incorporated into our source inversion algorithm with minimal modification. For this purpose, we have defined a microseismic data slice, `MS`. Bandpass filter corner frequencies for this slice must be determined on a dataset by dataset basis. Some minor book-keeping changes were made to accommodate, for example, microseismic datasets expressed in a local Cartesian, rather than geographical, coordinate system. The forward modelling code was also changed slightly, because for borehole recordings propagator matrices must be recalculated for each receiver depth. The calculation is therefore slightly more computationally expensive in comparison to the usual situation when all receivers are at the surface. However, it is still trivial to parallelize

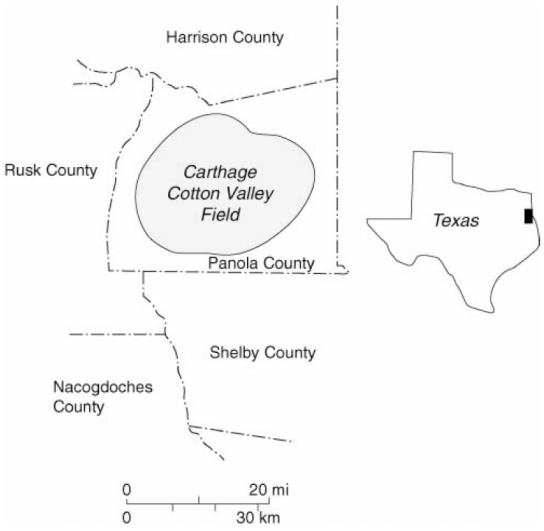

Figure 5.2: The location of the Carthage Cotton Valley hydrocarbon field (reproduced from Rutledge and Phillips, 2003, with kind permission of the Society of Exploration Geophysicists).

the calculation of the seismic spectra, and so routine inversion of microseismic waveforms is practical using the techniques developed in this thesis.

5.2 Case study: Cotton Valley

We use a microseismic dataset recorded in two monitoring wells during a hydraulic stimulation of a tight gas reservoir at Carthage Cotton Valley, Texas, USA, to investigate the application of our source inversion algorithm to this type of waveform data. This dataset was acquired in 1997 during a US government funded field experiment comparing the effectiveness of two different hydraulic fracturing approaches, one using a gel–proppant mixture and the other, more conventionally, using water and lower concentrations of proppant (Rutledge and Phillips, 2003). The exact location of the experiment is not publicly known, but the geographical setting is shown in Figure 5.2.

The Cotton Valley microseismic data are publicly available, and so have been well studied as a result. Rutledge and Phillips (2003) determined precise locations for 696 induced microearthquakes out of a total of 1122 detected, and calculated composite focal mechanisms for clusters of events, which were interpreted as showing the interaction of newly created fractures with isolated natural fractures (Rutledge *et al.*, 2004). Dinske *et al.* (2009) used diffusion models to interpret the spatial and temporal evolution of seismicity, while Wuestefeld *et al.* (2011) measured shear wave splitting to infer that temporal changes in fracture orientation and density occurred during the Cotton Valley treatment.

Waveform inversion for moment tensors has not previously been attempted using this dataset, although the availability of two monitoring wells did allow Šilený *et al.* (2009) to invert body wave amplitudes to obtain moment tensors for the largest 24 events; they found significant non double couple components for all of these microearthquakes. Such a comprehensive analysis is beyond the scope of the present work, however the results of Šilený *et al.* (2009) provide a useful check on the reasonableness of our waveform inversion results.

5.2.1 Waveform data and forward modelling

A total of six hydraulic fracturing stages were completed at Cotton Valley: three in well 21-10 followed by three in well 21-09, which was also used to monitor the earlier injection stages (see Figure 5.3). A third well (22-09) monitored both treatments. Here, we focus on events recorded during the second hydraulic fracturing stage in well 21-10. The microseismic cloud determined by Rutledge *et al.* (2004) contains 888 events with $-2.38 < M_L < -0.68$, and is interpreted as a classical hydraulic fracture, propagating along the inferred direction of maximum horizontal stress in a depth range confined to the treatment interval. In the following we refer to the monitoring wells 21-09 and 22-09 as well 1 and well 2 respectively, and well 21-10 simply as the treatment well (see also Figure 5.3.

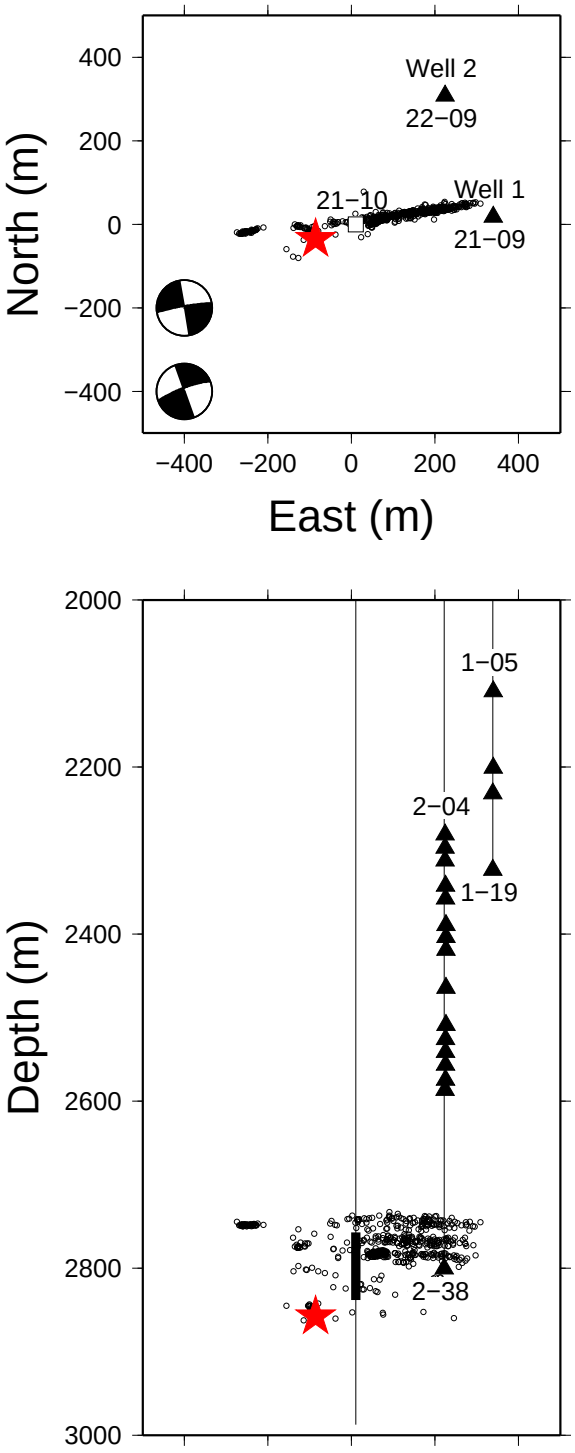

Figure 5.3: ***Top:*** Map showing the locations of the treatment well (square) and monitoring wells (triangles) at Cotton Valley. The beachballs are the composite focal mechanisms determined by Rutledge and Phillips (2003). ***Bottom:*** Cross-section showing the depth extent of the treatment and monitoring wells. Geophones are denoted by the triangles, and the treatment interval by the rectangle. Hypocentral locations determined by Rutledge and Phillips (2003) for events occurring during the second stage of stimulation in well 21-10 are indicated by the circles. The largest event, data from which are used in our waveform inversion, is denoted by the star.

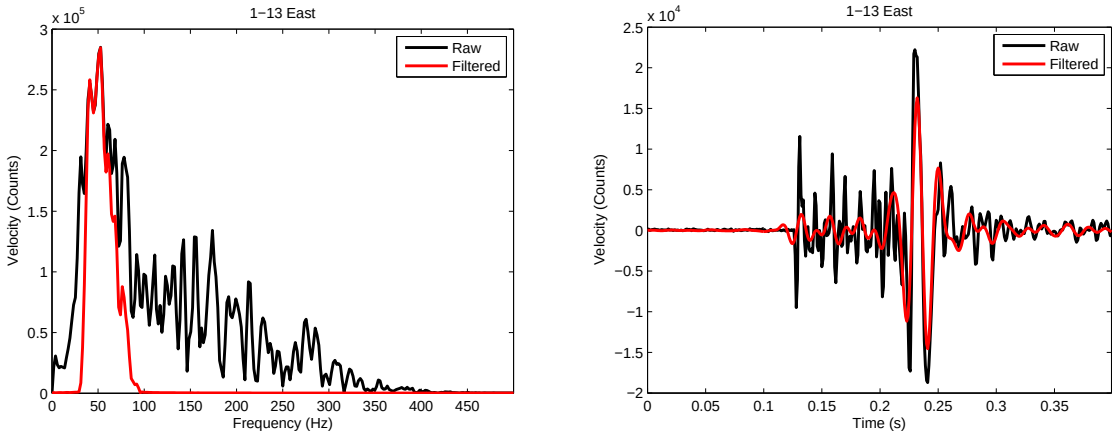

Figure 5.4: East component raw (black) and filtered (red) velocity spectra (left panel) and corresponding seismograms (right panel) recorded during the largest event at Cotton Valley by geophone 1-13.

A 705 m long geophone string containing 48 instruments at 15 m intervals was cemented into each monitoring well. Each instrument pod contained a triaxial geophone sensitive to ground velocity, with natural frequency 30 Hz, recording at a sampling frequency of 1000 Hz. The orientation of each instrument was determined from the back-azimuth of a number of check shots. During the stimulation only four geophone pods were operational in well 1, at depths between 2.109 and 2.323 km, and 16 in well 2 in the depth interval 2.281 km to 2.800 km.

Example raw and filtered velocity spectra and corresponding seismograms recorded during the largest event in our dataset are shown in Figure 5.4. A cosine high pass filter with corner frequencies of 30 and 40 Hz was applied in consideration of the natural frequency of the instrument, along with a cosine low pass filter with corner frequencies of 50 and 100 Hz. We use these filter parameters in the inversion of real and synthetic data that follow. The instrument response function is flat above 30 Hz, and so we only need to take account of a gain of $4.5216878 \times 10^{-11}$ m/s/count to convert the raw measurements into ground velocity.

Rutledge and Phillips (2003) noted that the ensemble of microearthquakes at Cotton Valley can be separated into two clusters based on waveform similarity. They constructed

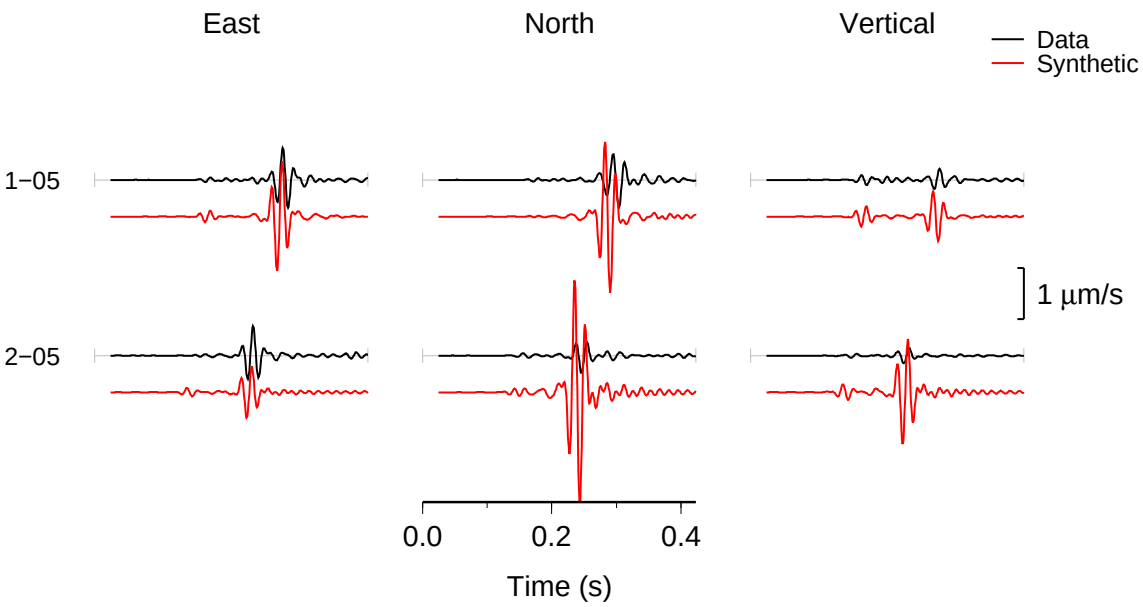

Figure 5.5: Waveform data and synthetics for the largest microearthquake in our Cotton Valley dataset, computed at receivers 1-05 and 2-05 using the right-lateral composite focal mechanism determined by Rutledge *et al.* (2004). The crustal model used is given in Table 5.1.

two composite focal mechanisms (see Figure 5.3) — one for each of these populations — using P-wave first motions from all of the events in a cluster. Interpreting the event cloud as a fracture plane, these focal mechanisms imply that failure occurred via both right-lateral and left-lateral strike-slip (Rutledge and Phillips, 2003).

Example synthetic seismograms computed using the right-lateral source are shown in Figure 5.5. The location and magnitude used in this calculation correspond to those determined by Rutledge and Phillips (2003) for the largest event in our dataset, observed waveforms from which are also plotted. The crustal model used here and throughout the following is based on the velocity model of Rutledge and Phillips (2003), supplemented with density information from well logs averaged over the depth interval of each layer (see Table 5.1). The fact that point-source synthetics, computed assuming a very simple structural model, show qualitative agreement to the data suggests that waveform inversion should be possible within our forward modelling framework.

Thickness (km)	v_{P} (km/s)	v_{S} (km/s)	ρ (kg/m^3)
2.497	4.841	2.934	2.57
0.069	5.279	2.924	2.63
∞	4.968	3.139	2.59

Table 5.1: Crustal model for Cotton Valley used in this study.

5.2.2 Waveform inversion

Song and Toksoz (2011) used inversions of synthetic microseismic waveforms to show that all elements of the moment tensor can be reliably recovered from data recorded by a single borehole array, provided that the monitoring well is located less than about 5 times the shear wave wavelength, λ_S, away from the source. However, they could not test the validity of this conclusion using real data, because they only had one monitoring well, located at a source–receiver distance of $15\lambda_S$, in their study region. The availability of microseismic waveform data from two monitoring wells at Cotton Valley does allow us to investigate this question. Do waveform inversions using data from either well alone produce comparable results, and do these results agree with those obtained using the whole dataset? Furthermore, the fact that moment tensor inversion can be performed using body wave amplitudes observed at two monitoring wells also allows us to use results determined in this way by Šilený *et al.* (2009) as an independent check on the reasonableness of our solutions.

To maximise the signal to noise ratio, we use seismograms from the largest event in our dataset for this test. Because this event was related to fluid injection, we do not require that the trace of the moment tensor is zero in our inversion, thus allowing for the possibility that the source contained some isotropic component. Initially, we also assume that the location and origin time determined by Rutledge and Phillips (2003) for this event are "correct", and so solve only the linear inverse problem for the best moment tensor at these hypocentral coordinates. Here, wells 1 and 2 are at a distance of $7.15\,\lambda_S$ and $7.70\,\lambda_S$ from the event respectively, assuming a dominant frequency of 50 Hz

	Two wells	Well 1 only	Well 2 only	Two wells
Location:	F	F	F	
Origin time	13:27:07.93	13:27:07.93	13:27:07.93	13:27:07.93
Easting (m)	-86.22	-86.22	-86.22	-69.00
Northing (m)	-34.99	-34.99	-34.99	-54.30
Depth (km)	2.858	2.858	2.858	2.864
Moment tensor:				
M_{rr}	0.0533	0.4363	0.0063	0.0536
$M_{\theta\theta}$	0.0926	2.8469	0.0054	0.1301
$M_{\phi\phi}$	-0.0366	0.5866	-0.1057	0.0419
$M_{r\theta}$	-0.0227	0.1005	-0.0533	-0.0658
$M_{r\phi}$	-0.0567	-0.4547	-0.0520	-0.1297
$M_{\theta\phi}$	-0.0082	0.1758	-0.0593	0.0392
Relative RMS:				
	0.85	0.87	0.81	0.70
Condition number:				
	64	6408	1877	64
				

Table 5.2: Results of waveform inversions for the largest event at Cotton Valley, using all available data, and data from each observation well individually. 'F' indicates that the location and origin time were fixed to the values determined by Rutledge and Phillips (2003) in the inversion. The moment tensors are expressed in units of 10^8 Nm.

and $v_s = 3.0\,\mathrm{km/s}$. Based on the results of Song and Toksoz (2011), this event is therefore located on the threshold of the domain that can be inverted using data from a single well. The results of our inversion using data from both wells, and wells 1 and 2 individually are shown in Table 5.2. Clearly, these solutions are inconsistent with each other.

The inverse problem of determining the location and moment tensor of a microseismic event from waveform data is fundamentally different to that of determining the hypocentral coordinates of the same event from body wave arrival times — the data are different, and our model parameterization, data selection and processing approached may be inconsistent with those used by Rutledge and Phillips (2003). Consequently, it is not reasonable to assume here that the hypocentre determined by Rutledge and Phillips (2003) will correspond to the optimal event location for the waveform inversion: we should simultaneously solve for the centroid location as well as the moment tensor. The result of such an in-

version, determined by an iterative least squares minimisation of waveform misfit with step-length damping, are included in Table 5.2. We only attempt iterative inversion using the combined dataset from both wells, as experience suggests that the inverse problem including centroid location will be unstable when we use only data recorded from a single azimuthal direction.

Allowing the centroid location to vary leads to a solution with a lower misfit value than that obtained from the same data when the hypocentre was fixed at the location of Rutledge and Phillips (2003). A comparison of data and synthetics computed for this new solution is shown in Figure 5.6. The waveform fit is particularly good in the horizontal components at stations 2-04 to 2-11, however there are significant amplitude and phase mismatches at other stations, and the vertical component data are poorly fitted at all of the receivers. Some of this misfit arises because we have neglected anisotropy in our forward modelling: it is clear that there is shear wave splitting in the data, which should, in future, be accounted for.

Šilený *et al.* (2009) expressed the moment tensors that they calculated for the Cotton Valley dataset in terms of their decompositions into isotropic, compensated linear vector dipole (CLVD), and double couple, components. The results of our two waveform inversions using data from both wells — assuming a fixed and variable hypocentral location — are compared to the corresponding solution of Šilený *et al.* (2009) in Table 5.3. It is interesting to note that, in addition to significantly improving the misfit, allowing the hypocentral location to vary in our inversion also removes the CLVD component of the source, implying that this event occurred with a mechanism of pure shear plus explosion.

5.3 Single-well monitoring for moment tensor retrieval

The inversion results just presented show that it is not possible to retrieve reliable moment tensors from the Cotton Valley waveform dataset when only one monitoring well is used: the solution depends on the data subset chosen for the inversion. This result is surprising if

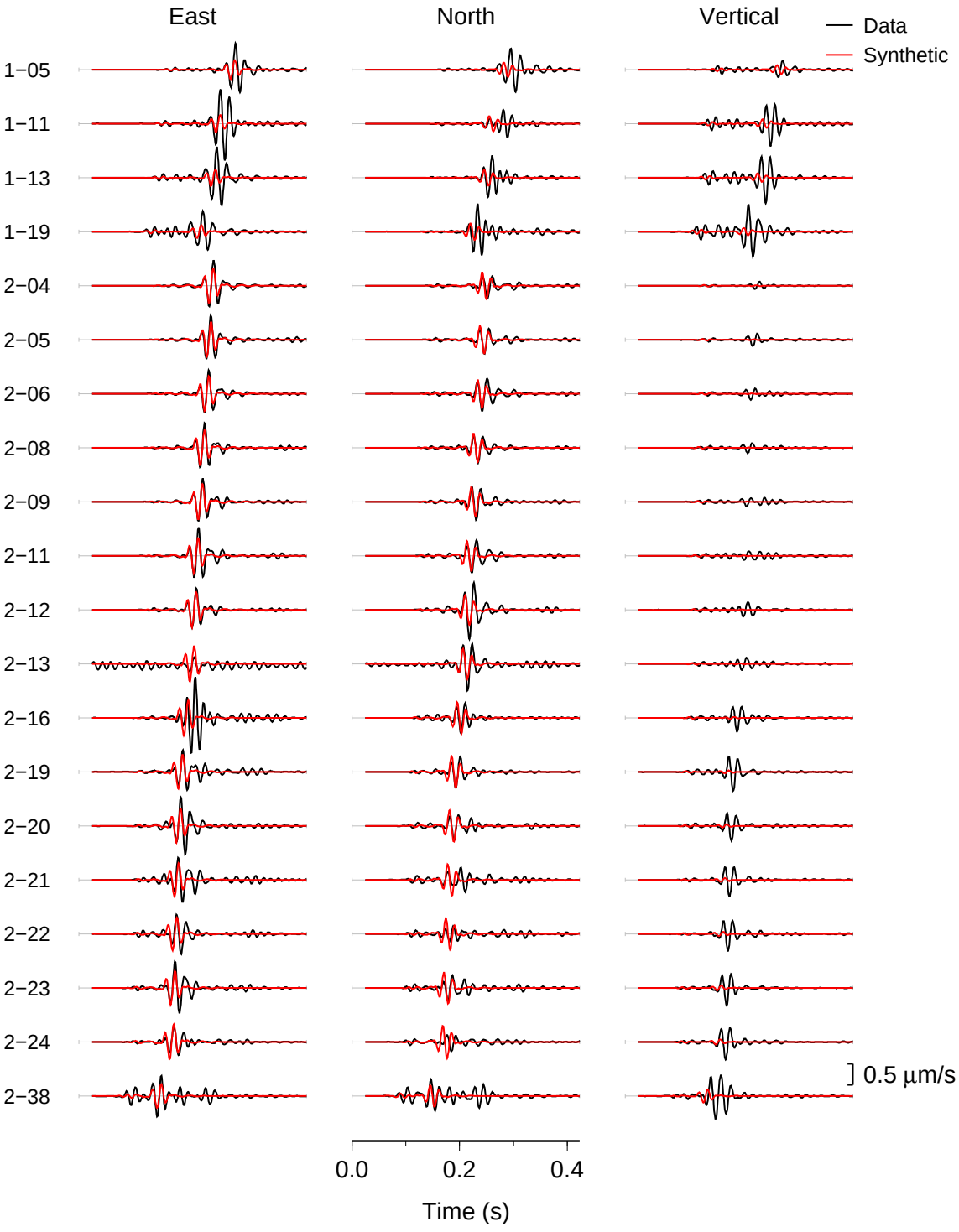

Figure 5.6: Microseismic waveform data (black traces) recorded by two downhole arrays for the largest event at Cotton Valley, and used in our source inversions. Synthetic seismograms (red traces), computed using the solution obtained when the centroid location was allowed to vary are also shown. The numbers to the left of the east-component traces are the station names.

	c^{ISO}	c^{CLVD}	c^{DC}
Fixed location	34.4	42.3	23.3
Variable location	32.3	1.2	66.4
Šilený *et al.* (2009)	30.2	53.7	16.1

Table 5.3: Moment tensors determined for the largest event in our Cotton Valley dataset by waveform inversion, assuming a fixed and variable source location, compared to the result of Šilený *et al.* (2009), which was determined by inversion of P and S wave amplitudes. Following Šilený *et al.* (2009) the moment tensors are decomposed into percentage isotropic (c^{ISO}), compensated linear vector (c^{CLVD}), and double couple (c^{DC}) components.

the conclusion of Song and Toksoz (2011) — that moment tensor inversion using waveforms from a single well is possible if the source–receiver distance is less than about 5 times the dominant shear wave wavelength — is taken at face value. The ability to calculate moment tensors using data from a single monitoring well has profound implications for downhole microseismic monitoring projects, as if it were possible much more information about the fracturing process could be obtained at much less expense. It is therefore important to try and understand why our results do not reflect those of Song and Toksoz (2011), *i.e* to investigate what controls the resolution of moment tensor inversions when waveform data from a single monitoring well are used.

Song and Toksoz (2011) used the condition number of $\mathbf{A}^{\mathrm{T}}\mathbf{A}$ to assess whether a synthetic dataset, computed using a particular monitoring geometry, could resolve all elements of the moment tensor. The condition number can be variously defined (see *e.g.* Tarantola, 2005), and Song and Toksoz (2011) do not explicitly state how they compute the condition number in their study, here we use

$$\mathrm{cond}(\mathbf{A}^{\mathrm{T}}\mathbf{A}) = \frac{\max|\lambda_i(\mathbf{A}^{\mathrm{T}}\mathbf{A})|}{\min|\lambda_i(\mathbf{A}^{\mathrm{T}}\mathbf{A})|} \tag{5.1}$$

where λ_i are the eigenvalues of $\mathbf{A}^{\mathrm{T}}\mathbf{A}$. The condition number essentially tells us the ratio of the extremal axis lengths of the uncertainty ellipsoid in model space, and so can be used as a proxy for the resolving power of a dataset (Tarantola, 2005).

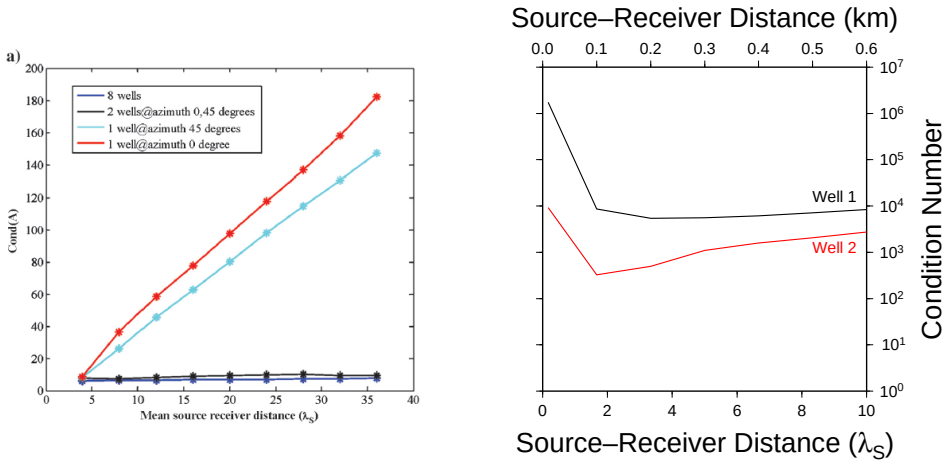

Figure 5.7: The relationship between condition number and source–receiver distance as determined by Song and Toksoz (2011) (left) and in this study (right). The distribution of receivers in wells 1 and 2 used in our synthetic tests corresponds to that of the two monitoring arrays at Cotton Valley.

Song and Toksoz (2011) showed that the conditioning of inversions of single well data becomes worse as the source–receiver distance increases (see Figure 5.7), without really explaining why this behaviour occurs. Their results suggest that our waveform inversions which use only one monitoring well are expected to yield condition numbers of around 20. The actual values that we obtain for inversions of data from well 1 and 2 individually are 6408 and 1877 respectively. Clearly, there is disagreement between the theoretical and observed condition numbers, and inversions of data from two monitoring wells can yield quite different values even though they are at a similar epicentral distance.

The condition number depends only on the excitation kernels, which are themselves a function of the earth model and receiver locations. Our parameterization of the crust as plane, elastic, isotropic layers is identical to that used by Song and Toksoz (2011). However, our structural model is much simpler, having only 3 layers to their 9, which may account for some of the disagreement between the expected and observed values of the condition number. The presence of additional reflected and refracted phases in the wave-train will provide a more complete sampling of the source radiation pattern, and so lower condition numbers may be obtained for more complicated earth models, although

the significance of this effect also depends on the location of receivers relative to the source and layer boundaries. We also note that the frequency range of the calculations performed by Song and Toksoz (2011) ($200 < f < 900$ Hz) is somewhat higher than that used here ($30 < f < 100$ Hz). Nevertheless, it is unlikely that this effect alone explains the discrepancy, because the conditioning of the inversion also depends on the monitoring geometry, which also differs significantly between the two studies.

Intuitively, we would expect better constraint on the moment tensor if we sample the seismic radiation pattern more completely. The azimuth of the monitoring well from the source should not therefore significantly affect the conditioning of the inversion, in agreement with the results of Song and Toksoz (2011). Rather, the aperture of the monitoring network should be critical in determining the condition number. Song and Toksoz (2011) assumed that the bottom of their monitoring array was 2 m above the event. In this case, the network aperture — the angle subtended by the monitoring array at the source — decreases as a function of horizontal distance between the source and the well. Thus the source–receiver distance dependence of the condition number found by Song and Toksoz (2011) was likely just a network aperture effect. For our Cotton Valley dataset, the bottom receiver in well 1 is 537 m above the event. As a consequence, the array will be foreshortened as it moves radially closer to the source: beyond some point the aperture will start decreasing. Does this foreshortening manifest itself as an increase in condition number? We can test this hypothesis using inversions of synthetic data.

We performed inversions of a synthetic single monitoring well dataset, calculated for source–receiver distances between 0.01 and 0.6 km, and computed the condition numbers corresponding to each inversion. This range essentially spans the source–receiver distances seen for the events plotted in Figure 5.3, and so this experiment should tell us which of the Cotton Valley events might be located such that inversion of single well data is possible. We used the source determined in our inversion of data from both wells to compute the synthetic dataset used in this test, although it should be noted that the condition number is independent of the particular moment tensor chosen. Results for single-well inversions

which mimic the receiver distribution of the two wells at Cotton Valley are shown in Figure 5.7.

The increase in condition number at epicentral distances less than 0.2 km for well 1, and 0.1 km for well 2, indicates that the arrays are being foreshortened. Because the vertical offset between the event and the deepest receiver in well 2 is smaller than that for well 1, well 2 can move closer to the well before its aperture begins to shrink. At all source–receiver offsets, we see that well 2 performs better than well 1: the fact that it has a longer array of working geophones and its lowermost receiver is closer to the event depth combine to consistently give well 2 a wider aperture than well 1.

5.4 Discussion

The inversions of real and synthetic microseismic data presented in this chapter suggest that waveform inversion is a promising technique for determining moment tensors of microearthquakes monitored using downhole arrays. However, they also serve to illustrate a number of challenges to using data obtained from a single observation well for source inversions.

Firstly, we saw that our inversions of data from two monitoring wells required that we simultaneously solve for the centroid location and moment tensor. Where moment tensor inversions of microseismic data have been carried out previously, it has been very common to fix the event location to that determined by conventional travel time and particle motion methods (e.g. Bleakly *et al.*, 2007; Šilený *et al.*, 2009; Baig and Urbancic, 2010b; Vera Rodriguez *et al.*, 2011), or to compute event locations in an anisotropic velocity model but then invert amplitudes assuming a homogeneous medium (e.g. Kuehn *et al.*, 2013). The assumed event location may not correspond to the actual best fitting location within the parameterization of the inverse problem, and so the recovered moment tensor will be sub-optimal. Because a mislocation of a pure shear source may introduce spurious non double couple components into the recovered moment tensor, we can hypothesize that

this effect accounts for some of the difference between our moment tensor for the largest Cotton Valley event and that obtained by Šilený *et al.* (2009) (see Table 5.3).

The need for using consistent modelling strategies when performing inversions that take the result of some other calculation as input has been emphasised by Valentine and Trampert (2012), and so event relocation should form part of the microseismic moment tensor determination process. We did not attempt an iterative inversion using seismograms from one well only, as experience with other types of waveform data suggested that such an inversion would be unstable. The most effective way of obtaining the location as well as the moment tensor may therefore be to perform a set of inversions fixed on a grid of points distributed in space around the hypocentre. In fact, such an approach was taken by Song and Toksoz (2011), and is also beneficial from the standpoint of quantifying location uncertainties in a realistic manner (see Chapter 6).

Secondly, the availability of data from two monitoring wells allowed us to check the consistency, or — as it transpired — the lack thereof, of moment tensors recovered by inverting data from both wells, and from each well individually. The disagreement between these results was in some sense surprising, given previous work which implied that the inversion of single well data should be well conditioned at these epicentral distances (Song and Toksoz, 2011), and prompted us to investigate controls on the conditioning of the inverse problem.

The results of our condition number experiment show qualitative agreement with those of Song and Toksoz (2011) down to $5\,\lambda_S$— the smallest offset investigated in the earlier study — although the values that we obtain are systematically larger because of earth model and monitoring geometry effects. The distribution of event locations shown in Figure 5.3 shows that many events at Cotton Valley occurred at epicentral distances smaller than $5\,\lambda_S$. We extended our condition number study to include these distances. This undertaking confirmed our hypothesis that conditioning of the inverse problem deteriorates when the monitoring array is close to, but shallower than, an event because the aperture of the network gets foreshortened. The corollary is that when the receiver array spans

the source depth, the aperture increases as the monitoring well is moved closer to the source. To our knowledge, this foreshortening effect has not been considered previously in designing microseismic monitoring networks that permit moment tensor inversion from waveforms recorded in a single monitoring well. Minimising the distance between a monitoring well and the event locations expected in a particular hydraulic fracturing stage may be beneficial for event detection, but could compromise our ability to determine moment tensors from the recorded waveforms.

The condition number is actually quite a simplistic way to assess model resolution, because it only tells us the ratio between the uncertainties on the best- and worst-constrained model parameters. It is therefore instructive to examine the eigenvector corresponding to the minimum eigenvalue (in the absolute sense) to see which components of the moment tensor are least well resolved; for example, for the inversion of data from well 2 we have $(M_{rr}, M_{\theta\theta}, M_{\phi\phi}, M_{r\theta}, M_{r\phi}, M_{\theta\phi}) = (-0.02, 0.99, -0.02, 0.00, 0.02, 0.13)$. The data therefore do not resolve the north–south orientated force dipole. Because the well is almost due east of the event, we can immediately see that this component approximates the force dipole normal to the source–receiver plane, and waveform inversion suffers the same problem as amplitude inversion. In some ways, this result is not surprising. A least squares inversion of waveform data will try to fit the largest amplitude phases — the direct P and S waves — over the smaller, later arrivals, which may not even be visible in a noisy dataset. As a consequence, our "waveform" inversion is not much more than an inversion of body wave amplitudes — albeit an automated version thereof — and therefore has similar limitations on resolution of the model parameters. This situation might be improved by modifying the inversion scheme to place more weight on the indirect arrivals, and future work should be directed towards this end.

Summary

In this chapter, we have shown that microseismic waveform data recorded in boreholes can be inverted for the moment tensor of a microearthquake by a minor modification of

the general waveform inversion algorithm developed earlier in this thesis. This information is useful for understanding the physics of hydraulic fracturing, and provides a useful constraint for reservoir modellers interested in how fracture networks affect hydrocarbon drainage. Preliminary inversions of real data suggest that donwhole monitoring using an array of instruments in just one well cannot be used to recover reliable moment tensor solutions, at least for the receiver geometries deployed at Cotton Valley.

In some situations, hydraulic fracturing for shale gas has led to seismic events that are somewhat larger than microearthquakes, and that may be felt at the surface. In these cases of induced seismicity, we may use surface instruments for monitoring purposes, as we investigate in the following chapter.

Chapter 6

Hydraulic fracturing induced seismicity at Preese Hall, UK

On 1 April 2011, the British Geological Survey (BGS) detected a M_l 2.3 earthquake located ~ 2 km north-west of the first shale gas exploration well to be drilled in the UK, at Preese Hall near Blackpool. This event occurred shortly after the well had been hydraulically fractured. The coincidence of the fluid injection and seismicity in space and time suggested that the former may have caused the latter. This suspicion was added further credence when a M_l 1.5 event occurred on 27 May 2011 following another hydraulic fracturing stage; this event could be more accurately located to within ~ 0.5 km of the injection well thanks to the temporary deployment of a local seismic monitoring network by the BGS.

At the time, hydraulic fracturing was not perceived as an activity that might produce felt induced seismicity. As of 2012, in the US — where the vast majority of global shale gas development has occurred — only one earthquake was suspected, but not proven, to be caused by shale gas hydraulic fracturing, even though a total of 35,000 shale gas wells had been drilled and completed (NRC, 2012). Consequently, the anomalous seismic activity at Preese Hall prompted the operating company, Cuadrilla, to suspend activities, pending the findings of a series of studies that they commissioned to investigate the reservoir's

geomechanics and its relationship to the putative induced seismicity (de Pater and Baisch, 2011; de Pater and Pellicer, 2011; GMI, 2011; Eisner *et al.*, 2011). The UK government also imposed a temporary suspension of all shale gas hydraulic fracturing operations, which was lifted in December 2012 following a review of Cuadrilla's studies (Green *et al.*, 2012), public consultation (Department of Energy & Climate Change, 2012) and a general assessment of technical risks from shale gas hydraulic fracturing (The Royal Society, 2012).

Here, we aim to reanalyse the small waveform dataset recorded by the two local monitoring stations that were installed after the first anomalous event was detected by the BGS. In so doing we hope to provide the first independent check on some aspects of the studies commissioned by Cuadrilla, specifically the analysis of seismic data performed by Eisner *et al.* (2011). Although there has been some impartial critique of this work (e.g. Green *et al.*, 2012; RS, 2012), as yet no one has gone so far as to reanalyse the original data. In addition, we make some suggestions about how operations could have been more effectively monitored — an important consideration given that all future shale gas hydraulic stimulations in the UK will require a real-time traffic light monitoring system to mitigate the risk of induced seismicity [1].

6.1 Induced seismicity due to shale gas hydraulic fracturing

The increased attention that induced seismicity has received of late, both in general (e.g. NRC, 2012) and — following the events at Preese Hall — specifically in the context of shale gas hydraulic fracturing, has resulted in the identification of other potential examples of hydraulic fracturing induced seismicity. Holland (2011) described a sequence of 50, small, shallow, earthquakes which occurred in January 2011 within 3.5 km of a well that had been hydraulic fractured seven hours earlier in the Eola oil field, Oklahoma. The correspondence in space and time between well stimulation and the events, combined with the fact that the observed waveforms were distinct from those of tectonic earthquakes from that region, led Holland (2011) to conclude that the earthquakes were likely to be induced.

[1] https://www.gov.uk/government/news/written-ministerial-statement-by-edward-davey-exploration-for-shale-gas

However, large uncertainties in event locations, which result from the sparse monitoring network — the nearest seismic station being 35 km away — along with the occurrence of natural seismicity, mean that a tectonic origin could not be ruled out from the available data.

BCOGC (2012) found several instances of induced seismicity related to shale gas hydraulic fracturing in the Horn River Basin, British Columbia, Canada. Similarly to Preese Hall, anomalous seismic activity was first detected by regional seismic networks operated by Natural Resources Canada. 38 earthquakes bigger than M_l 2.2 were recorded between April 2009 and December 2011 in a region where no previous earthquakes were known. This included a M_l 3.8 event that occurred on 19 May 2011 which was felt by workers at the surface, and represents the largest known hydraulic fracturing induced earthquake that has occurred to date. Subsequently, dense surface monitoring networks were deployed at two localities, allowing accurate determination of microearthquake hypocentres, which clustered around injection intervals. Linear and planar trends in the event locations were interpreted as fault reactivation due to intersection of hydraulic fracturing stages with preexisting faults. Seismicity was also correlated temporally with injection: the regional network detected no events before, or after, the time period when hydraulic fracturing operations were being carried out.

The hydraulic fracturing of shale gas and other unconventional hydrocarbon reservoirs is generally considered to pose little risk of causing felt induced seismicity, because the total volume of fluid injected is small, and is usually balanced by later production of water and gas (NRC, 2012). This suggestion is demonstrated empirically by the handful of known or suspected hydraulic fracturing induced events relative to the tens of thousands of shale gas wells that have been completed. However, this lack of seismicity should be tempered by two observational biases: seismic monitoring is only carried out for a small fraction of shale gas hydraulic fracturing operations, and induced events may be misclassified as natural in localities where tectonic seismicity is common. Furthermore, the examples of induced seismicity from Blackpool and Canada also suggest that it is the interaction of

injected fluids with preexisting faults that controls the occurrence of induced seismicity during hydraulic fracturing.

That hydraulic fracturing is associated in many peoples' minds with induced earthquakes is likely because this issue is often conflated with the disposal of large volumes of wastewater — often produced from shale gas wells — by injection into deep aquifers. The large, positive pore pressure perturbations caused by wastewater disposal can, and do, cause moderate magnitude earthquakes. A notable example is the 2011 Prague, Oklahoma earthquake sequence, where three M_w 5.0–5.7 events occurred unexpectedly after 18 years of injection of wastewater produced from conventional oil fields (Keranen *et al.*, 2013). Seismicity related to disposal of hydraulic fracturing waste fluids is also suspected at Dallas–Fort Worth, Texas (Frohlich *et al.*, 2011) and in Arkansas (Horton, 2012). As for hydraulic fracturing induced events, direct attribution of seismicity to water disposal is made more difficult due to a lack of local seismic monitoring, especially in regions where natural earthquakes occur.

6.2 Shale gas in the UK

Although shale gas was first detected in the UK in a well drilled in 1875 into the Upper Jurassic Kimmeridge Clay at Netherfield, West Sussex, the potential for UK shale gas development was not recognised then, and has since been largely ignored (Selley, 2012). As recently as 2006, shale gas was not included in official mineral resource estimates, even in highly prospective areas like Lancashire (McEvoy *et al.*, 2006). It was not until 2008 and the 13$^{\text{th}}$ Round of Onshore Licensing that any licenses were awarded to companies specifically exploring for shale gas (Selley, 2012). The most prospective UK shale gas basins correspond to those that are thought to be source rocks for existing conventional hydrocarbon fields (see Figure 6.1), particularly the Lower Carboniferous Namurian black shales such as the Bowland Shale — currently being appraised in Lancashire by Cuadrilla — and Jurassic shales of the Weald and Wessex basins (Harvey and Gray, 2011).

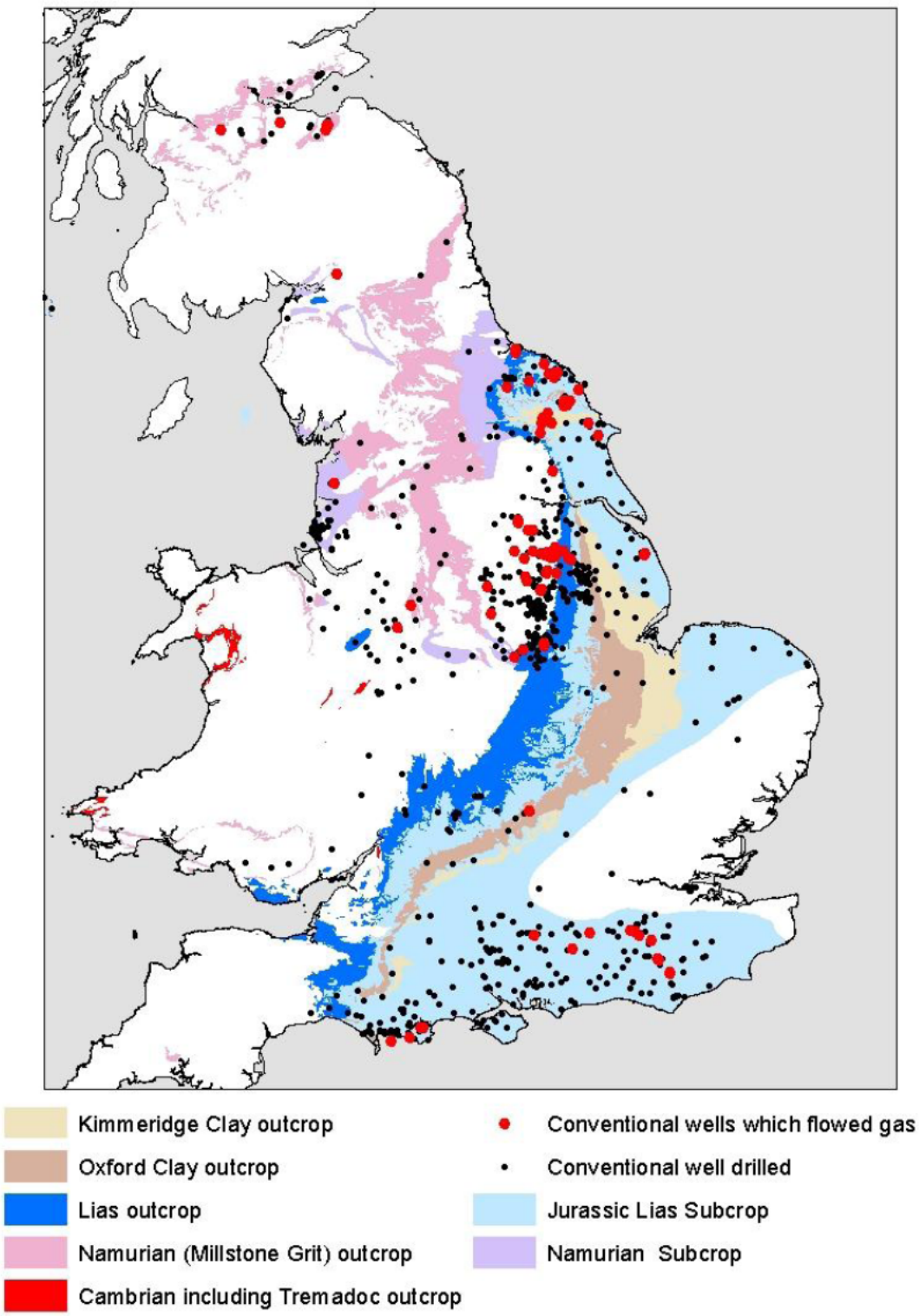

Figure 6.1: The geographical distribution of UK shale gas prospects (reproduced from Harvey and Gray, 2011, with kind permission of the Department of Energy and Climate Change).

	Total Resource ($10^9\,m^3$)	Recoverable Resource ($10^9\,m^3$)	
UK shale gas	2,750	570	EIA, 2011
		150	Harvey and Gray (2011)
Bowland Shale	5,670	1,130	www.cuadrillaresources.com
UK conventional gas	1,466		POST, 2013

Table 6.1: Estimates of the total shale gas in place, and technically recoverable shale gas resource for the UK and the Bowland basin. A recovery factor of 0.2 was assumed by EIA, 2011 and Harvey and Gray (2011).

A simple estimate of the UK's shale gas resource can be obtained by considering the total volume of prospective shale deposits and assuming a reasonable value for the amount of natural gas per unit volume of shale. Well cores and logs are therefore crucial for constraining depth extents and gas contents of shales. As Figure 6.1 shows, many wells have already been drilled in areas with shale gas potential. However, because they were drilled in pursuit of conventional hydrocarbons, these wells represent somewhat of a missed opportunity for shale gas exploration: the total depths of shale deposits were not established, gas contents of shales were not measured, and occurrences of shale gas may have been missed (Selley, 2012).

The lack of shale thickness information from wells, combined with the sparse coverage of seismic reflection survey lines, means that the depth extent of UK shale deposits is not well known. Furthermore, since no shale gas production has yet occurred, gas concentrations must be extrapolated from comparable US shale basins, which is potentially problematic because of the large degree of variability between different shale deposits (Harvey and Gray, 2011). As a consequence, estimates of technically recoverable UK shale gas resources are highly uncertain (see Table 6.1). In fact, these estimates are dwarfed by Cuadrilla's own calculation for *just* the Bowland Shale, which incorporates confidential information about shale thickness and gas content from a number of wells that they have drilled and flow tested.

When viewed in light of current UK natural gas consumption at $77 \times 10^9\,m^3$ per year

(POST, 2013), the potential impact of domestic shale gas production therefore ranges from minimal to significant. A revised shale gas resource estimate is expected from the BGS in the summer of 2013, although the absence of any production data means that this number will still be subject to considerable uncertainty. Ultimately, the results of Cuadrilla's next appraisal well, due to be hydraulically fractured and flow tested in 2014, may determine the future of shale gas development in the UK.

6.2.1 Operations at Preese Hall

On 16 August 2010, a well was "spudded" at Preese Hall farm, Weeton near Blackpool, UK (see Figure6.2). This well was drilled to a depth of 2.8 km by Cuadrilla, as part of their shale gas exploration activities within the Bowland Basin of Lancashire. In 2011, Cuadrilla drilled two more vertical wells to similar depths, at Becconsall, Banks and Grange Hill, Singleton. A fourth well, at Anna's Road, Westby, is currently being drilled; Cuadrilla intend to deviate this well and hydraulically fracture the horizontal leg[2].

The Preese Hall well was the first in the UK to be hydraulically fractured for shale gas, although over 200 hydraulic fracturing treatments have already been performed (P. Styles, pers. comm.): for conventional and tight hydrocarbon reservoirs (e.g. Wytch Farm, Dorset; RS, 2012), enhanced geothermal systems (e.g. Rosemanowes hot dry rock project, Cornwall; Parker, 1999), and coal bed methane. The treatment strategy employed at Preese Hall was fairly typical of vertical shale gas wells. A "plug and perf" completion was used whereby each stage was isolated from earlier ones via a plug, before perforating the cement casing of the well in a $\sim$ 8 m interval above the plug, to allow communication between the shale formation and well (de Pater and Pellicer, 2011). A "minifrac" treatment, which uses a small volume of fluid to assess the response of the reservoir to stimulation, preceded each of the main injections of water and proppant at volumes similar to those used in US shale gas operations (de Pater and Baisch, 2011). Finally, the plugs were drilled out to allow fluid and produced gas to flow to the surface.

[2]http://www.cuadrillaresources.com/our-sites/westby/

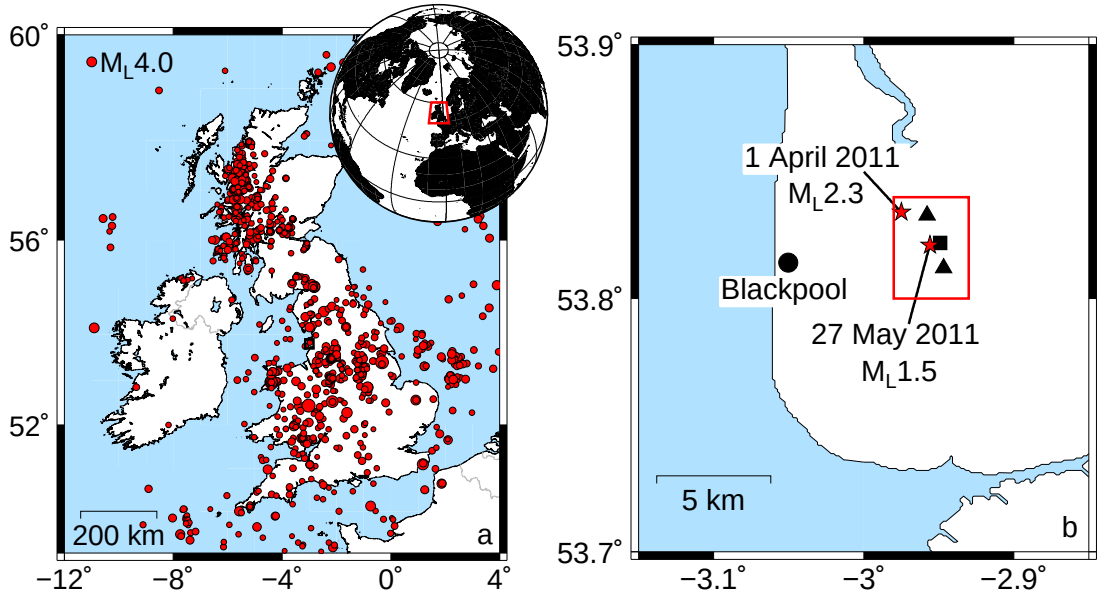

Figure 6.2: **(a)** UK seismicity since 1970 from the BGS catalogue of instrumentally recorded earthquakes; the black box in north-west England indicates the geographical setting of the study area, which is enlarged in the right-hand panel of this figure. **(b)** Location map showing the Preese Hall well (square) and two local seismic stations (triangles), which were installed after a M_l 2.3 earthquake was detected on 1 April 2011 by the BGS regional seismic network. Subsequently, a M_l 1.5 event occurred on 28 May 2011, and could be accurately located close to the well. The red rectangle indicates the area enlarged in Figure 6.4.

On 26 March 2011, the first of six hydraulic fracturing stages was performed at the Preese Hall well. The perforation interval was centred at a depth of 2,660 m, with subsequent stages at progressively shallower depths (see Figure 6.3). Although as we have already seen, microseismicity commonly occurs during hydraulic fracturing, and is a useful tool for understanding the effectiveness of a treatment, no microseismic monitoring network was deployed at Preese Hall. On 1 April 2011, a M_l 2.3 earthquake occurred $\sim$ 10 hours after the well was shut in following stage II of the hydraulic fracturing treatment. This event was sufficiently large to be detected by the UK seismic network and felt at the surface; the BGS location for this event placed it a few kilometres away from the Preese Hall well (see Fig .6.2b).

As Musson (2007) noted, "British earthquakes have always been so newsworthy that

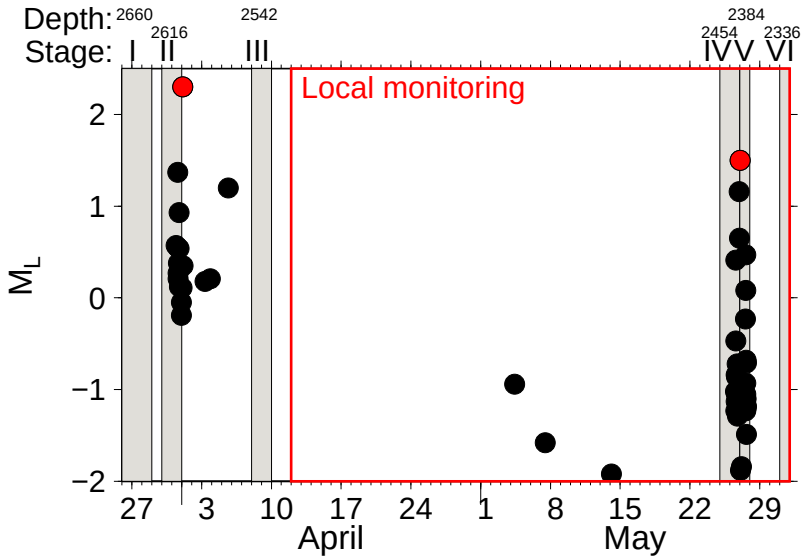

Figure 6.3: Time line of hydraulic fracturing operations and induced seismicity at Preese Hall. The two largest events (red dots) were detected by the BGS regional network. All other events (black dots) are taken from Eisner *et al.* (2011). The event detection threshold improved considerably after 12 April 2011, when two broadband seismometers were installed close to the well (see Figure6.2). The true vertical depth of each stage is given in metres.

even minor events have been recorded in some detail", and this event at Preese Hall was no exception, despite its relatively small size. The rarity of UK earthquakes, combined with the quality of historical records means that the catalogue of UK earthquakes is complete above M_l 4.0 from about 1850 on, and above M_l 5.0 since 1775 (Musson, 2007). Even so, no historical earthquakes are known in the region of interest in this study. Figure 6.2a shows all instrumentally recorded events from the BGS catalogue since 1 January 1970 that are larger than M_l 2.0. The catalogue is not uniform over this time period because the detection threshold has decreased as the monitoring network has become denser. However, in our area of interest the 1 April 2011 earthquake is the only known event, even though the catalogue is complete above M_l 2.5 from at least 2005 onwards (Musson, 2007), and above M_l 2.0 since at least March 2010[3]. Because there is no known seismicity in this area in either the historical or instrumental record, it was immediately suspected that this earthquake was related to the hydraulic fracturing operations at Preese Hall.

[3]http://www.earthquakes.bgs.ac.uk/monitoring/detection_capability.html

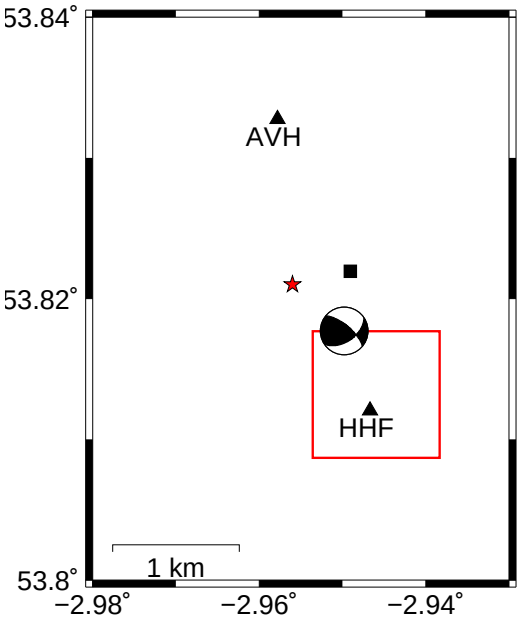

Figure 6.4: Map showing the locations of near-field seismic monitoring stations (triangles) around the Preese Hall well (square) used by Eisner *et al.* (2011) and the present study. The red star denotes the BGS epicentre of the M_l 1.5 event that occurred on 27 April 2011; the beachball indicates the focal mechanism and location determined by Eisner *et al.* (2011) for this event. The red rectangle indicates the area enlarged in the top left panel of Figure 6.9.

Consequently, on 7 April 2011, Keele University deployed two seismometers within 2 km of Preese Hall to monitor subsequent fracturing stages. However, no seismicity was detected after stage III, and so the two Keele instruments were redeployed to other projects on 21 April and 28 April respectively. However, local monitoring capabilities were maintained by the BGS, who installed two temporary stations close to the well on 12 April 2011 at Avenham Hall (AVH) and Hill House Farm (HHF) (Figs .6.2b and 6.4, triangles).

Following the fourth stage of hydraulic fracturing, a M_l 1.5 earthquake was detected on 28 May 2011 by the local and regional networks. This event could be much more accurately located than the previous one because of the availability of data from the local stations: the BGS hypocentre lies within 0.5 km of the Preese Hall well. The occurrence of a second, anomalously large, event — located close to the treatment in both space and

time — prompted Cuadrilla to suspend activities pending an investigation of the cause of the seismicity.

6.2.2 Analysis of the seismic data by Eisner *et al.* (2011)

Eisner *et al.* (2011) were commissioned by Cuadrilla to analyse the available seismic dataset: seismograms recorded on the BGS regional network for the duration of the Preese Hall operations, and on the local monitoring network from 12 April onwards. After compiling a catalogue of events, they relocated the largest of these, and applied the criteria of Davis and Frohlich (1993) to determine whether the seismicity was induced by hydraulic fracturing.

Given the typical frequency–magnitude scaling of earthquakes, it was expected that many events smaller than those detected by the BGS had occurred, but had not been identified. The first objective of Eisner *et al.* (2011) was therefore to construct a more complete event catalogue. For each data channel, they computed the cross correlation of the waveform from the largest recorded event with the entire seismic trace. Peaks in the cross correlation function indicate earthquakes with similar waveforms — and hence similar location and mechanism — to the "master" event, including those that may not be obvious or apparent in the raw time-series. Comparable waveform cross-correlation techniques have been widely used in earthquake seismology for earthquake cluster identification and relative relocation in verbose seismic datasets (e.g. Shearer, 2005).

For the regional stations, the cross correlation was run from 31 March to 27 May using both the M_l 2.3 and M_l 1.5 earthquakes as master events. In total 22 earthquakes were identified, 17 of which occurred before the local monitoring capability was installed. To control for the possibility that the detected events arose from a repeating and previously unidentified natural source, Eisner *et al.* (2011) performed the same cross correlation using data from the three months preceding the commencement of hydraulic fracturing. No events were found.

Because the local monitoring stations were installed after the M_l 2.3 event occurred, only waveforms from the M_l 1.5 event could be used as a cross correlation template for the local stations. 33 earthquakes were identified from the near-field recordings in the time interval from 12 April to 27 May, yielding a catalogue of 50 events when combined with those extracted from regional data.

A clear limitation of using cross correlation for event identification is that, by definition, any earthquakes that are dissimilar to the master event cannot be detected. Thus, it should be kept in mind that the catalogue of Eisner *et al.* (2011) very likely represents only a subset of the actual microseismicity. However, given the paucity of seismic monitoring at Preese Hall, cross correlation is the only tool that can really be used here for identifying events, and the fact that as many as 50 events were detected somewhat validates this approach.

For each event detected, Eisner *et al.* (2011) determined a magnitude, M_L, using

$$M_L = M_L^{Master} - \log\left(\frac{A}{A^{Master}}\right) \tag{6.1}$$

where M_L^{Master} is the local magnitude calculated for the master event by conventional means, and A/A^{Master} is the peak displacement amplitude ratio of the detected and reference events. The magnitude distribution of events detected by Eisner *et al.* (2011) over time is shown in Figure 6.3. A marked improvement in the detection threshold, from approximately $M_l = 0$ to $M_l = -2$, is apparent after the local monitoring stations are installed.

Eisner *et al.* (2011) located the largest four events from their catalogue using body wave arrival times measured at the two near-field stations. These locations were highly uncertain because of the minimal size of the dataset which — because the horizontal channels at AVH were not operational — consisted of just two P-wave picks and a single S-wave pick. Nevertheless, Eisner *et al.* (2011) also managed to determine focal mechanisms for these events by searching over double couple solutions using body wave amplitudes as data,

although again these were highly uncertain. Their preferred location and mechanism for the M_l 1.5 event of 27 May is shown in Figure 6.4.

In the following, we attempt to apply the waveform modelling and inversion techniques developed earlier in this thesis to the small seismic dataset acquired by the local monitoring stations during the latter stages of hydraulic fracturing operations at Preese Hall. We do not investigate whether the seismicity can be attributed to hydraulic fracturing. The relationship between the two has already been demonstrated for Preese Hall by Eisner *et al.* (2011) using the criteria of Davis and Frohlich (1993): these were the first known seismic events in the area, they were correlated spatially and temporally with injection, and the pressure perturbation at depth was likely big enough to induce events. Moreover this conclusion is not sensitive to details of the seismic event analysis. Rather we hope to find out whether reliable event locations and moment tensors can be determined from such a small dataset, and to see if waveform inversion yields source parameters that are consistent with those determined previously.

6.3 Reanalysis of the Preese Hall dataset

6.3.1 Waveform data

The two local stations, deployed by the BGS after the regionally recorded earthquake of 1 April 2011, were equipped with Gurälp 6TD three component broadband seismometers, recording ground velocity at a sampling frequency of 100 Hz. Raw seismic data from these sensors were supplied by the BGS for each event identified by Eisner *et al.* (2011). We preprocessed the data to remove the instrument response function and convert the time-series to displacement. The horizontal channels at station AVH operated intermittently, and unfortunately did not record any of the events analysed later, meaning that a total of only four data channels are available for analysis.

An example set of waveforms from the M_l 1.5 event of 27 May 2011, bandpass filtered between 5 and 20 Hz, is shown in Figure 6.5 (black traces). A shear wave arrival

dominates the horizontal component traces, and small P-wave arrivals are visible on all traces. Recalling that these waveforms were used as the cross correlation template for the construction of the event catalogue, these seismograms are representative of all of the events in the dataset, give or take a reduction in the amplitude scale and a commensurate decrease of the signal to noise ratio. We do not use seismograms recorded at regional stations because unknown complexities in the crustal structure mean that the waveform observation cannot be well modelled in the frequency range of interest at these distances.

6.3.2 Forward modelling

Before any attempt is made to invert these data, we should see whether synthetic waveforms computed for a plausible source and structural model show qualitative agreement with the observations. To obtain a crustal model for Preese Hall, we augmented the 1D velocity model of Eisner *et al.* (2011) — which was in turn modified from the BGS regional model — with depth varying ratios of P-wave velocity to density taken from the local earth model of CRUST2.0[4]. The resulting crustal model is given in Table 6.2, and is used throughout the following.

Synthetic seismograms computed using the location and focal mechanism determined by Eisner *et al.* (2011) for this event are shown in Figure 6.5 (red traces). A visual comparison of the data and synthetics shows that prominent features, such as the sense of motion and amplitude of the S-wave arrivals, are similar. This qualitative agreement suggests that waveform inversion assuming a simple layered elastic crustal model should be possible, even for these relatively high frequency data.

6.3.3 Inversion

The M_l 1.5 earthquake of 27 May 2011 was the largest event recorded by the local monitoring network, and so is a logical choice for our first attempt at inverting microseismic

[4]http://igppweb.ucsd.edu/gabi/rem.html

Thickness (km)	v_P (km/s)	v_S (km/s)	ρ (kg/m^3)
0.647	3.452	1.735	1.556
0.747	4.384	2.203	1.977
0.671	4.812	2.659	2.170
0.455	4.000	2.381	1.803
5.030	5.900	3.491	2.660
11.320	6.450	3.728	2.867
15.280	7.000	4.046	2.954
∞	8.000	4.624	3.376

Table 6.2: Crustal model for Preese Hall used in this study (adapted from Eisner *et al.*, 2011).

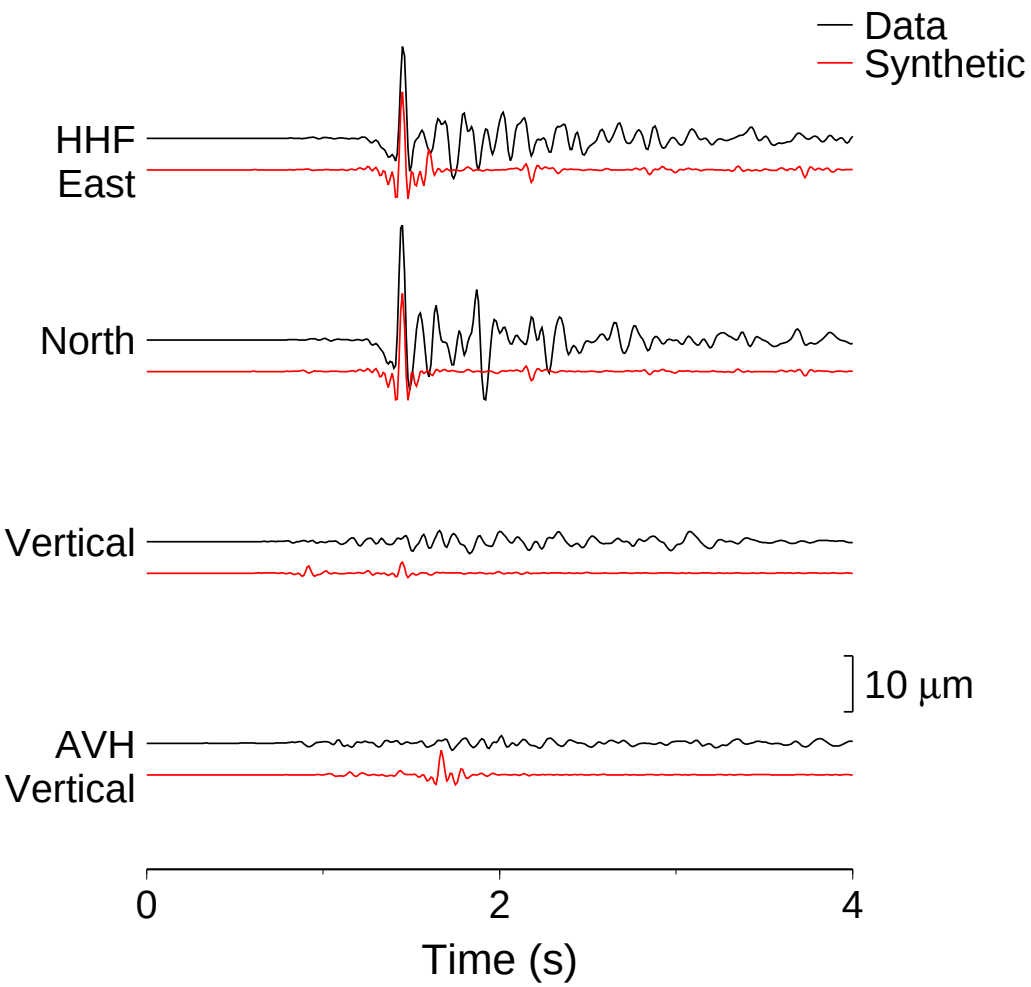

Figure 6.5: Waveform data (black traces) and synthetics (red traces) from the M_l 1.5 event of 27 May 2011 for the two near-field stations. The synthetic seismograms are calculated using the focal mechanism determined by Eisner *et al.* (2011) and the crustal model given in Table 6.2.

waveform data from Preese Hall. Seismograms for this event are shown in Figure 6.5, and contain a significant amount of scattered energy in the S-wave coda that cannot be reproduced using our waveform modelling approach and limited one-dimensional knowledge of the local crustal structure. To minimise the impact of the unmodelled part of the waveform on the inversion, we use only the first 2 s of the data in our inversion. The effect of structural heterogeneity can be further minimised by removing as much high frequency content from the data as is practicable. In the inversions that follow, data and synthetics are filtered in a passband between 5 and 20 Hz. These corner frequencies are chosen only for consistency with those used by Eisner *et al.* (2011); performance of the inversion could likely be improved if lower values were selected.

The waveform inversion method applied here is essentially the same as that described previously for GPS data in Chapter 3, except that an additional step has been added at the zeroth iteration. Because the origin time of our initial source — the hypocentre determined by Eisner *et al.* (2011) — is only given to the nearest second, we begin by determining the time shift that best aligns data with synthetics. This adjustment is obtained from the timing of the peak in the cross correlation between amplitude normalised data and synthetics computed using the focal mechanism for this event given by Eisner *et al.* (2011). Only east component data and synthetics from station HHF were used in the cross correlation, which is reasonable as the S-wave arrival at this receiver is the dominant signal that we attempt to fit in the inversion. Such a simple cross correlation rule would be inappropriate if all channels were operational at AVH, or data from more stations were available. If *a priori* information about the source mechanism was not available to compute the reference synthetic for the cross correlation then a generic source could be used. Some modification of the cross correlation would then be necessary to account for the possibility that the two waveforms are perfectly out of phase.

The source parameters of the M_l 1.5 earthquake of 27 May 2011 retrieved by our waveform inversion at a number of iterations are summarised in Table 6.3. For comparison, the pure double couple mechanism computed by Eisner *et al.* (2011) and fit of the corresponding waveform synthetics to data are also shown. Clearly our inversion returns a

source that explains the waveform data more fully than that of Eisner *et al.* (2011). A comparison of data and synthetics computed for our final source is shown in Figure 6.6.

The similarity of misfit values between iterations suggests that there is little reason to prefer the final source model, obtained after 20 iterations, to that obtained at the zeroth iteration, when the source location was fixed at the hypocentre of Eisner *et al.* (2011). Such behaviour may reflect uncertainties in the event location, which we investigate further in Section 6.4. At the same time, the fact that the mechanisms recovered at different stages of the inversion are fairly consistent with each other suggests that the moment tensor is fairly robust with respect to errors in source location.

The moment tensor that we recover is essentially a pure double couple, and implies strike-slip motion. The best double-couple decomposition of our moment tensor is shown in Table 6.4 compared to the mechanism of Eisner *et al.* (2011), who only considered pure double-couple mechanisms in their inversion. Thus far, we have assumed that this induced event was similar to a natural earthquake in the sense that it did not involve any volume change, which may be inappropriate given that it was related to fluid injection. By removing the constraint that the trace of the moment tensor equals zero, we can investigate whether the data require the source to have an explosive or implosive component. The results of such an inversion are shown in Table 6.5; the additional free parameter in the source model does not result in an improved fit to the data, implying that our previous assumption of conservation of volume is justified as it is more parsimonious. In the following, we impose this zero trace constraint throughout.

We applied the waveform inversion approach described above to determine centroid locations and moment tensors for as many of the Preese Hall events as possible. In total, data from 9 events with $M_L \geq -0.71$ had sufficiently high signal to noise ratios to be inverted; source parameters recovered for these events are listed in Table 6.6 and the corresponding beachballs shown in Figure 6.7. Given the similarity between the waveforms of these events — a direct consequence of the event detection algorithm — it is unsurprising that their locations and mechanisms also show a great deal of similarity. Eisner *et al.*

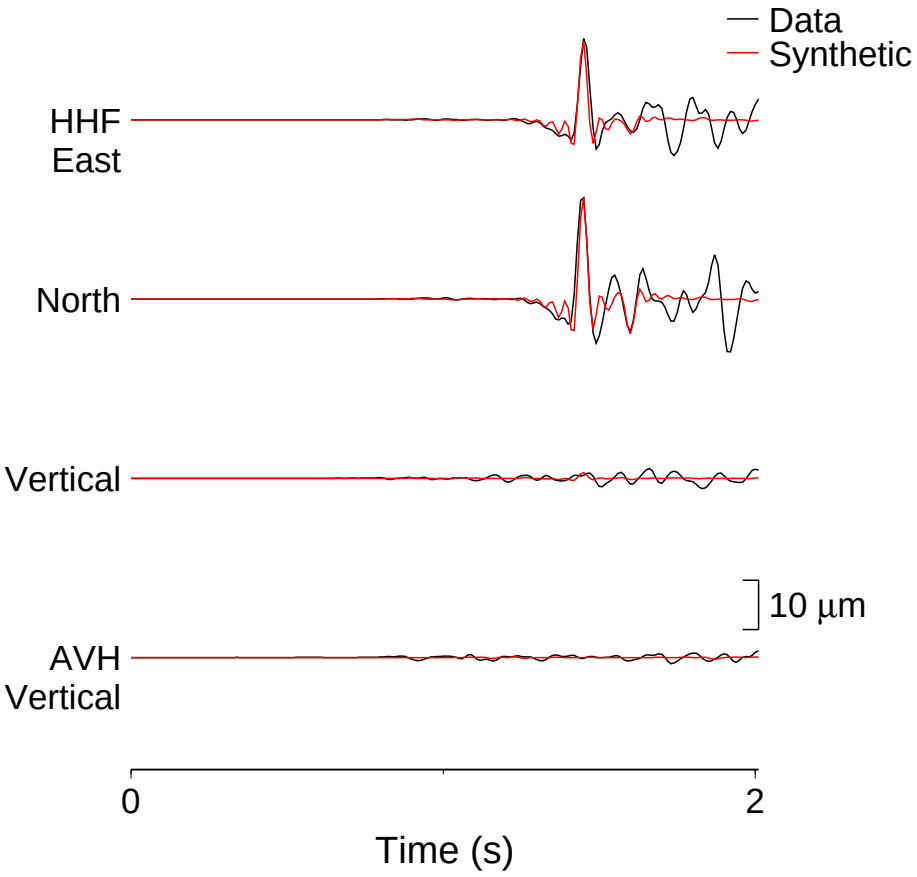

Figure 6.6: Data

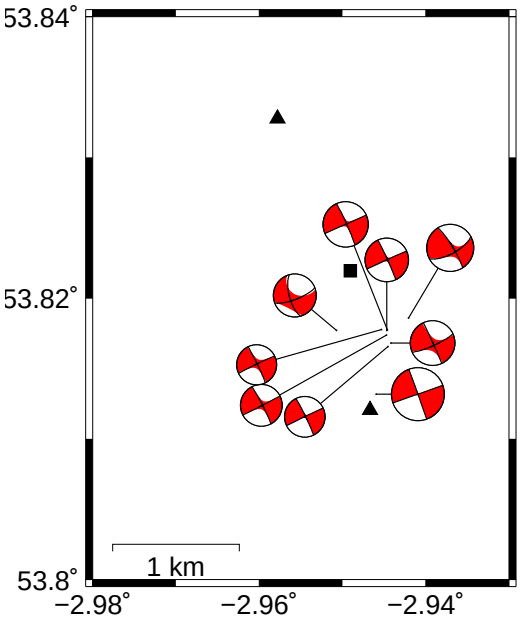

Figure 6.7: Map showing the location and mechanism of the 9 events listed in Table 6.6.

	Initial	Iteration 0	Iteration 5	Final	Eisner *et al.*
Location:					
Origin time	00:48:46.00	00:48:46.33	00:48:46.34	00:48:46.36	00:48:46.33
Longitude	2.9498°W	2.9498°W	2.9451°W	2.9460°W	2.9498°W
Latitude	53.8177°N	53.8177°N	53.8173°N	53.8132°N	53.8177°N
Depth (km)	2.332	2.332	2.337	2.343	2.332
Moment tensor:					
M_{rr}		0.0408	0.0298	0.0063	0.0888
$M_{\theta\theta}$		-0.5134	-0.7172	-2.1216	-0.2050
$M_{\phi\phi}$		0.4727	0.6875	2.1153	0.1160
$M_{r\theta}$		-0.0547	0.0621	0.0228	-0.0449
$M_{r\phi}$		-0.0155	0.0080	0.0180	0.1110
$M_{\theta\phi}$		0.3974	0.5975	2.5990	0.0169
Relative RMS:					
		0.53	0.50	0.49	0.69
Mechanism:					

Table 6.3: Results of a waveform inversion for the source parameters of the 27 May 2011 M_l 1.5 event at Preese Hall. The moment tensors are given in units of 10^{12} Nm.

	Nodal Plane 1			Nodal Plane 2				
	Strike	Dip	Rake	Strike	Dip	Rake	M_w	
Best double couple	70°	90°	0°	340°	90°	180°	2.3	
Eisner *et al.* (2011)	55°	53°	25°	310°	70°	140°	1.4	

Table 6.4: A comparison of the best double-couple solution determined in this study with the source mechanism determined by Eisner *et al.* (2011) for the 27 May 2011 M_l 1.5 event at Preese Hall, UK.

(2011) could not determine hypocentral coordinates for the smaller of these events, and so in these cases the inversion was started at the same location as used earlier in the analysis of the M_l 1.5 earthquake (see Table 6.3).

6.4 Error estimates for recovered source parameters

In the previous section we showed that it is possible to invert seismic waveforms, recorded at surface stations located within a few kilometres of a microseismic source, to obtain information about the location and moment tensor of the event. We used hydraulic fracturing

	Initial	Unconstrained
Location:		
Origin time	00:48:46.00	00:48:46.34
Longitude	2.9498°W	2.9453°W
Latitude	53.8177°N	53.8166°N
Depth (km)	2.332	2.338
Moment tensor:		
M_{rr}		0.0335
$M_{\theta\theta}$		-0.7708
$M_{\phi\phi}$		1.1082
$M_{r\theta}$		0.0453
$M_{r\phi}$		0.0107
$M_{\theta\phi}$		0.7016
Relative RMS:		
		0.50

Table 6.5: Source parameters of the 27 May 2011 M_l 1.5 event at Preese Hall, determined by waveform inversion without the imposition of a zero trace constraint on the moment tensor. The moment tensor is given in units of 10^{12} Nm.

induced earthquakes at Preese Hall, where only four channels of data from two seismometers were available, as a demonstration of the concept. How reasonable are the results of our inversions, given the small size of the seismic dataset? To answer this question, we must examine the uncertainties on the model parameters determined in our inversion.

So far in this thesis, we have been concerned with calculating a single solution of an inverse problem. Given some seismic observations — waveforms or static displacements — we have determined the set of model parameters — location, origin time and moment tensor — that best explains the data. This lone solution can alternatively be thought of as the most likely model taken from a probability density defined over all possible models. The shape of this distribution in the vicinity of the optimal solution then defines the uncertainty on each model parameter. Thus the problem of estimating uncertainties is really that of computing this probability distribution. Here we compare two approaches for estimating the so called posterior probability density function, using standard errors and grid inversion, with an emphasis on quantifying location errors.

Date	Time	Location			Moment Tensor						M_l	M_w	
		Lon	Lat	Depth (km)	M_{rr}	$M_{\theta\theta}$	$M_{\phi\phi}$	$M_{r\theta}$	$M_{r\phi}$	$M_{\theta\phi}$			
					($\times 10^{12}$ Nm)								
26/05/2011	14:39:38.23	2.9507°W	53.8177°N	2.388	0.0019	-0.0119	0.0100	-0.0127	0.0055	0.0142	0.41	0.85	
26/05/2011	22:35:59.76	2.9421°W	53.8186°N	2.240	0.0384	-0.1669	0.1285	-0.0190	0.0587	0.0884	1.16	1.48	
26/05/2011	23:06:02.36	2.9442°W	53.8168°N	2.224	0.0110	-0.0502	0.0391	-0.0052	0.0087	0.0394	0.65	1.15	
27/05/2011	00:48:46.36	2.9460°W	53.8132°N	2.343	0.0063	-2.1216	2.1153	0.0228	0.0180	2.5990	1.50	2.32	
27/05/2011	13:22:24.29	2.9447°W	53.8174°N	2.337	0.0013	-0.0119	0.0105	0.0008	0.0006	0.0081	-0.23	0.73	
27/05/2011	14:21:13.30	2.9447°W	53.8177°N	2.338	0.0006	-0.0251	0.0245	0.0020	0.0005	0.0215	0.08	0.98	
27/05/2011	14:21:28.18	2.9446°W	53.8177°N	2.337	0.0027	-0.0592	0.0566	0.0047	0.0014	0.0519	0.47	1.23	
27/05/2011	15:33:40.87	2.9445°W	53.8166°N	2.343	0.0001	-0.0056	0.0056	0.0004	0.0001	0.0044	-0.68	0.54	
27/05/2011	16:11:44.43	2.9453°W	53.8178°N	2.342	0.0006	-0.0041	0.0035	0.0004	-0.0001	0.0030	-0.71	0.42	

Table 6.6: Source parameters of microseismic events at Preese Hall determined by waveform inversion. For comparison purposes, the corresponding local magnitude values determined by Eisner *et al.* (2011) are also shown.

6.4.1 Standard errors

For linear or weakly non-linear inverse problems with Gaussian errors on the input data and *a priori* model $\mathbf{m}_{\text{prior}}$, the posterior model probability density, σ_{M}, is respectively Gaussian or approximately Gaussian in the region around *the* solution, and can be written (Tarantola, 2005; Duputel and Rivera, 2012)

$$\sigma_{\text{M}}(\mathbf{m}) \simeq \frac{1}{\sqrt{(2\pi)^N \det \tilde{\mathbf{C}}_{\text{M}}}} \mathrm{e}^{-\frac{1}{2}(\mathbf{m}-\tilde{\mathbf{m}})^{\text{T}} \tilde{\mathbf{C}}_{\text{M}} (\mathbf{m}-\tilde{\mathbf{m}})} . \tag{6.2}$$

where N is the number of model parameters. The mean value, $\tilde{\mathbf{m}}$, of this Gaussian is the converged solution given by the iterative scheme (2.180), which, under the assumption of Gaussian errors, becomes (Tarantola, 2005)

$$\mathbf{m}_{\text{i}+1} = \mathbf{m}_{\text{i}} + \left(\mathbf{A}^{\text{T}} \mathbf{C}_{\text{D}}^{-1} \mathbf{A} + \mathbf{C}_{\text{M}}^{-1}\right)^{-1} \left[\mathbf{A}^{\text{T}} \mathbf{C}_{\text{D}}^{-1} \left(\mathbf{d} - \mathbf{s}(\mathbf{m}_{\text{i}})\right) + \mathbf{C}_{\text{M}}^{-1} \left(\mathbf{m}_{\text{i}} - \mathbf{m}_{\text{prior}}\right)\right] , \tag{6.3}$$

while the covariance of (6.2) is given by the posterior covariance matrix $\tilde{\mathbf{C}}_{\text{M}}$

$$\tilde{\mathbf{C}}_{\text{M}} = \left(\mathbf{A}^{\text{T}} \mathbf{C}_{\text{D}}^{-1} \mathbf{A} + \mathbf{C}_{\text{M}}^{-1}\right)^{-1} . \tag{6.4}$$

We can calculate the standard errors on the model parameters simply from the square roots of the diagonal elements of $\tilde{\mathbf{C}}_{\text{M}}$ evaluated at the convergence point of our inversion, which requires us to determine specific forms for the the *a priori* data and model covariance matrices $\mathbf{C}_{\text{D}}$ and $\mathbf{C}_{\text{M}}$.

If we assume that data errors are uncorrelated, random, samples of a Gaussian with standard deviation σ, then the *a priori* data covariance matrix is diagonal and specifically $\mathbf{C}_{\text{D}} = \sigma \mathbf{I}$. Comparing (6.3) with the iterative scheme we have used in our source inversions (2.180) we see that our model update is not damped by our prior state of knowledge about the model, from which we can deduce that $\mathbf{C}_{\text{M}}^{-1} = \mathbf{0}$. Equivalently, we can say that we have no *a priori* information about the model parameters, which are assumed to be independent of each other, so the Gaussian describing their prior probability density is infinitely wide

	Initial	Final
Location:		
Origin time	00:48:46.00	00:48:46.36 ± 0.003 s
Longitude	2.9498°W	2.9460°W ± 0.028 km
Latitude	53.8177°N	53.8132°N ± 0.085 km
Depth (km)	2.332	2.343 ± 0.002 km
Moment tensor:		
M_{rr}		0.0063 ± 0.0358
$M_{\theta\theta}$		-2.1216 ± 0.8829
$M_{\phi\phi}$		2.1153 ± 0.8915
$M_{r\theta}$		0.0228 ± 0.0138
$M_{r\phi}$		0.0180 ± 0.0128
$M_{\theta\phi}$		2.5990 ± 1.2425

Table 6.7: Source parameters and standard error estimates for the 27 May 2011 M_l 1.5 event at Preese Hall, determined by waveform inversion. The moment tensor and its uncertainties are given in units of $\times 10^{12}$ Nm.

and $\mathbf{C}_{\mathrm{M}} = \infty\mathbf{I}$. Combining these results, we obtain

$$\tilde{\mathbf{C}}_{\mathrm{M}} = \sigma^2 \left(\mathbf{A}^{\mathrm{T}}\mathbf{A}\right)^{-1} . \tag{6.5}$$

Since we have implicitly assumed that our forward modelling method is exact, the misfit of our final solution is assumed to be entirely due to random data measurement errors, and hence σ is just the standard deviation of the residuals between data and corresponding synthetics. For the M_l 1.5 earthquake at Preese Hall, $\sigma = 1.50\,\mu$m, which leads to standard errors on the source parameters as shown in Table 6.7.

These uncertainty estimates suggest that this event is well located: the epicentral position is known to within 100 m laterally, and 2 m in depth, and the origin time is accurate to within 3 ms. The errors on each element of the moment tensor are typically between ∼40 and 70 % of their absolute values, with the exception of the M_{rr} component which is comparatively uncertain because of its small size. When compared to the location uncertainties, for which we have some physically intuitive idea as to what constitutes a "good" or "bad" error bound, it is harder to say whether the moment tensor is well constrained here, however these uncertainties appear to be relatively large in comparison

to those reported by the Global CMT project, which are computed in the a similar way to that described here (Dziewonski *et al.*, 1981).

A first check on the reasonableness of these standard error bounds can be made using Table 6.3, which shows source parameters for this event output after the zeroth, fifth and twentieth iterations of our inversion. The similar misfit values for each of these solutions shows that they all explain the observations about as well as the final result does. Hence the diversity of models presented in Table 6.3 should be encompassed by the standard error bounds if these are representative of the actual uncertainties on the model parameters. Clearly, this is not the case: neither the zeroth or fifth iteration solution is within one, or even two, standard deviations of the final source, suggesting that a more sophisticated treatment of errors is required.

From (6.3), it is clear that particular choices of the prior covariance matrices affect not only the posterior estimates of model uncertainties, but also the solution of the inverse problem itself. The use of inappropriate $\mathbf{C}_\mathrm{D}$ and $\mathbf{C}_\mathrm{M}$ can therefore introduce biases into the solution, as well as give rise to unrealistic error estimates. Various improvements to the calculation of standard errors have been described. Duputel and Rivera (2012) suggest it is not reasonable to assert that data measurement errors are samples of a single Gaussian distribution, but rather that they depend on noise levels at a particular location, and so can be characterized by a Gaussian specific to each station or channel. The validity of our simple, diagonal prior data covariance matrix is further questioned by the fact that modern seismometers with high sampling rates may over-sample the waveform. In this case data are not independent and so a block diagonal $\mathbf{C}_\mathrm{D}$ is more realistic as it accounts for data correlation over some characteristic timescale (Yagi and Fukahata, 2008; Duputel and Rivera, 2012). Spatial covariance of data is not expected to be a problem for global and regional waveform datasets because of the low station density of typical seismic networks, but is important in studies of earthquake sources using InSAR (e.g. Lohman and Simons, 2005).

Another significant source of error, which we have so far neglected, arises from the

fact that our forward modelling operator is, and always will be, imperfect. Our limited knowledge of the true earth structure and assumption of a point source means that we cannot take all possible rupture and wave propagation effects into account. These theoretical uncertainties, which are assumed to be Gaussian, can be included in the prior data covariance matrix $\mathbf{C}_\mathrm{D} = \mathbf{C}_\mathrm{d} + \mathbf{C}_\mathrm{T}$, where $\mathbf{C}_\mathrm{d}$ and $\mathbf{C}_\mathrm{T}$ are the data and forward modelling covariances respectively (Tarantola, 2005). Yagi and Fukahata (2011) demonstrated the importance of using this more realistic version of $\mathbf{C}_\mathrm{D}$; waveform inversions for earthquake slip distributions that included $\mathbf{C}_\mathrm{T}$ recovered physically plausible models without imposing a zero back-slip constraint. In general, it is difficult to know the structure of a realistic waveform data covariance matrix *a priori*, as evinced by the dearth of studies that have tried to use anything more complicated than $\mathbf{C}_\mathrm{D} = \sigma\mathbf{I}$. Meaningful uncertainty estimates may be more simply obtained by using forward modelling to explore the variation in misfit over the model space (e.g. Sambridge, 1999; Valentine and Trampert, 2012), or — for the case of location errors — by performing systematic inversions, as explored in the following section.

The above analysis is predicated on the assumption that all errors on the input data, arising from imperfect measurement and modelling, are Gaussian. A visual examination of the distribution of the residuals between data and synthetics, like that shown in Figure 6.8 for the M_l 1.5 event, should therefore form part of routine error analyses, to assess the validity of this assumption. The standard errors approach that we have adopted here appears to be justified as the misfit distribution is approximately Gaussian, although the presence of a few extreme outliers means that the actual distribution is more peaked and longer tailed than the corresponding Gaussian with standard deviation $\sigma = 1.50\,\mu$m and mean $\mu = -0.01\,\mu$m.

6.4.2 More realistic errors

The analysis of standard errors presented in the previous section suggests that the inverse problem under consideration is too strongly nonlinear for the posterior probability density

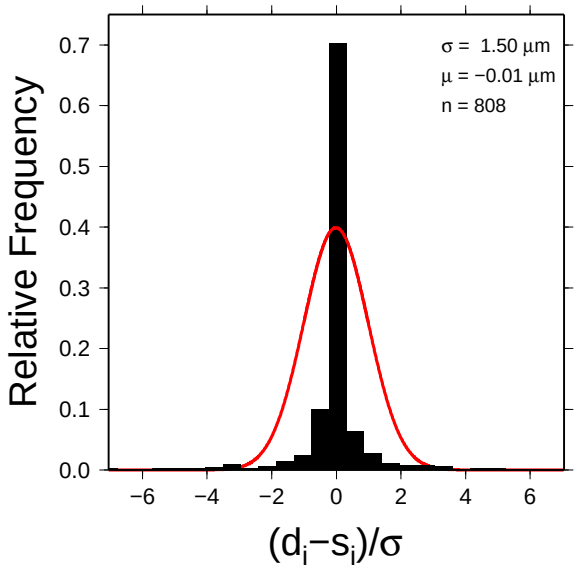

Figure 6.8: Histogram showing the distribution of residuals between observed and synthetic waveforms.

of the model, σ_{M}, to be approximated by a Gaussian. Rather, realistic model uncertainties may be determined directly from the misfit function, m^2, which is a proxy for the true σ_{M}. Various approaches have been devised for sampling the posterior probability density over the model space; methods such as the neighbourhood algorithm have had considerable success for nonlinear inverse problems with many unknown parameters (Sambridge, 1999). Here, our goal is to examine only uncertainties in the three spatial coordinates of the centroid, and so a systematic search of the solution space over these parameters is feasible. We use our converged solution for the M_l 1.5 event to define the centre of a cubic grid of dimension 1 km, (see Figure 6.4, red box) and map the spatial variation in the misfit function by inverting waveforms for the best moment tensor and origin time at fixed points seeded at 50 m intervals within this grid.

Figure 6.9 shows slices through the resulting misfit cube, centred on our preferred solution. Multiple misfit minima are visible, suggesting that the waveform inversion is highly non-unique. In fact, the best solution from our iterative inversion is not actually the global minimum, which actually occurs at a depth of 1.94 km. Oscillations are apparent in

the value of the misfit function as a function of depth, which occur due to cycle skipping. The white lines denote the size of the standard errors in latitude, longitude and depth determined previously; the depth uncertainty is too small to be visible at the scale of the plot. The standard errors are plotted at the event location preferred by our iterative inversion, which is situated in a balloon-shaped minimum in the misfit function. The non-Gaussian shape of this misfit minimum explains the inadequacy of the formal errors determined previously. While the absolute values of the standard error estimates are unreasonably small, the relative errors between location parameters are representative of the true relative uncertainties, as others have found (e.g. Valentine and Trampert, 2012), which suggests that, despite their known inadequacies, it is still useful to compute standard errors.

Eisner *et al.* (2011) also computed location uncertainties using the posterior probability density function computed from body wave arrival time data. They found that the event depth was essentially unconstrained, and lateral errors were of the order 1 km, which are broadly in agreement with those implied by our waveform inversion as shown in Figure 6.9. For obvious reasons such large location errors are unacceptable if, for example, one wishes to ensure that hydraulic fracture growth does not extend into the overburden or aquifer. Errors in event location also propagate into magnitude calculations, which is important given that the proposed traffic light scheme for UK shale gas hydraulic fracturing is controlled by magnitude, rather than ground motion, thresholds (Green *et al.*, 2012). For example, our best fitting source fixed at the location of Eisner *et al.* (2011) has $M_w = 1.8$, whereas the converged solution when the centroid location is allowed to vary has $M_w = 2.3$. On a more basic level, deciding which magnitude scale to use is important, as shown by the general disagreement between our calculations of moment magnitude and the local magnitudes from Eisner *et al.* (2011) that are shown in Table 6.6.

It is likely that our event location errors could be improved if separate P- and S-wave windows were extracted and appropriately weighted in the inversion. At present, the whole waveform is given equal weight, which means that the inversion only tries to fit the large amplitude shear wave because, in a least squares sense, it is the dominant contributor

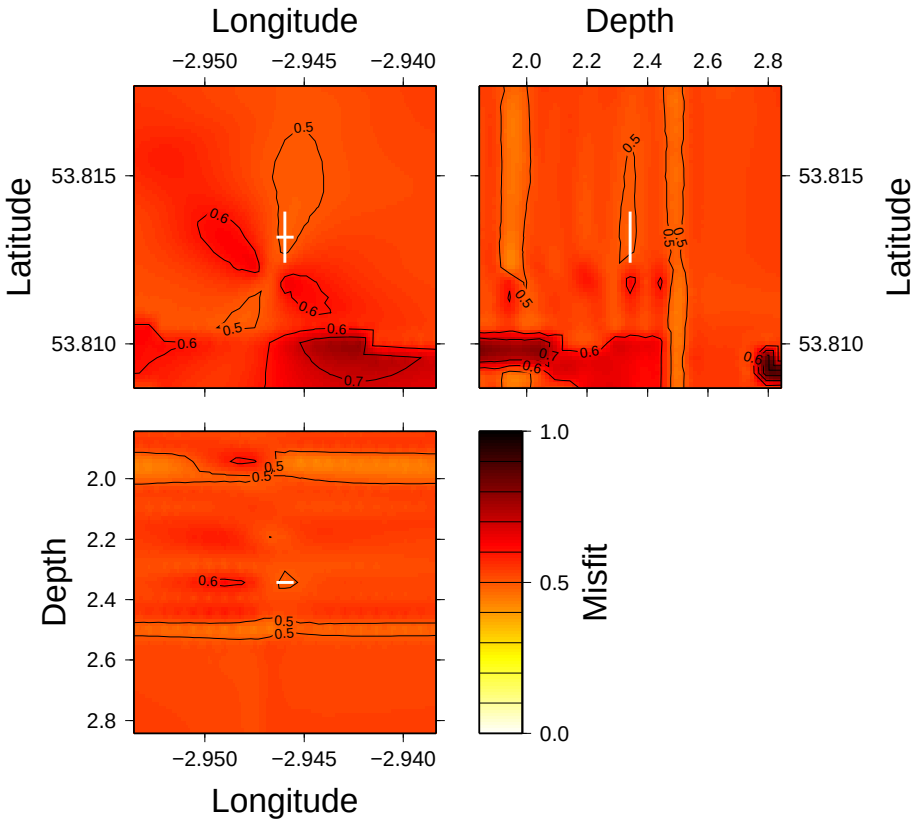

Figure 6.9: Map of the misfit function over centroid longitude, latitude and depth for the 27 May 2011 M_l 1.5 event at Preese Hall — a proxy for location error. The 1×1 km slices are centred on the centroid location recovered by iterative inversion of the waveform data, standard errors from which are indicated by the white bars (see Table 6.7).

to the overall misfit. However, event location precision is fundamentally controlled by the spatial distribution and density of seismic stations around a source, and so can most easily be improved by increasing the number and azimuthal coverage of instruments in the monitoring network, as we investigate in the following section.

6.4.3 Effect of monitoring geometry on location uncertainties

The fact that only four channels of waveform data were recorded during the induced microseismicity at Preese Hall represents something of a worst case scenario. We have tried to extract the maximum amount of information from these data by using the whole

waveform, rather that just travel times and amplitudes, to determine locations and moment tensors for these events. However, the sparsity of the monitoring network means that uncertainties in the recovered source models are so large as to render the results almost meaningless. What difference would it have made if all three channels had been operational at AVH, or if additional seismic stations had been deployed?

We can use inversions of synthetic datasets to try and understand the extent to which extra data would have reduced location errors. Because the true source and earth model are known, and the synthetic data are noise free, the effect of the monitoring geometry on location uncertainties can be isolated in synthetic inversions. In the following, we model waveforms for the M_l 1.5 event at Preese Hall assuming various monitoring networks; the whole synthetic dataset is shown in Figure 6.10. Subsets of these synthetic data are then used as input for grid inversions of the sort presented in Figure 6.9, from which realistic location errors can be deduced. The true source corresponds to the best moment tensor retrieved for this event by our waveform inversion when the location is fixed to that determined by Eisner *et al.* (2011) (see Table 6.3, iteration 0 column).

When the synthetic dataset is equivalent to that which was actually available at Preese Hall, *i.e.* comprises four channels of data from two stations — three components recorded at HHF and vertical motion recorded at AVH, we see that the event location is almost unconstrained (see Figure 6.11). Because the synthetic displacement amplitudes on the vertical channel at AVH are very much smaller than the shear wave seen in the horizontal channels at HHF (see Figure 6.10), the inversion only tries to fit the larger arrival. Since this is only recorded at one station, the event location and depth trade off with origin time so that the shear wave at HHF has the correct arrival time. This effect is apparent when one examines the spatial pattern of the origin times retrieved in the grid inversion relative to the true centroid time (see Figure 6.12). The origin time perturbation is clearly a function of the distance of the source from HHF. Sources closer to this station than the true location have positive origin time perturbations and vice versa: the mislocation is accommodated by switching the source on later or earlier respectively.

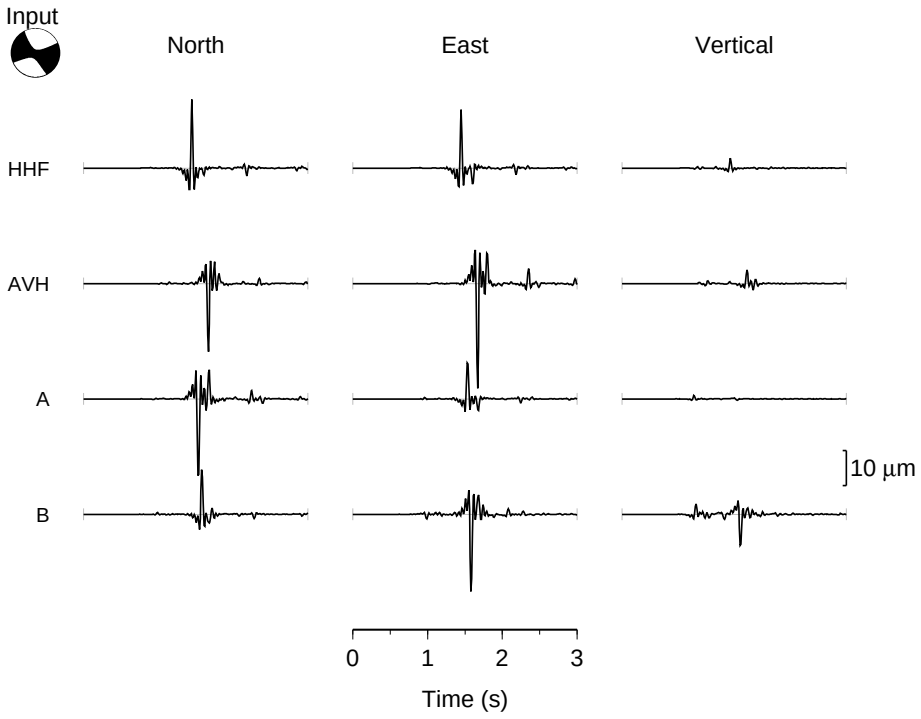

Figure 6.10: Synthetic dataset used in our experiments investigating the effect of station distribution on location errors (see Figs. 6.11, 6.13, 6.14 and 6.15).

Viewed together, Figs. 6.11 and 6.12 tell us that for each location explored in the grid inversion there is a source that fits the shear wave at HHF but does not generate significant energy on the vertical channel at AVH. That this is the case results from the particular source mechanism used to generate the synthetics: better constraint on event location would be achieved had there been larger vertical displacements at HHF. However, the input source for this test was not chosen to contrive this situation, but was actually that retrieved from the waveform observations, suggesting that the uncertainties shown in Figure 6.11 are representative of the true uncertainties in our data inversion that arise from the limitations of the monitoring geometry.

When three component data are also available at AVH, as shown in Figure 6.13, the epicentral latitude becomes better constrained, but the longitude and depth of the event remain highly uncertain as these parameters can still trade off with the origin time. Adding a third seismometer east of the event (see Figure 6.14), and a fourth to the west (Fig-

ure 6.15), allows the longitude to be better resolved. Despite these extra stations, depth is still relatively poorly constrained by the waveform data, and a network covering a larger range of epicentral distances would be needed to realise further improvements in event location errors.

6.4.4 Discussion

The stress regime at Preese Hall is expected to be conducive to strike-slip faulting, with the direction of maximum horizontal stress estimated to have a strike of $\sim 7^{\circ}$(de Pater and Baisch, 2011). The pure double-couple mechanisms that we recover imply strike-slip motion on vertical faults with strikes of $\sim 70^{\circ}$or $\sim 340^{\circ}$, and so are consistent with the in-situ stress conditions, perhaps more so than the oblique slip-mechanism recovered by Eisner *et al.* (2011). In agreement with the studies commissioned by Cuadrilla, our results are at least consistent with the hypothesis that the induced events originated by the reactivation of a suitably oriented pre-existing fault. Even though the relatively small volumes of fluid injected during shale gas hydraulic fracturing are not expected to pose any risk of inducing damaging earthquakes (NRC, 2012), if, as the UK government wishes, felt seismicity is to be entirely avoided during future operations then faults must be identified, and stress fields characterized, before drilling begins.

Although the standard error bounds computed on our CMT solution for the 27 May event appear to show that the source parameters are well constrained, a more thorough examination of the location uncertainties shows that our four-seismogram dataset is too small for us to have much confidence in our results. This installation of just a few more surface monitoring stations would have improved this situation considerably. As we have already mentioned, if the magnitude thresholds chosen for future traffic light monitoring schemes are to be meaningful, it is vital that we at least quantify the uncertainties in source parameters determined from microseismic data and ideally these should also be reduced through the installation of larger monitoring arrays.

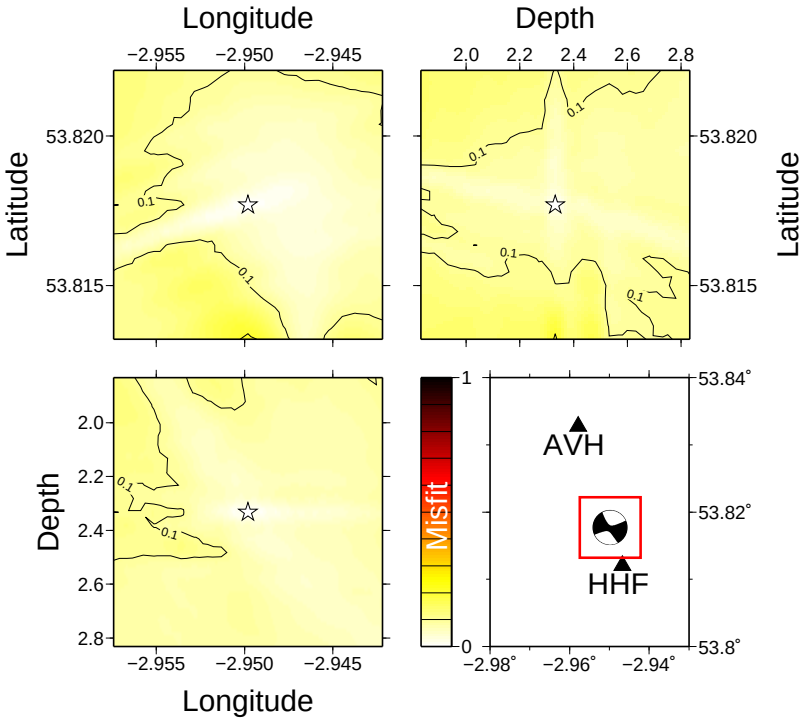

Figure 6.11: Waveform misfit — a proxy for location uncertainty — for a grid inversion using a total of four channels of synthetic waveform data: three from HHF and vertical component data from AVH. The stations used in the inversion, input source mechanism, and surface projection of the inversion grid are shown in the bottom right hand panel by the triangles, beachball and red square respectively. The true event location is indicated by the white star.

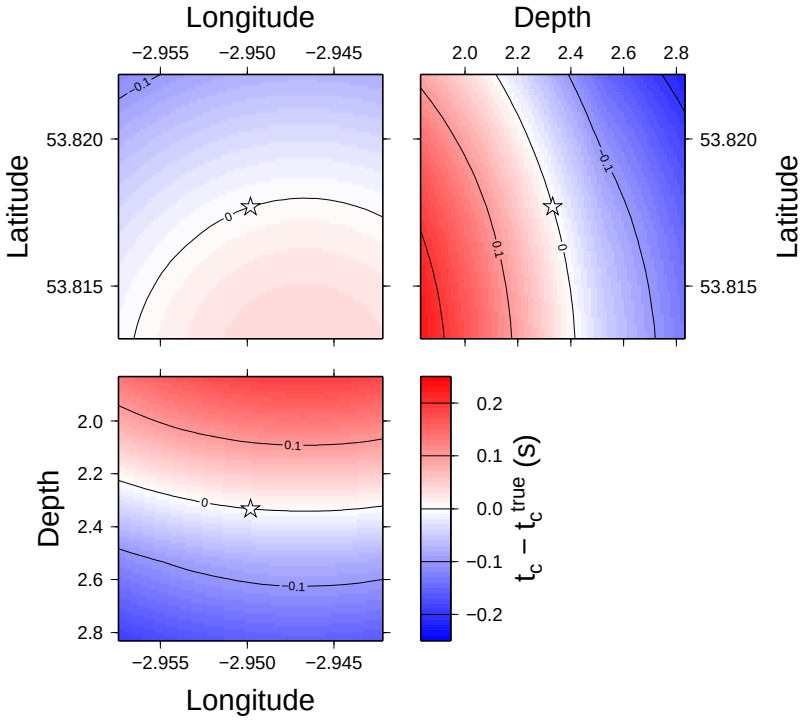

Figure 6.12: As for Figure 6.11 except that here origin time perturbations relative to the true centroid time are plotted.

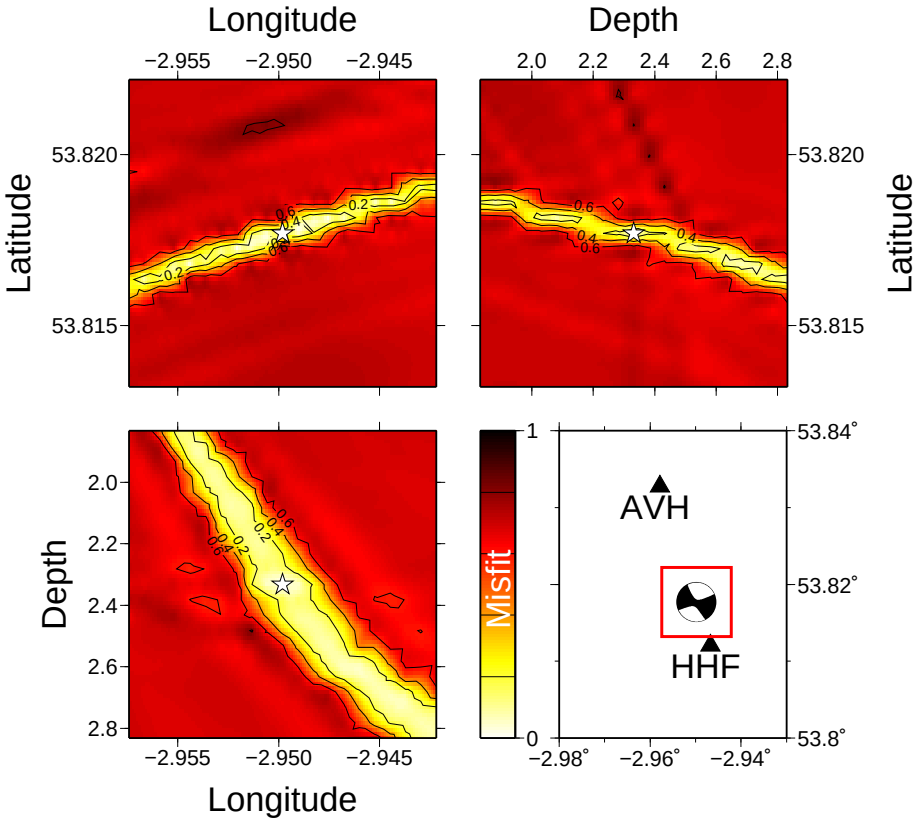

Figure 6.13: As for Figure 6.11 except that six channels of synthetic data — three from each of the stations shown — were used in the inversion.

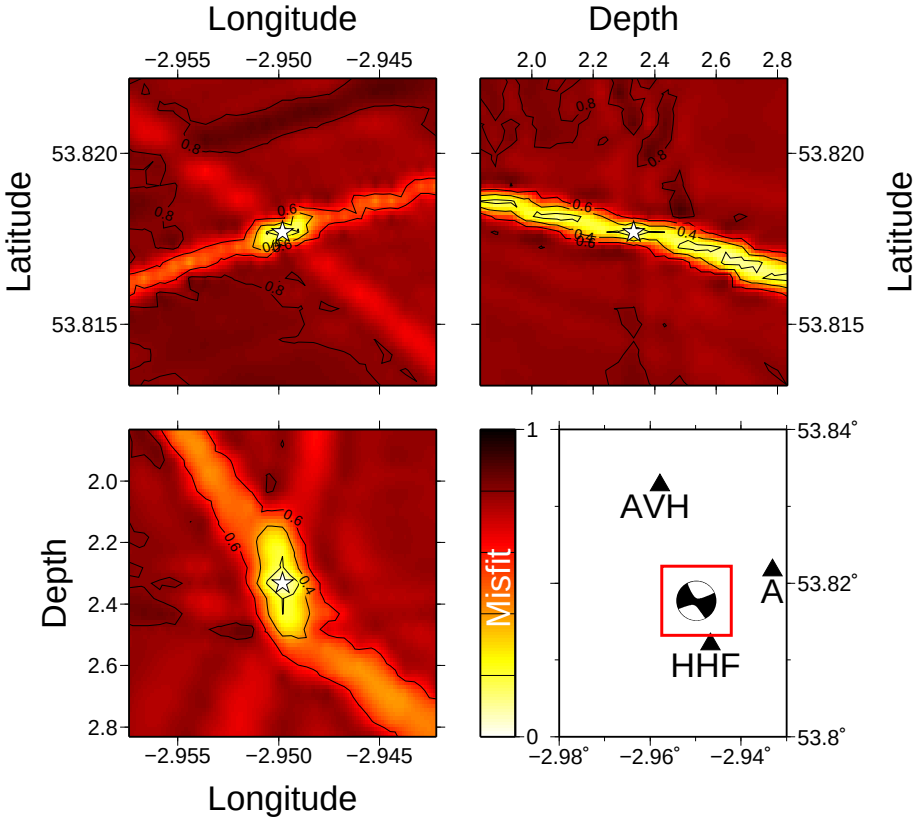

Figure 6.14: As for Figure 6.13 except that three component synthetics from station A were also used in the inversion.

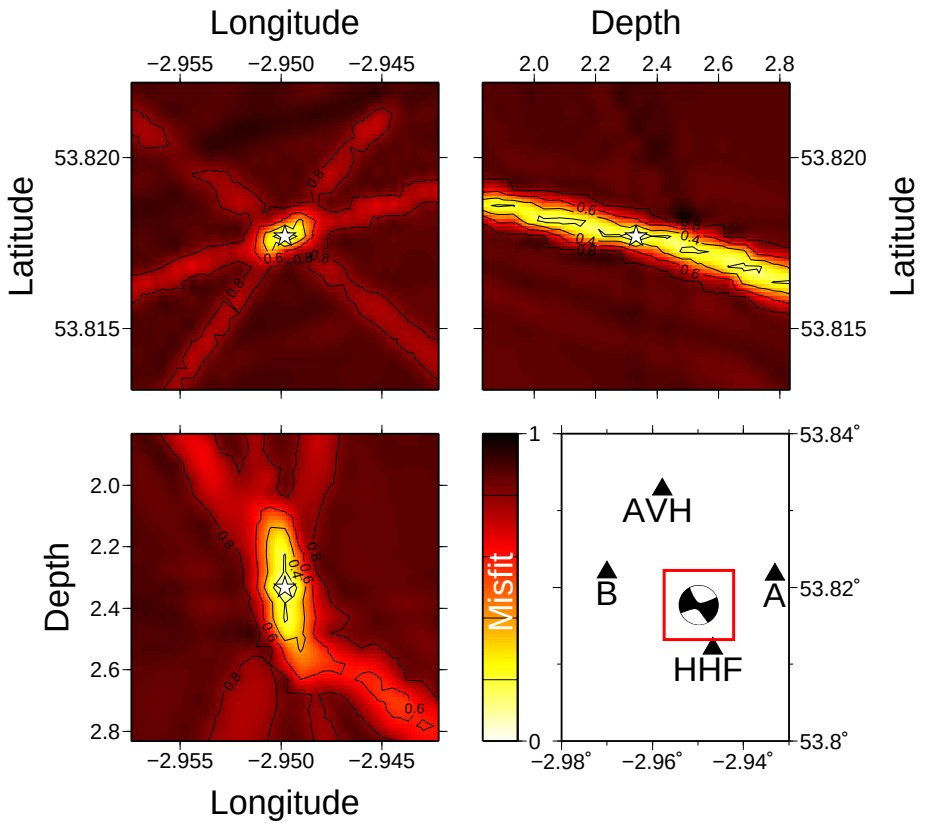

Figure 6.15: As for Figure 6.14 except that three component synthetics from station B were also used in the inversion.

An inadequate monitoring network appears to be a common feature amongst the known examples of injection induced seismicity related to shale gas — at Preese Hall, in Oklahoma and in British Columbia. This lack of data makes it difficult for seismologists to understand what went wrong after the event, and perhaps goes some way to explaining the levels of public concern about shale gas exploration and extraction. We note that legislation is expected to require microseismic monitoring of future onshore shale gas operations in the UK, and hope that these data will be made publicly available so that our understanding of the hydraulic fracturing process, and its associated risks, can be further studied.

Chapter 7

Concluding remarks

In this thesis, we have seen that high-rate GPS time series can be treated in much the same way as conventional seismogram data and used to study the earthquake source. The efficient and stable methods for computing seismo-geodetic observables in planar earth models that we have developed mean that real-time inversion of static displacement data is now possible with a minimal amount of *a priori* knowledge and computational resources. In principle, real-time inversion of the GPS waveform data themselves could now be achieved and, with access to a computational cluster, near real-time inversions for the spatio-temporal evolution of slip on a finite fault may even be within reach.

Another exciting opportunity for GPS seismology is presented by the addition of a third carrier frequency, L5, on the current generation of GPS satellites, which may be particularly useful for real-time applications as it enables rapid resolution of the integer ambiguity in carrier phase measurements of pseudorange (Geng and Bock, 2013). The relatively low cost of GPS receivers relative to seismometers (e.g. Houlié *et al.*, 2011), and the development of techniques for combining accelerometer and GPS data into broadband displacement time series with high sampling rates (e.g Bock *et al.*, 2011) also means that the field of GPS seismology should continue to grow as more observations of seismic displacement fields are made with these instruments. A particularly promising opportunity

for reducing the errors in source parameters determined from teleseismic data is presented by the possibility of performing joint inversions of conventional seismic data combined with GPS or other near-field observations. This thesis has developed the tools which should enable joint inversion experiments to be carried out.

A challenge to the wider use of GPS data for seismology is the fact that there is not yet a standard method for processing the raw observables into time series, nor is there an accepted format for archiving the resulting waveforms so that they can be conveniently used by seismologists. Attempts have been made to use existing repositories of seismic data, such as IRIS, for this purpose (e.g Larson, 2009), and we hope that it becomes standard practice to use these repositories, or ones that are specifically designed for GPS waveforms, for data archiving purposes. This undertaking would facilitate the use of GPS waveform data in tomographic inversions for earth structure, which are an obvious extension of the work presented here.

We have also seen that high-frequency waveform recordings of microearthquakes, made by seismic instruments deployed at the surface or in borehole arrays, can be used to study microseismic sources. As hydrocarbon fields become more densely instrumented, we anticipate that microseismic tomography will also be possible.

Preliminary analyses of a downhole microseismic monitoring dataset from Cotton Valley suggest that reliable moment tensor inversion using data from a single monitoring well may not be possible, although a more thorough resolution analysis than that presented here is required to verify this result. The treatment of microseismic data within our inversion framework could be refined by defining multiple data slices so that, for example, P- and S-waveforms are weighted appropriately. Presently, the use of a least squares misfit function and a single data window means that the inversion only attempts to fit the much larger amplitude S-wave arrival. It would also be interesting to investigate what effect the use a different misfit function would have, although such an undertaking would obviously mean that an alternative method of solution of the inverse problem would be required. The question of an appropriate misfit function is also relevant for GPS waveform data,

since a mismatch between the observed and modelled static offset will contribute to the total misfit at every time step and may, as a result, mean that this is the only part of the signal that the inversion tries to fit.

Related to the problem of monitoring microearthquakes, we have seen that waveform inversion may be useful for studying the source mechanisms of small, induced, earthquakes, using data from anomalous seismic events at Preese Hall as a case study. Using the waveform — rather than just parameters extracted from it — is useful when, as is often the case, monitoring arrays are limited, and could be applied very much more widely than is presently the case.

This thesis has mainly been concerned with developing new methods for the analysis of near-field seismic observables. We have also shown that a number of different types of data might be suitably treated using these techniques, and that the derived information is useful in a variety of contexts. It is not inconceivable that systematic analyses of near-field data using the CMT approach might lead to new insights into the seismic source. We leave this task to future researchers, and hope that they might also find additional uses for the methods described herein.

Appendix A

prop8a synthetic seismograms package

prop8a computes displacement spectra arising from a buried point source in a layered elastic and isotropic medium. The theory implemented by this algorithm is described in O'Toole and Woodhouse (2011), a pdf of which is included in this distribution. The main advantage of this method is that it is stable at all frequencies, including zero frequency, and so is useful for calculating displacement seismograms that include the static offset. Performing the calculation solely at 0 Hz yields an image of the static surface deformation, and so this algorithm may also be useful for geodetic studies of co-seismic displacements.

Since prop8a computes spectra, the output must be processed to obtain seismograms or static displacement fields. I include a minimal set of Matlab functions to enable the user to get started. Use help <function_name> within Matlab for information and examples.

In this documentation I have tried to give a fairly complete description of how to use prop8a. Of course, the only reliable record of the program's behaviour is the source code itself, and any user is encouraged to acquaint themselves with this as much as possible. Hopefully, the fact that the structure and naming conventions used in O'Toole and Woodhouse (2011) follow closely those used in the code will make this task a little easier.

While every effort has been made to validate the code and ensure that it is bug free, the usual caveats apply; the code is supplied "as is" and no warranty is given. If you encounter problems, you are welcome to contact the author by email at thomas.otoole@earth.ox.ac.uk, but we do not intend to provide detailed technical support. The author would be pleased to receive reports of bugs, comments and suggestions for improvements to the code and documentation.

Finally, a big thank you to Andrew Valentine at Utrecht University for (amongst many other things) much time and help checking that this software package ports to at least one system outside of Oxford.

A.1 Package contents

After extracting the tar archive, you should find the following:

`bin` directory

Holds the binary executable file (after compilation).

`Documentation` directory

Contains this documentation, as well as a `pdf` of O'Toole and Woodhouse (2011).

`Examples` directory

Contains some example input files, and the corresponding output files in the subdirectory `Sample_output`.

`obj` directory

Holds object files (after compilation).

`src` directory

Contains the `prop8a.f` source code.

`Makefile`

For compiling the code.

MATLAB directory

Contains the following MATLAB functions for processing and plotting .o8 output files from prop8a. These output files contain spectra calculated at equally spaced radii, which are independent of source-receiver azimuth (see §A.5 for a more detailed description of output from prop8a).

- tbot_get_args.m – reads in prop8a input arguments, some of which are needed for post-processing.
- tbot_static_o8.m – for generating and plotting static displacement fields. Reads a .o8 file containing spectra calculated only at zero frequency and generates static displacements at a specified number of azimuths to produce an image of the surface co-seismic deformation.
- tbot_dynamic_o8.m – for generating and plotting seismograms at equally spaced radii along a specified source-receiver azimuth. Reads a .o8 file containing spectra output at many frequencies.

No Matlab routines for the processing of .o9 (displacements at specific stations) or .o7 (wavenumber integrands) output files are provided; these are left as an exercise for the user.

A.2 Compilation

The source code has been successfully compiled and executed on `i686`, `x86_64` and `sun4` architectures. Compilers I have used successfully are

- the Sun Studio 12.1 Fortran compiler `f95`.
- the GNU Fortran compiler `gfortran`.
- g77.
- g95.

A `Makefile` is supplied which will likely need to be edited to suit your system; set `FCOMPILER` to your preferred `Fortran` compiler, and compile using

```
hooch% make all
```

Assuming a successful compile, you will have created the object `obj/prop8a.o` and executable binary `bin/prop8a`. Use

```
hooch% make clean
```

to remove these files for a clean compilation. *Please let the author if you have any compile problems, so that the source code and documentation can be kept up to date.*

A.3 Execution

prop8a reads in a single input file, named as a command line argument. This file contains a number of parameters which control the type of calculation being carried out (e.g. whether you wish to calculate spectra at many frequencies to obtain seismograms c.f. just at zero frequency to obtain the static displacement), the fault parameters, and earth model. Displacement spectra can be calculated

1. independently of source-receiver azimuth for equally spaced radii (in which case output is written to a file with the suffix .o8), or
2. at specific stations specified in the input file (output is then to files ending .o9).

More information about input and output to/from prop8a are given in § A.4 and A.5.

Assuming that the binary executable is in your search path, the command

```
hooch% prop8a <path_to_input_file>
```

will begin computation of displacement spectra. Depending on the inputs, output is written either to <inputfile>.o8 or <inputfile>.o9 – in both cases <inputfile>.o7 may also be written out optionally.

The following example input files are included in the Examples directory: Homog_static, PapMak_dynamic, PapMak_dynamic_o9 and PapMak_dynamic_o9_write7. The corresponding output files are also included in Examples/Sample_output, with the exception of PapMak_dynamic_o9_write7.o7 as this file is very large!

A.4 Input

Input parameters are read from an ASCII file, whose name is given as a command line argument. Take a look at the file `PapMak_dynamic` included in the `Examples` directory. The input file is structured as follows:

```
fmin fmax nord
kmax nk
alpha
write7

year month day hour minute second
lat lon sdep
scmom phs del rlam

ifradii rmin rmax nradii
stnam1 stlat1 stlon1 stelv1
...
stnamN stlatN stlonN stelvN

dep1 vp1 vs1 rho1
...
depN vpN vsN rhoN
```

Hopefully the meanings of these variables are fairly obvious. Explicitly:

`double precision fmin, fmax` = min./max. frequency to solve at (Hz)

`integer nord` = order of Fourier transform

`double precision kmax` = maximum wavenumber to solve at (km^{-1})

`integer nk` = number of wavenumbers to use

`double precision alpha` = imaginary frequency component

`integer write7` = flag to write out `.o7` file

`year, month, day, hour, minute, second` = event time (unused)

`double precision lat, lon, sdep` = source lat, lon (°), depth (km)

`real scmom, phs, del, rlam` = moment (dyn-cm), strike, dip, rake (°)

`integer ifradii` = flag to write out `.o8` c.f. `.o9` file

`double precision rmin, rmax` = min./max. radii to solve at (km)

`integer nradii` = number of radii to use

`character*5 stnam(i)` = station name

`double precision stlat(i), stlon(i)` = station latitude, longitude (°)

`double precision dep(j)` = layer thickness (km)

`complex double precision vp(j), vs(j)` = layer P and S velocity (km/s)

`complex double precision rho(j)` = layer density (kg/m^3)

The last lines of the input file describe the earth model to use in the calculation. Each line corresponds to a layer in the model; the first line corresponding to the top layer; the final line corresponding to the underlying halspace. It is required that this final layer has thickness `dep` $\geq$ 900 km, so `prop8a` knows that this layer terminates the earth model.

A.5 Output

Output will always be written to either `<inputfile>.o8` or `<inputfile>.o9`. If `write7`= 1 then additionally a `<inputfile>.o7` file will be written. Each output file contains a header which supplies the information needed to read the output into another program for inverse Fourier transforming or plotting.

`.o7` file: output wavenumber integrands if `write7`= 1

If you want to write out the wavenumber kernels before the integration over wavenumber, perhaps to check that you have chosen appropriate values for `kmax` and `nk`, set `write7`= 1.

The start of the `.o7` output file looks like:

```
integrands     6
omega       0.00000E+00  6.28319E+00   257
k           0.00000E+00  2.04000E+00  1200
station     1.00000E+00  5.00000E+00     5
component   1.00000E+00  3.00000E+00     3
m          -2.00000E+00  2.00000E+00     5
r/i         1.00000E+00  2.00000E+00     2
0.00000E+00  0.00000E+00  0.00000E+00  0.00000E+00  0.00000E+00  0.00000E+00  0.00000E+00  0.00000E+00  0.00000E+00  0.00000E+00
0.00000E+00  0.00000E+00  0.00000E+00  0.00000E+00  0.00000E+00  0.00000E+00  0.00000E+00  0.00000E+00  0.00000E+00  0.00000E+00
etc.
```

where `integrands` is a reminder of what is being written out, and the following `6` indicates how many more header lines to expect. These lines tell us that integrands have been written out for `257` angular frequencies between 0 and 2π rad/s, 1200 wavenumbers between 0 and 2.04 km^{-1}, at 5 stations, for all 3 components (r, ϕ, z), for $m \in \{-2, -1, 0, 1, 2\}$ and these complex values have been written out as real/imaginary pairs.

The following `nfrq` $\times$ `nk` $\times$ `nsta` $\times$ `ncomponent` lines contain the integrands; the ten values on each line correspond to the real and imaginary parts of the integrands for all 5 m values.

Warning: these `.o7` files can be extremely large due to the number of values being written out.

.o8 file: spectra at equally spaced radii if ifradii= 1

If you want to calculate displacement spectra at *nradii* equally spaced epicentral distances between *rmin* and *rmax* km, set `ifradii` = 1. In this case, the station information given in the input file is not used, and the output spectra $U_m(r, \omega)$ can be used to generate displacements at *any* azimuth ϕ, via

$$U(r, \omega, \phi) = \sum_{m=-2}^{2} U_m(r, \omega) \mathrm{e}^{\mathrm{i}m\phi} \,. \tag{A.1}$$

For example, the seismograms shown in Fig. 1 of O'Toole and Woodhouse (2011) were generated using spectra output as a `.o8` file – seismograms for any other azimuth could have also been produced from this same output file. The start of the `.o8` output file looks like:

```
integrals      5
f           0.00000E+00  1.00000E+00   257
r           1.00000E+01  2.00000E+02    20
component   1.00000E+00  3.00000E+00     3
m          -2.00000E+00  2.00000E+00     5
r/i         1.00000E+00  2.00000E+00     2
 2.35812E+02 -2.81030E+02 -8.06008E-05 -2.93363E-05  0.00000E+00  0.00000E+00 -8.06008E-05  2.93363E-05  2.35812E+02  2.81030E+02
-4.74587E+01 -3.98226E+01 -9.28877E-07  2.55207E-06  0.00000E+00  0.00000E+00 -9.28877E-07 -2.55207E-06 -4.74587E+01  3.98226E+01
etc.
```

The header is structured similarly to that of the `.o7` file. Here, the `integrals` have been written out, for `257` frequencies between 0 and 1 Hz, at 20 equally spaced stations between 10 and 200 km, for all 3 components (r, ϕ, z), for $m \in \{-2, -1, 0, 1, 2\}$ and these complex values have been written out as real/imaginary pairs.

The following `nfrq` × `nsta` × `ncomponent` lines contain the spectra; the ten values on each line correspond to the real and imaginary parts of the spectra for all 5 m values.

`.o9` file: spectra at specific stations if `ifradii`$\neq 1$

If you want to calculate displacement spectra at the specific stations given in the input file, set `ifradii` $= 0$. In this case, the azimuthal scaling and summation over m given by (A.1) is done internally by `prop8a`.

The start of the `.o9` output file looks like:

```
spectra        4
f           0.00000E+00  1.00000E+00   257
station     1.00000E+00  5.00000E+00     5
component   1.00000E+00  3.00000E+00     3
r/i         1.00000E+00  2.00000E+00     2
-3.84454E+00  0.00000E+00  8.07474E-02  0.00000E+00 -5.12198E-01  0.00000E+00
-8.92649E+00 -2.22045E-16  1.62233E-01  0.00000E+00 -2.51917E+00  5.55112E-17
etc.
```

Spectra are output for `257` frequencies between 0 and 1 Hz, at the 5 stations given in the input file, for all 3 components, and these complex values have been written out as real/imaginary pairs. Since the summation over m is done by `prop8a`, after the header there follows `nfrq` $\times$ `nsta` lines, the six values per line correspond to real and imaginary parts of the spectra for all 3 components.

A.6 Examples

Computing static displacements: Homog_static

The example input file `Homog_static` (included below) can be used to calculate static displacements at 201 radii from 0 to 200 km in a homogeneous half-space. What output file(s) will this input generate?

```
0.0   0.0  -1                    # fmin fmax nord (nfrq=2**nord+1). -1 to calculate for a single frequency
2.04   1200                      # kmax nk
0.0                              # alpha
0                                # flag to write out integrands on unit 7

2000 01 02 03 04 05.0            # event time
12.34 56.78 34.0                 # lat lon depth
2.4e+27 340.0 90.0 0.0           # M0 (dyn-cm) strike, dip, rake

1  0.0 200.0 201                 # flag to use equally spaced radii, rmin, rmax, nradii
OXFO 51.752  -1.258 130.00       # station names and lat,lon elv
GREN 51.478  00.000  46.00
                                 # blank station name to end station list
 1.e5   6.00   3.46   2.70       # homogenous halfspace
```

Since `nord` $= -1$ here, and `nfrq` $= 2^{\texttt{nord}} + 1$, Fortran gets `nfrq` $= 1$. Given that `fmin` $=$ `fmax` $= 0$ this input file therefore corresponds to doing the calculation at a single frequency, $f = 0$ Hz, i.e. the static calculation. As `ifradii` $= 1$, we compute spectra at 201 radii from 0 to 200 km. Even though some station information and the event latitude/longitude are provided, they are not used in any way. Using the output with (A.1) at many equally spaced azimuths allows an image similar to that shown in Fig. 2 of O'Toole and Woodhouse (2011) to be produced. Using the supplied `Matlab` function `tbot_static_o8('Homog_static',100)` you should be able to reproduce Fig. A.1

Note that ***alpha*** *should always be set to zero when you are carrying out just the static calculation.*

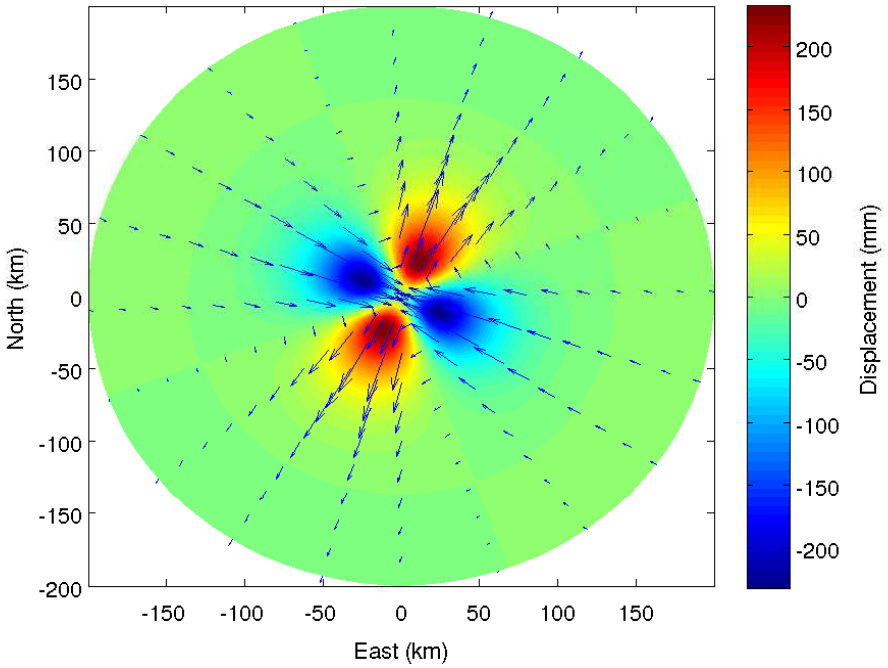

Figure A.1: Example static displacement output processed and plotted using the supplied `Matlab` function `tbot_static_o8.`

Computing displacement spectra at equally spaced radii: PapMak_dynamic

The example input file `PapMak_dynamic` (included below) can be used to calculate seismograms at 20 radii from 10 to 200 km in a plane layered medium.

```
0.0   1.0  8                    # fmin fmax nord (nfrq=2**nord+1). -1 to calculate for a single frequency
2.04   1200                     # kmax nk
0.023                           # alpha
0                               # flag to write out integrands on unit 7

2008 02 14 10 09 29.0           # event time
36.24 21.79 20.0                # lat lon depth
2.4e+27 340.0 90.0 0.0          # M0 (dyn-cm) strike, dip, rake

1  10.0 200.0 20                # flag to use equally spaced radii, rmin, rmax, nradii
                                # blank station name to end station list
 3.0   1.80   0.00   1.02       # Earth model from Papoulia and Makris (2004)
 2.0   4.50   2.40   2.57
 5.0   5.80   3.30   2.63
20.0   6.50   3.65   2.85
1.e5   8.00   4.56   3.34
```

Displacement spectra will be calculated for 257 frequencies between 0 and 1 Hz. Note that `alpha` $\neq 0$ for the dynamic calculation (see § 2.5 of O'Toole and Woodhouse

(2011)). Using the supplied Matlab function `tbot_dynamic_o8('PapMak_dynamic',10,3)` you should be able to reproduce Fig. A.2.

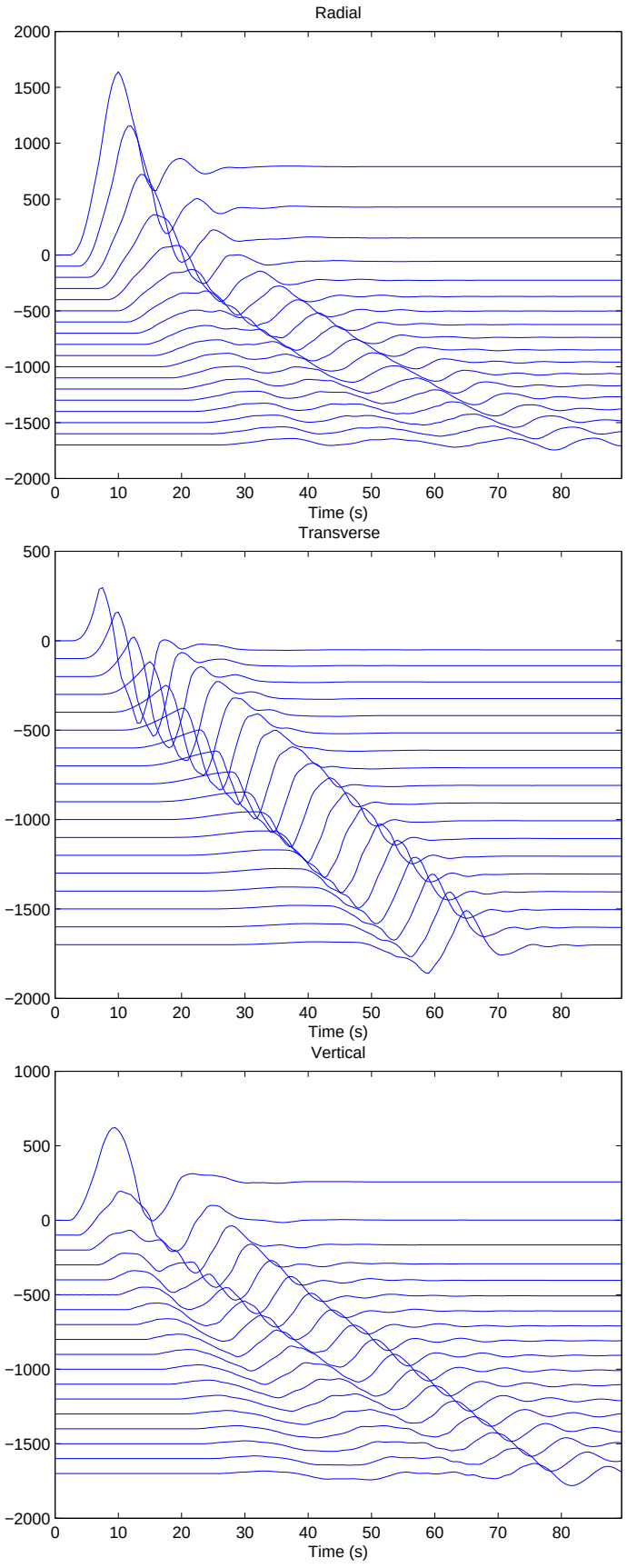

Figure A.2: Example dynamic displacement output processed and plotted using the supplied `Matlab` function `tbot_dynamic_o8.`

Computing displacement spectra at specific stations: PapMak_dynamic_o9

The example input file `PapMak_dynamic_2` (included below) can be used to calculate seismograms at the 5 stations given in this file. Compare it to `PapMak_dynamic` and `PapMak_dynamic_o9_write7`.

```
0.0   1.0  8                      # fmin fmax nord (nfrq=2**nord+1). -1 to calculate for a single frequency
2.04   1200                       # kmax nk
0.023                             # alpha
0                                 # flag to write out integrands on unit 7

2008 02 14 10 09 29.0             # event time
36.24 21.79 30.0                  # lat lon depth
2.4e+26 332.0 6.0 120.0           # M0 (dyn-cm) strike, dip, rake

0  0.0 200.0 201                  # flag to use equally spaced radii, rmin, rmax, nradii
SPRT 37.046015469    22.372099077    815.0011021   # station names and lat,lon elv
METH 36.825514429    21.704568928     76.1910688
VASS 37.430444728    21.899262528   1176.7780294
KITH 36.274524356    23.015162686    338.4237486
KERY 36.493270697    22.383514667    199.7927826
                                  # blank station name to end station list
 3.0   1.80   0.00   1.02         # Earth model
 2.0   4.50   2.40   2.57         # Earth model from Papoulia and Makris (2004)
 5.0   5.80   3.30   2.63
20.0   6.50   3.65   2.85
1.e5   8.00   4.56   3.34
```

Note that the `ifradii` flag is set to zero, meaning that spectra will be output for the 5 stations supplied. No `Matlab` routines for the processing of `.o9` output are provided; this is left as an exercise for the user.

A.7 General notes

Both dynamic and static displacements calculated using `prop8a` have been validated against other algorithms, as described in O'Toole and Woodhouse (2011). Users should carefully read the end of § 2.5 of this paper for guidance on choosing input parameters like `alpha`, and the wavenumber spacing Δ`k` – these must be sensibly chosen if accurate output is to be produced!

At present, receivers are assumed to be at the surface, although the only actual restriction on their location is that they are above the source depth.

Bibliography

Abo-Zena, A. Dispersion function computations for unlimited frequency values. *Geophysical Journal of the Royal Astronomical Society*, 58, pp. 91–105, 1979.

Aki, K. and Richards, P.G. *Quantitative Seismology*. University Science Books, second edn., 2002.

Al-Attar, D. and Woodhouse, J.H. Calculation of seismic displacement fields in self-gravitating earth models—applications of minors vectors and symplectic structure. *Geophysical Journal International*, 175, pp. 1176–1208, 2008.

Allen, R. Earthquake Hazard Mitigation: New Directions and Opportunities. In H. Kanamori, ed., *Earthquake Seismology*, vol. 4 of *Treatise on Geophysics*, chap. 21, pp. 607–647. Elsevier, Amsterdam, 2007.

Allen, R.M., Gasparini, P., Kamigaichi, O. and Bose, M. The Status of Earthquake Early Warning around the World: An Introductory Overview. *Seismological Research Letters*, 80, pp. 682–693, 2009.

Allen, R.M. and Ziv, A. Application of real-time GPS to earthquake early warning. *Geophysical Research Letters*, 38, 2011.

Ammon, C.J., Ji, C., Thio, H.K., Robinson, D., Ni, S., Hjorleifsdottir, V., Kanamori, H., Lay, T., Das, S., Helmberger, D., Ichinose, G., Polet, J. and Wald, D. Rupture rocess of the 2004 Sumatra-Andaman earthquake. *Science*, 308, pp. 1133–1139, 2005.

Ammon, C.J., Lay, T., Kanamori, H. and Cleveland, M. A rupture model of the great 2011 Tohoku earthquake. *Earth, Planets and Space*, 20, pp. 1–4, 2011.

Amoruso, a., Crescentini, L. and Fidani, C. Effects of crustal layering on source parameter inversion from coseismic geodetic data. *Geophysical Journal International*, 159, pp. 353–364, 2004.

Avallone, A., Marzario, M., Cirella, A., Piatanesi, A., Rovelli, A., Di Alessandro, C., D'Anastasio, E., D'Agostino, N., Giuliani, R. and Mattone, M. Very high rate (10 Hz) GPS seismology for moderate-magnitude earthquakes: The case of the M_w 6.3 L'Aquila (central Italy) event. *Journal of Geophysical Research*, 116, 2011.

Backus, G.E. Interpreting the seismic glut moments of total degree two or less. *Geophysical Journal of the Royal Astronomical Society*, pp. 1–25, 1977.

Backus, G. and Mulcahy, M. Moment Tensors and other Phenomenological Descriptions of Seismic Sources — I. Continuous Displacements. *Geophysical Journal of the Royal Astronomical Society*, 46, pp. 341–361, 1976.

Baig, A. and Urbancic, T. Magnitude Determination, Event Detectability, and Assessing the Effectiveness of Microseismic Monitoring Programs in Petroleum Applications. *CSEG Recorder*, (February), pp. 23–27, 2010a.

———. Microseismic moment tensors: A path to understanding frac growth. *The Leading Edge*, 29, pp. 320–324, 2010b.

———. Microseismic Detectability from Stacking Signals on Near-Surface Arrays. *SEG Technical Program Expanded Abstracts*, 2012.

Banerjee, P., Pollitz, F.F. and Bürgmann, R. The size and duration of the Sumatra-Andaman earthquake from far-field static offsets. *Science*, 308, pp. 1769–1772, 2005.

Barbot, S., Lapusta, N. and Avouac, J.P. Under the hood of the earthquake machine: toward predictive modeling of the seismic cycle. *Science*, 336, pp. 707–710, 2012.

Beroza, G.C. and Kanamori, H. Comprehensive Overview. In H. Kanamori, ed., *Earthquake Seismology*, Treatise on Geophysics, chap. 1, pp. 1–58. Elsevier, Amsterdam, 2007.

Bilich, A., Cassidy, J.F. and Larson, K.M. GPS Seismology: Application to the 2002 M_w 7.9 Denali Fault Earthquake. *Bulletin of the Seismological Society of America*, 98, pp. 593–606, 2008.

Bleakly, D.C., Wolfe, J.E., Leslie, I., Prince, M., Shumila, V. and Urbancic, T. Using Multi-Well Microseismicity to Identify Fracture Types Associated with Hydraulic Fracture Stimulations. *CSEG Recorder*, (September), pp. 48–51, 2007.

Blewitt, G. Carrier phase ambiguity resolution for the Global Positioning System applied to geodetic baselines up to 2000 km. *Journal of Geophysical Research*, 94, pp. 10,187–10,203, 1989.

———. GPS and Space-Based Geodetic Methods. In T. Herring, ed., *Geodesy*, Treatise on Geophysics, chap. 11, pp. 351–390. Elsevier, Amsterdam, 2007.

Blewitt, G., Heflin, M.B., Hurst, K.J., Jefferson, D.C., Webb, F.H. and Zumberge, J.F. Absolute far-field displacements from the 28 June 1992 Landers earthquake sequence. *Nature*, 361, pp. 340–342, 1993.

Blewitt, G., Hammond, W.C., Kreemer, C., Plag, H.P., Stein, S. and Okal, E. GPS for real-time earthquake source determination and tsunami warning systems. *Journal of Geodesy*, 83, pp. 335–343, 2009.

Blewitt, G., Kreemer, C., Hammond, W.C., Plag, H.P., Stein, S. and Okal, E. Rapid determination of earthquake magnitude using GPS for tsunami warning systems. *Geophysical Research Letters*, 33, 2006.

Bock, Y. Continuous monitoring of crustal deformation. *GPS World*, 2, pp. 40–47, 1991.

Bock, Y., Agnew, D.C., Fang, P., Genrich, J.F., Hager, B.H., Herring, T.A., Hudnut, K.W., King, R.W., Larsen, S., Minster, J.B., Stark, K., Wdowinski, S. and Wyatt, F.K. Detection of crustal deformation from the Landers earthquake sequence using continuous geodetic measurements. *Nature*, 361, pp. 337–340, 1993.

Bock, Y., Melgar, D. and Crowell, B.W. Real-Time Strong-Motion Broadband Displacements from Collocated GPS and Accelerometers. *Bulletin of the Seismological Society of America*, 101, pp. 2904–2925, 2011.

Bock, Y., Nikolaidis, R.M., de Jonge, P.J. and Bevis, M. Instantaneous geodetic positioning at medium distances with the Global Positioning System. *Journal of Geophysical Research*, 105, pp. 28,223–28,253, 2000.

Bock, Y., Prawirodirdjo, L. and Melbourne, T.I. Detection of arbitrarily large dynamic ground motions with a dense high-rate GPS network. *Geophysical Research Letters*, 31, 2004.

British Columbia Oil and Gas Commission. Investigation of Observed Seismicity in the Horn River Basin. 2012.

Bulant, P., Eisner, L., Pšenčik, I. and Calvez, J.L. Importance of borehole deviation surveys for monitoring of hydraulic fracturing treatments. *Geophysical Prospecting*, 55, pp. 891–899, 2007.

Bürgmann, R., Rosen, P.a. and Fielding, E.J. Synthetic Aperture Radar Interferometry to Measure Earths Surface Topography and Its Deformation. *Annual Review of Earth and Planetary Sciences*, 28, pp. 169–209, 2000.

Burridge, R. and Knopoff, L. Body force equivalents for seismic dislocations. *Bulletin of the Seismological Society of America*, 54, pp. 1,875–1,888, 1964.

Chambers, K., Clarke, J. and Wilson, S. Imaging Moment Tensors from Surface Arrays. *Proceedings of the fourth EAGE Passive Seismic Workshop*, 2013.

Chambers, K., Kendall, J.M., Brandsberg-Dahl, S. and Rueda, J. Testing the ability of surface arrays to monitor microseismic activity. *Geophysical Prospecting*, 58, pp. 821–830, 2010.

Chapman, C.H. A new method for computing synthetic seismograms. *Geophysical Journal of the Royal Astronomical Society*, 54, pp. 481–518, 1978.

———. Yet another elastic plane-wave, layer-matrix algorithm. *Geophysical Journal International*, 154, pp. 212–223, 2003.

———. *Fundamentals of Seismic Wave Propagation*. Cambridge University Press, 2004.

Choi, K., Bilich, A., Larson, K.M. and Axelrad, P. Modified sidereal filtering: Implications for high-rate GPS positioning. *Geophysical Research Letters*, 31, 2004.

Cormier, V.F. Theory and Observations - Forward Modeling / Synthetic Body Wave Seismograms. In B. Romanowicz and A. Dziewonski, eds., *Seismology and Structure of the Earth*, Treatise on Geophysics, chap. 5, pp. 157–189. Elsevier, Amsterdam, 2007.

Crowell, B.W., Bock, Y. and Squibb, M.B. Demonstration of Earthquake Early Warning Using Total Displacement Waveforms from Real-time GPS Networks. *Seismological Research Letters*, 80, pp. 772–782, 2009.

Crowell, B.W., Bock, Y. and Melgar, D. Real-time inversion of GPS data for finite fault modeling and rapid hazard assessment. *Geophysical Research Letters*, 39, 2012.

Das, S. and Kostrov, B. Diversity of solutions of the problem of earthquake faulting inversion; application to SH waves for the great 1989 Macquarie Ridge earthquake. *Physics of the Earth and Planetary Interiors*, 85, pp. 293–318, 1994.

Davis, J.P. and Smalley, R. Love wave dispersion in central North America determined using absolute displacement seismograms from high-rate GPS. *Journal of Geophysical Research*, 114, 2009.

Davis, S. and Frohlich, C. Did (or will) fluid injection cause earthquakes?-criteria for a rational assessment. *Seismological Research Letters*, 64, 1993.

Delouis, B., Nocquet, J.M. and Vallée, M. Slip distribution of the February 27, 2010 Mw = 8.8 Maule Earthquake, central Chile, from static and high-rate GPS, InSAR, and broadband teleseismic data. *Geophysical Research Letters*, 37, 2010.

Department of Energy & Climate Change. Synopsis of main questions raised in responses to DECC consultation on mitigation of seismic risks from hydraulic fracturing for shale gas , with Government responses. 2012.

Dewey, J. and Byerly, P. The early history of seismometry (to 1900). *Bulletin of the Seismological Society of America*, 59, pp. 183–227, 1969.

Dinske, C., Shapiro, S.a. and Rutledge, J.T. Interpretation of Microseismicity Resulting from Gel and Water Fracturing of Tight Gas Reservoirs. *Pure and Applied Geophysics*, 167, pp. 169–182, 2009.

Dunkin, J.W. Computation of modal solutions in layered, elastic media at high frequencies. *Bulletin of the Seismological Society of America*, 55, pp. 335–358, 1965.

Duputel, Z. and Rivera, L. Uncertainty estimations for seismic source inversions. *Geophysical Journal International*, 190, pp. 1243–1256, 2012.

Dziewonski, A. and Woodhouse, J.H. Studies of the seismic source using normal–mode theory. In H. Kanamori and E. Boschi, eds., *Earthquakes: Observation, Theory and Interpretation, Proceedings of the International School of Physics "Enrico Fermi", Course LXXXV*, pp. 45–137. 1983a.

Dziewonski, A.M., Chou, T.A. and Woodhouse, J.H. Determination of Earthquake Source Parameters From Waveform Data for Studies of Global and Regional Seismicity. *Journal of Geophysical Research*, 86, pp. 2825–2852, 1981.

Dziewonski, A.M. and Romanowicz, B.A. Overview. In B.A. Romanowicz and A.M. Dziewonski, eds., *Seismology and Structure of the Earth*, Treatise on Geophysics, chap. 1, pp. 1–31. Elsevier, Amsterdam, 2007.

Dziewonski, A.M. and Anderson, D.L. Preliminary reference Earth model. *Physics of the Earth and Planetary Interiors*, 25, pp. 297–356, 1981.

Dziewonski, A.M. and Woodhouse, J.H. An Experiment In Systematic Study Of Global Seismicity: Centroid–Moment Tensor Solutions For 201 Moderate And Large Earthquakes Of 1981. *Journal of Geophysical Research*, 88, pp. 3247–3271, 1983b.

Dziewonski, A., Friedman, A., Giardini, D. and Woodhouse, J. Global seismicity of 1982: centroid-moment tensor solutions for 308 earthquakes. *Physics of the Earth and Planetary Interiors*, 33, pp. 76–90, 1983.

Eaton, D. Resolution of microseismic moment tensors: A synthetic modeling study. *SEG Technical Program Expanded Abstracts*, pp. 3569–3573, 2009.

Eisner, L., Williams-Stroud, S., Hill, A., Duncan, P. and Thornton, M. Beyond the dots in the box: Microseismicity-constrained fracture models for reservoir simulation. *The Leading Edge*, 29, pp. 326–333, 2010.

Eisner, L., Janská, E., Opršal, I. and Matoušek, P. Seismic analysis of the events in the vicinity of the Preese Hall well. 2011.

Ekström, G., Nettles, M. and a.M. Dziewoski. The global CMT project 20042010: Centroid-moment tensors for 13,017 earthquakes. *Physics of the Earth and Planetary Interiors*, 200-201, pp. 1–9, 2012.

Elliott, J.R., Walters, R.J., England, P.C., Jackson, J.A., Li, Z. and Parsons, B. Extension on the Tibetan plateau: recent normal faulting measured by InSAR and body wave seismology. *Geophysical Journal International*, 183, pp. 503–535, 2010.

Elósegui, P., Davis, J.L., Oberlander, D., Baena, R. and Ekström, G. Accuracy of high-rate GPS for seismology. *Geophysical Research Letters*, 33, p. L11308, 2006.

Emore, G.L., Haase, J.S., Choi, K., Larson, K.M. and Yamagiwa, A. Recovering Seismic Displacements through Combined Use of 1-Hz GPS and Strong-Motion Accelerometers. *Bulletin of the Seismological Society of America*, 97, pp. 357–378, 2007.

Fialko, Y. Probing the mechanical properties of seismically active crust with space geodesy: Study of the coseismic deformation due to the 1992 M w 7.3 Landers (southern California) earthquake. *Journal of Geophysical Research*, 109, 2004.

Fox, B. *Seismic source parameter determination using regional intermediate-period surface waves*. Ph.D. thesis, University of Oxford, 2007.

Fox, B.D., Selby, N.D., Heyburn, R. and Woodhouse, J.H. Shallow seismic source parameter determination using intermediate-period surface wave amplitude spectra. *Geophysical Journal International*, 191, pp. 601–615, 2012.

Friederich, W. and Dalkolmo, J. Complete synthetic seismograms for a spherically symmetric earth by a numerical computation of the Green's function in the frequency domain. *Geophysical Journal International*, 122, pp. 537–550, 1995.

Frohlich, C., Hayward, C., Stump, B. and Potter, E. The Dallas-Fort Worth Earthquake Sequence: October 2008 through May 2009. *Bulletin of the Seismological Society of America*, 101, pp. 327–340, 2011.

Fuchs, K. and Müller, G. Computation of Synthetic Seismograms with the Reflectivity Method and Comparison with Observations. *Geophysical Journal of the Royal Astronomical Society*, 23, pp. 417–433, 1971.

Fukahata, Y. and Matsu'ura, M. General expressions for internal deformation fields due to a dislocation source in a multilayered elastic half-space. *Geophysical Journal International*, 161, pp. 507–521, 2005.

Ge, M., Gendt, G., Rothacher, M., Shi, C. and Liu, J. Resolution of GPS carrier-phase ambiguities in Precise Point Positioning (PPP) with daily observations. *Journal of Geodesy*, 82, pp. 389–399, 2007.

Geng, J. and Bock, Y. Triple-frequency GPS precise point positioning with rapid ambiguity resolution. *Journal of Geodesy*, 87, pp. 449–460, 2013.

Genrich, J. and Bock, Y. Rapid resolution of crustal motion at short ranges with the Global Positioning System. *Journal of Geophysical Research*, 97, pp. 3,261–3,269, 1992.

Genrich, J.F. and Bock, Y. Instantaneous geodetic positioning with 10-50 Hz GPS measurements: Noise characteristics and implications for monitoring networks. *Journal of Geophysical Research*, 111, 2006.

Giardini, D. and Grünthal, G. The GSHAP global seismic hazard map. *Annals of Geophysics*, 42, pp. 1,225–1,230, 1999.

Gilbert, F. Derivation of Source Parameters from Low-Frequency Spectra. *Philosophical Transactions of the Royal Society A: Mathematical, Physical and Engineering Sciences*, 274, pp. 369–371, 1973.

Gilbert, F. and Backus, G.E. Propagator matrices in elastic wave and vibration problems. *Geophysics*, 31, pp. 326–332, 1966.

Gilbert, F. and Dziewonski, A.M. An application of normal mode theory to the retrieval of structural parameters and source mechanisms from seismic spectra. *Philosophical Transactions of the Royal Society of London. Series A, Mathematical and Physical Sciences*, 278, pp. 187–269, 1975.

Gilbert, F. Excitation of the normal modes of the Earth by earthquake sources. *Geophysical Journal International*, pp. 223–226, 1970.

Gilligan, A. *Joint inversion of mantle wave and continuous GPS data for the fault mechanism to the 14th February 2008 M_w6.9 Greek earthquake.* Master's thesis, University of Oxford, 2010.

GMI. Wellbore Failure Analysis and Geomechanical Modelling in the Bowland Shale, Blackpool, UK. 2011.

Green, C.A., Styles, P. and Baptie, B.J. Prees Hall Shale Gas Fracturing Review & Recommendations For Induced Seismic Mitigation. 2012.

Guerrieri, L., Baer, G., Hamiel, Y., Amit, R., Blumetti, A.M., Comerci, V., Di Manna, P., Michetti, A.M., Salamon, A., Mushkin, A., Sileo, G. and

Vittori, E. InSAR data as a field guide for mapping minor earthquake surface ruptures: Ground displacements along the Paganica Fault during the 6 April 2009 L'Aquila earthquake. *Journal of Geophysical Research*, 115, 2010.

Gutenberg, B. and Richter, C.F. Frequency of earthquakes in California. *Bulletin of the Seismological Society of*, 34, pp. 32–35, 1944.

Hammond, W., Brooks, B., Bürgmann, R., Heaton, T., Jackson, M., Lowry, A. and Anandakrishnan, S. The Scientific Value of High-Rate, Low-Latency GPS Data. *White Paper*, Earthscope Plate Boundary Observatory Committee, Boulder, CO, 2010.

Harvey, T. and Gray, J. The Unconventional Hydrocarbon Resources of Britain's Onshore BasinsShale Gas. 2011.

Haskell, N.A. The dispersion of surface waves on multilayered media. *Bulletin of the Seismological Society of America*, 43, pp. 17–34, 1953.

Hauksson, E., Stock, J., Hutton, K., Yang, W., Vidal-Villegas, J.A. and Kanamori, H. The 2010 M w 7.2 El Mayor-Cucapah Earthquake Sequence, Baja California, Mexico and Southernmost California, USA: Active Seismotectonics along the Mexican Pacific Margin. *Pure and Applied Geophysics*, 168, pp. 1,255–1,277, 2010.

He, Y.M., Wang, W.M. and Yao, Z.X. Static deformation due to shear and tensile faults in a layered half-space. *Bulletin of the Seismological Society of America*, 93, pp. 2253–2263, 2003.

Hearn, E. and Bürgmann, R. The effect of elastic layering on inversions of GPS data for coseismic slip and resulting stress changes: Strike-slip earthquakes. *Bulletin of the Seismological Society of ...*, 95, pp. 1637–1653, 2005.

Hjörleifsdóttir, V. and Ekström, G. Effects of three-dimensional Earth structure on CMT earthquake parameters. *Physics of the Earth and Planetary Interiors*, 179, pp. 178–190, 2010.

Hofmann-Wellenhof, B., Licntenegger, H. and Collins, J. *GPS Theory and Practive*. Springer-Verlag Wien, fifth, revised edn., 2001.

Holland, A. Examination of possibly induced seismicity from hydraulic fracturing in the Eola Field, Garvin County, Oklahoma. 2011. http://www.protectsmc.org/impacts/Seismicity-Fracking_Oklahoma_OF1_2011.pdf.

Horton, S. Disposal of Hydrofracking Waste Fluid by Injection into Subsurface Aquifers Triggers Earthquake Swarm in Central Arkansas with Potential for Damaging Earthquake. *Seismological Research Letters*, 83, pp. 250–260, 2012.

Houlié, N., Occhipinti, G., Blanchard, T., Shapiro, N., Lognonné, P. and Murakami, M. New approach to detect seismic surface waves in 1 Hz-sampled GPS time series. *Scientific reports*, 1, p. 44, 2011.

Hsu, Y.J., Simons, M., Williams, C. and Casarotti, E. Three-dimensional FEM derived elastic Green's functions for the coseismic deformation of the 2005 M w 8.7 Nias-Simeulue, Sumatra earthquake. *Geochemistry Geophysics Geosystems*, 12, 2011.

Hudson, J.A. A Quantitative Evaluation of Seismic Signals at Teleseismic DistancesI Radiation from Point Sources. *Geophysical Journal of the Royal Astronomical Society*, 18, pp. 233–249, 1969.

Hung, H.K. and Rau, R.J. Surface waves of the 2011 Tohoku earthquake: Observations of Taiwan's dense high-rate GPS network. *Journal of Geophysical Research*, 118, pp. 332–345, 2013.

Irwan, M., Kimata, F., Hirahara, K., Sagiya, T. and Yamagiwa, A. Measuring ground deformations with 1-Hz GPS data: the 2003 Tokachi-oki earthquake (preliminary report). *Earth, Planets and Space*, 56, pp. 389–393, 2004.

Ji, C., Larson, K.M., Tan, Y., Hudnut, K.W. and Choi, K. Slip history of the 2003 San Simeon earthquake constrained by combining 1-Hz GPS, strong motion, and teleseismic data. *Geophysical Research Letters*, 31, 2004.

Jones, G., Raymer, D., Chamber, K. and Kendall, J.M. Improved microseismic event location by inclusion of a priori dip particle motion: a case study from Ekofisk. *Geophysical Prospecting*, 58, pp. 727–737, 2010.

Julian, B., Miller, A. and Foulger, G. Nondoublecouple earthquakes 1. Theory. *Reviews of Geophysics*, 36, pp. 525–549, 1998.

Kanamori, H. and Anderson, D. Theoretical basis of some empirical relations in seismology. *Bulletin of the Seismological*, 65, pp. 1073–1095, 1975.

Kanamori, H. Real-Time Seismology and Earthquake Damage Mitigation. *Annual Review of Earth and Planetary Sciences*, 33, pp. 195–214, 2005.

Kanamori, H. and Given, J.W. Use of long-period surface waves for rapid determination of earthquake-source parameters. *Physics of the Earth and Planetary Interiors*, 27, pp. 8–31, 1981.

Kennett, B.L.N. Reflections, rays, and reverberations. *Bulletin of the Seismological Society of America*, 64, pp. 1685–1696, 1974.

———. *Seismic Wave Propagation in Stratified Media*. Cambridge University Press, 1983.

Kennett, B.L.N., Engdahl, E.R. and Buland, R. Constraints on seismic velocities in the Earth from traveltimes. *Geophysical Journal International*, 122, pp. 108–124, 1995.

Kennett, B.L.N. and Kerry, N.J. Seismic waves in a stratified half space. *Geophysical Journal of the Royal Astronomical Society*, 57, pp. 557–583, 1979.

Keranen, K.M., Savage, H.M., Abers, G.a. and Cochran, E.S. Potentially induced earthquakes in Oklahoma, USA: Links between wastewater injection and the 2011 M_w 5.7 earthquake sequence. *Geology*, (March), 2013.

Knopoff, L. A matrix method for elastic wave problems. *Bulletin of the Seismological Society of America*, 54, pp. 431–438, 1964.

Knopoff, L. and Randall, M. The compensated linearvector dipole: A possible mechanism for deep earthquakes. *Journal of Geophysical Research*, 75, pp. 4,957–4,963, 1970.

Kobayashi, R., Miyazaki, S. and Koketsu, K. Source processes of the 2005 West Off Fukuoka Prefecture earthquake and its largest aftershock inferred from strong motion and 1-Hz GPS data. *Earth, Planets and Space*, 58, pp. 57–62, 2006.

Komatitsch, D., Liu, Q., Tromp, J., Suss, P., Stidham, C. and Shaw, J.H. Simulations of ground motion in the Los Angeles basin based upon the spectral-element method. *Bulletin of the Seismological Society of America*, 94, pp. 187–206, 2004.

Kouba, J. Measuring seismic waves induced by large earthquakes with GPS. *Studia Geophysica et Geodaetica*, 47, pp. 741–755, 2003.

Kreemer, C., Holt, W.E. and Haines, a.J. An integrated global model of present-day plate motions and plate boundary deformation. *Geophysical Journal International*, 154, pp. 8–34, 2003.

Kuehn, D., Vavryčuk, V., Aker, E., Gharti, H.N., Oye, V. and Huynh, K. Source Mechanisms of Acoustic Emissions due to Failure Around a Borehole in a Triaxial Lab Experiment. *Proceedings of the fourth EAGE Passive Seismic Workshop*, 2013.

Langbein, J. and Bock, Y. High-rate real-time GPS network at Parkfield: Utility for detecting fault slip and seismic displacements. *Geophysical Research Letters*, 31, pp. 2–5, 2004.

Larson, K.M. GPS seismology. *Journal of Geodesy*, 83, pp. 227–233, 2009.

Larson, K.M., Bodin, P. and Gomberg, J. Using 1-Hz GPS data to measure deformations caused by the Denali fault earthquake. *Science*, 300, pp. 1421–4, 2003.

Lay, T. Great Earthquake Ruptures in the Age of Seismo-Geodesy. *AGU Fall Meeting Abstracts*, 2011.

Lay, T. and Kanamori, H. Insights from the great 2011 Japan earthquake. *Physics Today*, 64, p. 33, 2011.

Li, X., Ge, M., Zhang, X. and Zhang, Y. Realtime highrate coseismic displacement from ambiguityfixed precise point positioning: Application to earthquake early warning. *Geophysical Research Letters*, 40, pp. 295–300, 2013.

Lohman, R.B. and Simons, M. Some thoughts on the use of InSAR data to constrain models of surface deformation: Noise structure and data downsampling. *Geochemistry, Geophysics, Geosystems*, 6, 2005.

Madariaga, R. Seismic source theory. In H. Kanamori, ed., *Earthquake Seismology*, Treatise on Geophysics, chap. 2, pp. 59–82. Elsevier, Amsterdam, 2007.

Maxwell, S., Rutledge, J., Jones, R. and Fehler, M. Petroleum reservoir characterization using downhole microseismic monitoring. *Geophysics*, 75, 2010.

McEvoy, F., Minchin, D., Harrison, D., Cameron, D., Evans, D., Lott, G., Hobbs, S. and Highley, D. Mineral resource information in support of national, regional and local planning: Lancashire (comprising Lancashire and the Boroughs of Blackpool and Blackburn. 2006.

McGuire, J., Zhao, L. and Jordan, T. Predominance of unilateral rupture for a global catalog of large earthquakes. *Bulletin of the Seismological Society of America*, 92, pp. 3,309–3,317, 2002.

Melgar, D., Bock, Y. and Crowell, B.W. Real-time centroid moment tensor determination for large earthquakes from local and regional displacement records. *Geophysical Journal International*, 188, pp. 703–718, 2011.

Mellors, R.J., Magistrale, H., Earle, P. and Cogbill, A. Comparison of four moderate-size earthquakes in southern California using seismology and InSAR. *Bulletin of the Seismological Society of America*, 94, pp. 2004–2014, 2004.

Menke, W. *Geophysical data analysis: discrete inverse theory*. Academic Press, 1989.

Miyazaki, S., Larson, K.M., Choi, K., Hikima, K., Koketsu, K., Bodin, P., Haase, J., Emore, G. and Yamagiwa, A. Modeling the rupture process of the 2003 September 25 Tokachi-Oki (Hokkaido) earthquake using 1-Hz GPS data. *Geophysical Research Letters*, 31, 2004.

Mooney, W.D., Laske, G. and Masters, T.G. CRUST 5.1: A global crustal model at 5 5. *Journal of Geophysical Research*, 103, pp. 727–747, 1998.

Morelli, A. and Dziewonski, A. Joint determination of lateral heterogeneity and earthquake location. In R. Sabadini, K. Lambeck and E. Boschi, eds., *Glacial Isostasy, Sea-Level and Mantle Rheology*, pp. 515–534. Kluwer Academic Publishers, Dordrecht, 1991.

Müller, G. The reflectivity method: a tutorial. *Journal of Geophysics*, 58, pp. 153–174, 1985.

Murray-Moraleda, J.R. and Simpson, R.W. Geodetically Inferred Coseismic and Postseismic Slip due to the M 5.4 31 October 2007 Alum Rock Earthquake. *Bulletin of the Seismological Society of America*, 99, pp. 2,784–2,800, 2009.

Musson, R. British earthquakes. *Proceedings of the Geologists' Association*, 118, pp. 305–337, 2007.

National Research Council. *Induced Seismicity Potential in Energy Technologies*. The National Academies Press, 2012.

Nikolaidis, R., Bock, Y., de Jonge, P., Shearer, P., Agnew, D. and Van Domselaar, M. Seismic wave observations with the Global Positioning System. *Journal of Geophysical Research*, 106, 2001.

Nolen-Hoeksema, R. and Ruff, L. Moment tensor inversion of microseisms from the B-sand propped hydrofracture, M-site, Colorado. *Tectonophysics*, 336, 2001.

Ohta, Y., Kobayashi, T., Tsushima, H., Miura, S., Hino, R., Takasu, T., Fujimoto, H., Iinuma, T., Tachibana, K., Demachi, T., Sato, T., Ohzono, M. and Umino, N. Quasi real-time fault model estimation for near-field tsunami forecasting based on RTK-GPS analysis: Application to the 2011 Tohoku-Oki earthquake (M_w 9.0). *Journal of Geophysical Research*, 117, 2012.

Okada, Y. Surface deformation due to shear and tensile faults in a half-space. *Bulletin of the Seismological Society of America*, 75, pp. 1,135–1,154, 1985.

Oliveira, S. and Stewart, D.E. *Writing Scientific Software*. Cambridge University Press, 2006.

O'Toole, T. and Woodhouse, J. Numerically stable computation of complete synthetic seismograms including the static displacement in plane layered media. *Geophysical Journal International*, 187, pp. 1,516–1,536, 2011.

O'Toole, T.B., Valentine, A.P. and Woodhouse, J. Earthquake source parameters from GPS-measured static displacements with potential for real-time application. *Geophysical Research Letters*, 40, 2013.

O'Toole, Thomas B. and Valentine, Andrew P. and Woodhouse, John H. Centroid-moment tensor inversions using high-rate GPS waveforms. *Geophysical Journal International*, 191, pp. 257–270, 2012.

Pan, E. Static Green's functions in multilayered half spaces. *Applied Mathematical Modelling*, 21, pp. 509–521, 1997.

Papoulia, J. and Makris, J. Microseismicity and active deformation of Messinia, SW Greece. *Journal of Seismology*, 8, pp. 439–451, 2004.

Parker, R. The Rosemanowes HDR Project 19831991. *Geothermics*, 28, pp. 603–615, 1999.

Parkinson, B. and Spiker, J.J. *Global Positioning System: Theory and Applications, Volume I*. American Institute of Aeronautics and Astronautics Inc, 1996.

Parliamentary Office of Science and Technology. UK Shale Gas Potential. 2013.

de Pater, C.J. and Baisch, S. Geomechanical Study of Bowland Shale Seismicity. 2011.

de Pater, H. and Pellicer, M. Geomechanical Study of Bowland Shale Seismicity – Fracture Geometry and Injection Mechanism. 2011.

Pavlis, G. and Booker, J. The mixed discrete-continuous inverse problem: application to the simultaneous determination of earthquake hypocenters and velocity structure. *Journal of Geophysical Research*, 85, pp. 4801–4810, 1980.

Pollitz, F. Coseismic deformation from earthquake faulting on a layered spherical Earth. *Geophysical Journal International*, 125, pp. 1–14, 1996.

Press, W.H., Teukolsky, S.A., Vetterling, W.T. and Flannery, B.P. *Numerical Recipes in FORTRAN; The Art of Scientific Computing*. Cambridge University Press, second edn., 1993.

von Rebeur-Paschwitz, E. The Earthquake of Tokio, April 19, 1889. *Nature*, 1889.

Riley, K.F., Hobson, M.P. and Bence, S.J. *Mathematical Methods for Physics and Engineering*. Cambridge University Press, third edn., 2007.

Ritsema, J., Deuss, a., van Heijst, H.J. and Woodhouse, J.H. S40RTS: a degree-40 shear-velocity model for the mantle from new Rayleigh wave dispersion, teleseismic traveltime and normal-mode splitting function measurements. *Geophysical Journal International*, 184(3), pp. 1223–1236, 2011.

Robinson, D.P. and Cheung, L.T. Source process of the M w 8.3, 2003 Tokachi-Oki, Japan earthquake and its aftershocks. *Geophysical Journal International*, 181, pp. 334–342, 2010.

Roumelioti, Z., Benetatos, C. and Kiratzi, A. The 14 February 2008 earthquake (M6.7) sequence offshore south Peloponnese (Greece): Source models of the three strongest events. *Tectonophysics*, 471, pp. 272–284, 2009.

Rutledge, J. and Phillips, W. Hydraulic stimulation of natural fractures as revealed by induced microearthquakes, Carthage Cotton Valley gas field, east Texas. *Geophysics*, 68, pp. 441–452, 2003.

Rutledge, J., Phillips, W. and Mayerhofer, M. Faulting induced by forced fluid injection and fluid flow forced by faulting: An interpretation of hydraulic-fracture microseismicity, Carthage Cotton Valley Gas Field, Texas. *Bulletin of the Seismological Society of America*, 94, p. 1817, 2004.

Sambridge, M. Geophysical inversion with a neighbourhood algorithmI. Searching a parameter space. *Geophysical Journal International*, pp. 479–494, 1999.

Satake, K. Tsunamis. In H. Kanamori, ed., *Earthquake Seismology*, Treatise on Geophysics, chap. 17, pp. 483–511. Elsevier, Amsterdam, 2007.

Scholz, C.H. *The Mechanics of Earthquakes and Faulting*. Cambridge University Press, second edition edn., 2002.

Segall, P. and Davis, J. GPS applications for geodynamics and earthquake studies. *Annual Review of Earth and Planetary Sciences*, 25, pp. 301–336, 1997.

Sella, G., Dixon, T. and Mao, A. REVEL: A model for recent plate velocities from space geodesy. *Journal of Geophysical Research*, 107, 2002.

Selley, R.C. *Elements of Petroleum Geology*. W. H. Freeman and Company, 1985.

———. UK shale gas: The story so far. *Marine and Petroleum Geology*, 31, pp. 100–109, 2012.

Shearer, P. Southern California Hypocenter Relocation with Waveform Cross-Correlation, Part 2: Results Using Source-Specific Station Terms and Cluster Analysis. *Bulletin of the Seismological Society of America*, 95, pp. 904–915, 2005.

———. *Introduction to Seismology*. Cambridge University Press, second edn., 2009.

Shi, C., Lou, Y., Zhang, H., Zhao, Q., Geng, J., Wang, R., Fang, R. and Liu, J. Seismic deformation of the Mw 8.0 Wenchuan earthquake from high-rate GPS observations. *Advances in Space Research*, 46, pp. 228–235, 2010.

Šilený, J., Hill, D.P., Eisner, L. and Cornet, F.H. Nondouble-couple mechanisms of microearthquakes induced by hydraulic fracturing. *Journal of Geophysical Research*, 114, 2009.

Simons, M., Fialko, Y. and Rivera, L. Coseismic deformation from the 1999 Mw 7.1 Hector Mine, California, earthquake as inferred from InSAR and GPS observations. *Bulletin of the Seismological Society of America*, 92, pp. 1390–1402, 2002.

Sobolev, S.V., Babeyko, A.Y., Wang, R., Hoechner, A., Galas, R., Rothacher, M., Sein, D.V., Schröter, J., Lauterjung, J. and Subarya, C. Tsunami early warning using GPS-Shield arrays. *Journal of Geophysical Research*, 112, pp. 1–18, 2007.

Song, F. and Toksoz, M.N. Full-waveform based complete moment tensor inversion and source parameter estimation from downhole microseismic data for hydrofracture monitoring. *Geophysics*, 76, 2011.

Stevens, P. The 'shale gas revolution': Developments and changes. 2012. http://kms2.isn.ethz.ch/serviceengine/Files/ESDP/152859/ipublicationdocument_singledocument/5a2f29de-7bb0-4dfe-bfd1-380c7e64a7de/en/bp0812_stevens.pdf.

Strang, G. and Borre, K. *Linear Algebra, Geodesy and GPS*. Wellesley–Cambridge Press, 1997.

Takeuchi, H. and Saito, M. Seismic Surface Waves. In *Methods in Computational Physics*, vol. 11 of *Methods In Computational Physics*, pp. 217–295. Academic Press, 1972.

Tarantola, A. *Inverse problem theory*. Elsevier, 2005.

Teunissen, P.J.G. and Kleusberg, A. *GPS for Geodesy*. Springer-Verlag, second edn., 1998.

The Royal Society. Shale gas extraction in the UK : a review of hydraulic fracturing. 2012.

Thomson, W.T. Transmission of Elastic Waves through a Stratified Solid Medium. *Journal of Applied Physics*, 21, pp. 89–93, 1950.

Thornton, M. and Duncan, P. Microseismic imaging with combined surface and downhole arrays Microseismic imaging with combined surface and downhole arrays. *SEG Technical Program Expanded Abstracts*, 2012.

Thrower, E.N. The computation of the dispersion of elastic waves in layered media. *Journal of Sound and Vibration*, 2, pp. 210–226, 1965.

Torge, W. *Geodesy*. de Gruyter, third edn., 1998.

Trampert, J. and Spetzler, J. Surface wave tomography: finite-frequency effects lost in the null space. *Geophysical Journal International*, 164, pp. 394–400, 2006.

Tsai, V.C. Multiple CMT source analysis of the 2004 Sumatra earthquake. *Geophysical Research Letters*, 32, 2005.

Tsui, J.B.Y. *Fundamentals of global positioning system receiver: a software approach.* Wiley, 2000.

Twardzik, C., Madariaga, R., Das, S. and Custódio, S. Robust features of the source process for the 2004 Parkfield, California, earthquake from strong-motion seismograms. *Geophysical Journal International*, 191, pp. 1,245–1,254, 2012.

Uchide, T., Yao, H. and Shearer, P.M. Spatio-temporal distribution of fault slip and high-frequency radiation of the 2010 El Mayor-Cucapah, Mexico earthquake. *Journal of Geophysical Research: Solid Earth*, 118, 2013.

US Energy Information Administration. World Shale Gas Resources: An Initial Assessment of 14 Regions Outside the United States. 2011.

Valentine, A.P. *Imaging the Earth : Methods and Algorithms for Global Seismic Tomography.* Ph.D. thesis, University of Oxford, 2010.

Valentine, A.P. and Trampert, J. Assessing the uncertainties on seismic source parameters: Towards realistic error estimates for centroid-moment-tensor determinations. *Physics of the Earth and Planetary Interiors*, 210-211, pp. 36–49, 2012.

Valentine, A.P. and Woodhouse, J.H. Reducing errors in seismic tomography: combined inversion for sources and structure. *Geophysical Journal International*, 180, pp. 847–857, 2010.

Valoroso, L., Chiaraluce, L., Piccinini, D. andDi Stefano, R., Schaff, D. and Waldhauser, F. Radiography of a normal fault system by 64,000 high-precision earthquake locations: the 2009 L'Aquila (central Italy) case study. *Journal of Geophysical Research*, 118, 2013.

Vavrycuk, V. On the retrieval of moment tensors from borehole data. *Geophysical Prospecting*, 55, pp. 381–391, 2007.

Vera Rodriguez, I., Gu, Y.J. and Sacchi, M.D. Resolution of Seismic-Moment Tensor Inversions from a Single Array of Receivers. *Bulletin of the Seismological Society of America*, 101, pp. 2634–2642, 2011.

Verdon, J., Kendall, J.M., White, D. and Angus, D. Linking microseismic event observations with geomechanical models to minimise the risks of storing CO2 in geological formations. *Earth and Planetary Science Letters*, 305, pp. 143–152, 2011.

Vigny, C., Simons, W.J.F., Abu, S., Bamphenyu, R., Satirapod, C., Choosakul, N., Subarya, C., Socquet, a., Omar, K., Abidin, H.Z. and Ambrosius, B.a.C. Insight into the 2004 Sumatra-Andaman earthquake from GPS measurements in southeast Asia. *Nature*, 436, pp. 201–206, 2005.

Vigny, C., Socquet, A., Peyrat, S., Ruegg, J.C., Métois, M., Madariaga, R., Morvan, S., Lancieri, M., Lacassin, R., Campos, J., Carrizo, D., Bejar-Pizarro, M., Barrientos, S., Armijo, R., Aranda, C., Valderas-Bermejo, M.C., Ortega, I., Bondoux, F., Baize, S., Lyon-Caen, H., Pavez, A., Vilotte,

J.P., Bevis, M., Brooks, B., Smalley, R., Parra, H., Baez, J.C., Blanco, M., Cimbaro, S. and Kendrick, E. The 2010 Mw 8.8 Maule megathrust earthquake of Central Chile, monitored by GPS. *Science*, 332, pp. 1417–1421, 2011.

Wang, G.Q., Boore, D.M., Tang, G. and Zhou, X. Comparisons of Ground Motions from Colocated and Closely Spaced One-Sample-per-Second Global Positioning System and Accelerograph Recordings of the 2003 M 6.5 San Simeon, California, Earthquake in the Parkfield Region. *Bulletin of the Seismological Society of America*, 97, pp. 76–90, 2007.

Wang, R. A simple orthonormalization method for stable and efficient computation of Green's functions. *Bulletin of the Seismological Society of America*, 89, pp. 733–741, 1999.

Wang, Y., Wen, L. and Weidner, D. Upper mantle SH- and P-velocity structures and compositional models beneath southern Africa. *Earth and Planetary Science Letters*, 267, pp. 596–608, 2008.

Wilson, S. Micro-seismic monitoring in the oil and gas industry. 2013. Presentation at AAPG Induced Seismicity Conference, London.

Woodhouse, J.H. Efficient and stable methods for performing seismic calculations in stratified media. In A.M. Dziewonski and E. Boschi, eds., *Proceedings of the International School of Physics 'Enrico Fermi', Course LXXVIII. Physics of the Earths Interior*, pp. 127–151. North-Holland, Amsterdam, 1980.

Woodhouse, J.H. and Deuss, A. Theory and Observations Earths Free Oscillations. In B.A. Romanowicz and A.M. Dziewonski, eds., *Seismology and Structure of the Earth*, Treatise on Geophysics, chap. 2, pp. 31–65. Elsevier, Amsterdam, 2007.

Woodhouse, J.H. and Dziewonski, A.M. Mapping the upper mantle: Three-dimensional modeling of earth structure by inversion of seismic waveforms. *Journal of Geophysical Research*, 89, pp. 5953–6297, 1984.

Wright, T.J., Houlié, N., Hildyard, M. and Iwabuchi, T. Real-time, reliable magnitudes for large earthquakes from 1 Hz GPS Precise Point Positioning: the 2011 Tohoku-Oki (Japan) earthquake. *Geophysical Research Letters*, 39, pp. 1–5, 2012.

Wuestefeld, A., Baig, A.M. and Urbancic, T.I. Bandwidth coupling issues in recording passive seismicity. 2013. Proceedings of the fourth EAGE Passive Seismic Workshop.

Wuestefeld, A., Verdon, J.P., Kendall, J.M., Rutledge, J., Clarke, H. and Wookey, J. Inferring rock fracture evolution during reservoir stimulation from seismic anisotropy. *Geophysics*, 76, 2011.

Yagi, Y. and Fukahata, Y. Importance of covariance components in inversion analyses of densely sampled observed data: an application to waveform data inversion for seismic source processes. *Geophysical Journal International*, 175, pp. 215–221, 2008.

———. Introduction of uncertainty of Green's function into waveform inversion for seismic source processes. *Geophysical Journal International*, 186, pp. 711–420, 2011.

Yang, H.Y., Zhao, L. and Hung, S.H. Synthetic seismograms by normal-mode summation: a new derivation and numerical examples. *Geophysical Journal International*, 183, pp. 1613–1632, 2010.

Yin, H., Wdowinski, S., Liu, X., Gan, W., Huang, B., Xiao, G. and Liang, S. Strong Ground Motion Recorded by High-Rate GPS of the 2008 Ms 8.0 Wenchuan Earthquake, China. *Seismological Research Letters*, 84, pp. 210–218, 2013.

Yokota, Y., Koketsu, K., Hikima, K. and Miyazaki, S. Ability of 1-Hz GPS data to infer the source process of a medium-sized earthquake: The case of the 2008 Iwate-Miyagi Nairiku, Japan, earthquake. *Geophysical Research Letters*, 36, 2009.

Young, R.P. *Rockbursts and Seismicity in Mines 93*. A. A. Balkema, 1993.

Yue, H. and Lay, T. Inversion of high-rate (1 sps) GPS data for rupture process of the 11 March 2011 Tohoku earthquake (M w 9.1). *Geophysical Research Letters*, 38, 2011.

Zheng, Y., Li, J., Xie, Z. and Ritzwoller, M.H. 5Hz GPS seismology of the El Mayor-Cucapah earthquake: estimating the earthquake focal mechanism. *Geophysical Journal International*, 190, pp. 1723–1732, 2012.

Zhu, L. and Rivera, L.A. A note on the dynamic and static displacements from a point source in multilayered media. *Geophysical Journal International*, 148, pp. 619–627, 2002.

Zumberge, J.F., Heflin, M.B., Jefferson, D.C., Watkins, M.M. and Webb, F.H. Precise Point Positioning for the Efficient and Robust Analysis of GPS Data from Large Networks. *Journal of Geophysical Research*, 102, pp. 5005–5017, 1997.